Domain wall dynamics driven by spin-current in ferrimagnetic alloys

Eloi Haltz

▶ **To cite this version:**

HAL Id: tel-02903018
https://theses.hal.science/tel-02903018

Submitted on 20 Jul 2020

université
PARIS-SACLAY

S UNIVERSITÉ
PARIS
SUD

Comprendre le monde,
construire l'avenir

Domain Wall Dynamics driven by spin-current in Ferrimagnetic alloys

Thèse de doctorat de l'Université Paris-Saclay
préparée à l'Université Paris-Sud

École doctorale n°572 École Doctorale Ondes et Matière (EDOM)
Spécialité de doctorat : Nanophysique

Thèse présentée et soutenue à Orsay, le 19/12/2019, par

ELOI HALTZ

Composition du Jury :

Vincent Cros Directeur de recherche, Laboratoire CNRS/Thales (Palaiseau)	Président
Stuart Parkin Professeur, Max Planck Institute - Institute of Physics of the Martin-Luther-University (Halle)	Rapporteur
Christian Back Professeur, Technical University (Munich)	Rapporteur
Laura Thevenard Chargée de recherche, Institut des NanoSciences (Paris)	Examinateur
Olivier Boulle Chargé de recherche, SPINTEC (Grenoble)	Examinateur
Alexandra Mougin Directrice de recherche, Laboratoire de Physique des Solides (Orsay)	Directrice de thèse
João Sampaio Chargé de recherche, Laboratoire de Physique des Solides (Orsay)	Co-directeur de thèse

Contents

List of Figures

List of Tables

Acknowledgment

The work I have accomplished during the three years of my doctorate would not have been possible without the invaluable help and strong commitment of the people whom I would like to thank now.

First of all, I would like to dedicate a special acknowledgment to my two supervisors: Alexandra Mougin and João Sampaio for their management, their trust and their inspiring guidance. All their scientific and human qualities gave me the opportunity to undertake this thesis in the best conditions. I also would like to thank them for the help with the manuscript writing. I would like also to thank Raphaël Weil for his help with the sample fabrication, his continuous support and for the teaching experience. More generally, I want to thank all the people of the IDMag team with whom I have had the pleasure of working or simply conversing. For all the advice, the inspiring, fruitful and enjoyable moments, I thank: Sachin Krishnia, André Thiaville, Léo Berges, Stanislas Rohart, Vincent Jeudy, Sougata Mallick, Pierre Gehanne, Jacques Miltat, Rebeca Diaz Prado, Lucas Albornoz, Ryuhei Kohno, Colin Avogadri, Gajanan Pradhan, Ales Hrabec, Souvik Das.

I am grateful to the members of my jury to have taken the time to read my manuscript and for their interesting questions and comments.

I would like to thank all the collaborators with whom I have had the pleasure of working: Vincent Jacques, Richard Mattana, Oliver Váhovský and the Rastislav Varga's group, Aurélien Masseboeuf, Cyril Bachelet, Zhizhong Li, the STEM team, Yves Dumont and the Synchrotrons local-contacts : Lucia Aballe and Michael Foerster (Alba), Florian Kronast and Mohamad Mawass (Bessy), Rachid Belkhou (Soleil), Marcus Weigand and Michael Bechtel (Bessy). I would like to thank all the administrative and technical services of the LPS and of the University: Mélanie Decraene, Véronique Thieulart, Jacques Robert, Pascale Senzier, Jean-Pierre Dalac, Vincent Klein, Jérémie Sanchez, Ilan Settouraman.

I would like to thank the EDOM for my PhD funding and the Labex Nano-Saclay and the IEEE for different grants that gave me the opportunity to enjoy very enrichening scientific experiences.

Finally, I would like to thank my family and friends for their support during the past three years.

Synthèse en français

Dans les matériaux magnétiques, l'aimantation est susceptible de s'organiser en différentes régions dont l'aimantation pointe dans la même direction appelées domaines magnétique. Ces domaines sont séparés par des zones où l'aimantation change continument d'un domaine à l'autre appelées parois magnétiques. Due à sa rémanence, cette organisation de l'aimantation en domaines est très utilisée par les technologies actuelles pour encoder et conserver l'information numérique de manière non-volatile. Toutefois, dans ces dispositifs, la manipulation de cette information est opérée par un déplacement mécanique du milieu magnétique ce qui limite intrinsèquement leur vitesse et leur robustesse pour la lecture et l'écriture. Une alternative pourrait donc être d'agir directement sur les parois magnétiques. Il a été démontré qu'un courant électrique permet d'obtenir un mouvement cohérent de ces parois (sans déformation des domaines) grâce à l'interaction entre le spin des électrons et l'aimantation locale du matériau. Plus qu'un simple moyen de transporter l'information, cette nouvelle approche propose également de nouveaux dispositifs permettant de la traiter.

Malgré les grands succès de la spintronique de ces dernières années, plusieurs questions demeurent quant à l'efficacité et la rapidité de la manipulation électrique de textures magnétiques telles que les parois de domaines. Ces problèmes semblent pouvoir être résolus en considérant de nouveaux matériaux, plus exotiques, mélangeant différents sous-réseaux magnétiques couplés antiferromagnétiquement. L'avantage d'utiliser de tels matériaux est double : minimiser leur aimantation totale ce qui réduit les tailles caractéristiques des textures magnétiques ; minimiser leur moment angulaire résultant ce qui accélère significativement leurs dynamiques. Plusieurs matériaux sont prometteurs: les matériaux antiferromagnétiques (qui présentent des dynamiques d'aimantation ultra-rapides mais pour lesquelles la manipulation et la lecture de l'aimantation reste complexe), les empilements de type antiferromagnétiques-synthétique (plus robustes et pour lesquels la lecture et la manipulation de l'aimantation semblent plus simples au dépend d'un couplage inter-sous-réseaux plus faible) ou encore les matériaux ferrimagnétiques (pour lesquels les deux sous-réseaux sont différents).

En particulier, les alliages ferrimagnétiques de type terrers rares-métaux de transition sont composés de deux populations magnétiques couplées antiferromagnétiquement. A l'inverse des matériaux antiferromagnétiques, leurs deux sous-réseaux sont différents et uniquement l'un d'eux interagit avec le courant électrique ce qui permet une lecture et une manipulation de l'aimantation beaucoup plus directes. De plus, les propriétés magnétiques de ces alliages changent drastiquement avec leur composition chimique ou, plus simplement, avec la température. Deux configurations particulièrement intéressantes se distinguent : les points de compensation magnétique et angulaire auxquels l'aimantation ou le moment angulaire totales de l'alliage s'annulent. Due aux natures différentes des deux sous-réseaux, ces deux configurations de compensations sont différents ce qui confère à ces alliages une très grande gamme de propriétés magnétiques. Toutefois, même si la plupart des propriétés statiques de ces matériaux sont désormais comprises, une compréhension fine de leurs propriétés dynamiques fait toujours défaut en particulier autour des points de compensation, où leur comportement s'écarte du cas ferromagnétique bien connu.

Dans cette thèse, ces propriétés dynamiques ont été étudiée expérimentalement et théoriquement sous le prisme de la dynamique de paroi magnétique sous courant de spin.

Des alliages ferrimagnétiques (comme le TbFe, le TbFeCo ou le GdFeCo) ont été déposés en couches minces par co-évaporation et étudiés en combinant plusieurs méthodes : magnétiques, électriques et optiques, ce qui a notamment confirmé le grand intérêt de ces matériaux des fin spintroniques Des techniques d'imagerie ont également montré une organisation en domaines magnétique, séparés par des parois mobiles. Une étude fine de la composition de ces alliages a également révélé l'existence d'un gradient chimique en épaisseur au sein des films. Ce gradient de composition induit une déviation des propriétés magnétiques ainsi que des effets habituellement surfaciques tels que le DMI. En particulier, une étude en imagerie X a révélé que la coexistence de ce gradient en épaisseur et d'une très faible aimantation permet la stabilisation de paroi, dite de Néel, en l'absence de couche à fort couplage spin-orbite.

La dynamique de ces parois sous courant de spin (par couple de transfert de spin et spin-orbite) a également été étudiée dans deux études. La première consiste à sonder les effets du courant électrique sur ces parois en mesurent leur déplacement sous les effets combinés d'un champ magnétique et d'un courant dans leur régime de reptation. Cette étude a mis en évidence une grande efficacité d'un courant de spin dans la manipulation d'une paroi de domaine. La seconde étude consiste à mesurer la dynamique interne de la paroi de domaine en mouvement en mesurant ses déplacement induits par un courant de spin (couple spin-orbite) sous un champ dans le plan. Cette seconde étude à notamment mis en évidence un pic de mobilité directement associé à un renversement de l'aimantation sans précession à la compensation angulaire.

Enfin, un modèle théorique effectif de ces matériaux multi-réseaux permettant de décrire et prédire à la fois leurs propriétés statiques et dynamiques a été développé pour ces alliages. Celui-ci révèle notamment de nouveaux modes de propagation de paroi comme le retournement de l'aimantation sans précession ou la disparition de régimes transitoires.

Introduction

Despite the large success of spintronics in applications such as hard-disk read heads, magnetic sensors and radiation-hard MRAM devices, the efficient and fast electrical manipulation of magnetic textures such as domain walls or skyrmions as information carriers remains a key challenge to develop low-power devices [1–10]. To overcome these fundamental limitations due to the ferromagnetic materials (classically used), more exotic systems have to be developed to become core elements for future spintronics. One of the proposed ways is to couple different magnetic sub-lattices to obtain optimal magnetization dynamic properties [11–17]. Promising theoretical results and experimental observations have been recently obtained in complex materials [18,19], multilayer architectures [12,16,17], or synthetic alloys [13,14,20–22]. In particular, it has been pointed out that an antiferromagnetic coupling between sub-lattices decreases drastically characteristic times of magnetization dynamics into the THz-ps range [23–25]. However, pure antiferromagnets are hard to probe and manipulate both magnetically, due their tiny magnetization, and electrically, due to the same nature of their two sub-lattices or the insulating nature of most of them. Furthermore, due to their magnetic moment organization, their manipulation by spin-current remains challenging and requires very specific structures [19, 26, 27]. One of the very promising and versatile alternative to antiferromagnets are ferrimagnetic materials such as rare earth-transition metal alloys.

RE-TM alloys are composed of two different magnetic sub-lattices antiferromagnetically coupled. Unlike to pure antiferromagnets, their two sub-lattices are different and just one of them interacts with the electrical current [28,29]. Thanks to this property, it should be much easier to probe and manipulate their magnetic carriers by electrically addressing just one of the sub-lattices. Furthermore, the magnetic properties of these alloys change drastically with temperature and with their chemical composition [30], which makes them a very interesting subject for fundamental studies of multi-sub-lattices materials. Recently, these ferrimagnets have revealed very convenient spintronic properties [13,14,21,22]. Two configurations, called the magnetic and the angular compensation points where either the net magnetization or the total angular momentum vanishes, are of particular interest. Due to the different nature of the sub-lattices, the two compensation points do not occur at the same temperature [31] and ferrimagnets can present a large diversity of properties. In particular, the vanishing of the net magnetization can be very convenient in order to reduce the size of magnetic textures [14,32] and the vanishing of the angular momentum can be exploited to induce fast magnetization dynamics [13]. However, even if most of the static properties of these materials are now well understood [30], a precise knowledge of their dynamic behavior is still lacking, in particular near the compensation points where the dynamics differ the most from the well-studied ferromagnetic case.

In this thesis, I have investigated the dynamic properties of RE-TM ferrimagnetic alloys through the prism of magnetic domain wall dynamics. I have grown RE-TM ferrimagnetic alloys (such as TbFe, TbFeCo or GdFeCo) as thin films by co-evaporation and studied the dynamics of DW driven by field and spin currents in these materials. I also have developed a theoretical model which describes both their static and dynamic properties.

This manuscript contains the most interesting and valuable results obtained during my thesis work. It is divided in four chapters, almost independent, that describe different areas of the DW dynamics study.

- **Chapter 1** I present the static properties of ferrimagnetic films. The deposition process, the characterization of films and their internal magnetic organization by a complementary set of methods are detailed. A focus is made on the internal domain structure whose nature impacts directly its dynamics.

- **Chapter 2** I propose a theoretical model on the dynamic properties of RE-TM ferrimagnets based on an effective parameters approach. This model is used to investigate analytically and numerically the DW dynamics driven by field or spin currents. Results on DW velocities are compared for different drives such as magnetic field, spin transfer and spin orbit torques. Three methods corroborate the results obtained during this study: two analytical methods based on collective coordinates by considering an infinite or finite coupling between sub-lattices and a numerical micromagnetic approach allowing much more degrees of freedom for the DW dynamics.

- **Chapter 3** I experimentally investigate the dynamics of a DW driven by spin transfer-torque. The current contributions are measured by studying the DW motions under combined effects of field and current in creep regime.

- **Chapter 4** I study DW dynamics driven by spin-orbit torques in a stack including adjacent heavy-metal layers. The internal DW dynamics is fully resolved using in-plane fields revealing new behaviors at the angular compensation point.

At the the end of each chapter, conclusions and perspectives are drawn. People involved in the work are named and publications in relation with the results are mentioned.

Static properties of rare-earth transition-metal ferrimagnetic thin films

In this chapter, I will introduce and characterize the static properties of the ferrimagnetic films I have studied in this thesis. This chapter is divided in four sections. Each section starts with a short introduction of the required theoretical concept for the following parts. In section 1.1, I briefly describe the understanding of the origins of the ferrimagnetic order in RE-TM alloys based on the mean-field model. In section 1.2, I describe the work developed to deposit RE-TM alloy thin films by co-evaporation and the basic structural and chemical properties of the films. In section 1.3, I present the macroscopic magnetic, electrical and optical properties of deposited thin films based on original experimental results measured in our sample. In sections 1.4, I consider microscopic magnetic properties by imaging methods (Kerr and XPEEM). Both the domain organization and the internal DW structure are investigated. Extended results and future perspective of these static studies of ferrimagnets are presented in the additional section 1.6. Finally, even though all the studied samples were deposited in our laboratory, additional experiments required for a further characterization of magnetic properties were done in partnership with others researchers. Their contributions are detailed in the part 1.7.

1.1 Ferrimagnetism in rare-earth transition-metal alloys

1.1.1 Exchange interaction and magnetic orders

As carriers of an intrinsic angular momentum called spin, electrons are the elementary building blocks of magnetism. In condensed matter, they can interact with each other and induce a macroscopic magnetic state. Due to the combination of the Coulomb repulsion and the Pauli exclusion principle, two neighboring magnetic moment holders (with magnetic moment $\vec{S}_i$ and $\vec{S}_j$) interact by the so called the exchange coupling. This interaction can be associated with an exchange coupling energy:

$$\epsilon_{ex\,ij} = J_{ij}\vec{S}_i \cdot \vec{S}_j \tag{1.1}$$

with J_{ij} the exchange coupling parameter between $\vec{S}_i$ and $\vec{S}_j$ moments. Depending on the symmetry and the overlap of the $\vec{S}_i$ and $\vec{S}_j$ states, the exchange parameter can be negative or positive. Considering a large assembly of magnetic moments, the full exchange interaction resulting from all moment pairs $< i, j >$ ($\sum_{<i,j>} \epsilon_{ex\,ij}$) aligns the magnetic moments parallel or anti-parallel which establishes a magnetic order. Depending on the J_{ij} sign, a ferromagnetic or an antiferromagnetic order emerges (as shown Fig. 1.1 (a) and (b)). In the classical ferromagnets or antiferromagnets, all active magnetic moments have the same nature with the same properties.

A ferrimagnet is another type of magnetic material containing two or more different magnetic populations with different magnetic properties called sub-lattices. Here, the word sub-lattice just refers to

the two magnetic populations and has no crystallographic meaning. The moments of each sub-lattice are ferromagnetically coupled, whereas the moments of two different sub-lattices can be ferromagnetically or antiferromagnetically coupled (as shown Fig. 1.1 (c)). The ferrimagnetic texture can be obtained in many different systems mixing different magnetic populations, such as: magnetite $Fe_3 O_4$ [33], rare-earth iron garnets $RE_3Fe_5O_{12}$ with RE a rare-earth (such as Gd, Tb, Dy, Yd...) [34] or RE-TM alloys with TM a *3d* transition metal (such as Mn, Co, Fe or Ni) [30, 35].

(a)　　　　　　　　　　(b)　　　　　　　　　　(c)
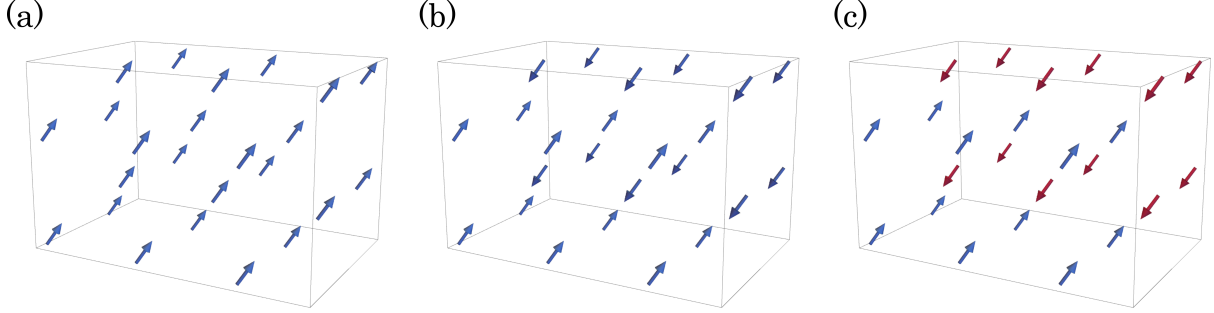
Figure 1.1 – Sketch of the different magnetically-ordered materials: (a) Ferromagnet, (b) Antiferromagnet and (c) Ferrimagnet.

In this thesis, we investigate the magnetic properties of RE-TM ferrimagnetic alloys containing RE such as Gd or Tb and TM such as Fe or Co. These artificial alloys can be created by co-sputtering [30, 36] or co-evaporation [37]. They were very well studied in their bulk form for data recording applications [38] or all optical switching [39, 40]. More recently, they have been studied in thin layers and have seen a renewed interest in their very interesting spintronic properties [13, 14, 20–22, 41–46].

1.1.2　Exchange and order in RE-TM ferrimagnetic alloys

In the studied RE-TM ferrimagnetic amorphous alloys (such as the GdFeCo, TbFe, TbFeCo, GdCo...), electronic states of the chemical elements interact to give a ferrimagnetic order [28–30, 35, 37, 47–54]. The complex coupling interactions between different occupied electronic states have already been well-investigated [28, 30, 35, 47, 49] revealing three main exchange interactions. Firstly, the most important is the intra-sub-lattice ferromagnetic exchange interaction between the *3d* e^- of the TM as described by the Stoner model [55–57]. Secondly, due to the band structure of the RE and TM elements, the overlap between their d electron states gives an extra-atomic antiferromagnetic coupling between these electron moments. Finally, the RE band structure induces an intra-atomic ferromagnetic coupling between the *4f* e^- and the *5d* e^- [28, 29, 47]. Due to the hybridization between the *3d* e^- and the s e^-, the d e^- of the alloy are delocalized as usual for TM ferromagnets [55]. The other second order exchange interactions, like between the *4f* e^- of the RE *via* the *5d* e^-, can be neglected [30, 51]. Fig. 1.2 (a) (from [49]) shows schematically the occupied electronic states and the two main exchange coupling interactions: the inter- and the intra-atomic couplings and their associated density of state distributions in Fig. 1.2 (b). Fig. 1.2 (c) (from [28]) shows the calculated spin-resolved electronic density of state of a GdCo alloy. It possible to see the good agreement with the schematic electronic structure (in (a) and (b)). Here, it is clear that the resulting delocalized magnetic moments (around the Fermi level) are anti-aligned with the localized moments (well below the Fermi Level) [28, 29].
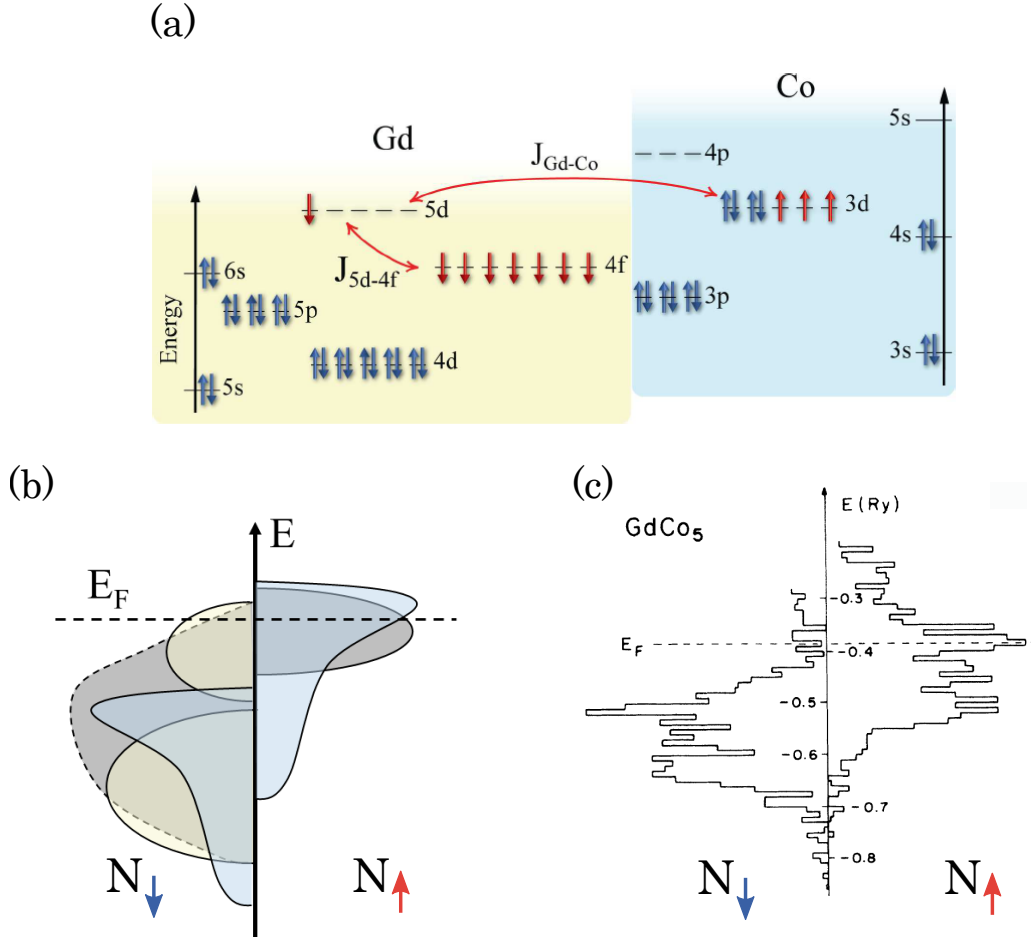
Figure 1.2 – Electronic structure of GdCo. (a) (from [49]) Sketch of the electronic occupied states in a GdCo alloy. The red double-arrows indicate the main exchange couplings between electron states. The J_{Gd-Co} one indicates the antiferromagnetic exchange between delocalized electrons [55] and the J_{5d-4f} one indicates the ferromagnetic exchange between localized and delocalized Gd electrons [28]. (b) Schematic spin-resolved density of state resulting from the electronic structure in (a). The blue and yellow regions correspond to states from Co and Gd and the gray region to the resulting GdCo alloy. (c) (from [28]) Calculated spin-resolved density of states for a GdCo ferrimagnetic alloy. The horizontal dashed line corresponds to the Fermi level.

Summary   In the RE-TM ferrimagnetic alloys, two sub-lattices can be identified: the localized and delocalized magnetic moments which correspond roughly to the *4f* and the *3-5d* e^-. The resulting delocalized moment is antialligned with the localized one that gives a ferrimagnetic order. In the next part, we speak abusively of RE and TM sub-lattices for localized and delocalized moments. This electronic structure and the resulting magnetic order do not depend much on the considered RE-TM alloy and the above detailed framework holds for all the considered Gd, Tb, Co,Fe-based alloys [30].

1.1.3 Mean-field analysis and alloy net-magnetization

Mean-field analysis   Knowing the different sub-lattices and their exchange interactions, it is possible to use a mean-field approach to quantify the resulting magnetization of each sub-lattice [30, 58]. This method accounts for the exchange interaction with a local field that depends on the magnetic states of the other moments. This field is called the molecular field, written here H_{mf} [55, 59]. Applying the Brillouin formalism [55], it is possible to calculate the temperature dependence of the magnetization *via* two coupled implicit equations [30, 51, 58, 60–63]:

$$\begin{cases} \vec{M}_1 = N_1 \vec{\mu}_1 \mathcal{B}_{J_1} \left(\frac{\mu_0 \vec{\mu}_1 \vec{H}_{1\leftarrow mf}}{k_B T} \right) \\ \\ \vec{M}_2 = N_2 \vec{\mu}_2 \mathcal{B}_{J_2} \left(\frac{\mu_0 \vec{\mu}_2 \vec{H}_{2\leftarrow mf}}{k_B T} \right) \end{cases} \tag{1.2}$$

where 1 and 2 designate, respectively, the TM and the RE sub-lattices. N_i is the atomic density of the i sub-lattice. $\mu_i = g_i J_i \mu_B$ is the magnetic moment per atom for the i magnetic population with a Landé g-factor $g_i = \frac{3J_i(J_i+1)+S_i(S_i+1)-L_i(L_i+1)}{2J_i(J_i+1)}$ (which takes into account the magnetic contribution of each quantum number S_i, L_i and J_i associated with the electronic state of the i sub-lattice given in Tab. 1.1). μ_0 is the vacuum permeability and μ_B is the Bohr magneton. $\mathcal{B}_J$ is the Brillouin function:

$$\mathcal{B}_J(X) = \frac{2J+1}{2J} \coth\left(\frac{2J+1}{2J} X \right) - \frac{1}{2J} \coth\left(\frac{1}{2J} X \right) \tag{1.3}$$

which takes into account the thermal effect on the resulting magnetization. Here, each sub-lattice feels a different molecular field H_{mf} of:

$$\begin{cases} \vec{H}_{1\leftarrow mf} = \lambda_{1\leftarrow 1}\vec{M}_1 + \lambda_{1\leftarrow 2}\vec{M}_2 \\ \\ \vec{H}_{2\leftarrow mf} = \lambda_{2\leftarrow 2}\vec{M}_2 + \lambda_{2\leftarrow 1}\vec{M}_1 \end{cases} \tag{1.4}$$

with λ the molecular field coefficients. $\lambda_{i\leftarrow j}$ are the inter-sub-lattice coefficients which represent the magnitude of the molecular field exercised on a i atom from the j atoms. $\lambda_{i\leftarrow i}$ are the intra-sub-lattice coefficients which represent the coupling between moments from the same sub-lattice i. They take into account: the exchange amplitude J_{ij} (as defined Eq. 1.1), Z_{ij}, the number of j-type neighbors around a i-type atom, g_j the Landé g-factor and N_i, the density of the i lattice (Eq. 1.5):

$$\lambda_{i\leftarrow j} = -\frac{Z_{ij}J_{ij}}{\mu_0 \mu_B^2 g_i g_j N_j} \tag{1.5}$$

Note that for a ferrimagnetic order, $J_{ij} < 0$ for $i = j$ and $J_{ij} > 0$ for $i \neq j$ (as disused Part. 1.1.2).

Element	e^- config.	S	L	J	g_J
Fe^{3+}	[Ar]3d^5	5/2	0	5/2	2
Fe^{2+} Co^{3+}	[Ar]3d^{6}4s^2	2	2	4	3/2
Co^{2+}	[Ar]3d^7	3/2	3	9/2	7/3
Gd	[Xe]4f^{7}5d^{1}6s^2	7/2	0	7/2	2
Tb	[Xe]4f^{8}5d^{1}6s^2	3	3	6	3/2

Table 1.1 – Electronic configuration of the considered elements and resulting quantum numbers.

Considering a RE-TM alloy, the mean-field model parameters depend on the alloy's chemical composition. Few empirical expressions are proposed [30, 62, 63]. Due to to the different sizes of atoms, the number of nearest neighbors and density changes with composition. Writing x the TM composition, the numbers of the nearest neighbors can be written: $Z_{TM \cdot TM} \approx (6 + 6x)x$, $Z_{RE \cdot RE} \approx (12 + 6x)(1 - x)$, $Z_{RE \cdot TM} \approx (12 + 6x)x$, $Z_{RE \cdot TM} \approx (12 + 6x)(1 - x)$ according to [60] and the sub-lattice densities: $N_{TM} = xN$ and $N_{RE} = (1 - x)N$ with $N \approx (7,27x + 0.85).10^{28}$ atoms/m^3 according to [54]. The exchange constants are symmetric and: $J_{RE \cdot TM} = J_{TM \cdot RE} \approx (-37.5x + 38.75).10^{-23}$J/m^3 according

to [60]. Due to the different filling of the electronic states of the TM sub-lattice, the total angular momentum number J_i changes with composition: $J_{TM}(x) = J_{TM}(x=1) \sum_{k=l}^{n} \frac{n!}{k!(n-k)!} x^k (1-x)^{n-k}$ with $n = 12$ and $l = 5$ for Fe and $l = 7$ for Co according to [30]. As discussed in part 1.1.2, the intra-exchange coupling of the RE can be neglected, $J_{RE \cdot RE} \approx 0$, whereas the intra-exchange coupling of the TM is large: $J_{TM \cdot TM} \approx 40.10^{-23} \text{J/m}^3$.
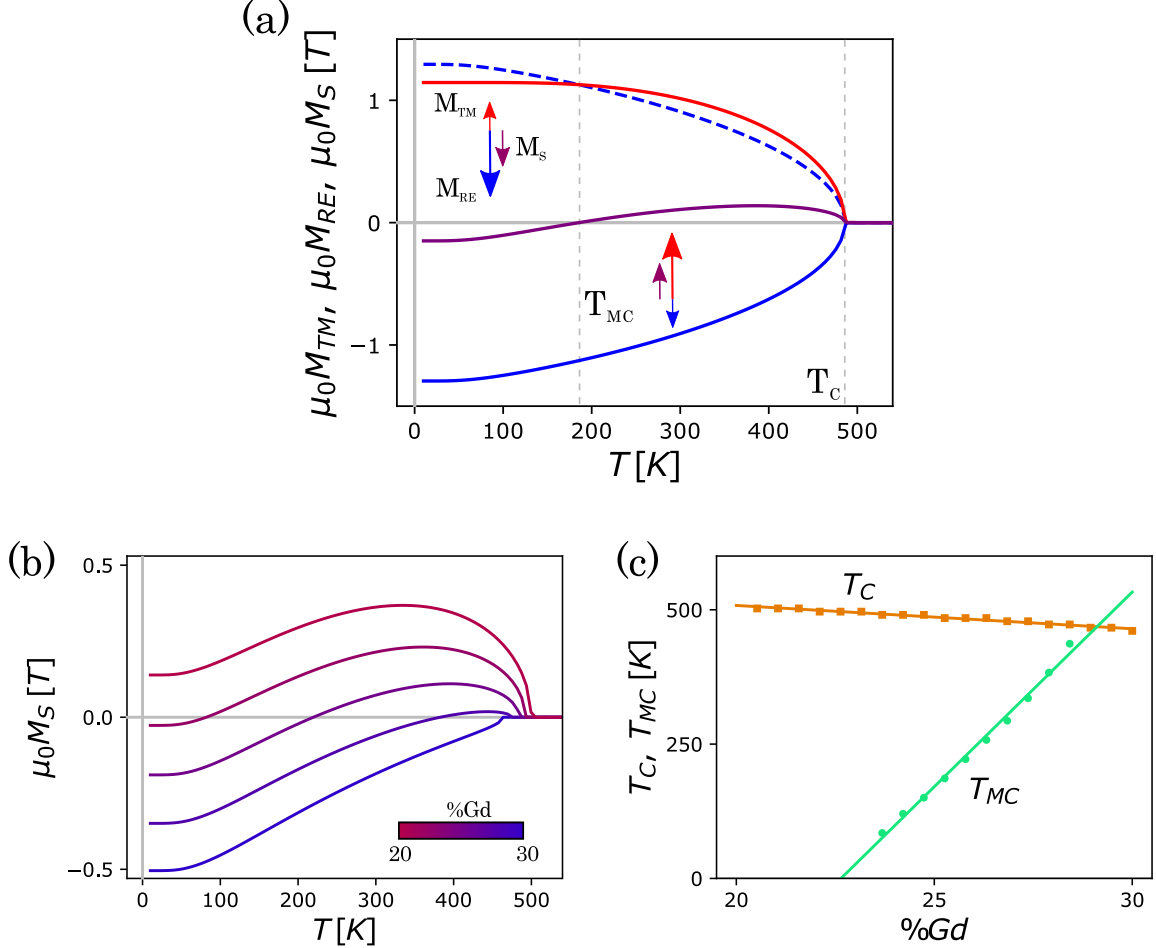
Figure 1.3 – Mean-field model of GdCo. (a) Magnetization of the TM and the RE sub-lattices and the net magnetization M_S *versus* the temperature T for a $Gd_{0.25}Co_{0.75}$. The red, blue and purple arrows represent the algebraic values of the magnetization of, respectively, TM, RE and of the full alloy. The blue dashed line corresponds to the absolute magnetization of the RE sub-lattice. (b) Net magnetization M_S *versus* the temperature T for a $\%Gd \in [0.2, 0.3]$. (c) The Curie temperature T_C and the magnetic compensation temperature T_{MC} for different alloy composition $\%Gd$. All these values are from a mean-field calculation (Eq. 1.2) considering standard values of $A_{TM-TM} = 40.10^{-23}$ J and $A_{RE-RE} = 0$.

Magnetization *versus* temperature Solving the equations 1.2, it is possible to calculate the magnetization of both sub-lattices M_{TM} and M_{RE} *versus* the temperature or the alloy chemical composition. The net magnetization of the alloy M_S is simply the algebraic sum of the magnetization of both sub-lattices: $M_S = M_{TM} + M_{RE}$. Note that the M_{RE} obtained values are negative and that it can be more intuitive to write $M_S = |M_{TM}| - |M_{RE}|$. Fig. 1.3 (a) shows the temperature dependence of M_{TM} (in red), M_{RE} (in blue) and M_S (in purple) *versus* the temperature T for a $Gd_{0.25}Co_{0.75}$ alloy considering the above parameters. The blue dashed lines corresponds to the absolute magnetization $|M_{RE}|$. Even if both sub-latice magnetizations are close to a pure Gd or Co material ones, the resulting alloy magnetization M_S is very small (10 times smaller) [30, 52]. Due to the inter-exchange coupling between sub-lattices,

both alloy components have the same Curie temperature T_C [30], lower than a pure TM material one. It is also possible to see that, due to the different quantum number of each sub-lattice, the $M_{TM}(T)$ is flatter than $M_{RE}(T)$. An interesting point is observed where both sub-lattice magnetizations have the same magnitude, $M_{TM} = -M_{RE}$, and so the resulting magnetization completely vanishes, $M_S = 0$. This situation is called the magnetic compensation point *MCP*. At *MCP*, the magnetization of both sub-lattices are non-zero. For temperatures below the *MCP*, the magnetization of the RE sub-lattice is larger than the TM one, which means the net magnetization is aligned along the RE one. In contrast, for temperatures above the *MCP*, the net magnetization is aligned along the TM sub-lattice. We say that the alloy is respectively RE or TM dominated. In the following parts, we consider M_{RE} as the absolute value *i.e.* $M_{RE} \equiv |M_{RE}|$.

Increasing/decreasing the *TM-TM* exchange parameter, mainly the T_C increases/decreases, and increasing/decreasing the RE-TM one, the T_{MC} increases/decreases. Changing the density mainly changes both RE and TM magnetization.

Magnetization *versus* alloy composition Fig. 1.3 (b) shows the calculated M_S *versus* T for different alloy composition in a range of $\%Gd \in [20, 30\%]$. The Curie temperature T_C does not depend much on the alloy composition. Conversely, the *MCP* changes greatly with $\%Gd$ [30, 54, 60]. It is possible to reach this *MCP* either by changing the temperature for a given composition or by changing the composition for a fixed temperature. In these situations, we speak about, respectively, magnetic compensation temperature T_{MC} or composition $\%Gd_{MC}$. Fig. 1.3 (c) shows the dependence of T_{MC} and of the Curie temperature T_C for different alloy compositions. As expected [30], the Curie temperature T_C is almost independent of the alloy composition wheres T_{MC} drastically changes (quasi-linearly with $\%Gd$: $70K/\%Gd$). The quasi-constant T_C value acts like a cut-off for the compensation temperature T_{MC}: T_{MC} can not be higher than T_C and the magnetic compensation exists just for a short range of $\%Gd$ $[0.2, 0.3]$. Below this range, the TM magnetization is always lower than the RE one and the ferrimagnet remains RE dominated at all temperatures. Conversely, above this range of $\%Gd$, the ferrimagnet remains TM dominated. The two lines of T_C and T_{MC} define the regions where the ferrimagnet is RE or TM dominated (as indicated Fig. 1.3 (c)).

Validity of mean-field approach for RE-TM alloys Even if the mean-field model gives quite satisfactory qualitative description of the magnetization properties of of RE-TM alloys, the calculated values of M_{TM} and M_{RE} remain very sensitive to the chosen parameters. Furthermore, for an alloy mixing more than two chemical elements, or for thin films or patterned structures, the required quantities deviate from the ideal bulk case and their determination is not trivial. Therefore, this approach cannot simply be used to quantitatively predict the magnetizations or the MCP. However, it can be used to interpret experimental results (as is done in Fig. 1.9, Fig. 3.2, Fig. 4.1 and Fig. 4.9) or to have realistic parameters for theoretical calculations or numerical simulations (as done in Fig. 2.9).

1.2 Fabrication and structural properties of RE-TM alloy thin films

1.2.1 Co-evaporation of RE-TM thin films

The ferrimagnetic alloys have been grown by co-evaporation of Tb, Gd, Co, Fe and a $Fe_{85}Co_{15}$ target in a dedicated ultra-high-vacuum chamber. Its base pressure is about 2.10^{-10} mbar and it is equipped with two electron guns allowing us to develop complex alloy or multi-layer-stacks (as shown in Fig. 1.4). For growing ferrimagnetic alloy thin films, pure RE (Tb, Gd) and pure TM (Co, Fe, $Fe_{85}Co_{15}$) were co-evaporated. The tuning of the alloy composition is a prerequisite to any further study. For that purpose, three independent quartz balances are available in the chamber (as shown in Fig. 1.4 (a)): one in the vicinity of each metallic target and a movable one that can be positioned at the exact substrate position to perform a precise determination of the geometrical tooling factors between the flux received

by the sample and those measured above each the electron gun. During growth, the evaporation rates were measured continuously on the lateral quartz balances. A home-made software, integrating systematic tooling factors and the feedback from the quartz balance readings, was used to continuously tune the electrical power applied on the two guns. Specular X-Ray Reflectivity was used to determine the thickness of evaporated single element layers and to calibrate the quartz balances of the evaporation chamber [64]. The deposition is done at room temperature at almost normal incidence and rotating the substrate continuously to ensure homogeneity and to avoid specific-atomic-flux-induced anisotropy [65]. Different substrates (typically 8×8 mm^2) have been tested, mainly Si[111] with oxide layers of 100 or 300 nm. Even if not discussed here, films with equally good properties were obtained with different substrates, such as intrinsic Si[100] substrates with no oxide, Si/Si$_3$N$_4$, or Si$_3$N$_4$ membranes. In each case, a cleaning process (including chemical solvents and O$_2$ plasma cleaner) is applied to the substrates. After the ferrimagnetic layer growth, a capping layer was deposited also by evaporation. This could be Al, V, SiOx or heavy metals like Pt or Ta, as discussed later.
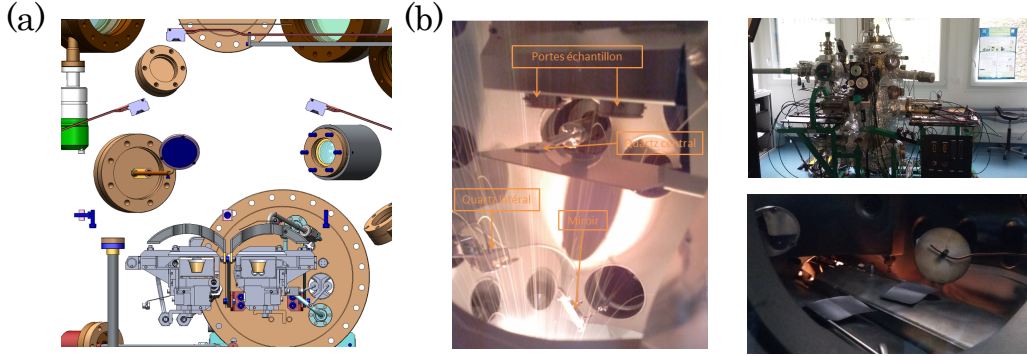
Figure 1.4 – MBE growing setup for amorphous RE-TM alloys. (a) Diagram of MBE setup: two electrons guns with their associated quartz balances, the movable quartz balance and the two positions of the sample holder. (b) Pictures of the MBE setup developed for the growth of alloys of defined stoichiometry.

1.2.2 Composition measurement by Rutherford Backscattering Spectroscopy

The depth-integrated film composition was determined by Rutherford Back scattering Spectroscopy (RBS). In this method, a 50 nA He beam of 0.5 mm-diameter was directed onto the samples at normal incidence. A Passivated Implanted Planar Silicon detector was placed to detect the He particles scattered from the sample [66]. The scattered particle spectra, which is proportional to the atomic number of the target atoms, give the integrated composition of the full depth of the thin film sample [67].

Fig. 1.5 shows an example of two measured spectra (on (a)) and the extracted depth-integrated Tb and Gd compositions (on (b)). Two sets of 7 nm thick thin films are shown: a set of Tb$_x$Fe$_{1-x}$/Al alloy films and a set of Gd$_x$(FeCo)$_{1-x}$/Al alloy films. In Fig. 1.5 (a), RBS spectra of two TbFe/Al films of two different Tb concentrations are shown. The ratio of the Tb to Fe (respectively Gd to FeCo) peak areas allows a direct measurement of the integrated composition x in Tb$_x$Fe$_{1-x}$ (respectively Gd$_x$FeCo$_{1-x}$). In the two TbFe/Al films shown, x is equal to 20 and 22 % and the difference in the spectra is clearly visible to the eye, giving an indication of the sensitivity of the RBS measurement to the global film composition. Fig. 1.5 (b) plots the effective depth-integrated Tb and Gd composition measured by RBS versus the corresponding set-point chosen for the evaporation process. The different points at the same set-point correspond to successive measurements of different areas on the samples, and a crude information on lateral homogeneity is here obtained (typically less than 0.5%). RBS results indicate a depth-integrated composition for the alloy and is used routinely to post-check the alloy composition. Note that RBS experiments cannot be used in stacks including both RE and heavy metal (such as Ta or Pt) because the peaks associated with those heavy elements are superimposed; the same holds for Co and Fe that cannot be individually resolved.
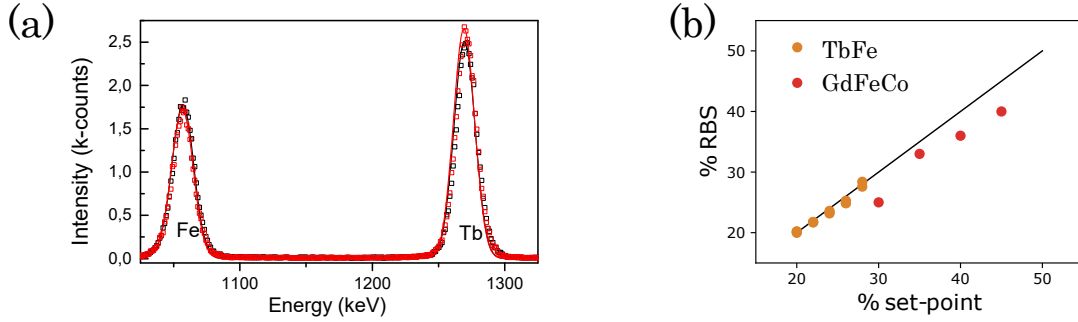
Figure 1.5 – RBS analysis of RETM films. (a) RBS spectra of 7 nm Tb_xFe_{1-x}/Al films with evaporation set points $x = 20\%$ (black) and $x = 22\%$ (red). Fe and Tb peaks are indicated. The solid lines correspond to fits to the raw data. (b) Depth-integrated Tb and Gd composition in several stacks including Tb_xFe_{1-x} (in orange) and $Gd_x(FeCo)_{1-x}$ (in red) alloy as a function of the x evaporation set-point. The points at the same set-point correspond to successive measurements of different regions on the same sample.

1.2.3 Cross-section: structure and composition measured by Scanning Transmission Electron Microscopy

To assess the crystallographic structure of the films and obtain informations on the spatial distribution of the chemical components of the alloy and interfaces, scanning Transmission Electron Microscopy (STEM) was used. Cross-sectional electron transparent samples were prepared by Focused Ion Beam following a standard procedure. To protect the sample surface during this preparation process, a thick carbon cap layer was deposited. STEM-EELS (Electron Energy Loss Spectroscopy) measurements, in which a whole EELS spectrum is acquired for each probed position (0.1 nm apart), was done across the film stack [68]. In an EELS spectrum, the area under a characteristic energy edge is proportional to the number of analyzed atoms of the given chemical species per unit area. Such EELS intensity profiles were measured for the characteristic edges of a few elements (here: for $Al-L_{2,3}$, $Si-L_{2,3}$, $Tb-N_{4,5}$, $O-K$ and $Fe-L_{2,3}$) revealing their concentration. Even if an absolute quantification of chemical component quantity requires precise information about the ionization cross section and about the measured film-slice thickness, the obtained profile gives a valid information about the depth distribution of elements. Furthermore, the measured values can be normalized by the depth-integrated composition using the associated RBS spectrum. Actually, this combined method probes simultaneously the structural and the chemical space organization of the thin film.

An image of a 10 nm thick TbFe/Al film is shown in Fig. 1.6 (a) and EELS profiles are shown in Fig. 1.6 (b). The film thermal history (heated/cooled in air up to $\approx 120°C$) is typical of the baking temperature used for patterning wires. This temperature is also of the order of the film Curie temperature, reached during basic magnetic characterization. The STEM image (Fig. 1.6 (a)) shows that the alloy is fully amorphous and homogeneous in its middle region, that the *Al* cover includes a few crystallized oxide particles and that the substrate is single crystalline with a very thin native oxide layer. The amorphous nature is of particular interest since it is expected to induce very homogeneous magnetic properties. Chemical EELS profiles across the film stack (Fig. 1.6 (b)) further show that both top and bottom interfaces are perturbed. At the top, the TbFe/Al interface looks rough and/or mixed. EELS confirms that both Tb and Fe migrate into the Al cover. At the bottom SiOx/TbFe interface with the substrate, Tb and O intensities show superimposed and abrupt (about 2 nm) peaks at the location of the native SiOx layer covering the Si substrate. This reflects both migration and oxidation of Tb of the bottom TbFe interface by the native SiOx with an enrichment in Tb. It also confirms the deep passivating oxidation of the Al cover: $\approx 3nm$ as expected. Integrating the EELS Tb and Fe intensities over the entire depth and normalizing them to the RBS-determined compositions (20.5% and 79.5%), we can plot the normalised composition depth profiles, shown in Fig. 1.6(c). The normalised Fe composition ($\%Fe/(\%Tb + \%Fe)$) is shown in red, the Tb ($\%Tb/(\%Tb + \%Fe)$) in blue, and the resulting alloy ratio ($\% \equiv \%Tb/\%Fe$) in purple. This resulting Tb/Fe ratio profile is not uniform in depth: the interfaces are richer in Tb, depleting the middle part. A variation of $\approx 1.14\%/nm$ is measured. Averaging along the

full ferrimagnetic region, we obtain a negative bias of about 4% in the composition of the middle part of the alloy compared to the depth-integrated average composition (measured by RBS) as indicated by the horizontal dashed black line. In consequence, the TbFe alloy concentration profile is, from the bottom to the top: an oxidized layer with a Tb excess followed by a thin layer with a Tb deficit (up to 30% less), at the middle, a film with an effective composition of 16.5%, biased of about $\sim -4\%$ from the total RBS composition of 20.5% and a top interface slightly mixed with the Al cover, also lacking a bit of terbium sunk by the aluminium oxide.
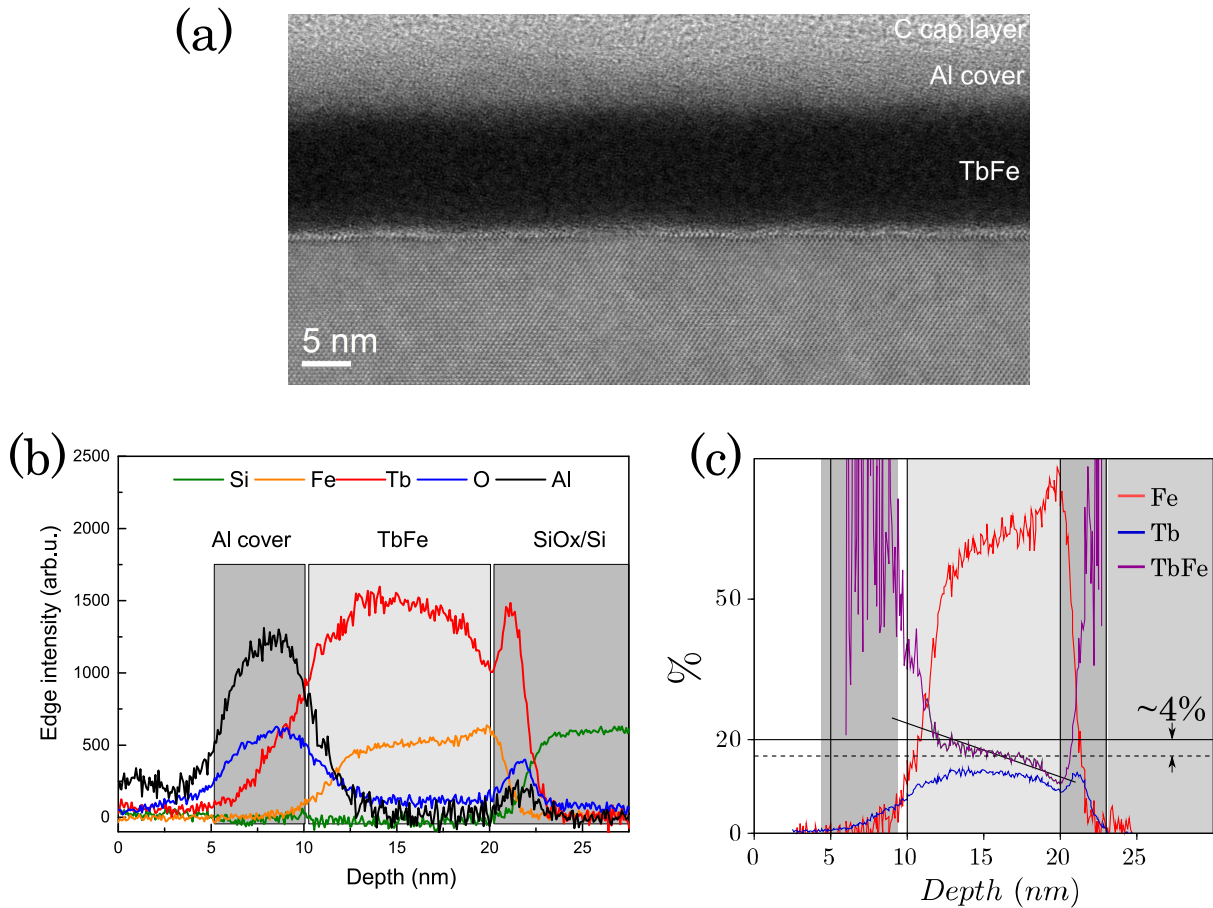
Figure 1.6 – STEM and EELS analysis of TbFe film. (a) STEM image of a cross-section of a Si/SiOx$_{(native)}$//Tb$_{20.5}$Fe$_{79.5\ (10nm)}$/Al$_{(5nm)}$ film. The amorphous structure of the constitutive TbFe layer is visible. (b) EELS intensity profiles showing the depth location of the different element constitutive of the stack. (c) Normalized $\%Fe/(\%Tb + \%Fe)$ and $\%Tb/(\%Tb + \%Fe)$ proportions (in red and blue) and quantitative alloy ratio $\%Tb/\%Fe$ (purple line), considering the depth-integrated RBS measurements.

The general features of our results agree with former results on GdCo films [69, 70] showing Gd surfactant and oxidation effects. This also supports a thickness dependence of the magnetic properties of the samples, as demonstrated in [70]. The magnetic properties of the film should correspond not to the depth-integrated composition (as measured by RBS) but to the composition of the middle of film, poorer in RE, as only this central part will be magnetically polarized. As will be seen below, the magnetic properties of the RE-TM alloys depend on this middle part which creates a deviation from a bulk material for films with different thicknesses, buffer or capping layers.

1.2.4 Biased composition dependence on stack interface

We investigate here the effect of the preferential oxidation at the interfaces and the resulting biased effective composition of the alloy on the resulting magnetic properties. Simple films of fixed thickness have been encapsulated with vanadium and aluminum or embedded between layers of heavy metals like Ta and Pt. We use the magnetic compensation point T_{MC} of the film to evaluate its effective composition, as it is very sensitive to alloy composition.
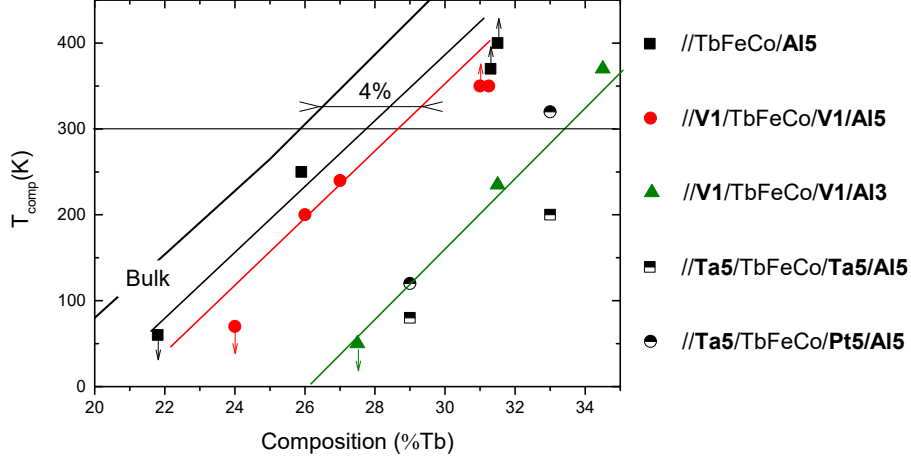
Figure 1.7 – Evolution of the T_{MC} measured by the AHE loops (see 1.3.4) in different stacks including a 7 nm Tb_xFe_{1-x} layer *versus* the Tb depth-integrated composition x. Different symbols are used for each stack. When arrows are drawn, it means that the samples did not transit up to this temperature in our experimental conditions and that T_{MC}, if it exists, is above (up arrow) or below (down arrow) the point. The thick black solid line corresponds to the bulk evolution of T_{MC} reported in [30]. Other solid lines shown for films embedded V and Al are supported by the assumption that T_{MC} is linear with the Tb with a slope of about 40 K per $\%Tb$ amount in the investigated range, like in the bulk (as validated in Fig. 1.3 (c)). For Pt and Ta buffer/cover layers, significant error in composition may exist due to limitations of the RBS method.

Effective composition bias Fig. 1.7 shows the evolution of the T_{MC} *versus* $\%Tb$ in different stacks including a 7 nm TbFeCo layer measured by AHE (see 1.3.4). For a given stack, T_{MC} increases with $\%Tb$ as expected from the mean-field calculation (see Fig. 1.3). A rate of about 40 K per $\%Tb$ can be measured. However, it is possible to see a horizontal shift of T_{MC} for the different stacks compare to the bulk values [30] (shown with the black line). This deviation of T_{MC} also depends on the stack architecture. Let us comment first on films encapsulated with V but covered with 5 nm of Al to be compared with the previous set of samples. A clear shift towards lower T_{MC} is observed in comparison with bulk like alloys. It further reveals a $\approx 4\%$ biased effective depth-integrated composition in thin films (as obtained from RBS experiments). We tried vanadium with the idea that it could prevent the diffusion of Tb, like niobium does efficiently for TbFe [71] and because of its small spin-orbit (the later being an important parameter for DW static and dynamical studies). However, T_{MC} of stacks including or not the 1 nm vanadium layer is not significantly different and corresponds maximum to a 1% reduction of the Tb composition. The effect of the biasing in the effective composition is even more drastic in the second type of stacks. When the Al cover thickness is reduced to 3 nm, the compensation is shifted to much lower temperature and shows that a much larger amount of terbium migrated towards the top and oxidized cover layer, as shown in TbFeCo depending on the Al buffer quality [72]. It reveals that terbium migrates across vanadium, which does not act as an efficient diffusion barrier. For ferrimagnetic films embedded between heavy metals like Pt or Ta, the estimated alloy composition may exhibit a significant error since RBS experiments are incapable of distinguishing Pt or Ta from RE. Therefore, no solid lines have been drawn but the tendency is obvious: a similar bias of composition occurs. This again reveals the very large sensitivity of the middle-part effective compensation to the amount of RE sunk in the interfaces.

In the RE-TM ferrimagnetic alloy, RE are heavy atoms and present a non-quenched spin-orbit coupling. Usually, at the interface between a magnetic film and a heavy metal, new effects can occur, such as DMI (see Part 1.3.1) or spin Hall effect (see Part 2.1.4.2). Here, this gradient of the effective local chemical alloy composition can induce interface-like effects in the ferrimagnetic layer itself. Recent studies highlight the link between this chemical gradient and the emergence of a bulk-like DMI in thicker SiN/GdFeCo/SiN stacks [70]. In part 1.4.3, it is shown that Néel DW stabilization occurs in a SiOx/GdFeCo/Al, which is a sign of DMI induced by the chemical gradient. Finally, we recently measured a bulk-like spin Hall effect in stacks which do not contain heavy metal layer, which can also explained by this chemical gradient.

Film sensitivity and corrections More generally, the samples are very sensitive to any process such as heating or patterning. Due to the strong variation of their magnetic properties with their chemical compositions, even a small variation of the RE composition induces a large modification. For instance, during the patterning process, a decrease of T_{MC} of more than 50 K is commonly observed. An aging process also occurs. To limit this effect, we have adapted the classical patterning process to minimize the baking steps and we conserve the samples in a vacuum box to limit oxidation effects. However, even if T_{MC} changes drastically with the chemical alloy composition, the magnetic properties are mainly shifted in temperature and their relative variations do not change significantly (far from T_c). For instance, in the Fig. 1.3 (c), even if T_{MC} changes with $\%Gd$, the slope of the magnetization does not change drastically for small deviations of the composition. This allows us to rectify the temperature shift by a corrective offset of temperature.

1.3   Macroscopic magnetic properties of RE-TM alloy thin films

In this part, we investigate the macroscopic magnetic properties of deposited ferrimagnetic thin films such as: their magnetization, their magnetic anisotropy, their electrical transport or optical properties which can be probed by a classical hysteresis loop method.

1.3.1   Magnetic energy in magnetic thin films

In a magnetic material, the magnetic static properties can be described considering a few energetic contributions [34, 73].

Exchange interaction The exchange interaction governs the alignment or the anti-alignment of the magnetic moments (Eq. 1.1). This interaction is important at two length scales: at the atomic scale, it describes the emergence of the local magnetization considering the first neighbors interactions (as detailed previously part 1.1.3) and, at a larger nanometer scale, it describes the slowly-varying magnetization spatial organization of an assembly of moments. At this nanometer scale, it is possible to describe this spatial distribution like a continuous vectorial field: $\vec{M} = M_S \vec{m}$ where M_S is the magnitude of the magnetization (taken as constant in time) and $\vec{m}(x, y, z)$ is a spatially-varying unit vector which describes the direction of the magnetic space-distribution. This framework is called the micromagnetic approximation. In it, the magnetization of neighboring moments can be described *via* a Taylor expansion of the local $\vec{m}$ the exchange energy can be written like:

$$\epsilon_{ex\,ij} = A\left(\nabla\vec{m}\right)^2 \tag{1.6}$$

Here A is the exchange stiffness parameter which depends on the time-averaged magnetization $< S >$, the exchange term J and the average of the spatial organization of the moments. Note that in this micromagnetic approach, A is positive and this framework can not be simply applied to describe antiferromagnetic exchange (such as for antiferromagnets of the inter-sub-lattices interaction for ferrimagnets). The exchange interaction is one of the intrinsic key element to describe the geometry of a magnetic texture and its dynamics.

Magnetic anisotropy   In a magnetic material, the magnetic moment carrier interacts with its environment *via* spin-orbit interaction. Due to the spatial organization of the material, some directions can exhibit an easy/hard axis for the magnetization. This phenomenon is called the magneto-crystalline anisotropy and can be associated to the energy term:

$$\epsilon_K = -\sum_i K_i \left(\vec{u}_i \cdot \vec{m}\right)^2 \tag{1.7}$$

where K_i is the anisotropy energy along the axis $\vec{u}_i$. If K_i is positive/negative, the axis $\vec{u}_i$ is an easy/hard axis. In an amorphous film, due to the degeneracy of the in-plane directions, there is *a priori* no preferential in-plane direction for the magnetization. Just one anisotropic axis along the normal direction is expected and $\epsilon_K \rightarrow -K\left(\vec{u}_z \cdot \vec{m}\right)^2$. Furthermore, in thin films, the anisotropy parameter K is governed by the stress of the film, the interface contribution [74, 75] and by the eventual anisotropic pairing of atoms [71, 76]. The resulting anisotropy is given by two contributions: $K = K_0 + K_s/t$ with K_0 the 'bulk' contribution (the stress and the pairing) and K_s the surface contribution and t the thickness of the film.

Zeeman energy   Under an external magnetic field $\vec{H}$, the magnetic moment feels another energy term called the Zeeman energy:

$$\epsilon_{Zeeman} = -\mu_0 M_S \vec{m} \cdot \vec{H} \tag{1.8}$$

In a presence of the external field, the Zeeman energy is lower if the magnetization is aligned along the field direction, which gives a possibility to manipulate the magnetization with an external action.

Demagnetization effect   The magnetic moments feel also the magnetic field created by the magnetization. This phenomenon is called the demagnetization effect and it describes the Zeeman effect produced by the resulting field of all the magnetic moments. The energy associated with this resulting field is:

$$\epsilon_{Demag} = -\frac{\mu_0 M_S}{2} \vec{m} \cdot \vec{H}_d \tag{1.9}$$

where H_d is the demagnetization field (also called stray field) that is a function of the magnetization $\vec{m}$ itself. H_d is typically hard to calculate for an arbitrary geometry and $\vec{m}$ distribution. For an uniformly-magnetized ellipsoid, or for a shape that can be approximated by an ellipsoid such as a film or a long cylinder [34], H_d is also uniform and can be written as $H_d = -M_S\left[N\right]\vec{m}$, where $[N]$ is the demagnetizing tensor (of unit trace and diagonal along the ellipsoid axis) for which an analytical formula is known. Note that this effect increases the energy of the uniformly-magnetised state, opposing the ferromagnetic exchange. It is possible to defined an 'exchange length' $\Lambda = \sqrt{A/\mu_0 M_S^2}$ above which the demagnetization is stronger than the exchange interaction (typically, $\Lambda \sim 0.1 - 1\mu m$). In the case of a thin film with perpendicular magnetic anisotropy, the out of-plane magnetization is unfavored by the demagnetization effect resulting in a apparent reduced perpendicular magnetic anisotropy [74] that can be approximated by: $K \rightarrow K_0 + \frac{Ks}{t} - \frac{\mu_0 M_S^2}{2}$.

Dzyaloshinskii-Moriya interaction   In materials including heavy metal elements (with strong spin-orbit coupling), due to the broken symmetry of the wave function overlap, a chiral interaction can appear: the Dzyaloshinskii-Moriya interaction (DMI) [77–79]. In contrast to the standard exchange energy, this asymmetric exchange favors a canting moment configuration [80–84]. Considering a magnetic thin film, this symmetry breaking occurs at the film interfaces in particular between the magnetic layer and a heavy material (such as Pt, Ta or W) [4, 79, 85–87]. In this situation the energy of the DMI can be written:

$$\epsilon_{DMI} = D\left(m_z \left(\vec{\nabla} \cdot \vec{m}\right) - \left(\vec{m} \cdot \vec{\nabla}\right) m_z\right) \tag{1.10}$$

where D is the micromagnetic DMI parameter and the z axis is normal to the magnetic layer [85]. Note that this effect has an interfacial origin and so D decreases with the film thickness t: $D \propto 1/t$.

Two sub-lattices ferrimagnetic framework Ferrimagnets can be considered as two ferromagnetic sub-lattices, $\vec{m}_1$ and $\vec{m}_2$, that are antiferromagnetically coupled. The resulting inter-sub-lattices coupling energy term can be written:

$$\epsilon_{ex12} = J_{ex12}\vec{m}_1 \cdot \vec{m}_2 \tag{1.11}$$

Note that $J_{ex12} > 0$ to favor the antialignment of the two sub-lattices. With this approach, the full energy of the system is the energy of each sub-lattices (ϵ_1 and ϵ_1) and this additional coupling contribution ϵ_{ex12}:

$$\epsilon = \epsilon_1 + \epsilon_2 + \epsilon_{ex12} \tag{1.12}$$

with ϵ_1 and ϵ_2 depending of the M_S, A, K, D quantities of each sub-lattice. In the case of a strong antiferromagnetic coupling, it is possible to consider that the two sub-lattices remain anti-aligned, $\vec{m}_1 = -\vec{m}_2$, and to define a unique unit vector $\vec{m}$ (taken arbitrarily along the $\vec{m}_1$) which fully describes the magnetization distributions of each sub-lattices. Developing the Eq. 1.12, it is possible to see that the $\vec{m}$ distribution is governed by the classical energy terms but with effective parameters:

$$
\begin{aligned}
M_S &= M_1 - M_2 \\
A_{eff} &= A_1 + A_2 \\
K_{eff} &= (K_{01} + K_{02}) + \frac{(K_{s1} + K_{s2})}{t} - \frac{\mu_0 M_S^2}{2} \\
D_{eff} &= D_1 + D_2
\end{aligned}
\tag{1.13}
$$

and an additional constant term depending of J_{ex12}. Note that here M_2 corresponds to the absolute value of the second sub-lattice magnetization and that its orientation is taken into account with the minus sign. In the following parts of this chapter, this strong inter-exchange coupling approximation is taken into account and the magnetic quantities are described like a standard ferromagnetic material with these effective parameters.

1.3.2 Hysteresis loop approach
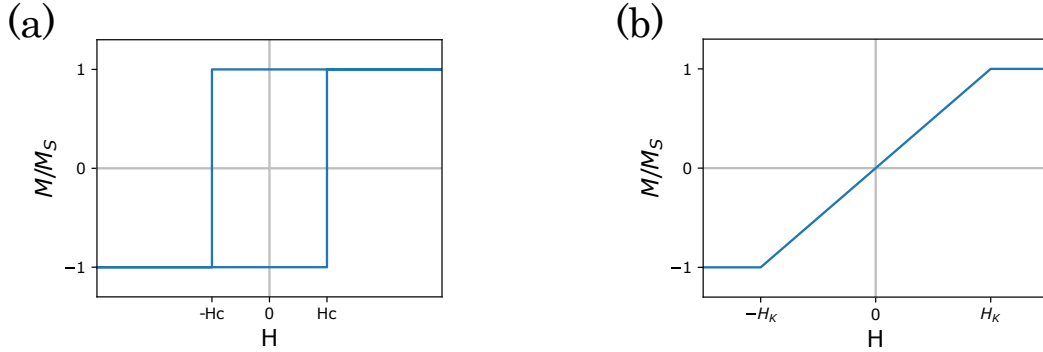
Figure 1.8 – Sketch of theoretic magnetic hysteresis loop of a thin film with (a) an out-of-plane and (b) an in-plane magnetic anisotropy.

To investigate macroscopic magnetic properties of the deposited thin films, a common approach consists in measuring the reversal hysteresis loops [55]. In this method, an external magnetic field is applied and we measure the response of the film magnetization. In our case, the external field is applied perpendicularly to the sample. If the anisotropy is out-of-plane: starting from a saturated state with a uniform magnetization pointing up or down and applying a magnetic field H in the opposite direction, the magnetization is reversed above a critical field called the coercitive field H_C. Roughly speaking, H_C is the field required to overcome the anisotropy effect. After the magnetization reversal the magnetization of the film is again saturated which gives a square hysteresis loop with a remanent part at zero field (as sketch in Fig. 1.8 (a)). This reversal of the magnetization can be described by an Arrhenius law considering its associated energy barrier: ΔE. In this approach, the reversal occurs after a typical time $\propto \exp(-\Delta E/k_B T)$ temperature dependent. Increasing the temperature T, the thermal activation

also increases and the field required for the reversal (H_C) decreases. Note that many different reversal modes can occur and that the uniform reversal is the most energetic process. In this upper limit, the coercitive field H_C depends mainly of the competition between the Zeeman and the anisotropy energies that gives an upper limit for the energy barrier: $\Delta E \leq (K - \mu_0 M_S H)$. If the anisotropy is in-plane: the magnetization is uniformly deviated (with H) from its stable in-plane orientation up to its saturated out-of-plane configuration above a saturation field $H_K = K/\mu_0 M_S$. In this situation, no remanent part appears in the hysteresis loop (sketch in Fig. 1.8 (b)). The main benefit of this method is to have access to the anisotropy (in-plane/out-of-plane) and all the magnetic properties in the saturated regions.

1.3.3 Magnetization properties

The net magnetization of the ferrimagnetic thin films can be measured by VSM, AGFM or VSM-SQUID [73]. The general method is common with the classical ferromagnetic films: it measures the effect of the magnetic moment of the sample on the vibration frequency of the sample (for AGFM) or the variation of the magnetic flux in a loop (for VSM or VSM-SQUID). In ferrimagnets, the expected magnetization is $\approx$10 times lower than the typical ferromagnets (as calculated Fig. 1.3), which requires a high sensitivity of the used setup. Also, due to the low M_S, the field required to obtain significant variation of the signal (typically the coercive field) can be very large. Finally, one of the interesting properties of ferrimagnets is their tunability with the temperature, which requires measuring in a large range of temperatures.
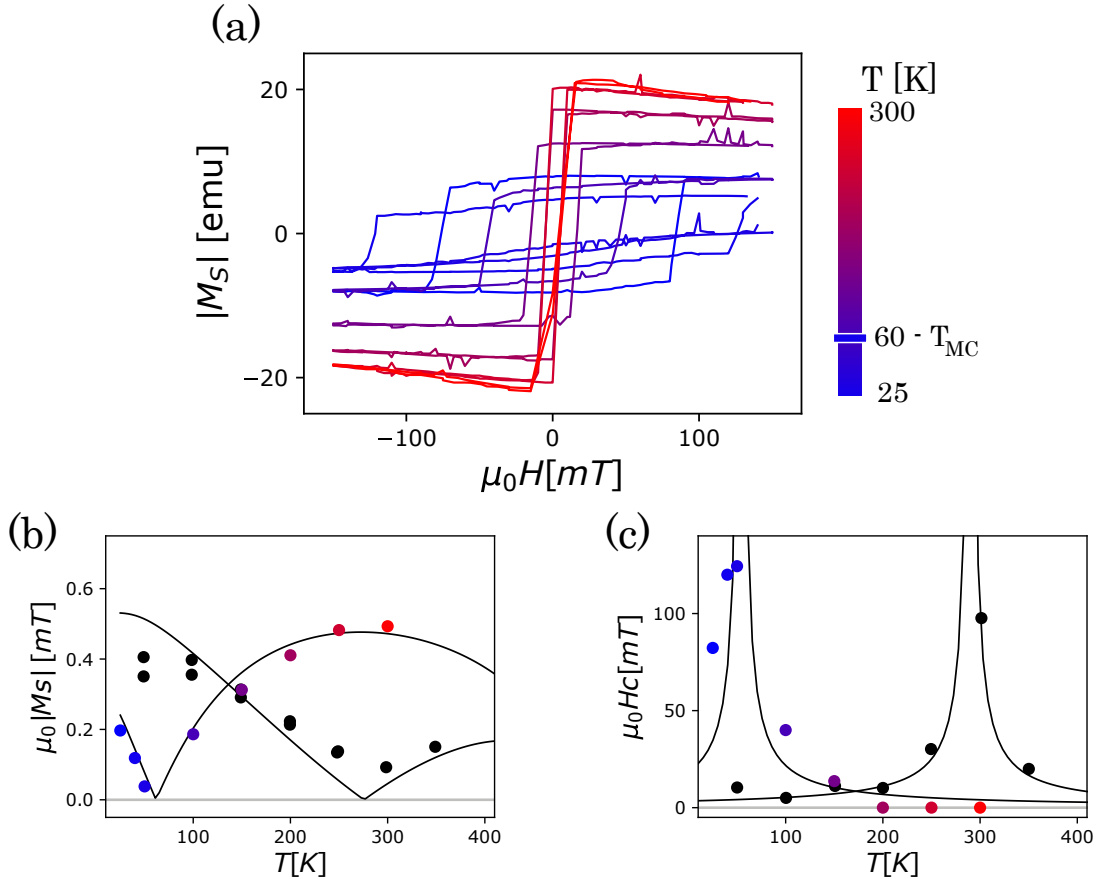
Figure 1.9 – M_S and H_C of GdFeCo films. (a) Magnetization hysteresis loops under perpendicular field for different temperatures of a Si/SiOx$_{(100nm)}$//Gd$_{32.5}$FeCo$_{(7nm)}$/Pt$_{(5nm)}$ thin film. (b) Magnetization $\mu_0|M_S|$ *versus T* for Si/SiOx$_{(100nm)}$//GdFeCo$_{(7nm)}$/Pt$_{(5nm)}$ thin films with %$Gd \approx 32.5$ (black circles) and %$Gd \approx 51$ (black diamonds). The background curves correspond to the associated mean-field calculation. (c) Coercive field $\mu_0 Hc$ *versus T* for the same two films. The background curves are just a guide.

Fig. 1.9 (a) shows the magnetization $|M_S|$ of a GdFeCo$_{7nm}$/Pt$_{5nm}$ stack with $\%Gd = 32.5$ *versus* the applied perpendicular magnetic field H for different temperatures measured with a VSM-SQUID setup. Each value is obtained under an increasing and a decreasing perpendicular field. Square hysteresis loops are observed which indicates a perpendicular magnetic anisotropy of the film (see part 1.3.2). The amplitude of the loop changes with the temperature T which indicates that the magnetization of the film $|M_S|$ changes. The coercive field H_C also changes with T. Fig. 1.9 (b) shows the extracted magnetization for Si/ SiOx$_{(100nm)}$// GdFeCo$_{(7nm)}$/ Pt$_{(5nm)}$ thin films with $\%Gd \approx 32.5$ (black circles) and $\%Gd \approx 51$ (black diamonds) . They are very low and change significantly with T and $\%Gd$ in agreement with the mean-field model (Fig. 1.3). M_S fully vanishes at $\approx$50K and $\approx$300K (for respectively $\%Gd \approx 32.5$ black circles and $\%Gd \approx 51$ black diamonds) which corresponds to their magnetic compensation points T_{MC}. It is possible to see that the T_{MC} increasing with $\%Gd$ (as shown Fig. 1.3). Lines on the background correspond to mean-field calculations with just $\%Gd$ as a tunable parameter. Fig. 1.9 (c) shows the coercive field of the hysteresis loops H_C. They diverge at T_{MC} and decrease after as expected from the Arrenius model of the reversal (part 1.3.2). It is more visible for the sample with $\%Gd \approx 32.5$ where T_{MC} is at the beginning of the temperature range. In ferrimagnets, the magnetic properties also change with T which modifies the Arrhenius law energy barrier. In particular, at T_{MC}, the net magnetization M_S vanishes and the Zeeman contribution is zero. Even with a very large field, it is not possible to reverse the film magnetization which is associated to a divergence of H_C.

These measurements directly show that the net magnetization of the ferrimagnet vanishes at T_{MC}. This zero magnetization induces a divergence of the coercive field H_C which is also a characteristic signature of the T_{MC}.

The measurement of these low-magnetized alloys remains challenging. Extracting the signal arising from the ferrimagnetic layer in question (typically 10^{-6} emu) from the background signals requires the minimization of the sample holders and substrate magnetic contributions. The best results are obtained with either a SQUID working in the RSO mode or with a VSM-SQUID setup. New NV-center magnetometry methods should also give a better sensitivity [88–90], as discussed at the end of this chapter (section 1.6.2).

1.3.4 Electrical transport properties
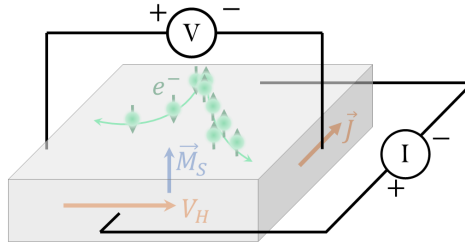
Figure 1.10 – Geometry of the anomalous Hall effect measurements with the used configuration of connections.

When an electrical current flows through a conducting magnetic material, it generates a transverse voltage [91–95] due to the anomalous Hall effect (AHE), which is typically dominant over other perpendicular voltages such as the classical Hall effect. The microscopic origin of this effect is the spin-dependent scattering of the electron flow perpendicularly to the local magnetization [93]. In a metallic magnetic material, the density of states at the Fermi level is different for each spin population, which induces this transverse AHE voltage. Two mechanisms coexist: the 'skew scattering' [93, 96, 97] and the 'side-jump' [98], which depend respectively on material defects and on the band structure. In the case of a conducting magnetic alloy, the AHE of the two conducting magnetic sub-lattices are superimposed. For amorphous materials, side-jump scattering is the dominant effect [93]. For magnetic thin films, just the longitudinal AHE can be detected that give a direct information on the out-of-plane component of the

magnetization. Finally, in this systems, the Hall resistivity $R_H = V_H/I$ measurement (where I is the injected current and V_H is the Hall voltage) gives the variations of the out-of-plane component of the magnetization.
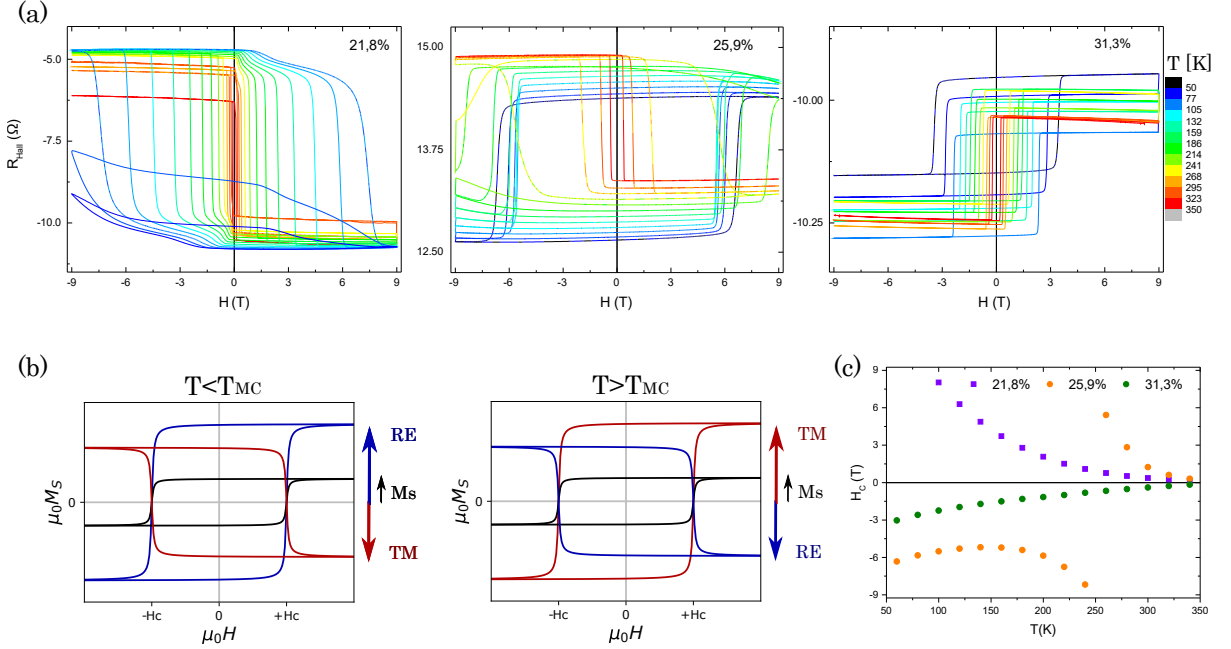
Figure 1.11 – AHE hysteresis loops under perpendicular field. (a) AHE hysteresis loops under perpendicular field for different temperatures for a $Si/SiOx_{(100nm)}//Tb_xFeCo_{1-x\ (7nm)}/Al_{(7nm)}$ thin films for $x = 21.8$, 25.9 and 31.3%. (b) Sketch of the orientation of the two sub-lattices during the hysteresis loops for RE and TM dominated alloy (respectively on the left and on the right). (c) Measured coercive fields $\mu_0 H_C$ *versus* T for $x = 21.8, 25.9$ and 31.3%. The sign of H_C is relative to the cycle orientation.

Fig. 1.11 (a) show the measured Hall resistance R_H *versus* the applied perpendicular field for different temperatures for $Tb_xFeCo_{(1-x)}/Al$ thin film with different compositions: $x = 21.8, 25.9$ and 31.3%. We find again the square hysteretic shape, characteristic of out-of-plane anisotropy. The coercive field changes drastically with temperature, whereas the amplitude of the R_H loops does not change significantly (compared to the measured M_S in Fig. 1.9). Furthermore, here, it is possible to see a reversal of the loops between the Tb-rich ($x = 31.3\%$) and the Tb-poor ($x = 21.8\%$) alloys (left and right plots in Fig. 1.11 (a)). For the intermediate Tb composition ($x = 25.9\%$), it is possible to see that the loop reverses at ≈ 230 K. As measured previously, the orientation of the net magnetization hysteresis loop $M_s(H)$ is the same in the full range of T and $\%Gd$ (see Part 1.3.3). In contrast, here, the AHE just depends on the electrical transport properties. As shown Fig. 1.2, in RE-TM ferrimagnetic alloy, they are dominated by the delocalized e^- mainly from the TM sub-lattice. The AHE is dominated by the relative orientation of this TM sub-lattice and the R_H hysteresis loop is directly correlated to the M_{TM} magnetization orientation. In TM materials, the number of occupied state at the Fermi level is larger for spins aligned along the macroscopic magnetization [55–57] therefore the scattering processes are less efficient for this population. Using the chosen configuration (shown Fig. 1.10), the electron deviation is lower for e^- aligned in the M_{TM} direction than for e^- aligned in the opposed one (as sketched Fig. 1.10). In this configuration, the AHE gives a lower R_H if the TM magnetization is up and a larger R_H if it is down [91,92,94]. If the alloy is TM dominated, M_{TM} is in the same direction as M_S (as shown Fig 1.3) and the R_H and the M_S cycles have opposite orientations (as for $x = 21.8\%$ Fig. 1.11 (a)). Conversely, if the alloy is RE dominated, M_{TM} is in the opposite direction that M_S (as shown Fig 1.3) and the R_H and the M_S cycles have the same loop orientation (as shown Fig 1.11 (a) for $x = 31.3\%$). The sketch Fig. 1.11 (d) shows the M_S, M_{TM} and the M_{RE} loops for a RE or TM dominated alloy (on respectively right and left panels). In this representation, it is expected that the R_H signal is in the opposite direction than the M_{TM} loop. The reversal of the cycles at $T = 230K$ for the $x = 25.9\%$ alloy (Fig. 1.11 (a)) is

30

the signature of the magnetic compensation point T_{MC}. In contrast with the M_S loops (Fig 1.9), the R_H hysteresis loop amplitude does not vary at the T_{MC} as M_{TM} is continuous at this temperature. The observed strange cycles (observable for $x = 21.8\%$) correspond to minor loops in the investigated field range (lower than the H_C). Fig. 1.11 (c) shows the variation of the coercive field for all the three samples. The sign of H_C corresponds to the orientation of the loops ($H_C > 0$ for a TM dominated loops and $H_C < 0$ RE dominated region). For all three cases, H_C decreases with T (due to the thermally-activated reversal processes) and for the case with a magnetic compensation ($x = 25.9\%$), its decrease is overridden by a divergence characteristic of T_{MC} (as discussed previously Part 1.3.3). Note that the H_C divergence corresponds to the reversion of loops.

To conclude, the AHE measurement is a very robust tool to get selective information relative to the TM sub-lattice orientation. Even if the Hall resistivity measurement does not give the directly quantitative values of M_{TM}, the sign of the hysteresis loops directly gives the type of the sample: RE- or TM-dominated. Here, the reversal of the cycles crossing the T_{MC} validates the sketch Fig. 1.3. In our case, AHE is a particularly convenient technique, as our setup allows for large range of both temperature (50 to 400K) and field(-9 to +9T), which permits measuring the TM magnetization state in an expended parameter range. However, this method only probes the macroscopic resistivity of the film which can give un-clear results in the case of film containing spatial inhomogeneities. Other studies using this method are presented in the part 1.6.1.

1.3.5 Magneto-optical properties

The Kerr effect is the magneto-optical effect in reflection geometry [99]. When a magnetic surface is illuminated, the excited electrons of the material re-emit light depending of their state [99, 100]. The properties of this reflected light, such as the polarization or the ellipticity, change from the incident beam depending on the magnetic state of the reflecting film which is called the Kerr effect [99, 101]. These modifications are proportional to the magnetization component along the wave vector of the incident beam. To study a magnetic thin film with perpendicular anisotropy, the polar configuration is the most convenient [100, 102]: the incident beam is normal to the film surface [100]. Measuring the difference between the linear polarization angle of the incident and reflected beams, called the Kerr rotation, it is possible to deduce the magnetization state of the film. It is very difficult to link quantitatively the value of the Kerr rotation and the magnetization [100, 101], however, a flip of the Kerr rotation reflects a reversal of the magnetization.

In ferrimagnetic thin films, the magnetization of both sub-lattices are correlated to the electronic states (See Fig. 1.2). Indeed, the electrons close to the Fermi level correspond to the delocalized TM sub-lattice whereas the valence band electrons correspond to the localized magnetization of the RE sub-lattice. Both sub-lattices have a magneto-optical activity but, by choosing the appropriate wavelength of the incident beam, it is possible to probe mainly one of the sub-lattices. This is called the chemical selectivity [30].

Fig. 1.12 (a) shows the macroscopic magneto-optical hysteresis loops of Si/SiOx//TbFeCo/Al films with different chemical compositions obtained at room temperature in the polar geometry with a red incident light beam (652 nm). The square shape of the loops indicates the perpendicular magnetic anisotropy. The reversal of the loops and the divergence of the coercive fields indicates a *MCP* around $x = 27\%$. The flat loop for $x = 25.9\%$ corresponds to an unsaturated minor-loop due to the divergence of H_C in the vicinity of compensation. The compensation temperature of the Tb-poor film (black) is below room temperature, the intermediate Tb composition (red/blue) corresponds to compensation around room temperature whereas the Tb-rich films (green/blue) have a compensation temperature above room temperature. At these energy levels (652 nm $\leftrightarrow$1.85 eV), the optical process occurs only for the $5d$ RE and $3d$ TM conduction electrons. Large Kerr rotations are observed ($>0.1^o$) increased by the RE [30] and thanks to the 100 nm SiOx layer which exalts the optical signal. Changing the wavelength of the incident beam loop for blue light (408 nm $\leftrightarrow$ 3.03883 eV), it is possible to observe a reversal of the Kerr rotation hysteresis loop. At this energy level, the light interacts mainly with the RE valence electrons and the resulting Kerr effect depends now of this RE magnetization state. Fig. 1.12 (b) shows two hysteresis

loops in polar configuration on the same film for two different wavelengths (at room temperature). Note that the signal is lower for the blue than for the red light.
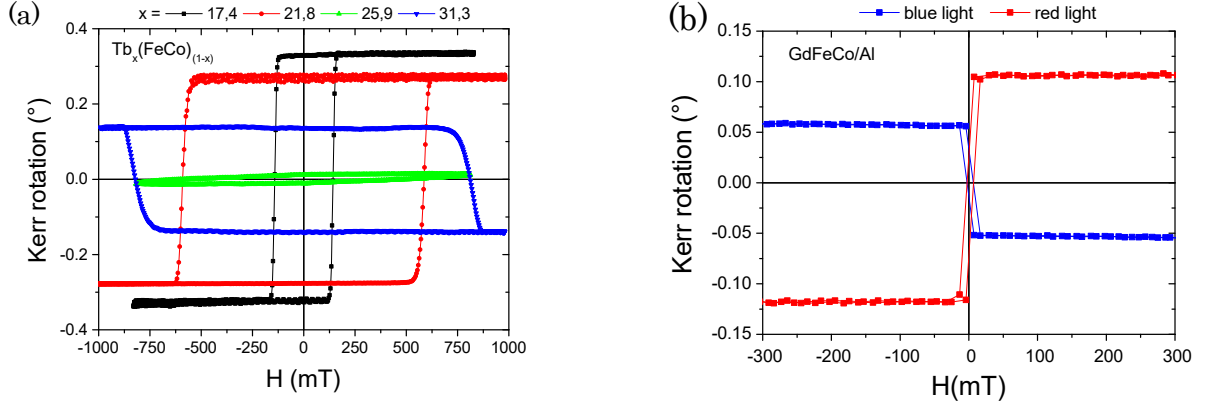
Figure 1.12 – (a) Kerr rotation hysteresis loops under perpendicular field for $Si/SiOx_{(100nm)}//Tb_xFeCo_{x-1\ (7nm)}/Al_{(5nm)}$ thin films with x = 17.5, 21.8, 25.9 and 31.3%. A red (652nm) incident beam light is used. (b) Kerr rotation hysteresis loops under perpendicular field for a $GdFeCo_{(5nm)}/Al_{(5nm)}$ thin films TM-dominated with two different incident beam wavelength: 652mn and 408nm.

Finally, this optical method gives the same information as the electrical measurements [63] (presented above in 1.3.4). In the case of our experimental setups, it allows a faster measurement than the AHE measurement, but in a smaller field and temperature ranges. As previously said, it is difficult to directly associate the measured Kerr rotation to the dominant sub-lattice of the sample. To associate the orientation of a hysteresis loop and the magnetization state of the film, two approaches can be used: *via* direct calibration the Kerr angle measuring precisely signal [102] or using a calibration sample in which the magnetization state (RE or TM-dominated) is known. The main advantage of this method is the possibility to directly image the spatial organization of the magnetization. Indeed, using a modified optical microscope [100], it is possible to use this Kerr effect to directly image the magnetic domain structures (above the optical limit) as detailed in part 1.4.2.

1.4 Microscopic magnetic properties of RE-TM alloy thin films

Minimizing all the energy terms (detailed in part 1.3.1), it is possible to consider the magnetization direction $\vec{m}$ as a non-uniform quantity and to calculate its spatial distribution. Combining different magnitudes of the previous quantities (M_S, A, K, D) and different sample geometries, it is possible to obtain many meta-stable magnetic textures [103] such as domains and DWs [100],stripes and bubble domains [34], vortexes [104] and anti-vortexes [105], skyrmions [4,32,83,106,107], or anti-skyrmions [108].

1.4.1 Domain wall structure

Considering a magnetic medium, due to the competition between the exchange coupling and the demagnetization effect, at short scales (shorter than the exchange length Λ), the exchange energy is dominant and it keeps the local alignment of the moments. For large scales (longer than Λ) the demagnetization effect is dominant and induces a modification from the uniform magnetization state. One of the possible resulting meta-stable states is an arrangement of several regions of uniform magnetization, called magnetic domains, aligned along different directions. To minimize the exchange energy, domains are separated by regions where the magnetization changes continuously from one domain to the next called domain walls [100].
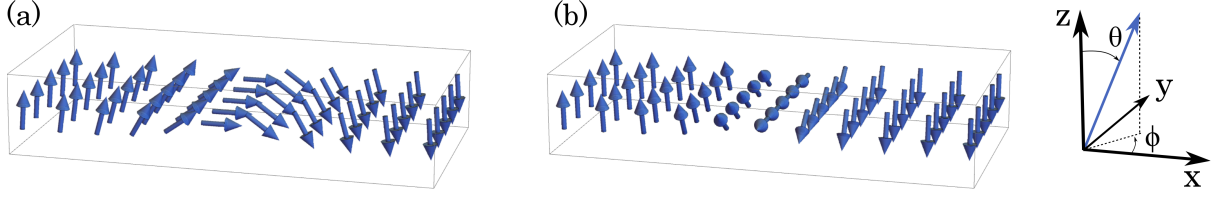
Figure 1.13 – Two types of 180° DW in magnetic thin film with perpendicular anisotropy: (a) Néel DW and (b) Bloch DW.

In a thin film with perpendicular magnetic anisotropy, two types of domains exist with up or down magnetization and the central magnetization of the DW is in the film plane. The in-plane orientation of the DW magnetization results from the competition between the stray field and the DMI. For a neglible DMI, the magnetization turns in the DW plane, whereas with DMI, it turns normal to the DW plane with a chirality according to the sign of D. For the case of uniaxial anisotropy, an analytical expression for the DW profile can be obtained. Using spherical coordinates for $\vec{m}$ ($\vec{m} = (\cos(\phi)\sin(\theta), \sin(\phi)\sin(\theta), \cos(\theta)))$, it is possible to minimize the total surface energy $\sigma = \int_{-\infty}^{-\infty} \epsilon dx$ fixing the boundary conditions $\theta(x = -\infty) = 0$ and $\theta(x = +\infty) = \pi$ (here x is the coordinate along the DW normal) [34]. For an up-to-down DW ($\uparrow\downarrow$), the spatial distribution of the magnetization along x can be obtained:

$$\begin{cases} \theta_{q,\Delta}(x) = 2\arctan\left(\exp\left(\frac{x-q}{\Delta}\right)\right) \\ \\ \phi(x) = \varphi \end{cases} \tag{1.14}$$

Here $\Delta = \sqrt{A/K}$ is the DW width parameter with $K = K_0 + \frac{Ks}{t} - \frac{\mu_0 M_S^2}{2}$ the effective magnetic anisotropy. φ is the constant DW in-plane angle of the magnetization obtained minimizing the surface energy [85]:

$$\sigma = \frac{2A}{\Delta} + 2\Delta\left(K + K_{BN}\sin^2(\varphi)\right) - \pi D\cos(\varphi) - \mu_0 M_S\left(\Delta H_x\sin(\varphi) - \Delta H_y\cos(\varphi) + H_z 2q\right) + \sigma_{\text{extra}} \tag{1.15}$$

where $K_{BN} \propto \mu_0 M_S^2$ the in-plane anisotropy resulting from the demagnetization effect. In this configuration, considering a ellipsoid approximation of the DW structure [109], $K_{BN} = (N_y - N_x)\mu_0 M_S^2$ and the demagnetization factor can be approximated by $N_x \approx \frac{t}{t+w}$, $N_y \approx \frac{t}{t+\Delta}$ with t the thickness of the film and w the width of the wire. In a full film, $w \to \infty$ and $N_x \to 0$. Here, the DW is Bloch type ($\varphi = \pm\pi/2$) in the absence of D and Néel type ($\varphi = 0[\pi]$) with a non-zero D [85]. The term σ_{extra} accounts for other energy terms of the system, such as magnetic spacial in-homogeneity [110], external coupling [12,16], structure geometry [111,112]. Note that the expression for the profile of the down-to-up ($\downarrow\uparrow$) DW is obtained by changing $\Delta \to -\Delta$, and all results for $\uparrow\downarrow$ DW can be applied to a $\downarrow\uparrow$ DW.

Note that for the case of small magnetic systems, when the exchange length is larger than the system dimensions, it is possible to consider that all spins are aligned and they can be considered as a single moment: the macro-spin [111,113–115].

All the previously-discussed experimental techniques do not provide spatially resolved information on magnetic textures. Here, two imaging methods are used to directly image magnetic domains or DW structure.

1.4.2 Imaging of domains by magneto-optical Kerr microscopy

As said previously, the magneto-optical Kerr effect can be used as an imaging technique to probe the magnetic domains [100]. Indeed, the Kerr rotation is opposite for an up or a down magnetization state. In the case of a thin film with perpendicular anisotropy, different types of domains exhibit different Kerr contrast. This method can be implemented in a classical optical microscope including a polarizer and an analyzer to reveal the magnetic domain pattern in real time thanks to the Malus law [100]. On top of the large Kerr rotation (Fig. 1.12), the optical contrast can be increased adding a $\lambda/4$ wave-plate. In our

case, due to the perpendicular magnetization, the polar configuration is used. As shown Fig. 1.12, with visible light, the Kerr rotation is larger for the TM sub-lattice except in the blue and a fine wavelength selectivity is not required. To have more signal, we use a white light source with high intensity.

Fig. 1.14 shows images of the magnetic contrast of up and down domains in a magnetic film. Fig. 1.14 (a) and (b), it is possible to observe large circular domains (even at 410K), which is the signature of a very good film quality with a low density of nucleation centers and no strong DW pinning centers. It is also possible to observe the position of the 180° DWs which separate magnetic domains, but the optical resolution ($\approx$0.5 μm) prevents the spatial resolution of their structure.

Applying a perpendicular up magnetic field, the Zeeman energy of the up domains decreases whereas it increases for the down ones. To minimize the total energy, the up domains grow and the down domains shrink, inducing a motion of the DWs. Fig. 1.14 shows the DW motion induced by the minimization of the Zeeman energy for a perpendicular field. The applied field does not induce further nucleation and the magnetization reversal occurs by DW propagation. It is also possible to see that the DW propagates without any drastic deformation which indicates also the absence of strong inhomogeneities in the film (that would constitute strong pinning centers). A straight propagation of the DW also occurs in patterned magnetic structure (c) without strong deformation due to the edge effect [116]. Fig. 1.14 shows the propagation of DWs driven by a negative field, at 350 K (a) and 410 K (b). Even if the field is negative in both cases, in (a) the dark domains grow, while in (b) it is the light domains that grow. Indeed, as for hysteresis Kerr loops shown Fig. 1.12, the Kerr rotation just depends on the probed sub-lattice: here the TM one. Below T_{MC}, the ferrimagnet is RE-dominated and a positive magnetic field increases the domains with M_{RE} pointing in its direction. In contrast, above T_{MC}, the ferrimagnet is TM-dominated and a positive magnetic field increases the domains with M_{TM} pointing in its direction. Note that at T_{MC}, the net magnetization is zero and the DW are insensitive to any applied fields.
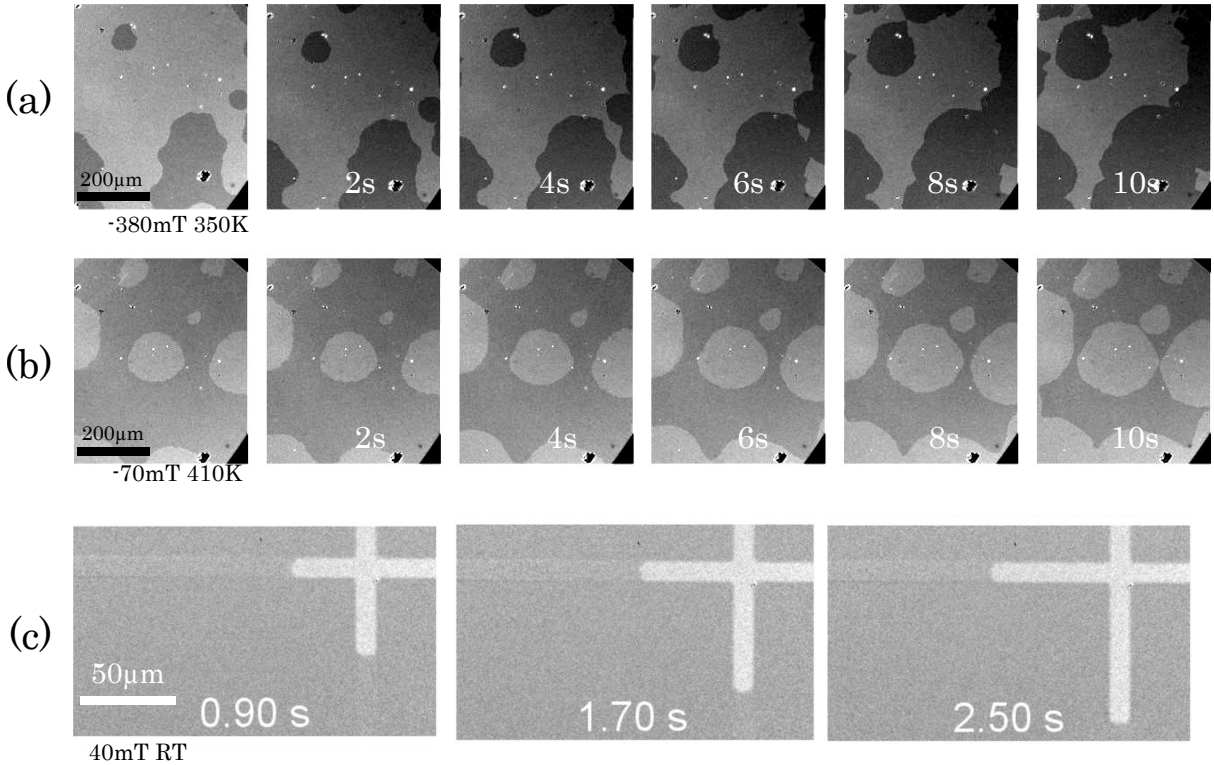
Figure 1.14 – DW propagation in a TbFeCo 7 nm thick film under a perpendicular field. $\mu_0 Hz =$-380 mT at 350 K for (a), -70 mT at 410 K for (b) 40 mT at RT in a 10 μm patterned wire for (c). In (c), a reference image was subtracted from the images, *i.e.*, the color shows the modification of the Kerr signal.

Crossing T_{MC}, the Kerr contrast is not reversed but a reversal of the DW propagation direction is evidenced. Examining the sense of propagation of a DW is a more precise method to determine the magnetic compensation than analyzing hysteresis loops (using either the divergence of the coercive field or the reversal of loops). In both methods we measure the effect of a field on the measured quantity. In our films the propagation field of DWs is much smaller than the nucleation field which gives a more sensitive information than H_C. This is also the reason why there is no much more nucleation during the DWM measurements.

1.4.3 Observation of internal domain wall structure by XPEEM

In a thin perpendicularly-magnetized film, two types of 180° DW may exist: Bloch and Néel DWs (see Fig. 1.15 (a) and Part. 1.4.1). The existence of each one results from an equilibrium between the DMI and the demagnetization effects. In ferrimagnetic thin films, the magnetization (and therefore the stray field proportional to M_S) changes drastically with temperature or chemical composition. Consequently, it should be possible to change the internal DW magnetization angle ϕ sweeping the temperature or the alloy composition. In particular, across T_{MC}, the net magnetization vanishes (as shown Fig. 1.9) and we suggest that this changes the equilibrium DW structure. Fig. 1.15 (c) shows a sketch of the expected stable DW structure in ferrimagnetic alloy versus T in this frame. The magnetization dependence of T is shown Fig. 1.15 (b). It is possible to see that through T_{MC}, since K_{BN} goes to zero, the DW flips into the Néel configuration even for a very weak DMI ($D = 10^{-6}$ mJ/m^2 taken in this calculation).
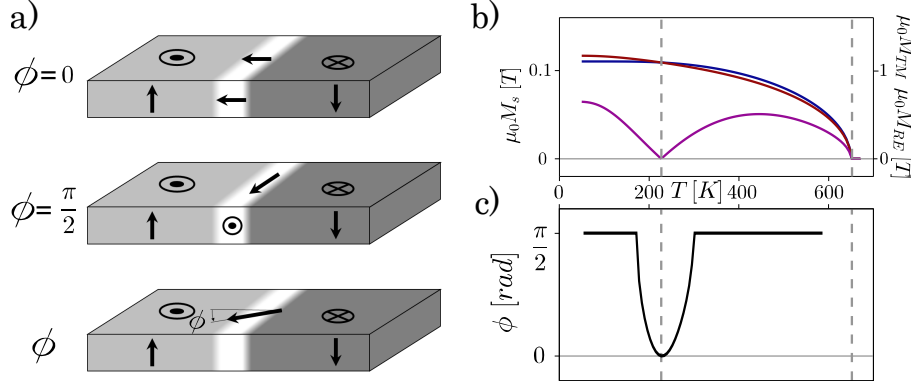
Figure 1.15 – Domain wall structure versus temperature in RETM films. (a) Different DW types (from the top to the bottom): Bloch, Néel and intermediate state. The gray contrast corresponds to the magnetization and the DW is shown in white. The ϕ angle indicate the in-plane DW magnetization angle: $\phi = 0 \rightarrow$ Néel and $\phi = \frac{\pi}{2} \rightarrow$ Bloch DW. (b) Mean-field calculations of M_S in a ferrimagnetic thin film (based on the *GdCo* quantities). (c) Calculated stable DW configuration. Here, we consider a DW width of $\Delta = 20\ nm$ (estimated value) and a constant interfacial DMI of $D = 10^{-6} mJ/m^2$ (low value compared to classical materials).

To investigate the internal DW structure, due to the optical limitation (resolution $\approx 0.5\mu m$), the classical Kerr imaging method is not usable. One of the most appropriate techniques is X-ray photoemission electron microscopy (XPEEM). XPEEM exploits the characteristics of synchrotron radiation to implement a laterally resolved version of x-ray photoelectron spectroscopy (XPS). It combines a microscope column with an energy analyzer of the photo-emitted electrons. It is a full-field technique, the magnetic sample is in a high level of energy under a voltage gate (of around 30 kV). The incident X-ray beam induces the emission of photo-electrons. If the incident X-ray is polarized, typically circularly right or left polarized, the electron emission is spin dependent. Furthermore, choosing an appropriate wavelength, it is possible to select a specific electronic state that is sensitive to the local magnetization. By collecting the emitted electrons, it is possible to reconstruct an image of the local spin density and, for a magnetic material, an image of the local magnetization [81, 117]. In this method, the signal is proportional to the magnetization projection along the wave vector of the incident beam. Using a beam at grazing incidence (16° in most experimental setups), it is possible to measure the in-plane magnetization components but also the out-of-plane component with a reduced sensitivity. One of the main advantages of X-ray

based microscopy compared to magneto-optical microscopy is its elemental sensitivity and the possibly to extract quantitative information, originating from the X-ray dichroism effect as magnetic contrast mechanism. In the case of a ferrimagnetic material, by choosing an appropriate wavelength, it is possible to get information about just one of the tow sub-lattices independently of the resulting magnetization. However, for our purposes, the main advantage of this technique is the high resolution (≈ 20 nm in the best conditions) which is sufficient to spatially resolve small magnetic textures such as DWs or skyrmions [81].

XPEEM profile of a domain wall Considering the DW theoretical profile (see section. 1.4.1) and an X-ray beam with an incidence direction along $\vec{u}_B$ (defined by the angle of (ϕ_B, θ_B)), it is possible to calculate the expected XMCD signal of a DW depending on φ (the internal angle of magnetization):

$$\frac{I}{I_0} = \vec{m}(x) \cdot \vec{u}_B = \cos(\varphi - \phi_B)\sin(\theta_B)\text{sech}(\frac{x}{\Delta}) - \cos(\theta_B)\tanh(\frac{x}{\Delta}) \tag{1.16}$$

Here, the X-ray angle θ_B is fixed by the experimental setup ($\approx 16^o$ in general *i.e.* $\theta_B \approx 74^o$) and ϕ_B represents the in-plane angle between the incident beam and the normal to the DW. I_0 is the maximum of intensity. It is possible to see that this intensity profile contains a symmetric term (in x), common to all the φ and ϕ_B configurations, and an asymmetric contribution maximized if $\varphi = \phi_B$ modulo π. This asymmetric contribution arises from the in-plane magnetization component along the X-ray incident beam. Note that in its maximized configuration, the asymmetric term is about four times larger than the contrast measured in saturated out-of-plane regions. Fig. 1.16 (a) shows all possible configurations of the beam angle ϕ_B for all in-plane DW angles φ and Fig. 1.16 (b) shows a sketch of the intensity contrast across the DW (from the bright to the dark domain) for all the different φ and ϕ_B configurations. Three types of profiles can be obtained (indexed (i), (ii) and (iii)). (a) shows all possible configurations grouped by the associated intensity profiles. If the in-plane DW magnetization is along the incident beam, the intensity profile exhibits a characteristic asymmetry of the XMCD contrast at one of the edges of the DW region. If the in-plane component is antialigned with the incident X-ray a peak appears (profile (i)) and a valley appears if the in-plane component is aligned with the beam. At the opposite, if the in-plane DW magnetization is perpendicular to the incident beam, the intensity profile along the normal of the DW remains perfectly symmetric (profile (ii)). Knowing the shape of the DW relative to that one of the incident x-ray beam, the intensity profile gives the internal DW structure.

In a real experimental setup, the setup resolution σ is expected to be lower than the expected characteristic DW width ($\Delta \approx$ 10-30 nm). To take into account the resolution effect on the intensity profile (Eq. 1.16), the theoretical signal has to be convoluted by a normalized Gaussian function $G_\sigma(x) = \exp\left(-\frac{x^2}{2\sigma^2}\right)/\left(\sqrt{2\pi}\sigma\right)$ which gives:

$$\frac{I}{I_0} \rightarrow \cos(\varphi - \phi_B)\sin(\theta_B)\int_{-\infty}^{+\infty}\text{sech}(\frac{\eta}{\Delta})G_\sigma(x-\eta)d\eta - \cos(\theta_B)\int_{-\infty}^{+\infty}\tanh(\frac{\eta}{\Delta})G_\sigma(x-\eta)d\eta \tag{1.17}$$

However, due to the parity of the convolutive Gaussian function, the two contributions of the signal remain symmetric and antisymmetric. Furthermore, due to the larger magnitude of the asymmetric part compared to the symmetric one, the peak is still visible even in the experimental resolution is larger than the DW width Δ. Fig. 1.16 (c) shows on the left panel how the two types of intensity profiles ((i) and (ii)) are affected by a degrading resolution. The symmetric profile is larger but still recognizable. In contrast, the asymmetric peak is flattened and it also appears as symmetric at low resolution (large σ). The right panel shows the relative amplitude of the peak I_{max}/I_0 *versus* the setup resolution σ. For a low resolution (σ larger than 10Δ), the peak is hardly distinguishable from the saturated out-of-plane signal (here 25% of I_0) and it is not possible to differentiate between the symmetric and the asymmetric profiles. Considering a noise of 10% of the saturated out-of-plane domain signal, this critical deterioration occurs for resolution just larger than 6Δ. For an higher resolution (σ smaller than the above limit), it is possible to fit the intensity profile and determine the DW parameters. The main advantage with this approach is that the internal DW in-plane angle φ, the DW width parameter Δ and the setup resolution parameter σ are independent: *i.e.* it is possible to extract independently both parameters form the intensity profile.
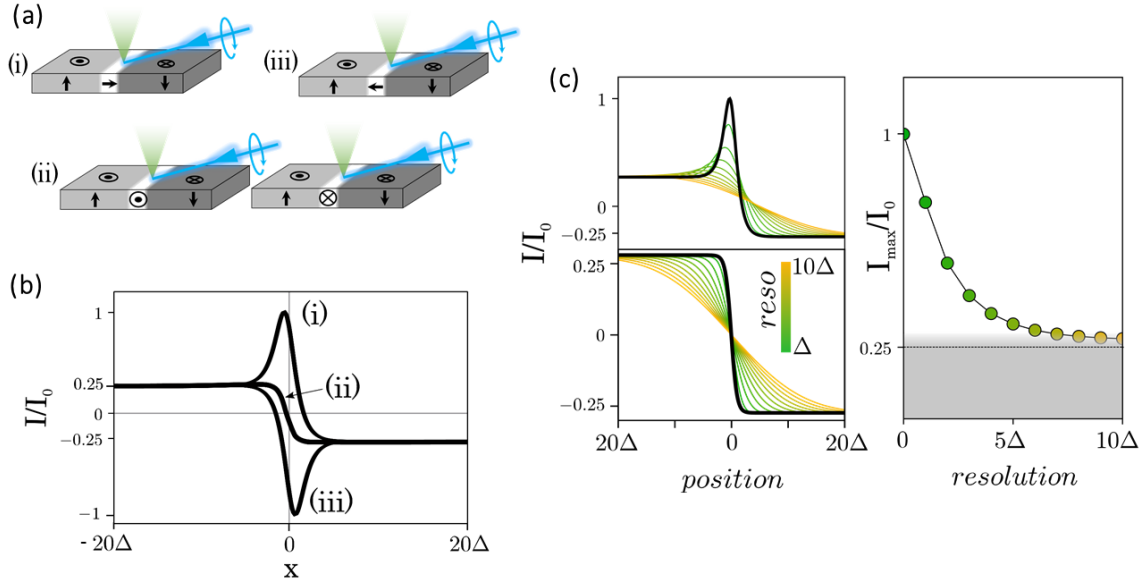
Figure 1.16 – XMCD-PEEM signal profile of a domain wall. (a) All the different relative orientations of the incident beam, the DW and its internal structure. (b) Calculated XMCD-PEEM profile along the normal of the DW (from the bright to the dark domain) indexed (i), (ii) and (iii) for different DW configurations sketched in (a). An almost grazing incidence of the X-ray ($\approx 16°$) is considered (*i.e.* $\theta_B = 74°$). (c) On the left panel: intensity profile (i) and (ii) (in black) for different setup resolutions (in a yellow to green colorscale). On the right panel, the peak amplitude of the profile (i) versus the setup resolution. The opaque gray region (from 0 to 25%) corresponds to the intensity of the saturated regions and the transparent gray region takes into account an intensity noise of 10%.

Experimental details We performed XPEEM experiments at the BESSY synchrotron in Berlin, at SOLEIL in Paris Saclay and at the ALBA synchrotron in Barcelona. Due to a lack of resolution, we could not resolve the DW structure of TbFeCo films at BESSY. In ALBA, on the CIRCE beamline, the DW structure could be determined in GdFeCo films as shown in the following text. We studied GdFeCo with the objective to work on samples with broader DWs since the anisotropy is smaller in Gd-based ferrimagnets than in the Tb-based ones. We observed that the GdFeCo samples changed under irradiation with the high intensity x-ray beam. In these samples, that have a quite small anisotropy, the x-ray irradiation changed the magnetic domains states, and could render the sample permanently in-plane magnetized. After reducing the x-ray beam intensity, we could see that DWs were moving under irradiation, preventing a quantitative analysis of DW profiles. To prevent this effect, samples were cooled down to lower temperatures with the aim of freezing the DW motion during imaging. This prevented us to work on an extended temperature range as initially foreseen.

PEEM experimental results Fig. 1.17 and Fig. 1.18 show the experimental measurements of DW structure in a SiOx/GdFeCo$_{5nm}$/Al$_{5nm}$ thin film. Fig. 1.17 Shows a spectrum of the signal intensity versus the wavelength at the Gd-edge for the two different circular-polarization of X-rays at room temperature. The subtraction of these two spectra reveals a maximum of the X-ray magnetic-circular dichroism (XMCD) [69] at the energy of 1178.7 eV used for the following results and characteristic for the M$_{4,5}$ edge of Gd. We also checked the sense of the beam line photons polarization. For RE sub-lattices, if the magnetization has a parallel component to the beam, intensity in circular positive (C^+) is lower than for circular negative (C^-) or the XMCD, if defined as $\frac{C^+ - C^-}{C^+ + C^-}$ is negative at the M$_{4,5}$ edge of Gd. For this sample, the T_{MC} is just above the experimental temperature and so, the net magnetization is along the Gd sub-lattice one. However, note that the knowledge of the magnetization orientation is not required to deduce both the DW type (Bloch/Néel) and its eventual chirality (according to Fig. 1.16).
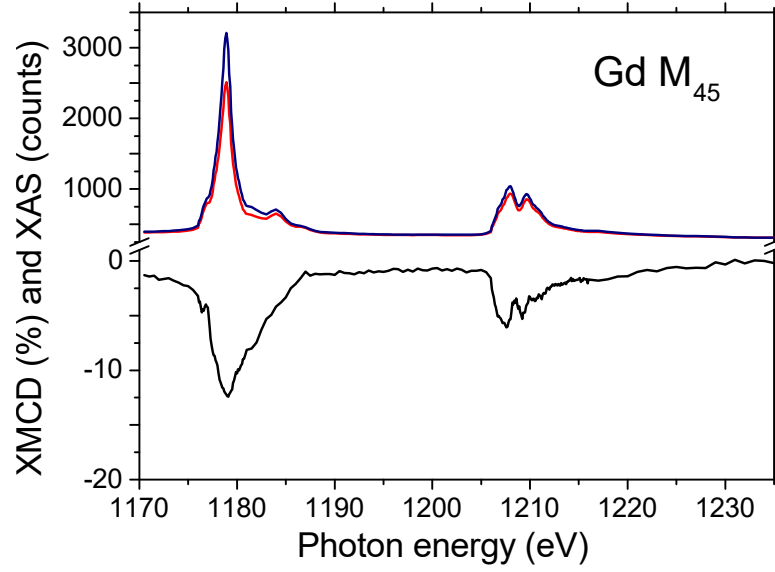
Figure 1.17 – XAS absorption for ± circular polarization of the X-ray beam (blue and red), and XMCD ratio (black) at 300K.

Fig. 1.18 shows an XPEEM image of the magnetic film kept at $T \approx 215$ K. The two grey regions reveal two out-of-plane domains separated by a magnetic DW. The domain pattern could be slightly modified by applying an out-of-plane magnetic field. On the part of the DW that is perpendicular to the X-ray beam, it is possible to observe different contrasts at each edge of the DW, whereas, on the part of the DW along the X-ray beam, the contrast is the same. The intensity profile of the XMCD signal are plotted for each DW. These are the signatures of symmetric and asymmetric contributions of the intensity profile (expected from our calculations). (i) and (iii) presents both the symmetric and the asymmetric components whereas (ii) does not present any asymmetric part. This exclusive presence of the asymmetric part in the DW profile normal to the X-ray beam clearly indicates the Néel structure of the DW. Using the theoretical model of the intensity profile containing the resolution effect (Eq. 1.17), it is possible to fit independently the φ, Δ and σ parameters (oranges curves). We obtain values of -0.05^o and 0° (fixed for the fitting) for φ the in-plane angle along the normal of the DW, 47 nm and 51 nm for Δ, and a resolution of almost 36nm.

The stabilization of the Néel wall indicates the presence of a chiral DMI [85]. However, this sample does not contain any heavy metal layer which could induce an interfacial DMI. One of the possible origins for this DMI is a composition gradient (see part 1.2.4) as already indirectly observed in similar samples [70]. Very recently, SOT experiments demonstrated the existence of bulk-like torques in the same sample and preliminary DMI measurements using Brillouin Light Scattering [118] indicate a sizable DMI.
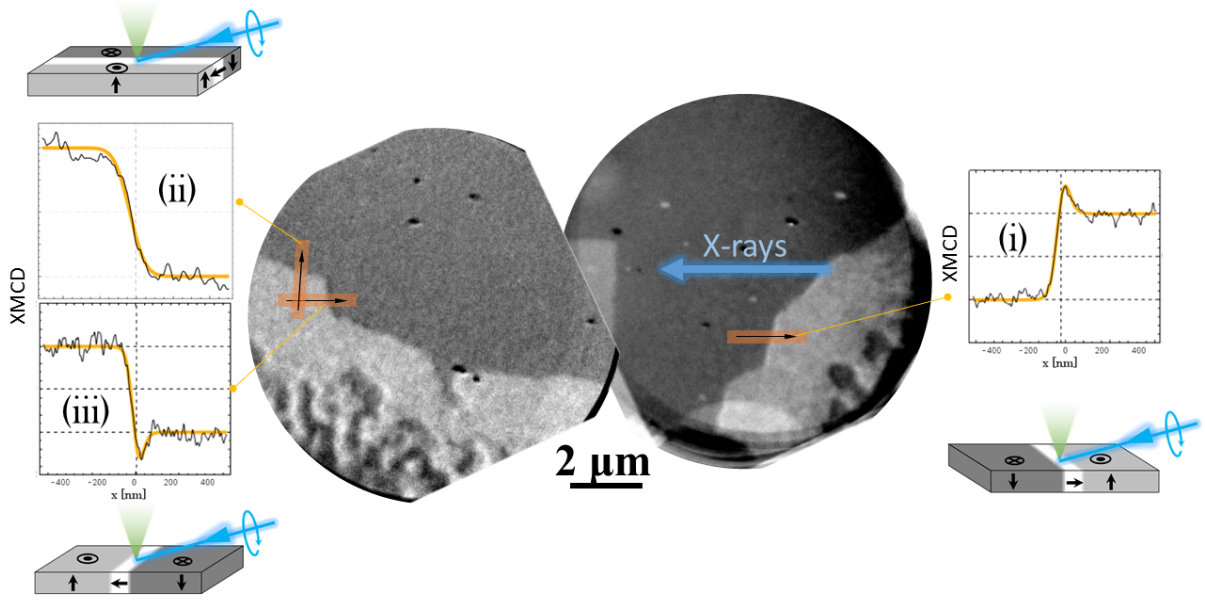
Figure 1.18 – XPEEM images of magnetic domains and DW in a SiOx/GdFeCo$_{5nm}$/Al$_{5nm}$ thin film. The two central images correspond to the XMCD contrast with an horizontal incident X-ray (as indicated by the blue arrow) at the Gd edge (1178.7 eV). The three around panels show the intensity profiles of the DW sections indicated in the central images. The oranges curves correspond to the fit of the intensity profile by considering the eq. 1.17. Each intensity profile is associated to a sketch of the DW internal structure.

1.5 Conclusions

In this chapter we measured the static magnetic properties of RE-TM ferrimagnetic thin films. First, we validated the control of both thickness and chemical composition of the alloy films deposited by co-evaporation (part 1.2). Furthermore, RBS measurements validated the lateral chemical homogeneity and STEM-LEEM experiment confirmed the amorphous structure of films. Comparing depth-integrated (from RBS) and local distribution (from STEM-LEEM) of chemical components, we revealed a biased composition effect associated to depth gradient of the magnetic layer composition (due to the high sensitivity of RE elements). The macroscopic magnetic properties were investigated comparing magnetization, transport and optical measurements (part 1.3). They revealed the perpendicular magnetic anisotropy of the films. Direct magnetization measurements showed the very small net magnetization of the alloy films (10 times lower than typical ferromagnets). This was related to the existence of a magnetic compensation point where the magnetization of the two sub-lattices are exactly opposed and the resulting magnetization of the ferrimagnet vanishes. Electrical AHE measurements showed that only the TM sub-lattice interacts with the electron flow. Magneto-optical experiments exhibit a strong signal and the chemical selectivity of both sub-lattices. We also investigated the local microscopic properties of the ferrimagnetic films using magneto-optical microscopy (part 1.4) that revealed a magnetic domain distribution of the magnetization separated by 180° DW. The homogeneous DW propagation driven by field confirmed the homogeneity of the magnetic properties across the full film or patterned structures. Finally, XPEEM imaging revealed the internal structure of the DW. A Néel stabilized configuration was observed, which is the signature of the presence of chiral DMI even in the absence of adjacent heavy metal layer.

1.6 Perspectives

In this section, I present studies that we have recently started and that have already given some initial results.

1.6.1 Extended studies of magnetic properties *via* Hall hysteresis loops

Moving from Tb-based to Gd-based based ferrimagnetic alloy is very convenient thanks to lower coercitive and propagation fields. However, it reduces drastically the anisotropy. In the studied films, two behaviors appear due to this modification: the transition from perpendicular to in-plane magnetized films and the spin-flop transition. In this section, two studies investigating these two effects using Hall measurements are presented.

1.6.1.1 Magnetic anisotropy and demagnetization effect

Fig. 1.19 shows AHE hysteresis loops of a $Si/SiOx_{(100nm)}//GdFeCo_{(7nm)}/Al_{(5nm)}$ film for different temperatures. Cycles are shifted vertically for each temperature. Starting from the hottest to the coldest (*i.e.* from the top to the bottom), it is possible to identify square hysteresis loops which indicates a perpendicular magnetic anisotropy. Note that here, for GdFeCo, the coercive field is much smaller than for the previous Tb-based alloy due to the much lower anisotropy. At 275 K, the coercive field diverges and the loops are reversed, which is the signature of the magnetic compensation point. Cooling again the sample, it is possible to see that the remanent part of the loop disappears which indicates that the magnetic anisotropy 'falls' in-plane (as discussed in part 1.3.2). Cooling again the film, the saturation field increases. This anisotropy modification comes from the reduction of the anisotropy term by the demagnetization effect (as discussed in part 1.3.1). Here, far from T_{MC} the magnetization increases drastically (see Fig 1.9), and the demagnetization effect becomes stronger than the bulk and surface anisotropy contribution. In order to reduce this effect, thinner magnetic layers (of typically 5 nm) were deposited to increase the surface anisotropy contribution and keep an out-of-plane magnetization. For standard experiments we have also inserted the GdFeCo layer in stacks containing Pt adjacent layer known to promote perpendicular anisotropy.
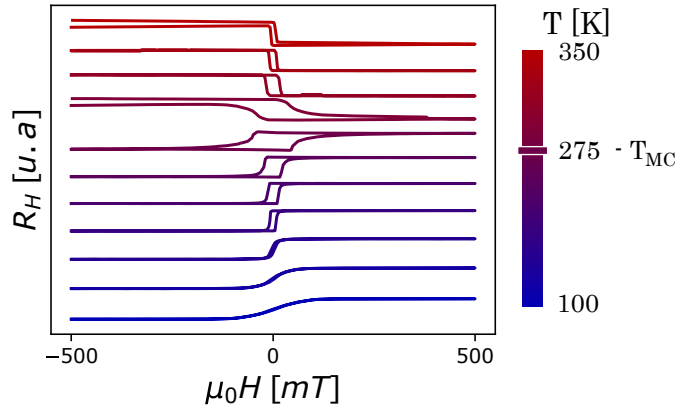
Figure 1.19 – AHE hysteresis loops under perpendicular field at different temperatures for a $Si/SiOx_{(100nm)}//GdFeCo_{(7nm)}/Al_{(5nm)}$ thin film. Loops are shifted for each temperature.

1.6.1.2 Spin-flop transition

In order to investigate the inter-sub-lattice exchange coupling, it is possible to measure the spin-flop transition. Above a critical field, called the spin-flop field H_{sf}, the magnetization of both sub-lattices are not colinear anymore and change continuously up to a new saturated situation in which both are parallel [50, 51, 119]. At this transition, the Zeeman contribution of both sub-lattices can overcome the antiferromagnetic exchange coupling and it induces the alignment of the two sub-lattice magnetizations.

Fig. 1.20 (a) shows the AHE of a GdFeCo film with perpendicular magnetic anisotropy for positive perpendicular field larger than the coercitive field for different temperatures. At the beginning of the investigated field range, the AHE curves are flat (R_H constant) which indicates that the sample is in its classical saturated state: the magnetization of the two sub-lattices are in opposite directions and the larger one is aligned along the applied field. The high and low values of R_H (around ±0.15Ω) indicate that the magnetic compensation occurs at 260 K (similarly to the hysteresis loops reversal detailed in part 1.3.4). Here the amplitude of the AHE in the saturated region does not change because of the weak variation of the TM magnetization in the short investigated range of temperature. Above a critical field, the AHE signal deviates from its saturation level, decreasing down to an intermediate state close to zero. This is the signature of the spin-flop transition. Indeed, the AHE signal depends on the perpendicular component of the TM magnetization. Above the critical spin-flop field, it tilts, decreasing the AHE signal.
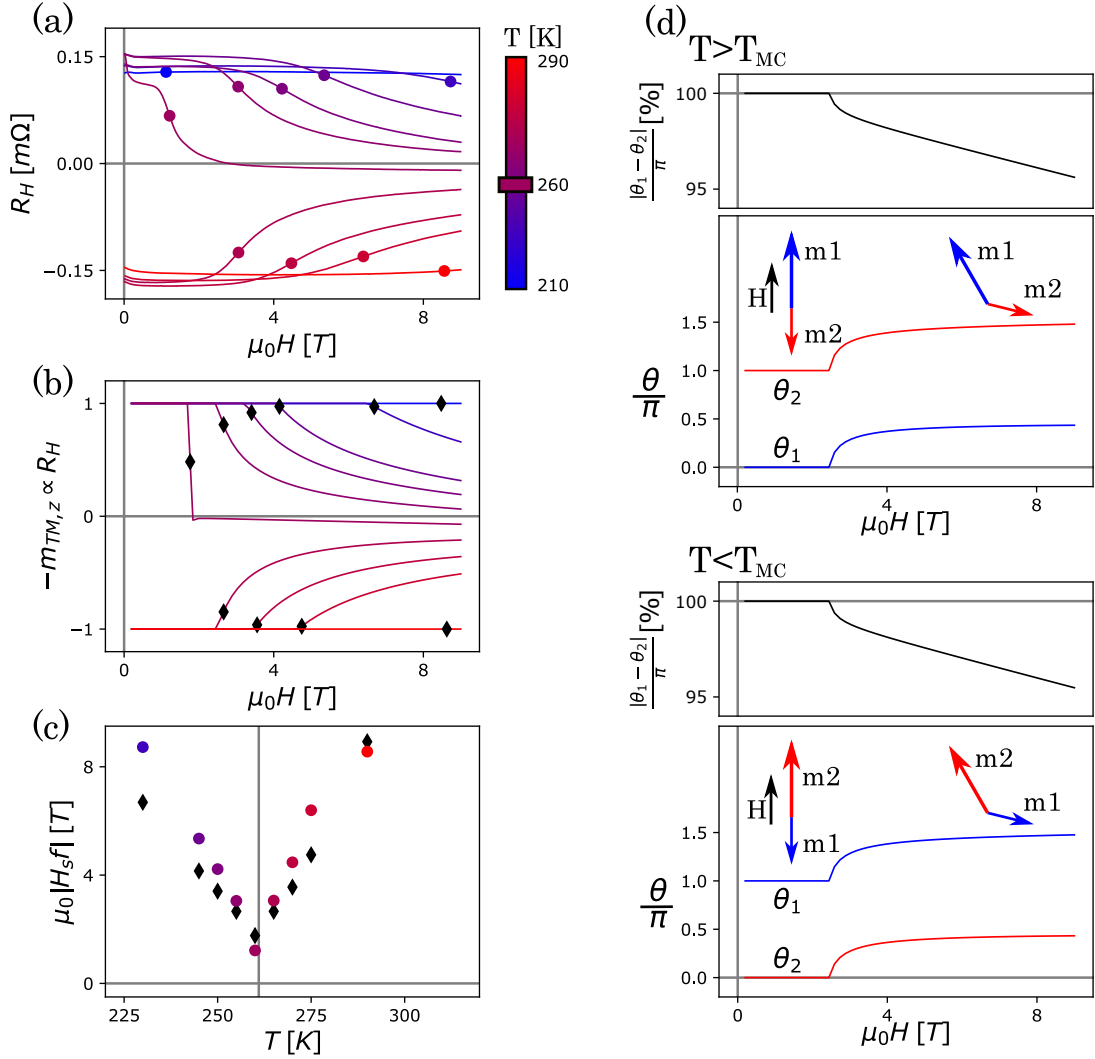
Figure 1.20 – (a) Experimental AHE signal of a SiOx$_{5nm}$/GdFeCo$_{5nm}$/Pt$_{5nm}$. A constant offset of 0.34Ω is removed for all curves in order to center the AHE signal from each part of the T_{MC}. Here the values of H_{sf} are taken at the maximums of the $\partial_H R_H$ slope. These values are indicated as color circles for each T. (b) Calculated perpendicular component to the TM sub-lattice during the spin-flop transition for different temperatures (dy minimizing eq. 1.18). The black diamonds indicate the extracted spin-flop fields (similarly defined as the maximum of $\partial_H R_H$). (c) Color circles show the Spin-flop field extracted from the experimental AHE curves and black diamonds from the calculated curves. The vertical line indicates $T_{MC} = 260$ K. (d) Sketch fo the magnetization variations for the two sub-lattices during the spin-flop transition above and below the T_{MC}.

The extracted values of H_{sf} are plotted as color points in Fig. 1.20 (c). They are minimum at T_{MC} but remain of the order of 1 T. These values correspond to the field above which the strong antiferromagnetic coupling approximation is no longer valid. The critical spin-flop field depends on both the anisotropy (which promotes the perpendicular direction of the magnetization) and the exchange coupling terms (which favors the anti-alignment of the magnetization) [51, 119]. In this situation, the total energy of the system can be written as:

$$\epsilon = -\mu_0 M_1 H \cos(\theta_1) - K \cos(\theta_1)^2 - \mu_0 M_2 H \cos(\theta_2) + J_{ex12} \cos(\theta_2 - \theta_1) + \frac{\mu_0}{2}(M_1 \cos(\theta_1) + M_2 \cos(\theta_2))^2$$
(1.18)

with K the anisotropy constant and J_{ex12} the antiferromagnetic coupling constant. The last term corresponds to the demagnetization effect which is no-longer negligible above the spin-flop transition (even around T_{MC}). Here, the anisotropy term associated to the sub-lattice indexed 2 is neglected. In this situation, the sample is saturated and the magnetization direction of the sub-lattices can be described by two polar angles θ_1 and θ_2. Minimizing the total magnetic energy (Eq. 1.18), it is possible to calculate the equilibrium θ_1 and θ_2 polar angles as shown Fig.1.20 (d). It is also possible to determine the spin-flop field H_{sf} for which $\theta_2 - \theta_1$ deviates from π. Fig. 1.20 (b) shows the calculated perpendicular component of the TM sub-lattices (almost proportional to R_H) during the spin-flop process for the same temperatures than the experimental curves shown Fig. 1.20 (a). Standard values of magnetization are considered and both the inter-exchange coupling J_{ex} and the anisotropy terms K were adjusted to reproduce the experimental data. The best values obtained are $J_{ex} = 5.10^7$ J/m^3 and $K = 2.10^4$ J/m^3 which gives a good idea of the magnitude of these two energy terms. The spin-flop field values extracted from this calculation are plotted in Fig. 1.20 (c) as black squares. To improve this study of the inter-exchange coupling, complementary measurement are required such as a quantitative anisotropy measurement (*via* in-plane field for instance). However, this measurement gives an order of the field magnitude for which the strong-coupling approximation remains valid.

1.6.2   Scanning NV-magnetometry experiments

The magnetization and the DW internal structure are very relevant for DW dynamics, however, remain challenging to probe experimentally. NV-magnetometry is an experimental method which measures precisely and locally the magnetic field [88]. It is based on the magnetic field dependence of the photo-desexcitation spectrum of a nitrogen vacancy in diamond (called NV-center). Measuring the Zeeman splitting between two characteristic peaks in its spectrum, it is possible to obtain the magnetic field at the position of the NV-center with a very high sensitivity (≈ 70 Hz/mT). Furthermore, coupling an NV-center to a scanning setup, it is possible to obtain a very high space and field resolution of the radiated field created by a magnetic texture in a thin film [84, 90, 120].

Fig. 1.21 shows different images obtained by this NV mapping method (in (b) and (c)). Fig. 1.21 (a) shows a Kerr image of the studied TbFeCo$_{7nm}$/Al$_{5nm}$ patterned thin film. The vertical gold line is an antenna required to excite the NV-center and obtain the photo-desexcitation spectrum. Fig. 1.21 (b) shows, on the top panel, a reconstructed image of the field radiated by a patterned 2μm-wide wire. The bottom panel shows a line scan of a cut perpendicular to the magnetic wire. Considering the theoretical expression of the field profile radiated by a saturated wire [90], it is possible to measure the magnetization of the film. It is also possible to use this method to obtain information about the DW structure [90]. Fig. 1.21 (c) shows on the top panel the measured field radiated by a DW in a full film region. The bottom panel shows the field profile along a cut perpendicular to the DW. Fitting this profile, it is possible to deduce the width parameter of the DW (Δ) and its type (Bloch or Néel) knowing the film magnetization. Here, the magnetization determination is not sufficiently accurate to get simultaneously all the required information. For this field profile fitting, the DW is considered as a Bloch one which gives a magnetization of $\mu_0 M_S \approx 43$ mT and a DW width parameter of $\Delta \approx 10$ nm.

This method is one of the most spatially resolved and is able to investigate both the magnetization and the DW structure. Even if it is based on the measurement of the field radiated by the magnetization (very low in ferrimagnets), it should be sensitive enough to probe the magnetization of films even close to the magnetic compensation. Furthermore, the determination of the DW structure remains very

complementary with Kerr microscopy technique.
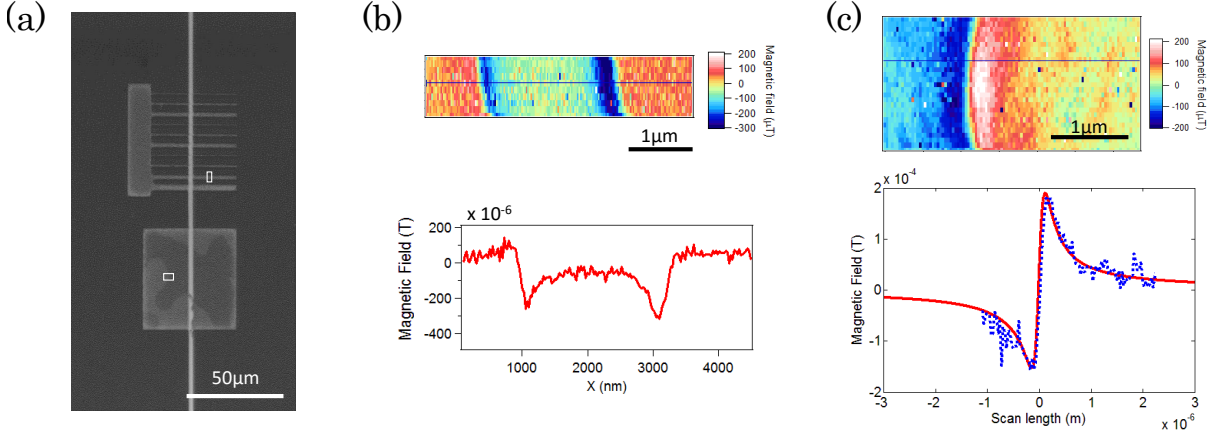
Figure 1.21 – (a) Kerr image of the studied $TbFeCo_{7nm}/Al_{5nm}$ patterned sample. The vertical gold wire is used as a rf excitation line. The two white squares mark the regions of interest detailed in (b) and (c). The top panels in (b) and (c) show NV-scanning images for a probe-sample distance of 130 nm. The color contrast corresponds to the measured magnetic field. (b) shows a perpendicular cut of a 2 μm magnetic wire and (c) shows a perpendicular cut of DW in a full-film region. The bottom panels show line scans of measured field along the line cut (in blue in the top panel). In (c) the red line corresponds to the theoretical model for a Bloch DW field-profile.

1.7 Contributions and publication

Collaborations All studied films were deposited in our laboratory, but their full characterization result from different collaborations. The X-ray reflectometry was performed in LPS with Li Zhizhang. The RBS measurements was realized with the support of Cyril Bachelet at the CSNSM in Paris-Sud University. The STEM-LEEM depth image was done by the STEM team in our laboratory. Magnetization measurements were realized in collaboration with Yves Dumont at Versailles Saint-Quentin University (for VSM), with Richard Mattana at the Unité Mixte de Physique in Palaiseau (for SQUID), and I did VSM-SQUID measurements at the Kosice University in Slovakia. Electrical, optical and Kerr imaging experiments were realized in our laboratory. Even if the presented XPEEM results correspond to the last night of measurements, four synchrotron campaigns were done from which we could learn and advance this work: at BESSY (Berlin) on the STXM MAXYMUS line with Marcus Weigand and Michael Bechtel, at BESSY on the X-PEEM line with Florian Kronast and Mohamad Mawass, at Soleil (Saint-Aubin) on the HERMES PEEM line with Rachid Belkhou and at ALBA (Barcelona) on the PEEM CIRCE line with Lucia Aballe and Michael Foerster. Finally, the NV-images were done in the group of Vincent Jacques at Montpelier University.

Publications. Some of the results in this chapter have given rise to a scientific publication: 'Deviations from bulk behavior in TbFe(Co) thin films: Interfaces contribution in the biased composition' in Physical Review Materials 2, 104410 (2018) [37]. It includes co-evaporation process details, different characterization methods and the correlation between the chemical depth gradient and the deviation of the magnetic properties of ferrimagnetic thin films. Another publication is in preparation about the bulk-interface-like effects in ferrimagnetic thin films. It will present two behaviors of our co-evaporated ferrimagnetic film usually obtained in stacks containing heavy metal layers: the DMI and the SOT, including the PEEM results, second harmonic Hall voltage SOT measurements (realised by Sachin Krishnia), and BLS experiments (realised by André Thiaville).

Dynamic properties in Ferrimagnets

In this chapter, the dynamic behavior of RE-TM ferrimagnetic alloys is investigated. It covers the dynamics of an isolated magnetic moment (part 2.1 and 2.2) and DW dynamics (part 2.3 and 2.4). In section 2.1, I present the existing model to describe the dynamics of magnetism in a magnetic material. In section 2.2, I extend the effective parameter approach to describe the dynamics of two coupled magnetic sub-lattices driven by field, STT, or SOT. In this part, I study in more detail the special behaviors occurring in two specific configurations: the magnetic and the angular compensation points. I present experimental results from the literature to illustrate these different features. The following parts are focused on the dynamics of DW in ferrimagnets. In a third section (part 2.3), two ways of modelling the dynamics of a DW in ferrimagnet are presented: an analytical one (considering a collective coordinate approach of the DW) and a numerical one (considering two sub-lattices interacting by a finite coupling). In the last section (part 2.4) these two models are used to investigate in detail the dynamics of a DW driven by field, STT or SOT. Other aspects, like the transient regime or the low coupling system, are also studied.

2.1 Dynamics of magnetic moments

2.1.1 Manipulation of a magnetic moment by external torques

The dynamics of a magnetic moment can be described by the Landau-Lifshitz-Gilbert equation [121, 122]. This equation describes the time evolution of the moment $\vec{M}$ with a magnitude M_S and unit vector $\vec{m}$ ($\vec{M} = M_S\vec{m}$) under an applied torque $\vec{\Gamma}$:

$$\partial_t\vec{m} = \vec{\Gamma} + \alpha\vec{m} \times \partial_t\vec{m} \tag{2.1}$$

Here, α is called the damping parameter. In a physical system, the spin couples to its environment and dissipates energy, which is expressed by the phenomenological damping torque ($\alpha\vec{m} \times \partial_t\vec{m}$). This term is equivalent to a dissipation term proportional to the time evolution of the magnetic moment itself: $\partial_t\vec{m}$ (like a viscous effect). Furthermore, it is transverse to $\vec{m}$ and to the external applied torque $\vec{\Gamma}$, which induces a relaxation of $\vec{m}$ towards an equilibrium position. The α damping parameter is an empirical dimension-less number which accounts for all the dissipation processes that may be present (from the SOC, phonons, magnons, ...).

Two geometries of the torque $\vec{\Gamma}$ exist called respectively field-like and damping-like torques:

$$\begin{aligned}
\vec{\Gamma}_{FL} &= \vec{m} \times \vec{u}_{FL}\,\Gamma_{FL} \\
\vec{\Gamma}_{DL} &= \vec{m} \times (\vec{m} \times \vec{u}_{DL})\,\Gamma_{DL}
\end{aligned} \tag{2.2}$$

where unit vectors $\vec{u}_{FL}$ and $\vec{u}_{DL}$ point in a particular direction depending on the torque origin. These torques induce two types of motion: the field-like one drives a precessional motion around $\vec{u}_{FL}$ whereas the damping-like one drives a relaxation towards $\vec{u}_{DL}$. Fig. 2.1 (b) shows the geometry of both torques. Depending on the damping α and the magnitude of the field-like and damping-like torques, many diverse dynamic behaviors can be obtained.
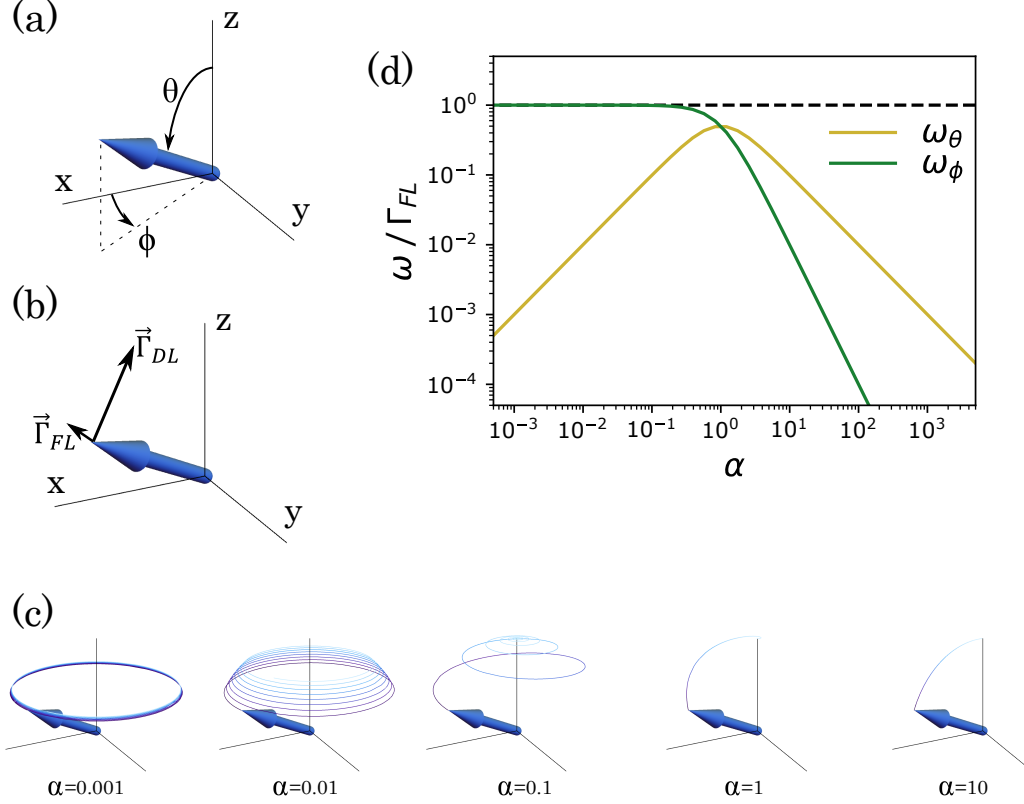
Figure 2.1 – Manipulation of a single magnetic moment. (a) Spherical description of a magnetic moment: $\vec{m}(\theta, \phi) = (\cos(\phi)\sin(\theta), \sin(\phi)\sin(\theta), \cos(\theta))$. (b) Field-like and damping-like torques actions on a magnetic moment. (c) Relaxation and precession of a magnetic moment under a field-like torque (with $\Gamma_{FL} = 1$ and $\vec{u}_{FL}$ along z) for different values of α. (d) relaxation and precession rates ω_θ and ω_ϕ of a magnetic moment under a field-like torque *versus* α.

By taking both $\vec{u}_{FL}$ and $\vec{u}_{DL}$ along the same z-direction and considering a spherical description of the magnetic moment: $\vec{m}(\theta, \phi) = (\cos(\phi)\sin(\theta), \sin(\phi)\sin(\theta), \cos(\theta))$ (in the $(\vec{x}, \vec{y}, \vec{z})$ space as shown Fig. 2.1 (a)), Eq. 2.1 gives the dynamic description of the precession (ϕ) and the relaxation (θ) of the magnetic moment:

$$\begin{cases} \theta(t) = 2\operatorname{arccot}(\cot\left(\frac{\theta_0}{2}\right)\exp\left(\omega_\theta t\right)) \\ \phi(t) = \omega_\phi t + \phi_0 \end{cases} \quad \text{with} \quad \begin{cases} \omega_\theta = \frac{\alpha\Gamma_{FL} + \Gamma_{DL}}{1+\alpha^2} \\ \omega_\phi = \frac{-\Gamma_{FL} + \alpha\Gamma_{DL}}{1+\alpha^2} \end{cases} \tag{2.3}$$

with θ_0 and ϕ_0 the initial configuration of the moment. The relaxation and the precession rates are associated with two characteristic angular frequencies ω_θ and ω_ϕ. Note that in many cases Γ_{DL} and Γ_{FL} depend on $\vec{m}$. If it is the case, the $\theta(t)$ and $\varphi(t)$ expressions (Eq. 2.3) describe the instantaneous evolution of θ and φ in the position θ_0 and ϕ_0. In contrast, if Γ_{DL} and Γ_{FL} are independent of $\vec{m}$, θ and φ describe the full evolution of $\vec{m}$.

First, let's consider the moment manipulation by a field-like torque. Fig. 2.1 (c) shows different reversal modes of the magnetic moment direction for different damping parameters α. Fig. 2.1 (d) shows the angular frequencies ω_θ and ω_ϕ associated with the relaxation and the precession rates. For low

damping, the precession rate is larger than the relaxation rate and the magnetic moment relaxes slowly compared to the precession rate (almost independent of α in this range). Increasing the damping, the precession does not change significantly but the relaxation rate increases up to a maximum value of $\Gamma_{FL}/2$ reached for $\alpha = 1$ [123]. At this critical value, the precession rate decreases and is overtaken by the relaxation rate. Above this value, both the relaxation and the precession rates decrease with $\omega_\theta > \omega_\phi$. However, even if the precession rate may be much smaller than the relaxation rate or the inverse, both dynamics remain observable and ω_θ and ω_ϕ never vanish. Considering now field-like and damping-like contributions, a larger variety of dynamics exists. In this case, the relaxation or the precession dynamics may vanish in two cases, $\Gamma_{DL}/\Gamma_{FL} = -\alpha$ or $= 1/\alpha$. Note that in a classical ferromagnetic material, the ratio Γ_{DL}/Γ_{FL} is of constant sign and so just one of this special points is reachable as $\alpha > 0$.

2.1.2 Magnetic dynamics driven by field

One of the more common ways to manipulate a momentum consist in applying an external magnetic field. The magnetization of the moment is coupled to this applied field $\vec{H}$ which is associated with a torque:

$$\vec{\Gamma}_H = -\gamma_0 \vec{m} \times \vec{H} \tag{2.4}$$

This torque is obviously a field-like torque with a magnitude proportional to the applied field and to the gyromagnetic ratio of the moment γ_0 ($\gamma_0 = \mu_0 \gamma$ and $\gamma = g\mu_B/\hbar$ with g the Landé factor given in table 1.1). Neglecting the damping parameter α, the applied field induces a precession of the magnetic moment around its equilibrium direction with an angular frequency of $\omega_L = \gamma_0 H$ called the Larmor frequency [34]. Increasing α, this precession frequency deviates from and is lower than ω_L (as shown Fig. 2.1 where the Larmor frequency corresponds to the dashed black line).

2.1.3 External environment and magnetic dynamics

The dynamics of a magnetic moment is also sensitive to its environment through interactions such as magnetic anisotropy, DMI, exchange coupling with its neighbors or demagnetization effect (as detailed in part 1.3.1). All these contributions can be taken into account by an effective field $\vec{\mathcal{H}}$ which corresponds to the variation of the total energy ϵ (per unit volume) with respect to the variation of the magnetization distribution $\delta \vec{m}$:

$$\vec{\mathcal{H}} = \frac{-1}{\mu_0 M_S} \frac{\delta \epsilon}{\delta \vec{m}} \tag{2.5}$$

Implementing this effective field as the applied field $\vec{H} \leftarrow \vec{\mathcal{H}}$, the LLG equation is the minimal model to describe the dynamics of the magnetization $\vec{m}(\vec{r}, t)$ in the magnetic media. Note that, the action of an applied field is taken into account through the Zeeman energy term: $\epsilon_{Zeeman} = -\mu_0 M_S \vec{m} \cdot \vec{H}$. All other non-conservative torques, such as the spin-transfer torque or the spin-orbit torques are added directly in the LLG equation.

2.1.4 Magnetic dynamics driven by spin currents

To manipulate a magnetic moment, it is also possible to use a spin current. Due to the exchange interaction, the spin flow interacts with the local magnetization and locally, if the spin direction $\vec{\sigma}$ is non-aligned with the magnetization $\vec{m}$, it relaxes (along $\vec{m}$) exerting additional torques on $\vec{m}$ called generally spin-torques [124–127]. The two field-like and damping-like geometries of torque can exist such as:

$$\begin{aligned} \vec{\Gamma}_{\vec{\sigma} FL} &= -\gamma_0 H_{FL} \, \vec{m} \times \vec{\sigma} \\ \vec{\Gamma}_{\vec{\sigma} DL} &= \gamma_0 H_{DL} \, \vec{m} \times (\vec{m} \times \vec{\sigma}) \end{aligned} \tag{2.6}$$

where H_{FL} and H_{DL} are the fields associated with the field-like and damping-like torques (*i.e.* $H_{FL} = -\Gamma_{FL}/\gamma_0$ and $H_{DL} = \Gamma_{DL}/\gamma_0$) as shown Fig. 2.2 (a).

In order to electrically manipulate the magnetization of a magnetic layer, several ways to inject a spin current have already been studied (shown in Fig. 2.2).
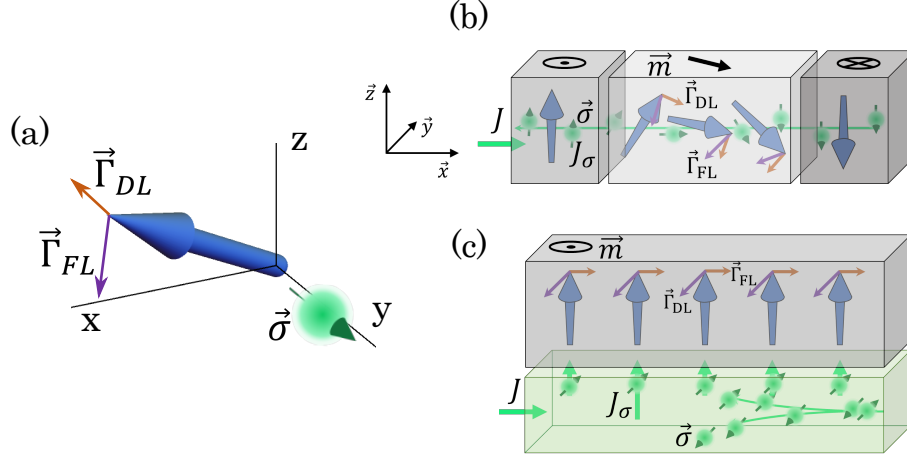
Figure 2.2 – Magnetisation manipulation by spin current. (a) Field-like and damping-like torques induced by a spin current polarized along $\vec{\sigma} = y$ (Eq. 2.7). (b) STT mechanism applied on a spin texture (here a DW). (c) SOT mechanism applied on a saturated layer. In (b) and (c) J and $J_{\vec{\sigma}}$ refer to the charge current and to the spin current. In (c), the green region corresponds to an adjacent layer with strong spin-orbit coupling (such as a heavy metal).

2.1.4.1 Spin transfer torques

If an electrical current is injected into a conducting magnetic layer containing non-colinear magnetic texture such as a DW, a skyrmion or a vortex (see Part 1.4), the non-uniform spatial distribution of the magnetization $\vec{m}$ can induce a misalignment between the spin density of the carrier electrons and the local $\vec{m}$. Indeed, as detailed before (see section 1.3.4), in TM based materials, the spin polarization of the carrier electrons is along the magnetization direction. When an electrical current flows through a magnetic texture, its polarization state changes according to the local magnetization of the texture $\vec{m}(\vec{r}, t)$. If the characteristic length of the magnetic variation along the texture ($\sim 10-50$ nm as shown in Part 1.4) is shorter than the spin diffusion length ($\sim 5-50$ nm [128]), the spin flow moves faster than it relaxes and, locally, is misaligned with the magnetization (as shown in Fig. 2.2 (b)). This misalignment of the spin density induces a torque on the local magnetization called the spin transfer torque [124,129–131].

The STT results from the competition between two phenomena. Firstly, the exchange interaction between the magnetic moment of the electrical current (associated with the moving s electrons) and the local magnetization (associated with the d electrons) acts on $\vec{m}$ as a local field inducing a precession of $\vec{m}$ around the spin direction. Secondly, due to relaxation, the spin polarization eventually aligns along the $\vec{m}$ direction due to spin-flip process. Both effects induce torques on the local $\vec{m}$: the precession induces a torque perpendicular to the gradient of the magnetization called the non-adiabatic torque, which has a field-like geometry, and the relaxation induces a torque along the magnetization gradient called adiabatic torque, with a damping-like geometry [130] (as shown in Fig. 2.2 (b)). The adiabatic and non-adiabatic torques can be written as:

$$
\begin{aligned}
\vec{\Gamma}_{STT_{adiab}} &= -(\vec{u}.\vec{\nabla})\vec{m} \\
\vec{\Gamma}_{STT_{non-adiab}} &= \beta\vec{m} \times (\vec{u}.\vec{\nabla})\vec{m}
\end{aligned}
\tag{2.7}
$$

where u is a drift speed representing the ratio between the electron angular moment $JP\hbar/2e$ and the local angular moment $\mu_0 M_S/\gamma_0$. The drift speed magnitude is [131]:

$$
u = \gamma_0 \frac{\hbar}{2e} \frac{1}{\mu_0 M_S} PJ
\tag{2.8}
$$

As expected, both STTs are proportional to the gradient of the local magnetization along the current flow direction $\vec{u}.\vec{\nabla} \propto \vec{J}.\vec{\nabla}$. Furthermore, the non-adiabatic torque is proportional to the β term which compares characteristic times of the precession and relaxation associated with exchange and spin-flip of the electron flow. [130, 131].

2.1.4.2 Spin Hall effect

It has also been shown that the injection of an electric current J into a heavy material with a strong spin-orbit coupling (such as Pt, Ta or W) generates a pure spin current, transverse to the electrical current [132, 133]. Unlike the STT mechanism, in this transverse direction, there is a current of spin without any charge motion. This mechanism is called spin Hall effect (SHE). Adjoining a magnetic layer to a strong spin-orbit coupling material, it is possible to use this pure spin current to manipulate electrically its magnetization [126, 127, 134–137]. The SHE creates a damping-like torque on the magnetization (as shown in Fig. 2.2 (c)) and its amplitude can be associated with a field:

$$H_{SHE} = \frac{\hbar}{2e} \frac{1}{\mu_0 M_s} \frac{\Theta_{SH}}{t} J \tag{2.9}$$

Here, t is the film thickness and Θ_{SH} is the spin Hall angle witch describes the ratio between the electrical current in the heavy metal layer and the generated perpendicular spin current.

In this geometry, another torque can occur due to the Rashba effect [126, 138, 139]. This other torque has a field-like torque geometry and it is associated with a field:

$$H_{Rashba} = \frac{\alpha_R}{\mu_0 M_s} P J \tag{2.10}$$

where α_R is the Rashba coefficient averaged along the magnetic layer [139]. Generally, it is much lower in our systems and will be neglected in most of the cases.

More generally, in multi-layer stacks including magnetic and heavy-metal layers, we speak about damping-like and field-like torques for the SHE and the Rashba effect, as shown in Fig. 2.2 (c).

2.1.5 LLG equation

To summarize, to describe the space and time evolution of the magnetization in magnetic media the full LLG equation can be written as:

$$\partial_t \vec{m} = -\gamma_0 \vec{m} \times \vec{\mathcal{H}} + \alpha \vec{m} \times \partial_t \vec{m} - (\vec{u}.\vec{\nabla})\vec{m} + \beta \vec{m} \times (\vec{u}.\vec{\nabla})\vec{m} + \gamma_0 H_{FL} \ \vec{m} \times \vec{\sigma} + \gamma_0 H_{DL} \ \vec{m} \times (\vec{m} \times \vec{\sigma}) \tag{2.11}$$

In the following parts, the current flows along the x direction which gives: $(\vec{u}.\vec{\nabla})\vec{m} \rightarrow u\partial_x \vec{m}$. The z direction is defined by the out-of-plane perpendicular magnetic anisotropy. Finally, the SHE is mainly considered which gives a spin direction $\vec{\sigma}$ along y.

Other approaches consider also thermal effects on the moment dynamics, which can be large especially in the vicinity of the Curie temperature [140–142]. In this situation, due to thermal agitation, the net mean-magnetization is reduced by the temperature which can be associated to changes of the micromagnetic parameters. These modifications leads to a new equation called LLB [142]. To model the time stochastic dependence of these thermal effects [140], it is also possible to use the LLG equation with a stochastic field called thermal field H_{Th} [143].

2.2 Dynamics in ferrimagnetic alloys

In the case of a multi-lattice material, the magnetization of each sub-lattice can be described by a LLG equation (Eq. 2.11) depending on the sub-lattice parameters with an extra term to account for the coupling interaction between the sub-lattices [15, 16, 26, 144, 145]. In the case of a RE-TM ferrimagnetic alloy, the two magnetic populations (indexed 1 and 2) interact with each other *via* an antiferromagnetic coupling (see section 1.1) and two LLG equations have to be considered (one for each sub-lattice) including an additional antiferromagnetic inter-exchange $J_{ex12} > 0$ between the two magnetic populations. The inter-exchange energy is given by:

$$\epsilon_{ex12} = J_{ex12}\vec{m}_1\vec{m}_2 \tag{2.12}$$

Incidentally, this energy can be associated with an effective exchange field $\vec{H}_{ex,1} = -(J_{ex12}/\mu_0 M_1)\vec{m}_2$ acting on sub-lattice 1, and a similar field $\vec{H}_{ex,2}$ acting on sub-lattice 2. Here, it is taken into account in the total energy ϵ which gives:

$$\begin{cases} \partial_t\vec{m}_1 = & -\gamma_{01}\vec{m}_1 \times \vec{\mathcal{H}}_1 + \alpha_1\vec{m}_1 \times \partial_t\vec{m}_1 \\ & -(\vec{u}_1.\vec{\nabla})\vec{m}_1 + \beta_1\vec{m}_1 \times (\vec{u}_1.\vec{\nabla})\vec{m}_1 + \gamma_{01}H_{FL1}\ \vec{m}_1 \times \vec{\sigma} + \gamma_{01}H_{DL1}\ \vec{m}_1 \times (\vec{m}_1 \times \vec{\sigma}) \\ \partial_t\vec{m}_2 = & -\gamma_{02}\vec{m}_2 \times \vec{\mathcal{H}}_2 + \alpha_2\vec{m}_2 \times \partial_t\vec{m}_2 \\ & -(\vec{u}_2.\vec{\nabla})\vec{m}_2 + \beta_2\vec{m}_2 \times (\vec{u}_2.\vec{\nabla})\vec{m}_2 + \gamma_{02}H_{FL2}\ \vec{m}_2 \times \vec{\sigma} + \gamma_{02}H_{DL2}\ \vec{m}_2 \times (\vec{m}_2 \times \vec{\sigma}) \end{cases} \tag{2.13}$$

with effective fields $\vec{\mathcal{H}}_1 = \frac{-1}{\mu_0 M_1}\frac{\delta\epsilon}{\delta\vec{m}_1}$ and $\vec{\mathcal{H}}_2$ (similarly defined) derived from the energy per unit of volume $\epsilon = \epsilon_1 + \epsilon_2 + \epsilon_{ex12}$. Note that here we consider that the applied field H and current density J are the same for both sub-lattices.

2.2.1 Effective parameter approach of ferrimagnetic dynamics

Considering the cases when the magnitudes of the applied torques are negligible compared with the torque associated to the inter-lattice coupling it is possible to write:

$$J_{ex12} \gg \begin{cases} \mu_0 M_{1/2}H(\text{or } \mathcal{H}_{1/2})(\times\alpha_{1/2}) \\ \\ \frac{1}{\Delta}\frac{2e}{\hbar}P_1 J(\times\beta_1) \\ \\ \frac{2e}{\hbar}\frac{\Theta_{SH1}}{t}J \end{cases} \tag{2.14}$$

As demonstrated in part 1.6.1.2 describing the investigation of the spin-flop transition, this approximation remains valid for applied fields lower than a few Tesla in our systems. For the spin torques, the framework is different than in the case of the spin-flop approach. Indeed, here, the spin just interacts with the TM sub-lattice (see part 1.3.4) and no spin-flop-like transition occurs.

In this case of strong inter-lattice coupling, the anti-alignment of magnetic moments $\vec{m}_1$ and $\vec{m}_2$ is not significantly disturbed. It is then possible to consider $\vec{m}_1 = -\vec{m}_2$ and the two sub-lattices can be associated with an equivalent effective magnetic material with a net magnetization $M_S = M_1 - M_2$ and $\vec{m} = \vec{m}_1 = -\vec{m}_2$, similarly to [145, 146]. Summing the two LLG equations (Eq. 2.13) it is possible to get an effective LLG equation which describes the dynamics of this effective magnetic medium. $(M_1/\gamma_{01}) \times$

$LLG_{1(\vec{m}_1 \leftarrow \vec{m})} + (M_2/\gamma_{02}) \times LLG_{2(\vec{m}_2 \leftarrow -\vec{m})}$ yields:

$$\left(\frac{M_1}{\gamma_{01}} - \frac{M_2}{\gamma_{02}}\right) \partial_t \vec{m} = \frac{1}{\mu_0} \vec{m} \times \frac{\delta\epsilon}{\delta\vec{m}}$$
$$+ \left(\alpha_1 \frac{M_1}{\gamma_{01}} + \alpha_2 \frac{M_2}{\gamma_{02}}\right) \vec{m} \times \partial_t \vec{m}$$
$$- \left(\left(\vec{u}_1 \frac{M_1}{\gamma_{01}} - \vec{u}_2 \frac{M_2}{\gamma_{02}}\right).\vec{\nabla}\right) \vec{m}$$
$$+ \vec{m} \times \left(\left(\beta_1 \vec{u}_1 \frac{M_1}{\gamma_{01}} + \beta_2 \vec{u}_2 \frac{M_2}{\gamma_{02}}\right).\vec{\nabla}\right) \vec{m}$$
$$- (M_1 H_{FL1} - M_2 H_{FL2}) \vec{m} \times \vec{\sigma}$$
$$+ (M_1 H_{DL1} + M_2 H_{DL2}) H_{DL2} \vec{m} \times (\vec{m} \times \vec{\sigma})$$

where $\frac{\delta\epsilon}{\delta\vec{m}} = \frac{\delta\epsilon}{\delta\vec{m}_1}\frac{\partial\vec{m}_1}{\partial\vec{m}} + \frac{\delta\epsilon}{\delta\vec{m}_2}\frac{\partial\vec{m}_2}{\partial\vec{m}} = \frac{\delta\epsilon}{\delta\vec{m}_1} - \frac{\delta\epsilon}{\delta\vec{m}_2}$. Comparing term to term with the LLG equation (Eq. 2.11), it is possible to extract effective parameters associated with the equivalent magnetic medium [145, 146]:

$$
\begin{aligned}
\gamma_{0eff} &= \frac{M_S}{L_S} \\
\vec{\mathcal{H}}_{eff} &= \frac{-1}{\mu_0 M_S} \frac{\delta\epsilon}{\delta\vec{m}} \\
\alpha_{eff} &= \frac{L_\alpha}{L_S} \\
u_{eff} &= \gamma_{0eff} \frac{\hbar}{2e} \frac{1}{\mu_0 M_S} P_{eff} J \text{ with } P_{eff} = P_1 - P_2 \\
\beta_{eff} &= \frac{\beta_1 P_1 + \beta_2 P_2}{P_{eff}} \\
H_{FLeff} &= \frac{M_1 H_{FL1} - M_2 H_{FL2}}{M_S} \\
H_{DLeff} &= \frac{M_1 H_{DL1} + M_2 H_{DL2}}{M_S}
\end{aligned}
\tag{2.15}
$$

where $L_S \equiv \left(\frac{M_1}{\gamma_{01}} - \frac{M_2}{\gamma_{02}}\right)$ is the net angular moment and $L_\alpha \equiv \left(\alpha_1 \frac{M_1}{\gamma_{01}} + \alpha_2 \frac{M_2}{\gamma_{02}}\right)$. Note that torques that are even in $\vec{m}$ add up (e.g. H_{DLeff}), while torques that are odd subtract (e.g. H_{FLeff}). When the DL torque is due to a SHE field, the expression of the associated effective field becomes:

$$H_{SHEeff} = \frac{\hbar}{2e} \frac{1}{\mu_0 M_S} \frac{\Theta_{SHeff}}{t} J \text{ with } \Theta_{SHeff} = \Theta_{SH1} + \Theta_{SH2} \tag{2.16}$$

Even if we consider that the applied field H and current density J are the same for both sub-lattices, they each have a different susceptibility to spin currents which can be taken into account considering two different polarization factors P_1 and P_2. For the same reason, it is also possible to consider two spin Hall angles Θ_{SH1} and Θ_{SH2} to model the torques due to the spin current from the heavy metal layer. Note that, by considering the expressions of effective parameters, the STT would have opposite effects on both sub-lattices whereas the SOT would be in the same direction due to the parity of torques [26]. However, in a RE-TM alloy, only the TM population interacts with the spin currents (as discussed Part. 1.3.4) which means: $P_{RE} \approx 0$ and $\Theta_{SH\,RE} \approx 0$ that gives $P_{eff} = P_{TM}$, $\beta_{eff} = \beta_{TM}$ and $\Theta_{SHeff} \approx \Theta_{SH\,TM}$.

Finally, in this strong antiferromagnetic coupling approximation, the ferrimagnetic alloy can be modelled as a ferromagnetic-like material with effective parameters and all models developed for ferromagnets can be applied for RE-TM ferrimagnets.

Low coupling case   In a case of a lower antiferromagnetic coupling between RE and TM magnetic populations (when condition 2.14 is not satisfied), the alignment of the two sub-lattices can be canted and the effective parameter approach is not valid anymore. A few alternative theories have already been developed for antiferromagnets where the canting of moment is a key issue of the dynamics [26, 147]. However, in a ferrimagnetic material, the two sub-lattices are different and simplifications applicable to the antiferromagnetic case are not applicable here. In part 2.4.5, we propose a model that accounts for this canting between magnetic moments during the DW motion and in part 2.3.2 we describe numerical simulations of a double lattice system with finite coupling.

2.2.2   Magnetic and angular compensation points

In RE-TM ferrimagnetic alloys, the magnetization of both sub-lattices, here M_{TM} and M_{RE}, are tunable just by acting on the temperature or on the chemical composition of the alloy [30] (see chapter 1.1.3). Considering the expression of the effective parameters (Eq. 2.16) strong variations of the material behavior are expected just changing M_{TM} and M_{RE}. In particular, two specific points, called compensation points, induce divergences of some of the above mentioned parameters: for a vanishing net magnetization M_S and for vanishing net angular momentum L_S. We speak about magnetic compensation point (MCP) when $M_S = 0$ (see part 1.1.3) and angular compensation point (ACP) when $L_S = 0$. In the case of a ferrimagnetic material, the two sub-lattices are different ($\gamma_{01} \neq \gamma_{02}$) which means that the two compensation points are different [31] (as discussed below). As shown in part 1.1.3, it is approximately equivalent to change the temperature T or the composition % of the alloy to reach independently the magnetic or the angular compensation points. That is why we speak in the following about T_{MC} and T_{AC} or $\%_{MC}$ and $\%_{AC}$.

2.2.2.1   Specific features at MCP: static signatures

First, considering a static situation where $\partial_t \vec{m} = 0$, Eq. 2.11 becomes:

$$
\begin{aligned}
\vec{0} &= \vec{m} \times \vec{\mathcal{H}}_{eff} - \left\{ \frac{u_{eff}}{\gamma_{0eff}} \right\} \nabla_x \vec{m} + \left\{ \beta \frac{u_{eff}}{\gamma_{0eff}} \right\} \vec{m} \times \nabla_x \vec{m} \\
&+ \left\{ H_{FLeff} \right\} (\vec{m} \times \vec{\sigma}) - \left\{ H_{DLeff} \right\} \vec{m} \times (\vec{m} \times \vec{\sigma})
\end{aligned}
$$

Using the expressions for the effective parameters (Eq. 2.16), all these static terms are homogeneous to fields (associated to the torques as $H_i = \Gamma_i / \gamma_{0eff}$) and are directly proportional to $1/M_S$, and all diverge at the magnetic compensation point MCP. It is the case for the fields associated with the current torques such as: H_{FL}, H_{DL}, $H_{STT_{adiab}} = u_{eff}/\gamma_{0eff}$, $H_{STT_{nonadiab}} = \beta u_{eff}/\gamma_{0eff}$ and also for some of the fields associated with the local energy $|\vec{\mathcal{H}}_{eff}| \propto \epsilon_{eff}/M_S$. While the respective fields diverge, the energy associated to the conservative torques $\epsilon_i \propto \mu_0 M_S H_i$ (e.g. Zeeman, Anisotropy) does not diverge at the MCP, preserving the physical coherence of the model.

State-of-the-art and experimental observations.   The divergence of fields associated with the energy terms at the MCP can be directly probed using hysteresis loops (as discussed in the part. 1.3). It is possible to see a divergence of coercitive fields Hc (as shown part. 1.3) or anisotropy fields H_K. This method is the most convenient to determine the magnetic compensation.

To measure the efficiency of the SOTs regardless of the magnetization dynamics, a method based on harmonic Hall measurements was proposed in [148–150]. This method gives the amplitude of the fields associated to SOTs (H_{DL} and H_{FL} respectively) measuring the external in-plane field required to counterbalance the action of the torques associated with the current. Both equivalent H_x and H_y fields are obtained measuring the Hall signal that gives the angle of the magnetization (as sketched Fig. 2.3 (a)). To increase the signal, the applied current is AC and a lock-in measurement of the first and the second harmonic Hall voltage (V_ω and $V_{2\omega}$) versus the external in-plane fields is required [45, 148–150].

For small in-plane fields compared to the perpendicular magnetic anisotropy:

$$H_{DL} = -2\frac{\partial V_{2\omega}}{\partial H_x}\Big/\frac{\partial^2 V_\omega}{\partial H_x^2} \quad \text{and} \quad H_{FL} = -2\frac{\partial V_{2\omega}}{\partial H_y}\Big/\frac{\partial^2 V_\omega}{\partial H_y^2}$$

Note that this method investigates a saturated magnetic layer at frequencies of few hundreds of Hz, which means that the dynamic properties of the material (with characteristic frequencies typically around or above GHz [151, 152]) are not probed and the magnetic layer can be considered as being at equilibrium. Many experimental studies directly observed a divergence of the fields associated with these torques, H_{DL} and H_{FL} [43–46]. Fig 2.3 (b) shows H_{DL} measured in a $Pt_{5nm}/GdFeCo_{10nm}/SiN_{5nm}$ thin film with this method by Ham *et al.* [45] for different temperatures. The top panel shows the divergence of $|H_{DL}|$ around T_{MC} and the bottom panel shows the proportionality relation between $|H_{DL}|$ and $|1/M_S|$. Fig 2.3(c) shows similar results for both $|H_{DL}|$ and $|H_{FL}|$ in a $Ta_{5nm}/GdFeCo_{10-30nm}/Pt_{5nm}$ thin film measured by Roschewsky *et al.* for different alloy compositions [46]. It is possible to see a divergence of both $|H_{DL}|$ and $|H_{FL}|$ around the $\%_{MC}$. The constant value of the extracted Hall angle $\theta_{eff\ DL/FL} \propto H_{DL/FL}/M_S$ (Eq. 2.9) means that both $|H_{DL}|$ and $|H_{FL}|$ are proportional to $1/|M_S|$. Other methods can be used to get the SOT efficiency such as current induced switching in thin films with variable composition [153] or SOT-driven domain wall dynamics [14] (as discussed in the following part. 3.4). However, in the later cases, a non-negligible dynamic part may affect the measurements of the static H_{DL} and H_{FL} parameters.
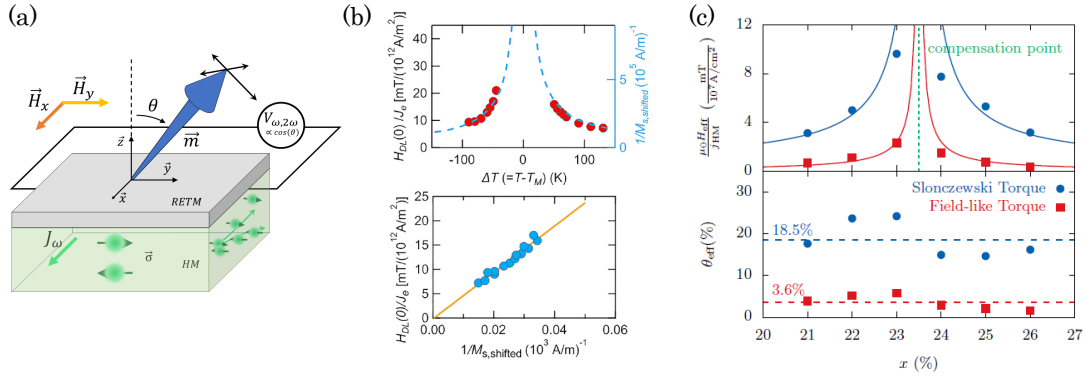
Figure 2.3 – H_{DL} and H_{FL} in RETM films measured by second harmonic Hall voltage. (a) Sketch of the harmonic Hall measurement method. Here, the electrical current J is represented as DC but an AC current is used in practice. (b) (from [45]) Measured $|H_{DL}|$ via harmonic Hall voltage in a $Pt_{5nm}/GdFeCo_{10nm}/SiN_{5nm}$ ferrimagnetic thin film. The top panel shows its variations versus temperature and the bottom one shows its variations directly versus $|1/M_S|$. (c) (from [46]) Measured $|H_{DL}|$ and $|H_{FL}|$ via harmonic Hall voltage in a $Ta_{5nm}/GdFeCo_{30nm}/Pt_{5nm}$ ferrimagnetic thin film versus the chemical composition on the top panel. The bottom panel shows the value of the extracted Hall angle: $\theta_{eff\ DL/FL} \propto H_{DL/FL}/M_S$ (Eq. 2.9).

The measurements of the fields associated with the STTs are more challenging and intrinsically require a non-colinear magnetic texture. However, few methods considering only quasi-static DW motions could be done such as the spin-torque-meter [112], the DW faceting [154], the DW depinning [155] or propagation in the creep regime under combined effects of field and current [41] (see the chapter 3.1).

2.2.2.2 Specific features at ACP: dynamical signatures

In a non-static case ($\partial_t \vec{m} \neq 0$), all the terms entering the LLG equation (Eq. 2.11) diverge at the ACP where the net angular momentum L_S changes sign crossing zero. The effective parameters (Eqs. 2.16) and, consequently, the effective magnetization dynamic properties change dramatically.
To see the impact of these divergences on the magnetization dynamics, we investigate the relaxation and precession angular frequencies ω_θ and ω_ϕ under field or damping-like torque in a similar way as for the macrospin described in section 2.1.1. We use a toy model where the evolution of $M_1(T)$ and

$M_2(T)$ are represented in fig. 2.4(a) *versus* a parameter x which can be taken to be proportional to the temperature or the alloy composition. In this toy model, MCP occurs at $x = 1/3$ and ACP at $x = 2/3$, however, the qualitative results are valid for other parameters. Fig. 2.4 shows the evolution of the dynamic parameters γ_{0eff} and α_{eff} (the bottom panel of (a)) and their impact on ω_θ and ω_ϕ during a relaxation of an isolated effective momentum, first under external field (in (b)) and secondly under a combination field-like/damping-like torques (in (c)). On Fig 2.4 (a) it is possible to see that both parameters γ_{0eff} and α_{eff} diverge and change sign at the ACP where L_S vanishes changing its sign. The divergence of γ_{0eff} directly induces a divergence of the Larmor angular frequency ω_L at the ACP (Fig 2.4 (b)). However, at the ACP, α_{eff} also diverges (being much larger than 1) which reduces the precessional angular frequency ω_ϕ (as shown and discussed in the Fig. 2.1 of section 2.1.1). The lower α_1, the closer the crossing with 1 occurs in the vicinity to the ACP and ω_ϕ deviates from ω_L.
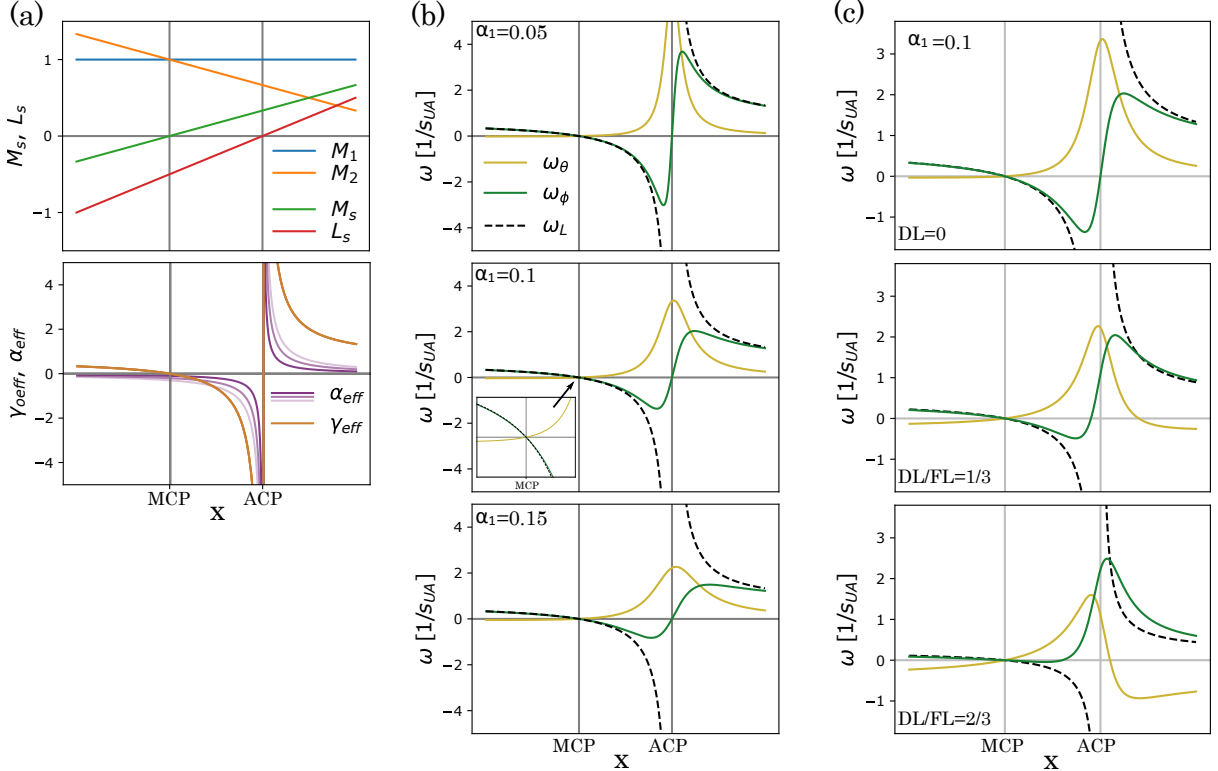
Figure 2.4 – Dynamic parameters through compensation point in RE-TM films. (a) Evolution of the effective values M_S, L_S, γ_{0eff} and α_{eff} (for $\alpha_{01} = 0.05 - 0.15$) depending on a parameter x which can be taken to be proportional to temperature or alloy composition. (b) Evolution of the relaxation and precession rates (ω_θ and ω_ϕ) for dynamics driven by an external field across compensation points from Eq. 2.3 (considering different values of α_1 written on the left). The inset shows a zoom around the MCP for the case $\alpha_1 = 0.1$ but a similar behavior is obtained for the other values of α_1. (c) ω_θ and ω_ϕ through compensation points for $\alpha_1 = 0.1$ considering a combination of field $\vec{H}$ and damping-like torques (with $\Gamma_{DL} = \gamma_{0eff} H_{DL}$ and $\vec{u}_{DL}$ along $\vec{H}$). Three cases are shown: $1 \times H_{FL} + 0 \times H_{DL} = 1$, $2/3 \times H_{FL} + 1/3 \times H_{DL} = 1$ and $1/3 \times H_{FL} + 2/3 \times H_{DL} = 1$. For these plots, the calculation uses $M_1 = 1$, $\gamma_{01} = 1$, $\alpha_1 = 0.05 - 0.15$ and $M_2 = 1 - (x - 1/3)$, $\gamma_{02} = 2/3$, $\alpha_2 = 0$ were x represent the temperature/alloy characteristic.

At the ACP, the precessional angular frequency ω_ϕ is zero which means that the magnetic moment can be manipulated without any precessional motion. Note that in contrast to a ferromagnet (with finite γ_0 and a large α), where the relaxation is just faster than the precession (see part 2.1.1), here, for a ferrimagnet there is no precession at all and the motion can be called precession-free. This precession-free dynamics induces a peak of the relaxation frequency ω_θ, *i.e.* a faster response to a manipulation driven by an applied field. Fig 2.4 (a) it is also possible to see that γ_{0eff} changes sign twice (at the MCP and ACP). The precession angular frequency ω_ϕ is directly proportional to γ_{0eff} so the precession

direction changes two times: counterclockwise before the MCP, clockwise between MCP and ACP and counterclockwise again after ACP (for a positive H).

Let us introduce effective angular frequencies $\omega_{\theta eff}$ and $\omega_{\phi eff}$ defined as:

$$\begin{cases} \omega_{\theta eff}/H = \mu_0 M_S \frac{L_\alpha}{L_S^2 + L_\alpha^2} \\ \omega_{\phi eff}/H = \mu_0 M_S \frac{L_S}{L_S^2 + L_\alpha^2} \end{cases} \tag{2.17}$$

The quantity L_α does not vary much with the x parameter (it is finite and always positive) whereas M_S and L_S vanish changing sign at the MCP and ACP. It is easily seen that $\omega_{\theta eff}$ changes sign at the MCP where M_S changes sign. A finite maximum value of $\omega_{\theta eff} = M_s/L_\alpha$ is reached at the ACP. In contrast, $\omega_{\theta eff}$ is zero and changes sign at both the MCP and the ACP where M_S ans L_S change sign. The fact that both $\omega_{\theta eff}$ and $\omega_{\varphi eff}$ are zero at the MCP illustrate the magnetic un-susceptibility: no field can manipulate the magnetic moment at the MCP.

Considering a combination of field-like and damping-like torques the previous frequency analyses become more complex. Fig 2.4 (c) shows the relaxation and precession frequencies for a combination of field-like and damping-like torques. Increasing the damping-like torque, it is possible to see that the precession-free point (where $\omega_\phi = 0$) is no longer at the angular compensation point but is lowered. It is also possible to identify another point of interest where the relaxation vanishes (i.e. $\omega_\theta = 0$) above T_{AC}. As discussed in part 2.1.1, these two behaviors arise for a specific rate Γ_{DL}/Γ_{FL}: here $H_{DL}/H_{FL} = -1/\alpha_{eff}$ gives a precession-free dynamics and $H_{DL}/H_{FL} = \alpha_{eff}$ gives the relaxation-free dynamics. Note that considering the evolution of the effective damping parameter, α_{eff} the precession-free dynamics occurs below the ACP and the relaxation-free dynamics occurs above the ACP. In contrast to ferromagnets (with a positive α and a fixed sign of H_{DL}/H_{FL}), for ferrimagnets, even if the sign of H_{DL}/H_{FL} is the same, α_{eff} changes sign at the ACP and both configurations are reachable.

Finally, even considering diverging effective parameters, neither relaxation and precession rates (ω_θ nor ω_ϕ) diverge. The evolution of the magnetization reorientation has finite characteristic time (as detailed below) preserving the physical coherence of the model.

Experimental state-of-the-art. The dynamic properties of ferrimagnets are revealed by out-of-equilibrium techniques, which makes them more challenging to study than the static properties. Few experimental results measured directly the variations of the effective dynamic parameters γ_{0eff} and α_{eff} based on time-resolved relaxation measurements [151, 152]. For example, Stanciu *et al.* measured the ultra-fast spin dynamics (sub-ps) in a $SiN_{5nm}/$ $GdFeCo_{20nm}/$ SiN_{60nm} ferrimagnetic thin film by an all-optical pump-probe technique [151]. The optical excitation reduced the anisotropy energy, driving the magnetization out of equilibrium; both the ferromagnetic resonance frequency (which can be associated to ω_ϕ) and the relaxation time (which can be associated to ω_θ) were measured. Fig. 2.5 (a) shows the time-resolved measured relaxation and the extracted values of the effective damping parameter versus temperature. The extracted α_{eff} exhibits a peak at T_{AC}. Similar results have been observed by Binder *et al.* in a $SiOx/$ $CoGd_{30nm}/$ Al thin film with or without a composition gradient (of around $0.16\%/mm$) comparing frequency (VNA-FMR) and time-resolved (pump-probe) methods [152]. Fig. 2.5 (b) shows the effective factor g_{eff} (directly proportional to γ_{0eff}) and α_{eff} measured by VNA-FMR versus the Co concentration of the alloy or the temperature. Both quantities exhibit a maximum (more visible versus T) which are attributed to the ACP. Note that, even if these two approaches clearly reveal significant variation of the dynamic parameters of the alloy, they are not sign-resolve (they just give the absolute values of both the relaxation and the precession frequencies $|\omega_\phi|$ and $|\omega_\theta|$) that can hide phenomena. Typically, because of the shape of the $|\omega_\phi|$ variations (shown Fig. 2.4) the vanishing of the precession frequency can appear now as a peak due to an insufficient resolution (as suggested in [151, 152]).

One of the interesting dynamic properties of ferrimagnets is the change of the effective parameters sign, which could not be probed by the above methods (which are not sign-resolved). Jiang *et al.* proposed a very robust method [156] to measure the ACP via a sign reversal of the effective damping parameter α_{eff}. This method also simultaneously determines the MCP for in-plane magnetization. The magnetization reversal of the free GdCo layer in a spin-valve with in-plane anisotropy $GdCo_{5nm}/Cu_{10nm}/CoFe_{10nm}$

was driven by field and current at different temperatures. Fig. 2.5 (c) shows the measured loops. As expected, at $T_{MC} \approx 125K$ the loops reversed for both the field and the current switching process (as discussed in the section 1.3) but another reversal occurs at $\approx 225K$ only for the current induced switching. In contrast with what occurs during field switching, the current driven magnetization reversal is a dynamic process which depends on the balance between spin current and damping term. The reversal of the critical current required to switch the GdCo free layer is a signature of a change of sign of its effective damping parameter.
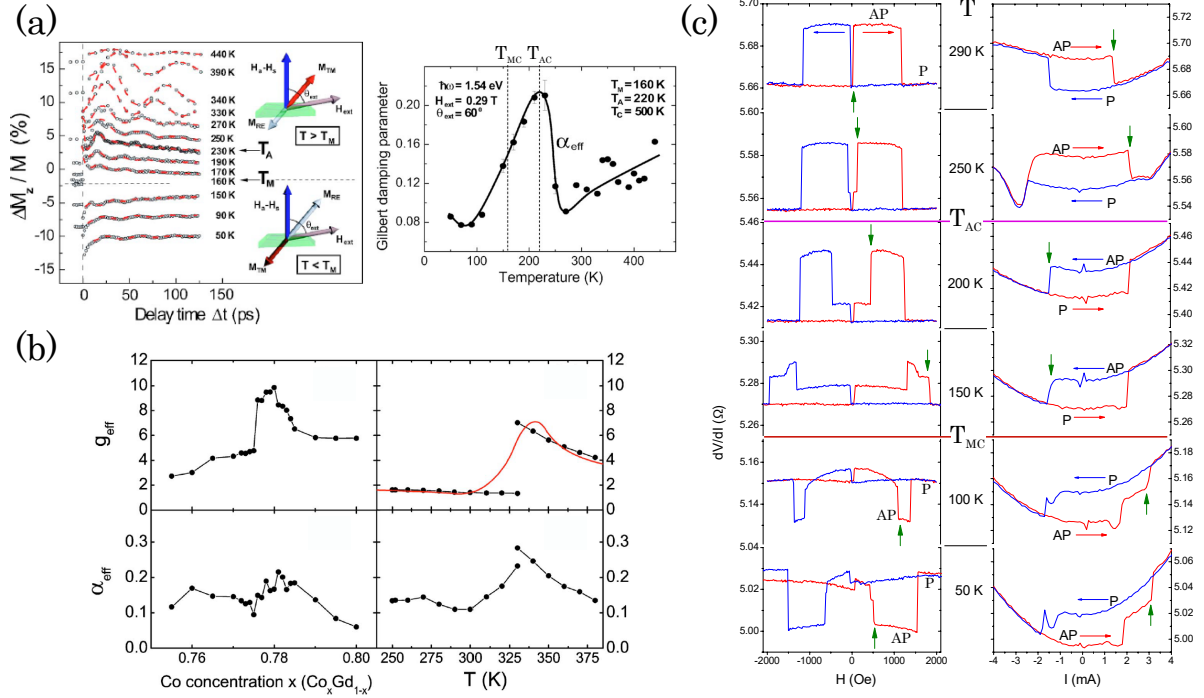
Figure 2.5 – Previous measurements of dynamic parameters in RE-TM films. (a) (from [151]). Left panel: time resolved relaxation of the magnetization measured by all-optical pump-probe technique under a tilted external field (as indicated in the inset) in a $SiN_{5nm}/GdFeCo_{20nm}/SiN_{60nm}$ ferrimagnetic thin film for different temperatures. Right panel : effective damping parameter α_{eff} extracted from the relaxation characteristic time. (b) (from [152]). Variations of the effective factor $g_{eff} = \frac{\hbar}{\mu_0 \mu_B} \gamma_{0eff}$ and of α_{eff} in a $SiOX/CoGd_{30nm}/Al$ thin film versus the $\%_{Co}$ or versus temperature. (c) (from [156]) Field and current hysteresis loops of an in-plane magnetized spin-valve with a ferrimagnetic free layer $GdCo_{5nm}/Cu_{10nm}/CoFe_{10nm}$. The value of the spin-valve resistance (dV/dI) indicates the magnetic state of both layers (parallel: P or anti-parallel: AP). Green arrows indicate the reversal of the ferrimagnetic free-layer.

Other experimental studies show really interesting dynamic properties of magnetic textures in ferrimagnets at the ACP [13, 14, 20, 21] as discussed in following part.

Remaining issues. In addition to the difficulties in accurately measuring the magnetic behavior at the ACP, it is very difficult to determine T_{AC} or $\%_{AC}$ of a ferrimagnetic alloy as quickly and easily as for T_{MC} and $\%_{MC}$. Since T_{MC} is one of the more sensitive characteristics of a ferrimagnetic film (as discussed in part 1.3), Hirata *et al.* proposed a model to roughly evaluate T_{AC} as a function of T_{MC} close to the Curie temperature T_C [31]. However, it remains a challenging issue to determine T_{AC} reliably. Fig 2.6 (a) shows T_{AC} as a function of T_{MC} for different stacks based on GdFeCo alloys [13,14,31,42,157]. As exposed by Caretta *et al.* [14], to take advantage of both MCP and ACP, the most suitable situation is when the compensation points are as close as possible. Fig 2.6 (b) shows $T_{AC} - T_{MC}$ as a function of T_{MC}.
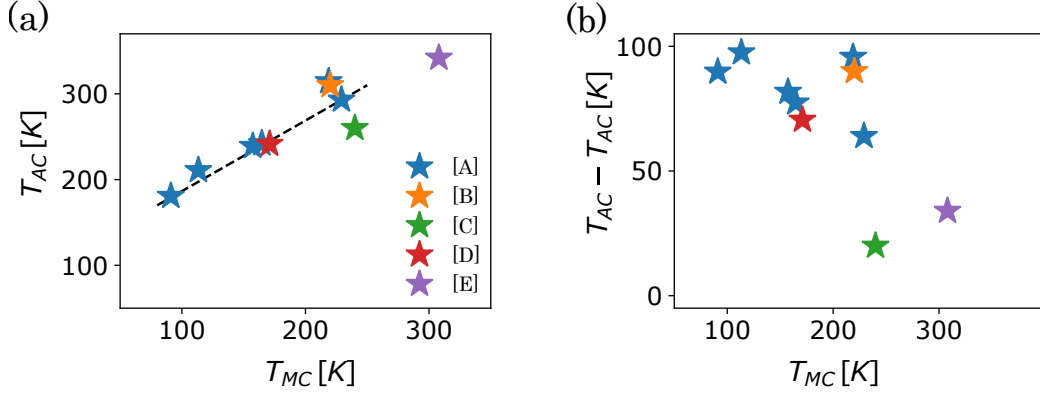
Figure 2.6 – (a) T_{AC} *versus* T_{MC} and (b) $T_{AC} - T_{MC}$ *versus* T_{MC} for different stacks based on GdFeCo alloy: [A]→ [31], [B]→ [13], [c]→ [14], [D]→ [157] and [E]→ [42] our results. The dashed line corresponds to the model exposed by Hirata *et al.* [31].

Summary In RE-TM ferrimagnetic alloys, two different sub-lattices are antiferromagnetically coupled. In the case of a strong coupling the two magnetic populations can be associated with an effective ferromagnetic-like material with effective static and dynamic parameters tunable with the alloy composition or just with the temperature. Two interesting situations are characteristic of a ferrimagnetic material: the magnetic compensation point, MCP, where the net magnetization is reversed, and the angular compensation point, ACP, where the net angular momentum is reversed. At the MCP, all static parameters of the alloy diverge whereas all dynamic parameters diverge at the ACP, inducing new interesting behavior such as a strong efficiency of the SOTs or a precession-free dynamics. However, these divergences do not induce any un-physical phenomena.

2.3   Modeling domain wall dynamics in ferrimagnets

In this thesis, we use two approaches to study the ferrimagnetic DW dynamics. First, using the standard collective coordinates approach developed for ferromagnets, transposed to ferrimagnets using the effective parameters. The second approach is to solve numerically the double LLG equation (Eq. 2.13).

2.3.1   Collective coordinates approach

To understand the dynamics of a complex magnetic texture such as a DW, a skyrmion or a vortex (see part. 1.4), an analytical model is often useful. However, it is rarely possible to solve the LLG equation (Eq.2.11). Indeed, if we consider a non-colinear spatial distribution of the magnetization, the LLG equation describes the evolution of magnetic moments 'one by one' which produces, at the end, the global motion of the texture. Even if this method is exact, it makes impossible any analytical calculations for a large number of magnetic moments. Another approach consists to reverse the description scheme: in a first step, a space-integrated LLG equation is considered for a given magnetic texture and in a second step, the evolution of the global texture dynamics is considered [34, 158]. For this second method, the integrated LLG equation gives the evolution of the so-called collective coordinates that describe the magnetic texture. For the description of DW dynamics, two models are commonly used: the $q - \varphi$ model detailed below [34, 85, 131, 150, 158] and the Thiele equation [159], more appropriate for 2D dynamics like for skyrmions [160] or vortices [161]. In the following sections, the motion of an isolated 180° DW in perpendicular ferromagnetic wire will be described to investigate the DW dynamics in a RE-TM ferrimagnetic wire.

2.3.1.1 $q - \varphi$ model: 1D DW motion

As discussed in part 1.4.1, a domain wall in a ferromagnetic thin film with perpendicular anisotropy can be described by the Bloch DW profile (eq. 1.14), with two collective coordinates, q the position of the DW, φ the angle of the magnetization at the DW center and the parameter Δ that defines the DW width and polarity (positive for $\uparrow\downarrow$ or negative for $\downarrow\uparrow$).
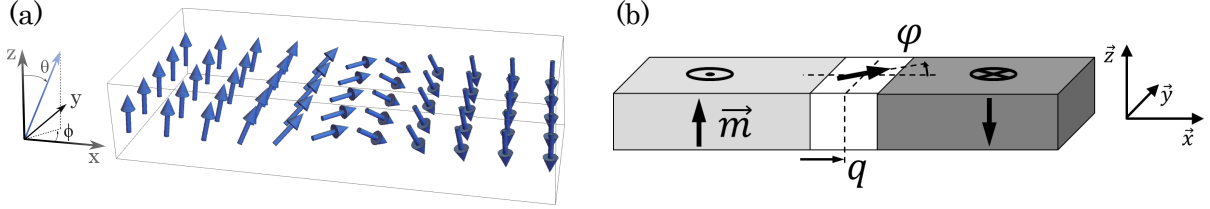
Figure 2.7 – Collective coordinate description of a DW. (a) Shows a typical DW and (b) its associated collective coordinate description.

Integrating the LLG equation (eq. 2.11) along the x direction considering the DW profile (Eq. 1.14) gives the following coupled equations [34, 158]:

$$
\begin{cases}
\alpha\frac{\dot{q}}{\Delta} + \dot{\varphi} = \gamma_0 \left(\frac{\pi}{2} H_{DL}\cos(\varphi) - \frac{\partial_q \sigma}{2\mu_0 M_s} \right) + \beta\frac{u}{\Delta} \\[2mm]
\frac{\dot{q}}{\Delta} - \alpha\dot{\varphi} = \gamma_0 \left(-\frac{\pi}{2} H_{FL}\cos(\varphi) + \frac{\partial_\varphi \sigma}{2\Delta\mu_0 M_s} \right) + \frac{u}{\Delta}
\end{cases}
\tag{2.18}
$$

where $\sigma(q(t),\varphi(t)) = \int_{-\infty}^{+\infty} dx\,\epsilon(x,y,z,t)$ is the surface energy of the DW discussed in part 1.4.1 (eq. 1.15). In its more general form σ is given by:

$$
\sigma = \frac{2A}{\Delta} + 2\Delta\left(K_0 + K_{BN}\sin^2(\varphi)\right) - \pi D\cos(\varphi) - \mu_0 M_s\left(\Delta H_x\sin(\varphi) - \Delta H_y\cos(\varphi) + H_z 2q\right) + \sigma_{\text{extra}}
\tag{2.19}
$$

with A the exchange constant, $K_0 = K_u - 1/2\mu_0 M_S^2$ the effective perpendicular anisotropy, K_{BN} the in-plane shape anisotropy required to switch from a Bloch to a Néel wall, D the DMI parameter (as detailed in part 1.4). Note that the field effect is taken into account in σ. Here, the term σ_{extra} accounts for the other energy terms of the system, such as the pinning of the DW [110], external coupling [12, 16], structure geometry [112]. Finally, implementing this surface energy σ in the coupled LLG equations (Eq. 2.18), it is possible to obtain the full description of the DW dynamics under field (H_x, H_y and H_z), STT (u) and SOT (H_{DL} and H_{FL}). Two degrees of freedom are allowed: the position of the DW along the x direction noted $q(t)$ (associated with the velocity of the DW $v = \dot{q}$) and the internal angle of the magnetization inside the DW $\varphi(t)$ (associated with the precession rate of the DW $\dot{\varphi}$):

$$
\begin{cases}
\alpha\frac{\dot{q}}{\Delta} + \dot{\varphi} = \gamma_0 \left(H_z + \frac{\pi}{2} H_{DL}cos(\varphi) - \frac{\partial_q \sigma_{extra}}{2\mu_0 M_s} \right) + \beta\frac{u}{\Delta} \\[2mm]
\frac{\dot{q}}{\Delta} - \alpha\dot{\varphi} = \gamma_0 \left(H_{BN}\frac{sin(2\varphi)}{2} + \frac{\pi}{2}\left((H_{DMI}+H_x)sin(\varphi) - (H_y+H_{FL})cos(\varphi)\right) + \frac{\partial_\varphi \sigma_{extra}}{2\Delta\mu_0 M_s} \right) + \frac{u}{\Delta}
\end{cases}
\tag{2.20}
$$

Here, the in-plane (Bloch-Néel) anisotropy and the DMI contributions are associated with fields H_{BN} and H_{DMI} which take into account the resulting effect of both the demagnetization and the DMI on the DW:

$$
H_{BN} = \frac{2K_{BN}}{\mu_0 M_s} \quad\text{and}\quad H_{DMI} = \frac{D/\Delta}{\mu_0 M_s}
\tag{2.21}
$$

with $K_{BN} \propto M_S^2$, as discussed in section 1.4.1. In this integrating description of the magnetization, despite of their field-like or damping-like geometry for an isolated moment, the SHE acts on the DW like a field. By contrast, the geometry of the adiabatic and the non-adiabatic contributions of the STT are conserved.

Considering this description of the DW dynamics, two propagation modes can exist [162]: the translational (or steady) one where, the internal magnetization of the DW is fixed (after a transient regime) and the precessional one where it is not (even after a transient regime). Substituting $\dot{q}$ in both equations and fixing $\dot{\varphi} = 0$ in (Eq. 2.20) for a precession-less motion, a condition for φ is obtained:

$$\alpha \left(H_{BN} \frac{\sin(2\theta)}{2} + \frac{\pi}{2} \left((H_{DMI} + H_x) \sin(\varphi) - (H_y + H_{FL}) \cos(\varphi) \right) + \frac{\partial_\varphi \sigma_{extra}}{2\Delta \mu_0 M_s} \right) + \alpha \frac{u}{\gamma_0 \Delta} = \quad (2.22)$$

$$= H_z + \frac{\pi}{2} H_{DL} \cos(\varphi) - \frac{\partial_q \sigma_{extra}}{2\mu_0 M_s} + \beta \frac{u}{\gamma_0 \Delta}$$

This equation has a solution only for values of field H_z and current J below a critical threshold called the Walker limit [34, 85, 109, 162] (written W). Below this limit, the DW moves in the translational regime with a fixed angle φ solution of Eq. 2.22. Above this limit, Eq. 2.22 does not have any solution and the DW cannot have a uniform angle φ and the DW propagates in its precessional regime. For field and current much higher than the Walker limit, the precession rate $\dot{\varphi}$ is very large and uniform and it is possible to consider that the angle of the DW has a time-averaged value $\langle \varphi \rangle \approx 0$. In this case we speak about the asymptotic precessional regime or, abusively, just precessional regime. Note that for a DW just driven by SHE, the precessional regimes does not exist (as discussed in the part 2.4.3).

Considering the $q - \varphi$ model, the velocity law can be calculated for a DW driven by field, STT or SHE. Table 2.1 summarizes the Walker condition and expressions of the DW velocity driven by field, SOT or STT in the translation and the asymptotic precessional regimes.
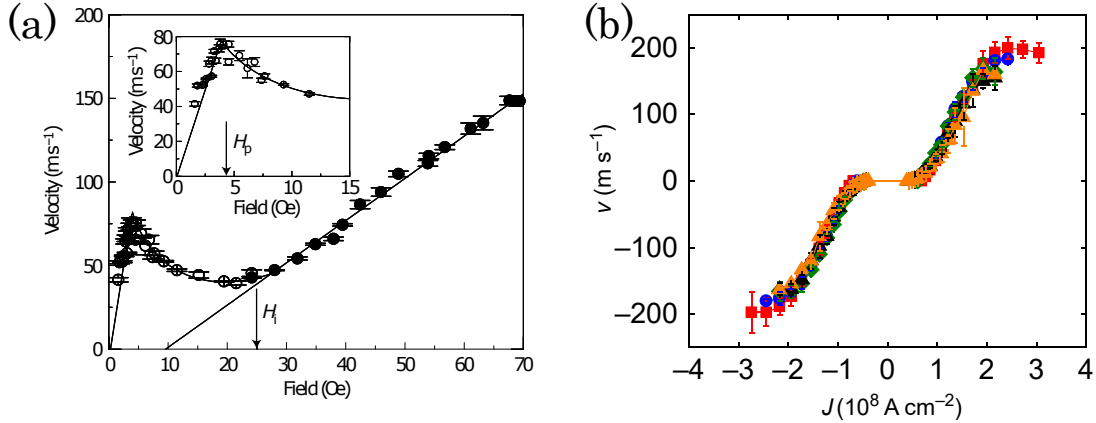
Figure 2.8 – Previous observations of steady and precessional regimes. (a) (from [163]): DW velocity *versus* applied field in a $Ta_{3nm}/Py_{20nm}/Ta_{5nm}$ nano-wire. (b) (from [164]): DW velocity *versus* current density in a $Pt_{5nm}/Co_{0.3nm}/Ni_{0.7nm}/Co_{0.15nm}$ magnetic wire with perpendicular magnetic anisotropy. Colors correspond to current pulse width between 5 to 100ns.

Many studies have already explored the DW dynamics in ferromagnetic systems and validated the $q - \varphi$ model [163–171]. As an illustration, Fig. 2.8 (a) shows the DW velocity versus the applied field in a NiFe wire (in-plane magnetized). It is possible to observe two linear regimes of propagation which can be associated with the translational (for low field) and the precessional (for high field) regimes. Both regimes are separated by a Walker threshold (here ≈ 0.5mT). Fig. 2.8 (b) shows the DW velocity versus the applied current in a magnetic wire with a heavy metal adjacent layer (here Pt). It is possible to see that the velocity increases linearly after a critical current and saturates above a saturation current as expected from the SHE induced DW motion [85] and discussed later (see section 2.1.4).

Force	Steady $\dot{\varphi} = 0$	Walker threshold	Precessional $\langle\varphi\rangle \approx 0$
H	$v = \frac{\gamma_0\Delta}{\alpha} H$ $\varphi = \begin{cases} \frac{1}{2}\arcsin\left(\frac{2H}{\alpha H_{BN}}\right) \\[2mm] \arcsin\left(\frac{2H}{\alpha\pi H_{DMI}}\right) \end{cases}$	$|H_W| = \begin{cases} \frac{|\alpha H_{BN}|}{2} \\[4mm] \frac{\pi}{2}|\alpha H_{DMI}| \end{cases}$	$v = \frac{\gamma_0\Delta\alpha}{1+\alpha^2} H$ $\dot{\varphi} = \frac{\gamma_0}{1+\alpha^2} H$
STT	$v = \frac{\beta}{\alpha} u$ $\varphi = \begin{cases} \frac{1}{2}\arcsin\left(\frac{2u}{\alpha H_{BN}}\frac{\beta-\alpha}{\gamma_0\Delta}\right) \\[2mm] \arcsin\left(\frac{2u}{\alpha\pi H_{DMI}}\frac{\beta-\alpha}{\gamma_0\Delta}\right) \end{cases}$	$|u_W| = \begin{cases} \frac{|\alpha H_{BN}|}{2}\left|\frac{\gamma_0\Delta}{\beta-\alpha}\right| \\[4mm] \frac{\pi}{2}|\alpha H_{DMI}|\left|\frac{\gamma_0\Delta}{\beta-\alpha}\right| \end{cases}$	$v = \frac{1+\alpha\beta}{1+\alpha^2} u$ $\dot{\varphi} = \frac{\beta-\alpha}{1+\alpha^2}\frac{u}{\Delta}$
SOT	$v = \frac{\gamma_0\Delta}{\alpha}\frac{\pi}{2} H_{SHE}\cos(\varphi)$ $\varphi = \arctan\left(\frac{H_{SHE}}{\alpha H_{DMI}}\right)$	$\varnothing$	$\varnothing$

Table 2.1 – $q-\varphi$ model solution for v, φ, $\dot{\varphi}$ and the Walker condition of a DW in ferromagnetic wire with perpendicular anisotropy driven by field H, STT or SOT in translational and asymptotic precessional regimes. Here, H_x, H_y and H_{FL} are not considered.

2.3.1.2 Beyond $q-\varphi$: DW tilt and distortions

Even if this $q-\varphi$ model can describe the DW dynamics, other approaches can be developed to describe more complex DW behaviors by adding new collective coordinates using the Lagrangian formalism and the fluctuation-dissipation theorem [172]. It is based on the Euler-Lagrange-Rayleigh equation:

$$0 = \partial_{\lambda_i} L - \partial_x(\partial_{\lambda_i'} L) - \partial_t(\partial_{\dot{\lambda}_i} L) + \partial_{\dot{\lambda}_i} F \tag{2.23}$$

where λ_i represents each collective coordinate of the structure and its variations $\lambda_i' = \partial_x\lambda_i$ and $\dot{\lambda}_i = \partial_t\lambda_i$. For a magnetic DW, the Lagrangian function and the dissipation function correspond to the space integration of the Lagrangian and the dissipation function for a magnetic moment $\mathcal{L}$ and $\mathcal{F}$: $L = \int_{-\infty}^{-\infty} dx\,\mathcal{L}$ and $F = \int_{-\infty}^{-\infty} dx\,\mathcal{F}$ with:

$$\begin{cases} \mathcal{L} = \epsilon + \frac{\mu_0 M_s}{\gamma_0}\dot{\phi}\cos(\theta) - u\frac{\mu_0 M_s}{\gamma_0}\phi\partial_x\cos(\theta) \\[3mm] \mathcal{F} = \frac{\mu_0 M_s}{2\gamma_0}\left(\alpha\partial_t\vec{m} + \beta u\partial_x\vec{m} - \gamma_0 H_{DL}\vec{m}\times\vec{\sigma} + \gamma_0 H_{FL}\vec{\sigma}\right)^2 \end{cases} \tag{2.24}$$

as detailed in [172] and there stations. The main advantage of this method is the possibility to include additional information on the DW such as its tilt angle χ or its width Δ:

$$\begin{cases} \theta_{q,\chi,\Delta}(x,y) = 2\arctan\left(\exp\left(\frac{(x-q)\cos(\chi)+y\sin(\chi)}{\Delta}\right)\right) \\ \\ \phi(x) = \varphi \end{cases} \tag{2.25}$$

with more degrees of freedom such as: (q,φ,χ) [173], (q,φ,χ,Δ) [174] or the effect of a non-homogeneous φ along the DW: $\varphi \to \varphi(x)$. Other models consider the deformation of the DW during the propagation [175, 176]. In this situation, the DW does not remain straight and its central position depends of x: $q \to u(x)$. This model can be used to describe the propagation or the deformation of a circular DW.

2.3.2 Numerical resolution of the LLG equation

The previously discussed analytical model can present limitations in the study of more complex dynamical behaviors, such as any 2D deformations or internal dynamics (Bloch lines), or more complex magnetic systems, such as multi-layer stacks or finite geometries. In these cases, it is useful to numerically solve the LLG equations in space and time, which has been widely used to study DW dynamics in ferromagnets. Here, the extension for simulating ferrimagnetic systems is described.

Software and sample geometry   To simulate our antiferromagnetically-coupled sub-lattices, we use the *Mumax3* software [177] with some adaptations. In this software, the magnetic material is spatially discretized into a rectangular mesh (finite difference method) with possibly space-varying properties, and the LLG equation (Eq. 2.11) is integrated in time in each cell, giving the evolution of the magnetization $\vec{m}(x,y,z,t)$. This micromagnetic simulation does not consider a rigid texture, and so it can give all possible deformations of the texture. To simulate a ferrimagnetic thin film, we consider a two-level mesh with different magnetic properties for each level associated with the two sub-lattices. A finite exchange coupling is set between the two levels, making it possible to simulate a non-zero tilt between sub-lattices. Note that, with this approach, the two magnetic populations are spatially separated, which is not the case of the real samples we studied. This spatial separation leads to a calculated dipolar field which is very different and much larger than the one in the real ferrimagnetic system. By removing the dipolar interaction in the software, this simulation corresponds to our physical, single-layer system neglecting the demagnetization effects.

Micromagnetic simulations of DW motion   Using the double-layer procedure, we have simulated the motion of a DW with different compositions, across compensation points, and for different driving forces: magnetic field, STT, and SOT. We have used a mesh of size $256 \times 8 \times 2$, with a cell size of $2 \times 2 \times 3.8 nm^3$. Before each simulation, the mesh was initialized with a DW in each layer ($\uparrow\downarrow$ for Co and $\downarrow\uparrow$ for Gd) and relaxed minimizing the total energy. As further discussed below, to study the dynamics both below and above the Walker limit (i.e. translational and precessional regimes), we have performed simulations with and without DMI. In systems with DMI, especially if the net magnetisation is low, the Walker limit is dominated by DMI and the demagnetization contribution to $K_{BN} \propto M_S^2$ can be neglected (as we have to do in our procedure). So, without DMI, the in-plane component of the DW is free to precess and the precessional regime can be studied (wherever-whenever it exists), and, with DMI, the translational regime can be observed. It has been demonstrated that DMI does not change the mobility in the translational regime [85], and many of the experimental systems presented in this thesis have non-zero DMI (see part 1.4.3), making this approach convenient. To investigate independently both propagation regimes, we tune the DMI to lock or to release the DW precession.

2.3.3 Material and effective parameters for ferrimagnets

To perform the micromagnetic simulations across the compensation points, we used the parameters calculated with the mean-field calculations for archetype ferrimagetic GdCo alloy (see part 1.1.3), based on the raw parameters summarized in Table 2.2. The antiferromagnetic coupling was $1.3\,10^8\,J/m^3$. Apart from this parameter thermal dependence, we have not considered the effects of temperature on the system (i.e. thermal oscillations).

layer	Lande factor g	Damping α	Exchange $A\,[J/m]$	Anisotropy $K\,[J/m^3]$	DMI $D\,[J/m^2]$
Co	2.22	0.013	$1.6\,10^{-11}$	$3.0\,10^5$	10^{-3}, 10^{-4} or 0
Gd	2.0	0.02	$10^{-20} \approx 0$	$10^{-20} \approx 0$	0

Table 2.2 – Parameters of GdCo ferrimagnetic alloy used in the micromagnetic simulations.
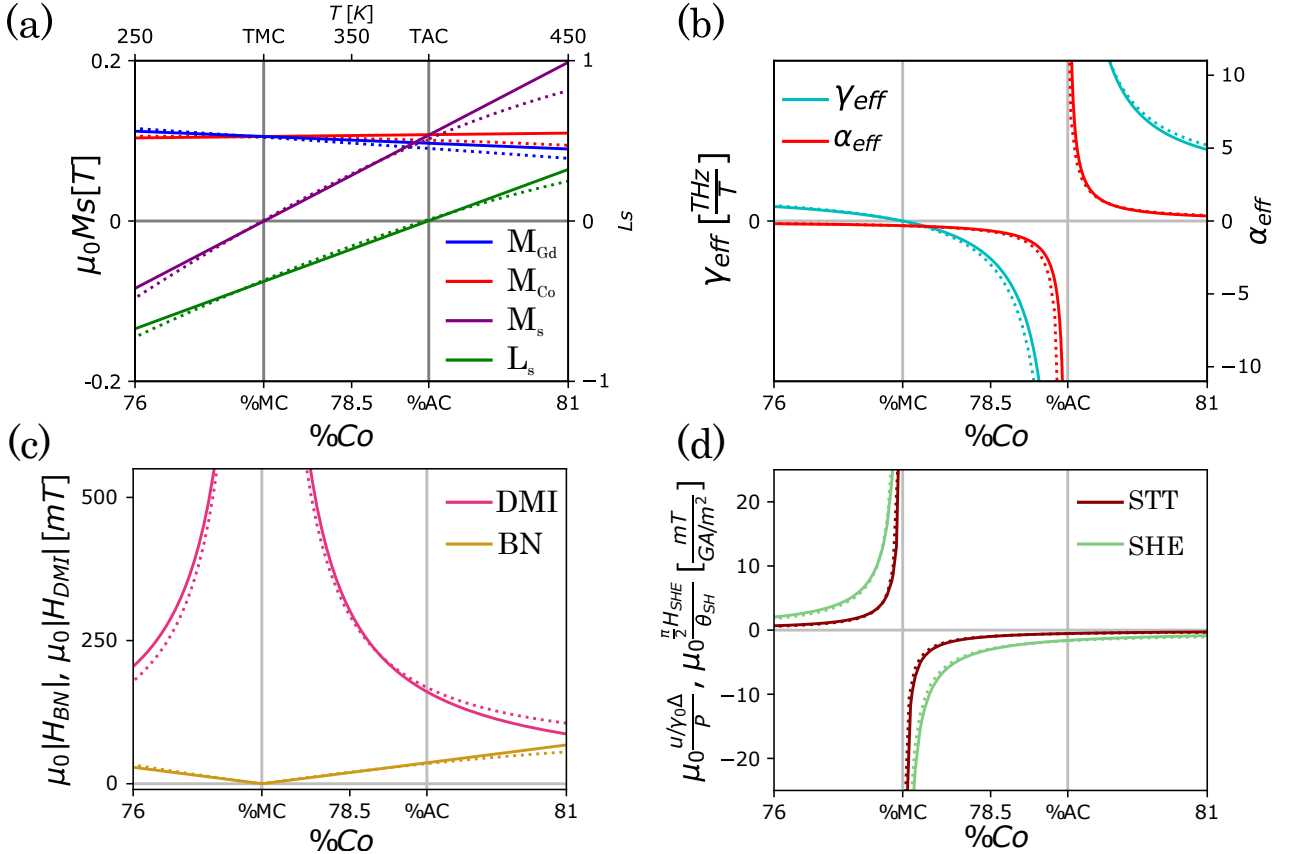
Figure 2.9 – Effective parameters of the GdCo ferrimagnetic alloy: (a) Sub-lattices magnetization, M_S and net-angular momentum L_S (b) γ_{0eff} and α_{eff} (c) H_{DMI} and H_{BN} fields (d) $H_{STT} \equiv \frac{u}{\gamma_0 \Delta}$ and $H_{SOT} \equiv \frac{\pi}{2} H_{SHE}$ fields. Full lines and bottom scale show the variations of the effective magnetic parameters *versus* the alloy chemical composition $\%Co$. Dotted lines and top scale show the variations of the effective magnetic parameters *versus* temperature T. Both are adjusted with a linear function of the down x-axis scale ($\%Co$) to have a good matching between effective parameters versus T and versus $\%Co$.

Fig. 2.9 shows variations of the effective magnetic parameters of the full alloy versus its chemical composition $\%Co$ (full lines) and versus the equivalent temperature T (dotted lines). In Fig. 2.9, the top x-axis scale (T) (only written in the Fig. 2.9 (a)) is adjusted with a linear function of the down x-axis scale ($\%Co$) to have a good matching between effective parameters *versus* T and versus $\%Co$. This shows that the results presented in the following parts can be obtained as well by sweeping the chemical composition of the alloy (for a given temperature, typically 300 K in the calculations), or by sweeping the temperature for a given alloy (experimentally easier). In this study, $\%Co$ is chosen as the tuning parameter. It is possible to see a behavior similar to the one observed with the toy model introduced in section 2.2.2: M_S and L_S change sign at respectively the MCP and the ACP (Fig. 2.9 (a)), γ_{0eff} and α_{eff} diverge and change sign at the ACP and γ_{0eff} vanishes and changes sign at the MCP. It is possible to see that the DMI field diverges at the MCP whereas the demagnetization field H_{BN}, always much smaller than H_{DMI}, vanishes because the net magnetization goes to zero. Fig. 2.9 (d) shows the amplitude of the STT and SOT taken as fields (associating in Eq. 2.20). Both have strong magnitude and diverge at the MCP.

Experimental observations   Several experimental studies already probed the behavior of these quantities and are consistent with the proposed material parameter model. The vanishing of the magnetization at the MCP was discussed in part. 1.3. The variations of the effective gyromagnetic ratio γ_0 and the damping parameter α have been probed measuring the magnetic relaxation or the ferromagnetic resonance [151, 152] (see part. 2.2.2). The divergence of the DMI field has been probed by direct DW dynamics measurement [14, 20]. Fig 2.10 (from [14]) gathers some more illustrations of the thermal behavior of the effective parameters: measuring the DWM driven by SOT under in-plane field, they measured the field associated to the DMI (Fig 2.10 (a)) and comparing the DWM driven by either a field or SOT they measured the field associated with the SHE (Fig 2.10 (b)). Both quantities diverge at the MCP and Fig 2.10 (c) and (d) shows that the H_{DMI} and H_{SOT} divergences fit with the vanishing of M_S at MCP. The divergence of H_{SOT} as reported as well from harmonic Hall voltage measurements [43–46] and discussed earlier in part 2.2.2.
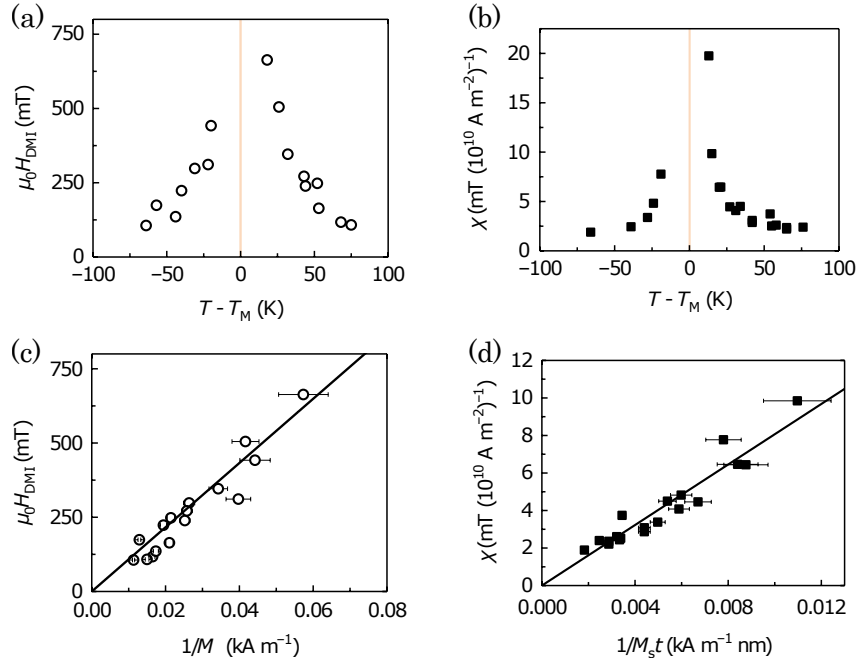
Figure 2.10 – Experimental observations showing the thermal evolution of effective fields. (from [14]). (a) Variation of H_{DMI} versus T probed measuring the DWM driven by SOT under in-plane field. (b) Temperature dependence of $\chi \propto H_{SOT}/J$ probed comparing the DW velocity driven by either field or current. (c) and (d) show that the divergence of both H_{DMI} and H_{SOT} fits with the vanishing of M_S.

2.4 Dynamical regimes of domain walls under different drives

In order to describe the different dynamics of the DW, we use the two above methods: the analytical $q - \varphi$ model with effective parameters (Eq. 2.20 and Tab. 2.1)) and micromagnetic numerical simulations (considering the two sub-lattices with finite coupling). Both models consider realistic parameters presented above for an GdCo ferrimagnetic alloy.

In the following parts of this chapter, even if quantities are not indexed 'eff', they refer to effective parameters.

2.4.1 Domain wall motion driven by an external field

In ferrimagnets the applied field H acts on both Gd and Co sub-lattices. Fig 2.11 (a) and (b) show DW velocity v and precession rate $\dot{\varphi}$ versus the amplitude of a perpendicular field H for different alloy compositions %Co. The results of the numerical simulations appear with full lines and the dotted lines correspond to the analytical model (Tab. 2.1).
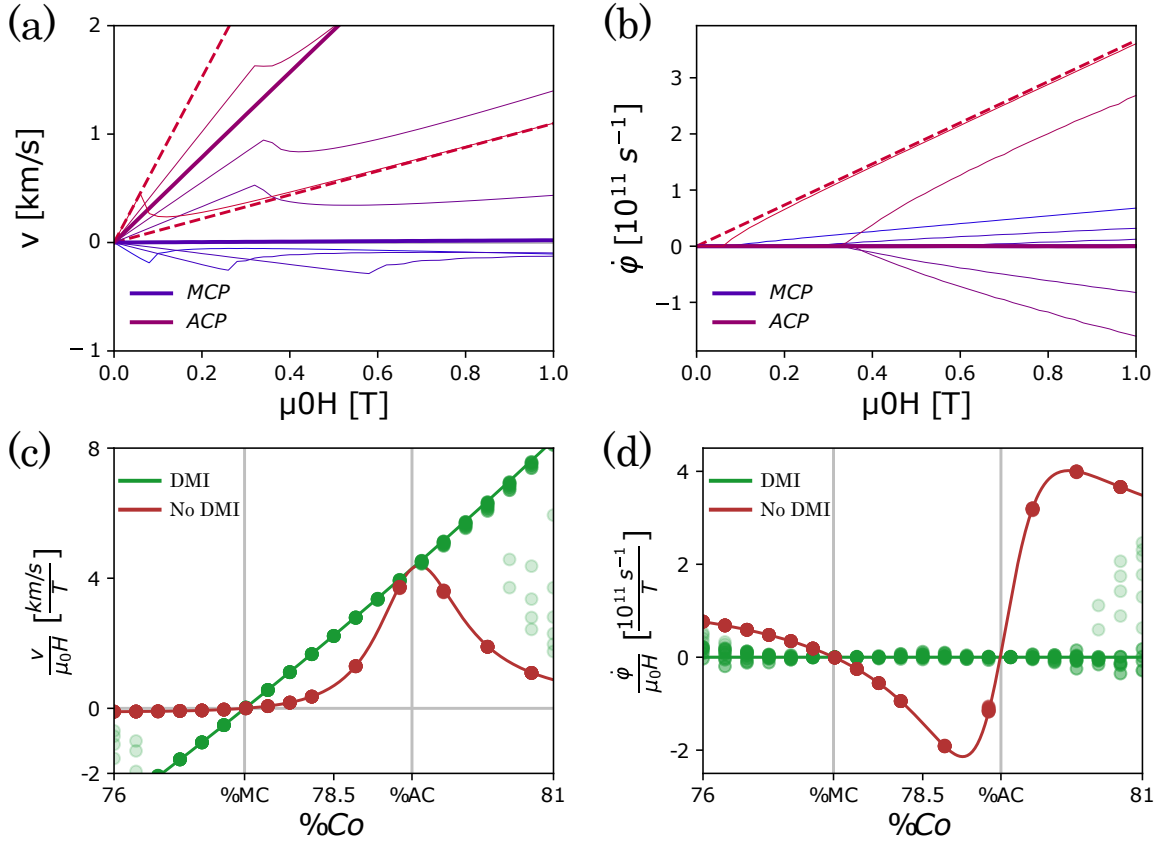
Figure 2.11 – Micromagnetic simulations and analytical calculations of field-driven DW dynamics. DW velocity v (a) and precession rate $\dot{\varphi}$ (b) versus the applied perpendicular field H for different alloy compositions %Co (represented in different colors). Thick lines correspond to the MCP and to the ACP (in (b), both thick lines are superimposed with the H axis). The red dashed lines correspond to the analytical q-φ expressions for v and φ for the two propagation regimes (translational and precessional; Tab. 2.1) using the effective parameters corresponding to the composition of the red line. The results in (a) and (b) are obtained with an intermediate DMI parameter $D = 1.10^{-4} \text{J/m}^2$. DW mobility $v/\mu_0 H$ (c) and normalized precession rate $\dot{\varphi}/\mu_0 H$ (d) for $\mu_0 H \in [0\,;1\text{T}]$. Dots correspond to micromagnetic simulations considering $D = 1.10^{-3} \text{J/m}^2$ (green points) and $D = 0$ (red points). Lines show the values of $v/\mu_0 H$ and $\dot{\varphi}/\mu_0 H$ from the analytical expressions in translational (green) and in precessional (red) propagation regimes. Transparent green points in (c) and (d) correspond to an applied field higher than the Walker threshold in presence of a strong DMI.

First, we can see the very high values of the DW velocity (a few km/s) as observed experimentally [13]. Next, it is possible to observe the two propagation regimes: the translational one ($\dot{\varphi} = 0$) and the precessional one ($\dot{\varphi} \neq 0$) for (respectively) low and high field. For both regimes, the DW velocity and precession rate change drastically with the alloy composition $\%Co$. Whatever the field, the simulated values (full lines) follow with a very good agreement those obtained from the analytical expressions, for translational and precessional regimes (red dashed lines). The Walker field for the case with DMI, evidenced by non-zero $\dot{\varphi}$, also changes greatly with $\%Co$. Below this threshold, the equilibrium in-plane angle of the DW φ (not plotted) exhibits roughly the same behavior (sign and amplitude) as the precession rate $\dot{\varphi}$. Finally, a wide range of the DW behavior can be observed in the studied range of $\%Co$ with successive reversal of the propagation direction or of the precession (as detailed below).

To investigate independently both propagation regimes, we examine the dynamics with different magnitudes of DMI in order to lock or to release the DW precession (as discussed above in part 2.3.2). Furthermore, to see more clearly the variation of DW dynamics, we consider the mobility ($\mu = v/\mu_0 H$) and the normalized precession rate ($\dot{\varphi}/\mu_0 H$) variations. Fig. 2.11 (c) and (d) shows the mobility and the normalized precession rate *versus* the alloy composition $\%Co$ with or without DMI (green and red respectively). Dots correspond to the simulated values for $\mu_0 H$ in a range between $0 - 1T$ with or without DMI. The continuous lines correspond to $v/\mu_0 H$ and $\dot{\varphi}/\mu_0 H$ from analytical expressions for translational and precessional regimes (in respectively green and red) (Tab. 2.1). First, it is possible to see the perfect matching between μ and $\dot{\varphi}/\mu_0 H$ with or without DMI (dots) and in both regimes (lines) which validates our precession locking approach. It is also possible to verify that in the translational regime, $\dot{\varphi}$ remains zero. Transparent green points in (c) and (d) correspond to an applied field higher than the Walker threshold (for the corresponding $\%Co$). As highlighted by their positions, these points are in an intermediate state, between translational and asymptotic precessional regimes, with a non-zero precession even in presence of a strong DMI.

It is possible to note that μ and $\dot{\varphi}$ change sign at the MCP. Indeed, at this point, the dominant magnetic moment changes, reversing the effect of the external field (as detailed Part 1.3). Furthermore, at MCP, the magnetization of the two sub-lattices is the same and the resulting field torque on both vanishes and μ and $\dot{\varphi}$ are zero in both regimes (the case is different for very high fields, as discussed Eq. 2.14 and in part 1.6.1.2). Secondly, at the ACP, the precession rate changes sign, crossing zero. As discussed part. 2.2.2, at the ACP, the precession of an isolated magnetic moment driven by a field vanishes and changes sign. The DW motion is due to collective motion of magnetic moments and this $\dot{\varphi}$ behavior is the signature of these precession-free individual dynamics. The velocity (as well as the mobility) of the DW in the precessional regime depends on both the applied field and precession rate (Eq. 2.20): $\alpha \frac{v}{\Delta} = \gamma_0 H - \dot{\varphi}$ and a reduction of the precession rate induces a velocity peak. Furthermore, at the ACP, the magnetic moment does not precess anyway, so the velocity and precession rate coincide in both regimes.

Even if both regimes can be reached by tuning the DMI amplitude, in a real material, with a fixed intermediate DMI, both regimes are not necessary reachable. Figs. 2.12 (a) and (b) show the simulated mobility $v/\mu_0 H$ and the normalized precession rate $\dot{\varphi}/\mu_0 H$ versus $\%Gd$ for $D = 1.10^{-4}$ J/m^2 (from Fig. 2.11 (a) and (b)). Lines correspond to the analytical expression of $v/\mu_0 H$ and $\dot{\varphi}/\mu_0 H$ (similarly to Fig. 2.11 (c) and (d)). As expected, values associated with low fields (green points) roughly follow the translational regime behavior (green line) and the precessional one (red line) for high fields (red point). However, around the ACP, the precessional regime is not reached even for large field. The DW is locked in the translational regime and the precession rate $\dot{\varphi}$ is still zero even for high fields ($H = 1$ T for red points) as indicated by the dotted region of the red line (Fig. 2.12 (b)). To understand this phenomena, the evolution of the Walker field which separates the two regimes has to be taken into account. The Walker field H_W is the maximum field for which φ satisfies:

$$H = \alpha H_{BN} \sin(\varphi) \left(\frac{\pi}{2} \frac{H_{DMI}}{H_{BN}} - \cos(\varphi) \right) \tag{2.26}$$

(from Eq. 2.22). Fig. 2.12 (c) shows the Walker field H_W versus $\%Co$. The gray region corresponds to the field range ($H \in [50\text{mT}, 1\text{T}]$) of the simulations. Full lines correspond to the value of H_W calculated from Eq. 2.26 for different values of D. Note that this values of H_W takes into account the in-plane

anisotropy (Bloch-Néel) *via* the term H_{BN} neglected in the micromagnetic simulations.
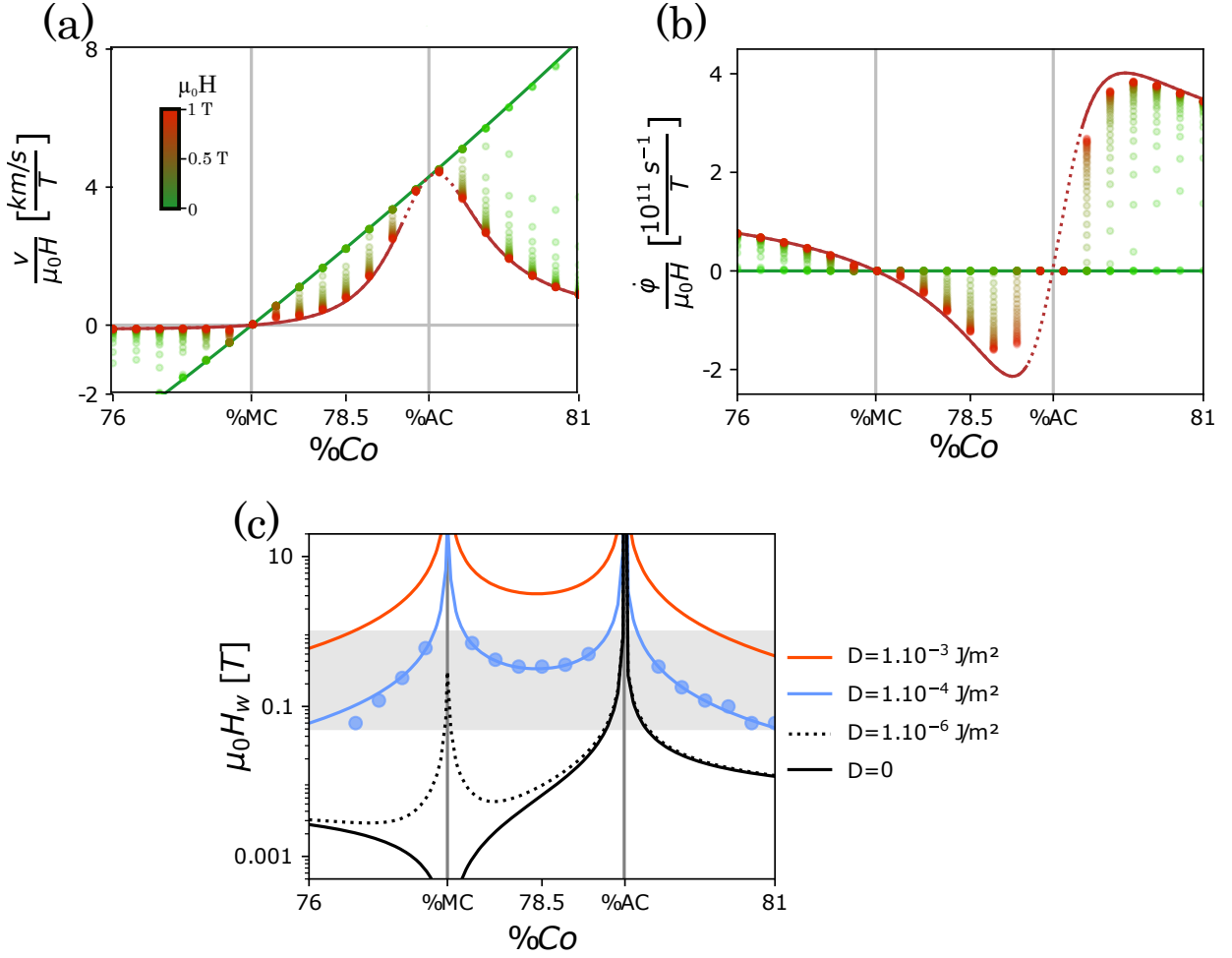
Figure 2.12 – Mobility $v/\mu_0 H$ (a) and normalized precession rate $\dot{\varphi}/\mu_0 H$ (b) versus $\%Gd$ for $D = 1.10^{-4} \mathrm{J/m^2}$ (from simulations in Fig. 2.11). The color corresponds to the amplitude of the applied field H. Green and red lines correspond to $v/\mu_0 H$ and $\dot{\varphi}/\mu_0 H$ from analytical expressions in Tab. 2.1. The red dotted region corresponds to the unreachable precessional regime. (c) Walker field H_W (lines) calculated from Eq. 2.26 versus $\%Co$ for different values of D (written in the legend). Blue dots correspond to values of H_W extracted from simulations with $D = 1.10^{-4} \mathrm{J/m^2}$ shown Fig. 2.11 (a) and (b). The gray background region corresponds to the field range probed in previous micromagnetic simulations: $H \in [50\mathrm{mT}, 1\mathrm{T}]$.

If there is no DMI (D=0), H_W goes to zero at MCP and diverges around the ACP. For a non-zero DMI, it is possible to see that H_W diverges two times: around the MCP and the ACP. For large DMI ($D \geqslant 1.10^{-3} \mathrm{J/m^2}$), the Walker field is not reachable in the main part of the field range which means that the DW propagates in a translational regime. For intermediate lower values of D (1.10^{-4} and 1.10^{-6} J/m²), H_W is lower and can be reached for the main part of the field range (as visible Fig. 2.12 (c) for $D = 1.10^{-4}$ J/m²). The blue points in Fig. 2.12 (c) correspond to the Walker fields extracted for values Fig. 2.11 (a) and (b) and Fig. 2.12 (a) and (b) for $D = 1.10^{-4}$ J/m². They are below the calculated value because of the fact that it takes into account the demagnetization effect whereas the simulation does not. This gives higher calculated values of H_W. However, H_W is not reached in the vicinity of the two compensations points which means that the DW precession remains locked (as visible Fig. 2.12 (a) and (b)). Note that this is always true even for a very low DMI (as shown with the dotted line Fig. 2.12 (c) for $D = 1.10^{-6}$ J/m²).

For zero DMI, the Walker field just depends on the demagnetization effect which vanishes at the MCP where the magnetization vanishes too. At this point, there is no longer any preferential direction for the DW, which could precess freely for any field and which would be associated with a vanishing of H_W. However, at the MCP, the field does not have any effect on the magnetization. For this same reason, for non-zero DMI, H_W diverges at MCP where the DMI is opposed to the precession and the field does not have any effect. Furthermore, this demagnetization effect is proportional to M_S (very low in ferrimagnets) which always gives a very low Walker field (negligible far from ACP). At the ACP, the field does not induce any precession of the magnetic moment even for high values, and so the Walker field diverges.

Note that if we cross ACP with a constant field H, two jumps in the velocity are expected when $H = H_W$ due to the divergence of H_W, associated with a switching of propagation regimes, whatever the DMI or demagnetization effect.

Experimental observations in the literature Mobility peaks have already been experimentally observed by Kim *et al.* [13]. They measured the DW velocity in a $SiN_{5nm}/GdCo_{30nm}/SiN_{100nm}$ wire with time-resolved Hall measurements. They nucleated a DW with a pulsed current (via heating and Oersted field) as shown in Fig. 2.13 (a). The DW was pushed by the field and when it goes through the cross part, the Hall signal is reversed which gives the time required to complete the track and the velocity is then evaluated. Fig. 2.13 (b) shows the velocity of the DW *versus* the temperature for different applied field and (c) the associated peak of mobility. In this study, the authors considered to be in the precessional regime due to the absence of an adjacent heavy metal layer (DMI is not expected) and associated these mobility peaks to the ACP.
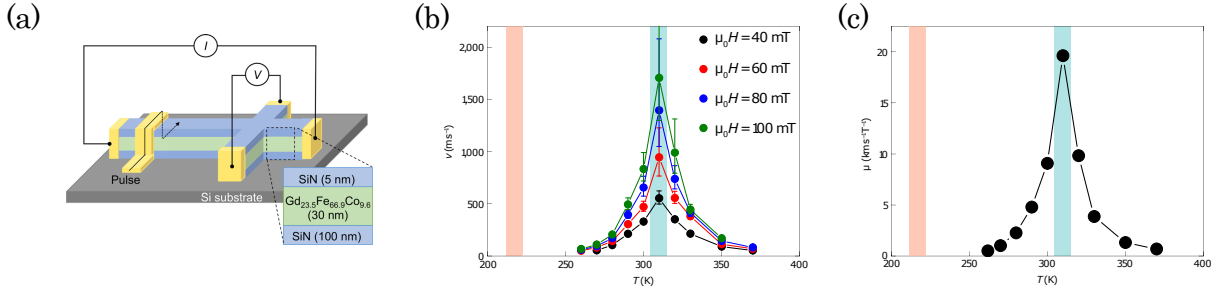
Figure 2.13 – Previous results of DW dynamics at T_{AC} in GdFeCo (from [13, 178]) (a) Sketch of a device used for high DW velocity measurements. (b) (from [13]) DW velocity *versus* the sample temperature T for different applied fields. (c) Mobility maximum associated to the velocity maximum of (b).

Summary Not surprisingly, considering the effective parameters of the GdCo alloy, both DW propagation regimes exhibit strong variations around the compensation points. Furthermore, the Walker field H_W also presents a strong dependence on $\%Co$. If there is no DMI, the H_W is very low and the DW will propagate in the precessional regime, except close to the ACP where H_W diverges and the DW propagates in the translational regime. If there is DMI, H_W diverges around the magnetic and the angular compensation points which makes the precessional regime inaccessible and locks the DW in its translational regime most of the time. This precession-locking induces a jump in the velocity and the precession rate between precessional and translational behaviors. Note that this effect should be larger around the ACP than around the MCP where the field does not have any effect on the DW. Note also that, at both compensation points, v and $\dot{\varphi}$ are the same for both regimes which means that this jump should be hard to be observed experimentally.

2.4.2 DW motion driven by STT

Here, we investigate the DW motion driven by STT comparing the analytical $q - \varphi$ model with effective parameters and the *Mumax3* micromagnetic simulations. As previously developed in part 3.1, the spin polarized current exerts two torques on the magnetic texture: the adiabatic and the nonadiabatic one (which depends on the β term) [130, 131]. In ferrimagnets, it is possible to consider that the spin current just interacts with the TM sub-lattice (here the Co one) (see part 1.3) which simplifies the effective parameters: $P_{eff} \approx P_1$ written for simplicity P and $\beta_{eff} \approx \beta_1$ written β (as discussed in Part 2.2). For the micromagnetic simulation, we consider that $\beta = 0.2$ but other values of β are considered in analytical calculations to see the impact of the non-adiabatic contribution of the spin current on the DW dynamics. To simplify the analysis, we consider that the spin current is fully polarized ($P = 1$) which means that the magnitude of the spin current PJ is directly associated with the electrical current. This assumption is just a normalization of the current values. Fig 2.14 (a) and (b) show the DW velocity v and precession rate $\dot{\varphi}$ *versus* the amplitude of PJ for different alloy compositions %Co. Thicker lines corresponds to the MCP and to the ACP values. It is also possible to observe the two propagation regimes: the translational one ($\dot{\varphi} = 0$) and the precessional one ($\dot{\varphi} \neq 0$) for respectively low and high current amplitudes. The DW also exhibits different dynamics with different propagation and precession directions. In the translational current range, Fig 2.14 (a), the velocity is negative for a positive current density which indicate that the DW moves along the electron flow, as expected for DW driven by STT [131]. Surprisingly, the mobility in the translational regimes does not depend significantly on the alloy composition %Co. The equilibrium in-plane angle of the DW φ is not plotted but it shows the same variation (amplitude and sign) as the the precession rate $\dot{\varphi}$ Fig. 2.14 (b). In the precessional regime, a more complex behavior of the DW propagation is observed Fig. 2.14 (a) and (b).

To investigate independently the two propagation regimes, we turn on and off the DMI, as done previously for field. Fig. 2.14 (c) and (d) show the mobility ($\mu = v/PJ$) and the normalized precession rate ($\dot{\varphi}/PJ$) *versus* the alloy composition %Co. Dots correspond to the simulated values for PJ in a range between $0 - 1000 \, \text{GA/m}^2$ with or without DMI (respectively, green and red) with $\beta = 0.2$. The continuous lines correspond to the analytical expressions of v/PJ and $\dot{\varphi}/PJ$ for translational and precessional regimes (also green and red) with $\beta = 0.2$ (Tab. 2.1). The perfect agreement between simulations and analytical values validates again that the DW is in the translational or in the precessional regime with or without DMI [85] and the single-lattice $q - \varphi$ model. The dotted lines correspond to analytical calculations for $\beta = 0.6$. It is possible to see in Fig. 2.14 (c) and (d) that around the MCP, nothing apparently modifies these two quantities ($\mu = v/PJ$ and $\dot{\varphi}/PJ$). This is in agreement with the fact that the STT just interacts with the TM sub-lattices and is not directly coupled to the net magnetization of the alloy. As shown in Fig. 2.14 (a), in the translational regime, the mobility does not change significantly in comparison to the precessional regime. Indeed, considering the effective parameters, the DW mobility in the translational regime is $\mu \propto \beta L_\alpha$ which is almost constant in the investigated %Co range. That also means that the DW velocity (or mobility) does not depend much %Co as shown in Fig. 2.14 (a) and (c). Increasing the β term, the mobility increases as shown with the dotted line in Fig. 2.14 (c). In the precessional regime, a much more complex behavior appears: the DW propagation direction is reversed and the precession rate exhibits a peak around the ACP. Note that the reversals do not occur exactly at ACP but a little before or after. Considering the DW geometry (Eq. 1.14), at the center of the DW, the non-adiabatic term exerts a field-like torque with $H_{FL\,STT} = \beta u/\gamma_0 \Delta$ and the adiabatic term is a damping-like torque with $H_{DL\,STT} = u/\gamma_0 \Delta$. It is also visible in the $q - \varphi$ model (Eq. 2.20). As detailed in part 2.2.2 and 2.1.1, the dynamics of a magnetic moment driven by a field-like and a damping like-term depends on the ratio H_{DL}/H_{FL}, here: $H_{DL\,STT}/H_{FL\,STT} = \beta$. Comparing this ratio with the effective damping parameter α, different reversal regimes can be obtained for a magnetic moment. For a ferrimagnet, the ratio β is almost constant (and positive) but the damping parameter changes greatly with %Co (see Fig. 2.9 (b)) which can give different reversal modes across %Co. Considering an STT-driven DW, both torques act differently on the DW position q (and $\dot{q}$) and on the DW precession (the DW angle φ and $\dot{\varphi}$). The $q - \varphi$ equations (Eq. 2.20) can be written as:

$$\begin{cases} \frac{\dot{q}}{\Delta} & = \frac{\frac{u}{\Delta}(1+\alpha\beta)+\gamma_0 h(\varphi)}{1+\alpha^2} \approx \frac{\frac{u}{\Delta}(1+\alpha\beta)}{1+\alpha^2} \\ \\ \dot{\varphi} & = \frac{\frac{u}{\Delta}(\beta-\alpha)-\alpha\gamma_0 h(\varphi)}{1+\alpha^2} \approx \frac{\frac{u}{\Delta}(\beta-\alpha)}{1+\alpha^2} \end{cases} \qquad (2.27)$$

68

with $h(\varphi)$ being a periodic function of φ homogeneous to a field that can be neglected in the asymptotic precessional regime (here: $h(\varphi) = H_{BN} \frac{\sin(2\varphi)}{2} + \frac{\pi}{2} H_{DMI} \sin(\varphi)$). As expected, the resulting contributions of the two torques on the DW depend on the relative magnitude of the β and α effective parameters.
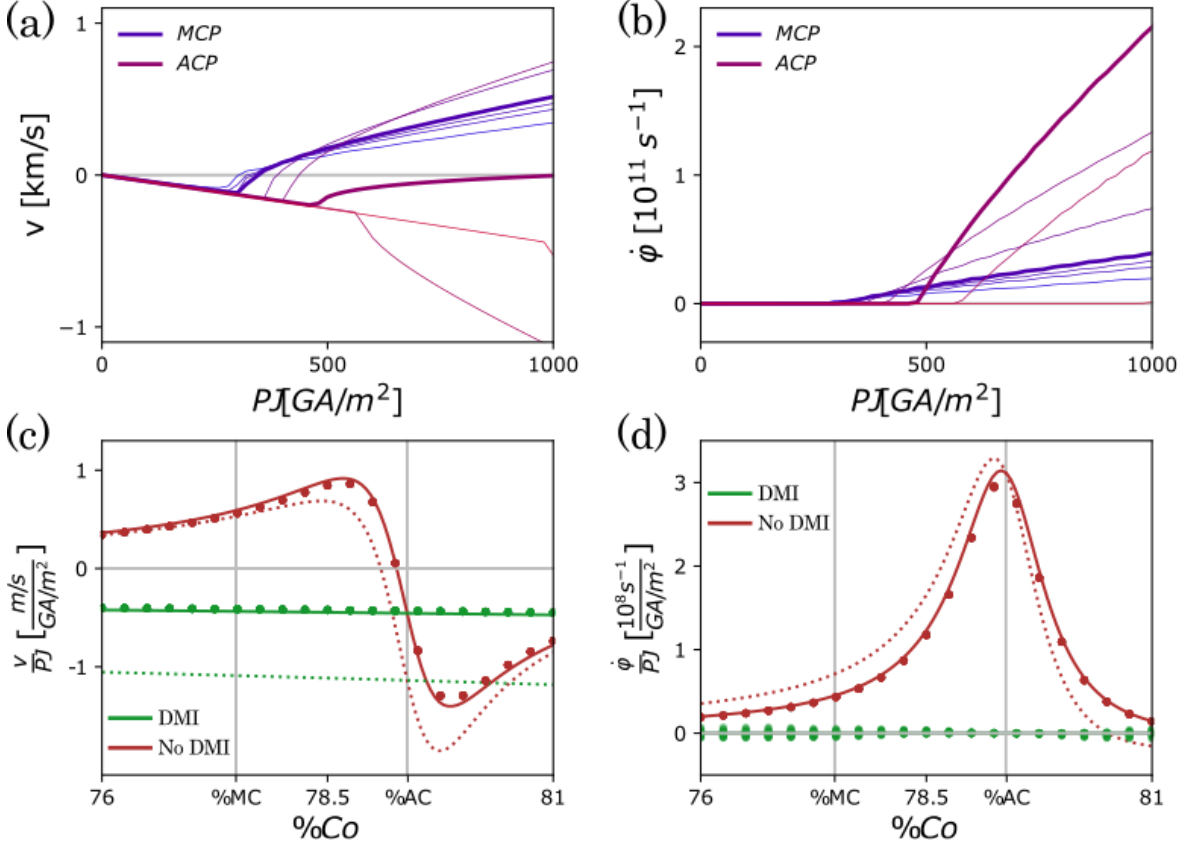
Figure 2.14 – (a) and (b) DW velocity v and precession rate φ *versus* the spin current density PJ for $\beta = 0.2$ and different alloy compositions $\%Co$. Thicker lines corresponds to the MCP and to the ACP. All these results are obtained with a medium DMI amplitude $D = 1.10^{-4}$ J/m^2 and $\beta = 0.2$. (c) and (d) DW mobility v/PJ and normalized precession rate $\dot{\varphi}/PJ$ for $PJ \in]0\,; 1000$ GA/m$^2]$ for $\beta = 0.2$. Dots correspond to micromagnetic simulations considering $D = 1.10^{-3}$ J/m^2 (green points) and $D = 0$ (red points). Lines represent the analytical expressions of v/PJ and $\dot{\varphi}/PJ$ in the translational (in green) and in the precessional (in red) propagation regime (Tab. 2.1). The dotted lines correspond to the analytical results for $\beta = 0.6$.

First, let us consider the propagation direction $\dot{q}$ in Eq. 2.27. Above the ACP, the effective α is positive and $(1 + \alpha\beta) > 0$, meaning both torques act on the DW in the same direction and push the DW in a negative direction $\dot{q} < 0$ for $PJ > 0$ (*i.e.* $u < 0$). Below, the ACP, α is negative and $(1 + \alpha\beta)$ changes sign for $(\beta = -1/\alpha)$. Below this critical point, the two torques act on the DW in opposite ways, and the resulting effect of the STT is to push the DW in the opposite direction: $\dot{q} > 0$ for $PJ > 0$ (*i.e.* $u < 0$). This change of the DW propagation direction results from the reversal of the individual flipping direction of moments for $(H_{DL}/H_{FL} = -1/\alpha)$ as shown in Fig. 2.4. For higher values of β, a lower α is required to reverse the sum $(1 + \alpha\beta)$ and the mobility reversal occurs further from the ACP (where α diverges). Conversely, the mobility is reversed closer to the ACP for lower values of β and for $\beta \approx 0$, the mobility occurs at the ACP where α diverges. Fig. 2.14 (c) shows the analytical expressions for $\beta = 0.2$ (in agreement with simulations) and the expected behavior for $\beta = 0.6$ *i.e.* for a higher non-adiabatic torque. In the precessional regime, the DW mobility overturns further from the ACP. It is also possible to note that, at the ACP, the mobility in both regime are equal. Indeed, the effective α diverges and the mobility in the precessional regime $\frac{1+\alpha\beta}{1+\alpha^2} \approx \frac{\beta}{\alpha}$ *i.e.*, the mobility in the translational regime. That means, if there is no precession locking (as discussed below), for the same mobility (*i.e.*

the same velocity), the DW can precess or not. In other terms, at ACP, the DW propagation and precession are uncorrelated because of the fact that α diverges in the equation $\dot{q} = \frac{\beta}{\alpha}u - \dot{\varphi}\frac{\Delta}{\alpha}$ from (Eq. 2.20).

Secondly, lets consider the precession rate $\dot{\varphi}$ shown in Fig. 2.14 (d). Surprisingly, it exhibits a peak around the ACP. As visible in Eq. 2.27, both torques act on the in-plane DW angle φ and the resulting effect depends of the term $(\beta - \alpha)$. Before the ACP, the effective α is negative (see Fig. 2.9 (b)) and $(\beta - \alpha) > 0$. For a positive PJ (i.e., $u < 0$), the precession is positive. After the ACP, the effective α is positive (see Fig. 2.9 (b)) and $(\beta - \alpha)$ changes sign for $\alpha = \beta$. Above this point, the precession is reversed ($\dot{\varphi} < 0$ for $PJ > 0$). This change of the DW precession direction results from the individual precession direction during the reversal of an individual moment for $(H_{DL}/H_{FL} = \alpha)$ as shown Fig. 2.4. For a higher β, the reversal occurs closer to the ACP (where the effective α diverges) and for a lower β, the reversal occurs further to the ACP. For $\beta \approx 0$, the reversal of the precession never happens. Fig. 2.14 (d) shows the precession rate expected for $\beta = 0.6$ (red dotted line). The precession reverses above the ACP and closer for higher β. Note that the precession rate exhibits a maximum for $\alpha = \frac{-1 \pm \sqrt{1 + \beta^2}}{\beta} \approx \frac{-1}{\beta}$ (for low β) which corresponds to the reversal of μ (see Fig. 2.14 (c)).
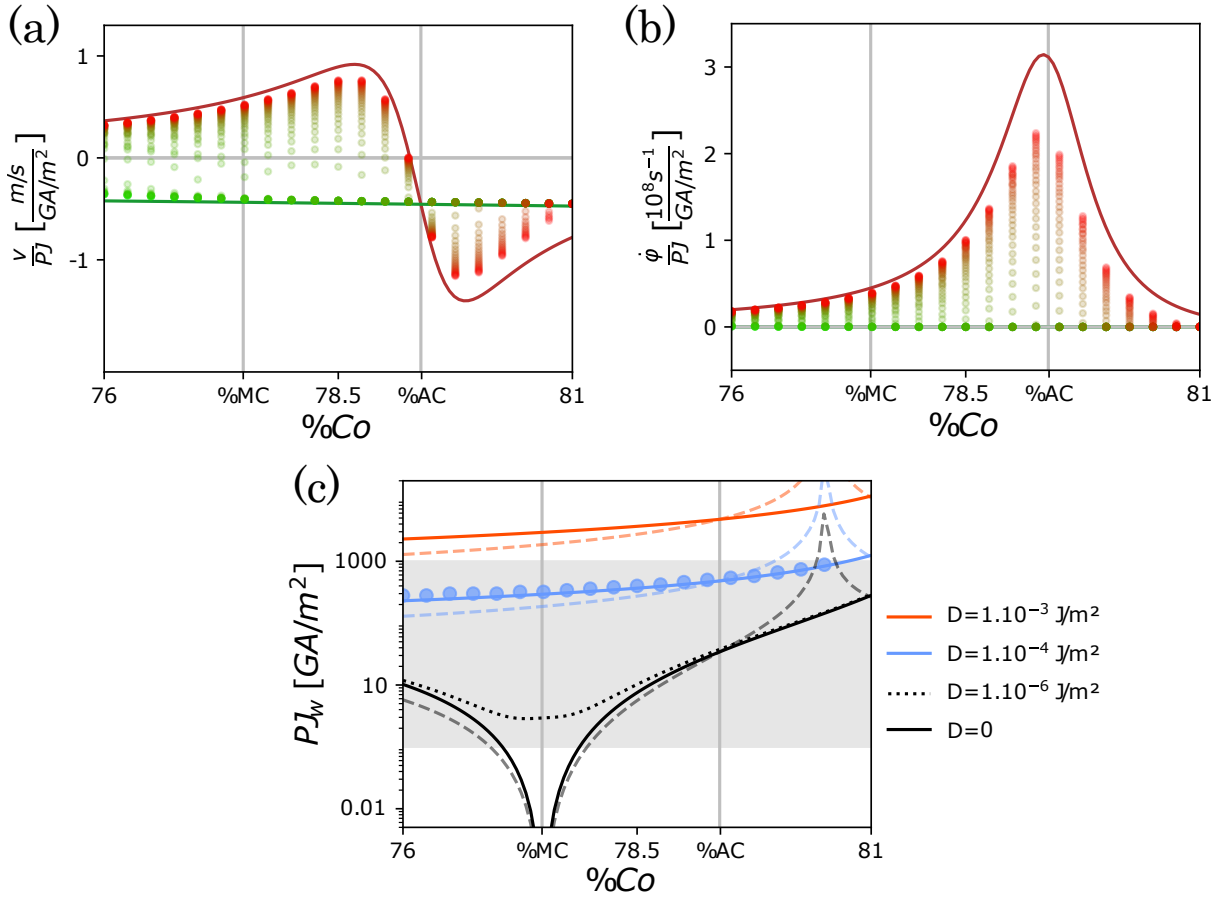
Figure 2.15 – (a) and (b) calculated mobility v/PJ and normalized precession rate $\dot{\varphi}/PJ$ *versus* %Gd for $D = 1.10^{-4}$J/m^2 (from Fig. 2.14 (a) and (b)). The color corresponds to the amplitude of the spin current PJ (green for low current and red for high current). Green and red lines correspond to the analytical expressions of v/PJ and $\dot{\varphi}/PJ$ from Tab. 2.1. (c) Lines correspond to the Walker current PJ_W calculated from Eq. 2.28 *versus* %Co for different values of D (written in the legend). Continuous lines are for $\beta = 0.2$ and dashed lines for $\beta = 0.6$. Blue dots correspond to values of PJ_W extracted from simulations with $D = 1.10^{-4}$J/m^2 shown Fig. 2.14 (a) and (b). The background gray region corresponds to the current range probed in micromagnetic simulations: $PJ \in [0, 10^3 \text{GA/m}^2]$.

Fig. 2.15 (a) and (b) show the mobility and normalized precession rate *versus* %*Co* for different current densities and for $D = 1.10^{-4}$ J/m^2 and $\beta = 0.2$. At low current (green points), the DW follows the translational laws for mobility and precession and, for higher currents (red points), the DW tends to follow the precessional laws. This means that there is not blockage regime. Fig. 2.15 (c) shows the Walker current ($PJ_W = (2e\mu_0 M_s/\hbar\gamma_0)u_W$) for different amplitudes of DMI resulting from the maximum u which fulfills the equation:

$$\frac{u}{\Delta} = \frac{\alpha\gamma_0}{\beta - \alpha} H_{BN} \sin(\varphi) \left(\frac{\pi}{2} \frac{H_{DMI}}{H_{BN}} - \cos(\varphi) \right) \tag{2.28}$$

adapted from Eq. 2.22.

For high values of DMI ($D = 1.10^{-3}$J/m^2), the Walker current is higher than the probed current range (the gray region Fig. 2.14 (c)) and the translational regime is not reachable [85]. In the intermediate case, ($D = 1.10^{-4}$J/m^2) the Walker current is almost constant and reached for the full range of %*Co*. In the absence of DMI, similarly to what was discussed for field, the only opposition to the precession is the demagnetization effect which vanishes at MCP. For very low DMI (such as $D = 1.10^{-6}$J/m^2), far from MCP, the demagnetization governs the Walker threshold but around MCP, it is dominated by the DMI. However, in contrast to the DW driven by field, the DMI does not induce a divergence of PJ_W which remains small. All these results are obtained for a value of $\beta = 0.2$ (full lines Fig. 2.14 (c)). If we increase the amplitude of the non-adiabatic torque (increasing β), the Walker threshold changes significantly. Dashed lines in Fig. 2.15 (c) show the Walker current PJ_W for $\beta = 0.6$. Divergences of PJ_W appear above ACP. As discussed previously, for $\alpha = \beta$, the DW does not precess (see Eq. 2.27). Any spin current could not tilt φ, which can be associated to a divergence of the Walker current. This situation can also be explained by the fact that the precession-free reversal of an isolated magnetic moment is reached if ($H_{DL}/H_{FL} = \beta = \alpha$) which is independent of the current density. Around this regions, the Walker current is never be reached and the DW is locked in the translational regime. For lower β, the divergence of PJ_W appears further away from the ACP and, for higher β, it appears close to ACP.
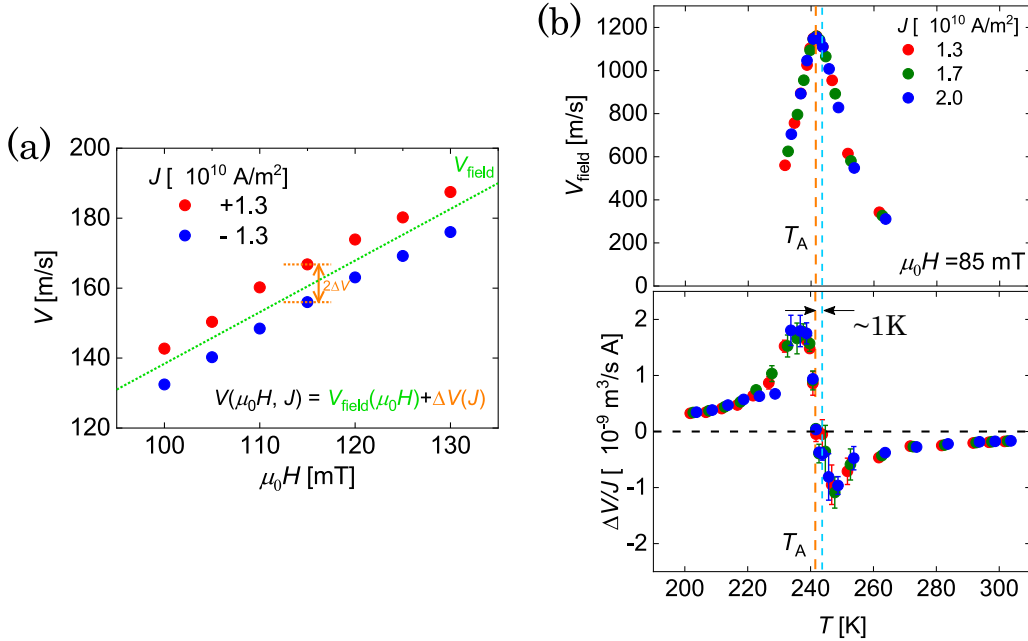
Figure 2.16 – (a) (from [179]) DW velocity driven by field under a $\pm J$ biased current. (b) (from [179]) mean DW velocity $v_{field} = (v(H,+J) + v(H,-J))/2$ and difference velocity $\Delta v = (v(H,+J) - v(H,-J))/2$ (normalized by the current density) *versus* the temperature for different current densities and for an applied perpendicular field of 85mT. The orange dotted line corresponds to the maximum of the v_{field} and the blue one to $\Delta v = 0$.

Experimental observations in the literature Some of these behaviors of the STT-driven DW dynamics have recently been observed by Okumo *et al.* in a $SiN_{5nm}/GdFeCo_{30nm}/SiN_{100nm}$ ferrimagnetic thin films [179]. They measured the velocity of a field-driven DW with a $\pm J$ bias current (shown in Fig. 2.16 (a)). Assuming the linearity between field and current, they separate the mean velocity $v_{field} = (v(H,+J) + v(H,-J))/2$ relative to the field effect and the difference of velocities $\Delta v = (v(H,+J) - v(H,-J))/2$ relative to the STT effect shown in Fig. 2.16 (b). Note that the associated mobility is in very good agreement with our micromagnetic simulations and our model. They observe a peak of v_{field} associated to the T_{AC} (as discussed above) indicated by the orange line and a reversal of Δv for a different temperature indicated by the blue line. They claim that the two lines are separated by ≈ 1 K.

Summary Different DW propagation regimes driven by STT are observed. At low currents, the DW moves in the translational regime, which does not vary significantly with the alloy composition. At higher current, the DW precesses and both its mobility and precession rate are much more dependent on %Co. In the STT-driven DW, the spin current exerts two torques on the DW: the adiabatic and the non-adiabatic torque. Their respective resulting effect depends of the relative magnitude of α and β parameters. Considering the effective parameters of the ferrimagnetic alloy (here $GdCo$), α varies significantly whereas β is almost constant. Here, main features (reversing of propagation/precession or precession locking) do not appear precisely at the MCP or at the ACP, but around the ACP where the effective damping α diverges changing sign. Depending on the value of β, a divergence of the Walker critical current can appear above the ACP, which blocks the precession of the DW. In this range of %Co, the DW mobility is very different in the two regimes, and the precession-locking should lead to a jump in the measured velocity.

2.4.3 DW motion driven by SOT

Here, we investigate the DW motion driven by SHE comparing the analytical $q - \varphi$ model with effective parameters and the *Mumax3* micromagnetic simulations. As previously developed in Part 2.1.4, if we inject an electrical current in a bi-layer stack that includes a heavy metal layer, the current flowing through the heavy metal layer will generate a perpendicular pure spin current in the magnetic layer: a spin current without any electrical current [180–182]. This perpendicular spin current exerts a damping-like torque on the magnetization which can drive a DW in a magnetic wire [85, 164, 167]. In ferrimagnets, it is possible to consider that the spin current just interacts with the TM sub-lattice (here the Co one) (see part 1.3) which simplifies the effective parameters: $\Theta_{SHeff} \approx \Theta_{SH1}$, written for simplicity Θ_{SH}. To simplify the analysis, we consider $\Theta_{SH} = 1$. This assumption is simply a normalization of the values of current density.

Fig 2.17 (a) and (b) show the DW velocity v and the DW in-plane angle φ *versus* the spin current $\Theta_{SH}J$ for different alloy compositions %Co. Thicker lines corresponds to the MCP and the ACP. The velocity of the DW is in the same range as for STT-driven DWs. However, here, just the translational regime ($\dot{\varphi} = 0$) is observable for the full range of current as expected (see Table 2.1). Across the ACP, the DW still moves in the same direction but the in-plane angle φ is reversed. Note that the velocity is positive for a positive current density which indicates that the DW moves along the current flow, as expected for DW driven by SHE with $\theta_{SHE} > 0$. It is possible to see that the velocity saturates above a current density which coincides with an in-plane angle of $\mp\pi/2$. As reported for ferromagnetic thin films [85], the SHE acts on the DW like a field dependent on the in-plane magnetization of the DW: $H \propto \cos(\varphi)$ (see Tab. 2.1). Increasing the current, the φ angle increases, which saturates the velocity of the DW [85, 164] (see Tab. 2.1). However, in a ferrimagnet at the ACP, φ remains zero (even for high current) due to the precession-free dynamics, and the DW velocity is unsaturated.
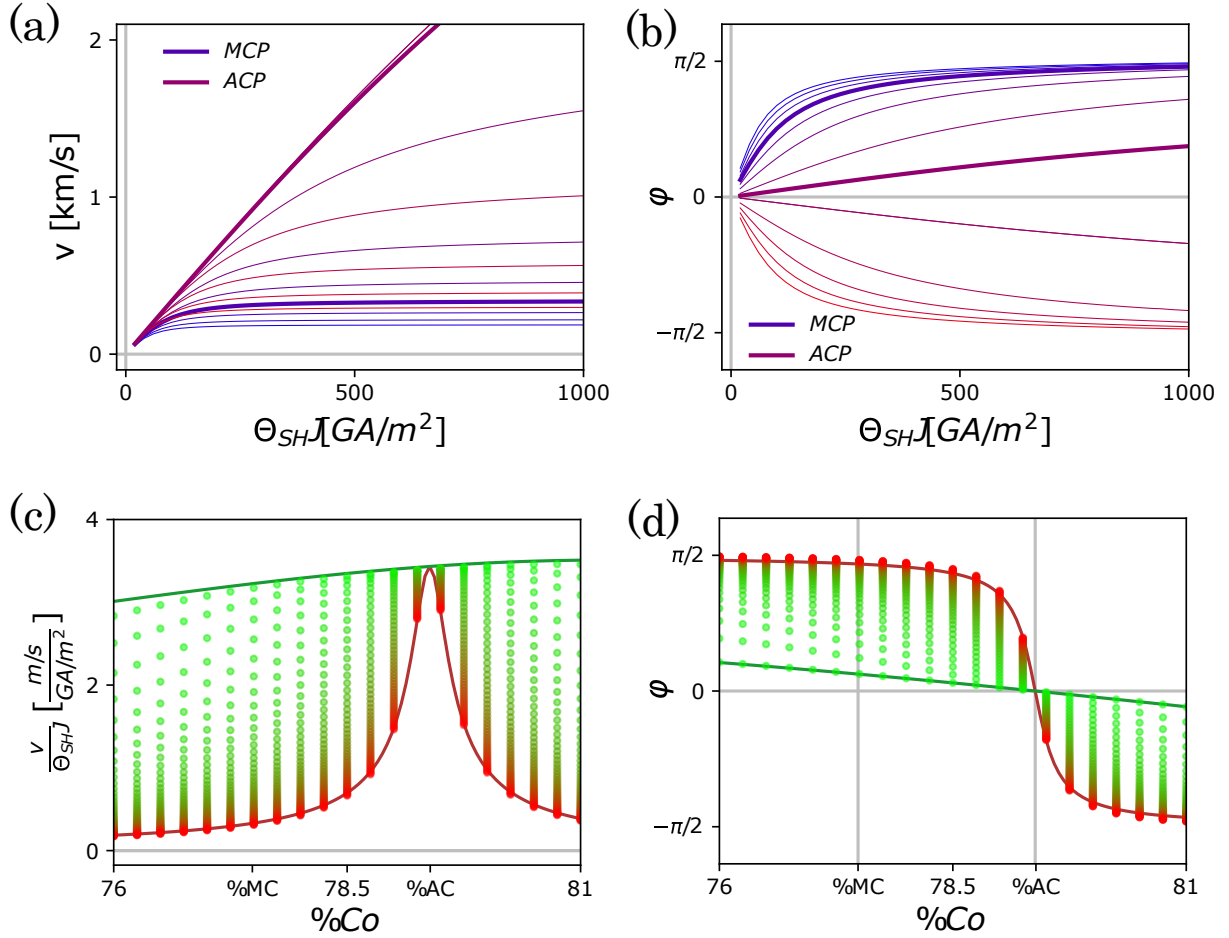
Figure 2.17 – SOT-driven DW dynamics (calculations and simulations). (a) and (b) show the DW velocity v and the in-plane angle φ *versus* the spin current density $\Theta_{SH}J$ for different alloy composition $\%Co$. Thick lines corresponds to approximately the MCP and ACP (the small numeric difference between the $\%Co$ of the thick line and ACP is specially pronounced here). All these results are obtained with a medium DMI amplitude of $D = 1.10^{-4}\text{J/m}^2$. (c) and (d) show the DW mobility $v/\Theta_{SH}J$ and the in-plane angle φ for $\Theta_{SH}J \in \,]0\,;1000\text{GA/m}^2]$. Dots correspond to the micromagnetic simulations for different current densities (green points for low current and red points for higher currents). Lines represent the analytical expressions of $v/\Theta_{SH}J$ and φ for low and high current respectively in green and red (Tab. 2.1).

Fig 2.17 (c) and (d) show the calculated mobility $v/\Theta_{SH}J$ and φ angle *versus* the alloy composition $\%Co$ for different current densities. Due to this saturation effect, the DW behavior is non-linear and the points are not superimposed. In (c), the green line corresponds to the mobility in low current approach (*i.e.* un-saturated velocity) and the red line in strong current approach (*i.e.* saturated velocity):

$$v \approx \begin{cases} \frac{\pi}{2} H_{SHE} \frac{\gamma_0 \Delta}{\alpha} & \text{for low } J \\[2ex] \frac{\pi}{2} H_{DMI} \gamma_0 \Delta & \text{for high } J \end{cases} \tag{2.29}$$

For low currents, the φ angle remains small (see Fig 2.17 (d)) and the saturation effect is negligible. In this range of currents, the mobility does not depend significantly on $\%Co$. For high currents, far from the ACP, the φ angle is larger and the saturation effect is dominant. At the opposite, close to the ACP, due to the non precessional regime, the φ angle remains zero and the saturation vanishes (see Fig 2.17 (d)). In this range of currents, the mobility depends strongly on the $\%Co$ with a mobility peak at the ACP. This mobility behavior induces a large variation of the DW velocity *versus* $\%Co$ for large currents and a low variation of v for low currents (see Fig 2.17 (a)).

Note that in this section, just the SHE contribution is taken into account. Adding other torques, like the Rashba term, the presented behaviors deviate from the pure SHE-driven dynamics and more complex dynamics appear (similarly to the dynamics driven by the two contributions of STT).

Experimental observations in the literature   Several experimental results have shown these DW dynamics. Siddiqui *et al.* measured the DW velocity driven by SHE in a Pt_{3nm}/ $CoTb_{3nm}$/ SiN_{3nm} micro wire with variable composition [20]. Fig. 2.18 (a) shows the DW velocity *versus* the current density in the left panel and the mobility *versus* the ferrimagnetic alloy composition in the right panel. For the first time, it was possible to see a mobility peak which could be associated to the ACP. However, the investigated velocity range and the offset current is not enough to consider the mobility peak unambiguously. Also, the velocities have been measured in different devices (with different compositions) which can present deviations of parameters such as the anisotropy or the pinning. Surprisingly, the $\%Tb_{AC}$ is lower than the $\%Tb_{MC}$. Fig. 2.18 (b) shows the DW velocity *versus* the current density in a Ta_{1nm}/ Pt_{6nm}/ $GdCo_{6nm}$/ $TaOx_{3nm}$ $20\mu m$-width wire for different temperatures measured by Caretta *et al.* [14]. These experimental results are in very good agreement with our simulations. For high currents, it is possible to see a velocity peak which is the signature of the ACP. For low currents, the peak fades and the velocity does not depend significantly on the temperature. Very recently, we have investigated the DW dynamics driven by SOT under in-plane field and we have directly shown the vanishing of the precession at the ACP (see ref. [42] and section 2.1.4).
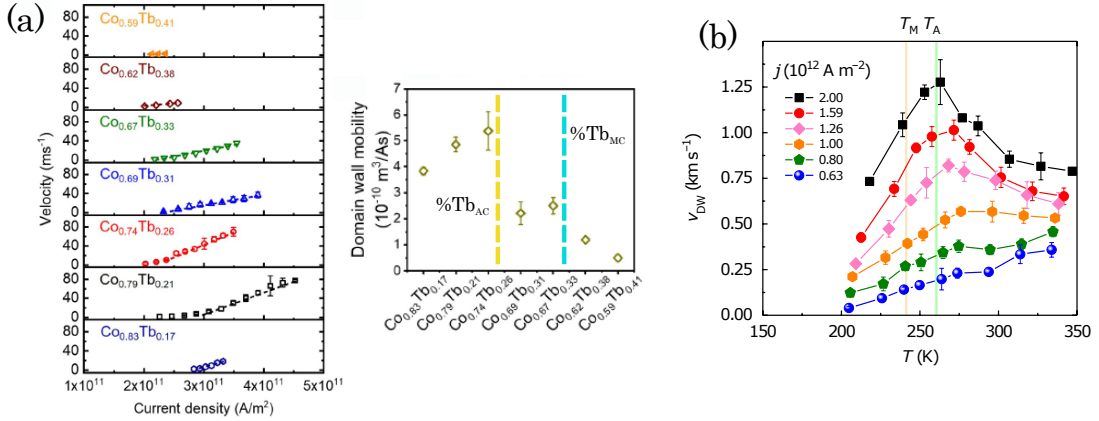
Figure 2.18 – Previous results on SOT-driven DWs in GdCo. (a) (from [20]) left panel: DW velocity *versus* applied current J in a Pt_{3nm}/ $CoTb_{3nm}$/ SiN_{3nm} $4\mu m$-wide wires with variable composition. Right panel: mobility v/J *versus* the CoTb alloy composition. The orange and the blue lines correspond to the angular and magnetic compensation compositions. (b) (from [14]) DW velocity driven by SOT *versus* the current density in a Ta_{1nm}/ Pt_{6nm}/ $GdCo_{6nm}$/ $TaOx_{3nm}$ 20 μm-width wire for different temperatures.

Summary   For a DW driven by SHE, the DW velocity is governed by the in-plane angle of the DW: $v \propto J\cos(\varphi)$ (see Tab. 2.1). Far from the ACP, the SHE exerts a torque on the DW which increases φ and saturates the velocity. At the ACP the DW does not precess which suppresses the saturation effect.

2.4.4 Transient propagation regime

Up to now, we considered a steady DW propagation driven by an applied force (field, STT or SOT) and we neglected the transitional regime. In this part, we investigate the transient regime and how the 'equilibrium' dynamics is reached after a step excitation. First, lets consider a force in the range of the steady-state translational propagation regime. In this situation, before the force step, the DW is in its equilibrium state of minimal system energy (as discussed in part 1.4). The force step starts to push the DW and tilts the in-plane angle up to the steady DW velocity v_0 with an internal angle φ_0 given in the Table 2.1 (in this part we write (t) quantities in the transient regime and we index 0 the quantities in the steady regime). This transient regime is non-instantaneous and requires a characteristic time (written τ) that we study in this part.
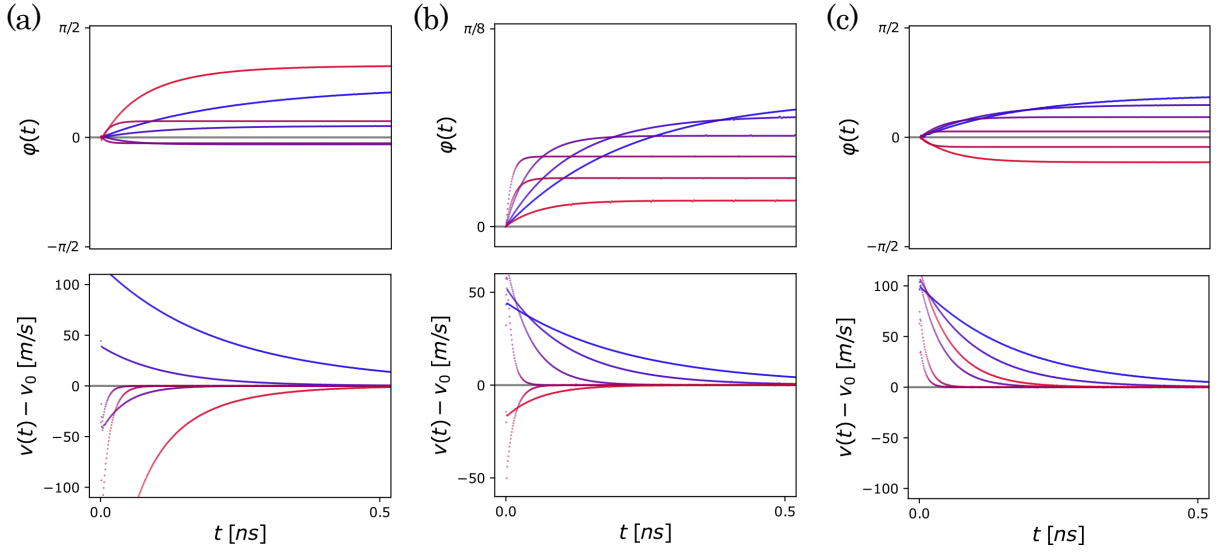
Figure 2.19 – transient propagation regime of the DW in-plane angle $\varphi(t)$ and velocity $v(t)$ for (a) a step of field ($\mu_0 H = 40$mT), (b) a step of STT ($PJ = 60$GA/m^2 with $\beta = 0.2$) and (c) a step of SHE ($\Theta_{SH} J = 40$GA/m^2) with a DMI amplitude of $D = 1.10^{-4}$J/m^2 for different $\%Co \in [76\% \, ; 81\%]$ (colored from red to blue). The top panels show the evolution of the in-plane angle of the DW $\varphi(t)$ and the bottom panels show the difference between the instantaneous DW velocity $v(t)$ subtracted by the steady-state DW velocity v_0.

Fig. 2.19 shows this transient regime for a DW driven by field (a), STT (b) and SOT (c) in the translational regime. The top panels show the time evolution of the DW in-plane angle $\varphi(t)$ and the bottom panels show the time evolution of the instantaneous DW velocity minus the steady-state velocity $v(t) - v_0$ for different alloy composition $\%Co \in [76\% \, ; 81\%]$. It is possible to see that $\varphi(t)$ moves from its equilibrium position (without force) up to its steady-state situation φ_0. Here a DMI of $D = 1.10^{-4}$J/m^2 is considered, which gives an equilibrium angle of $\varphi(t = 0) = 0$ before the force step. After the force step, it reaches its steady-state value φ_0 (see Table 2.1). It is also possible to see that the time required to reach φ_0 depends on $\%Co$. The instantaneous DW velocity $v(t)$ changes and reaches its steady-state value v_0, also in agreement with previous observation (*i.e.* $v(t) - v_0$ goes to zero). It is possible to see that its rising time required to reach v_0 is the same that the one required to reach the in-plane angle one.

At the beginning of this transient regime, $\varphi(t \approx 0)$ is close to its equilibrium position. If the precession is mainly limited by DMI, the initial equilibrium angle is zero: $\varphi \to 0$ and $\sin(\varphi) \approx \varphi$ and $\cos(\varphi) \approx 1$. Note that this approximation overestimates the effects of the SHE and of the DMI. The equations of the

$q - \varphi$ model (Eq. 2.20) become:

$$\begin{cases} \alpha \frac{\dot{q}}{\Delta} + \dot{\varphi} = \gamma_0 \left(H + \frac{\pi}{2} H_{SHE} \cos(\varphi) \right) + \beta \frac{u}{\Delta} \approx \gamma_0 \left(H + \frac{\pi}{2} H_{SHE} \right) + \beta \frac{u}{\Delta} \\[2mm] \frac{\dot{q}}{\Delta} - \alpha \dot{\varphi} = \gamma_0 \frac{\pi}{2} H_{DMI} \sin(\varphi) + \frac{u}{\Delta} \approx \gamma_0 \frac{\pi}{2} H_{DMI} \varphi + \frac{u}{\Delta} \end{cases} \quad (2.30)$$

which gives the instantaneous velocity $v(t)$ and angle $\varphi(t)$ of a DW driven by field, STT or SOT in the transient regime:

$$v(t) \approx \begin{cases} v_{0\,H} \left(1 - \frac{e^{(-t/\tau)}}{1+\alpha^2} \right) \\[2mm] v_{0\,STT} \left(1 - \frac{(\beta-\alpha)e^{(-t/\tau)}}{\beta(1+\alpha^2)} \right) \\[2mm] v_{0\,SHE} \left(1 - \frac{e^{(-t/\tau)}}{1+\alpha^2} \right) \end{cases} \quad \text{and} \quad \varphi(t) \approx \begin{cases} \varphi_{0\,H} \left(1 - e^{(-t/\tau)} \right) \\[2mm] \varphi_{0\,STT} \left(1 - e^{(-t/\tau)} \right) \\[2mm] \varphi_{0\,SHE} \left(1 - e^{(-t/\tau)} \right) \end{cases} \quad (2.31)$$

where $v_{0\,H}$, $v_{0\,STT}$, $v_{0\,SHE}$, $\varphi_{0\,H}$, $\varphi_{0\,STT}$, $\varphi_{0\,SHE}$ are values corresponding to the steady-state regime given in Table 2.1 in the low φ approximation. Here, τ is a characteristic rising time of the transient regime:

$$\tau = \frac{1 + \alpha^2}{\frac{\pi}{2} H_{DMI} \alpha \gamma_0} \quad (2.32)$$

It is possible to see that all $v(t)$ and $\varphi(t)$ depend of the same characteristic time τ independent of the applied force on the DW. This time corresponds to the duration of the transient regime. For large times $t \gg \tau$, the instantaneous velocity tends towards its value in the steady-state regime. This transient regime has already been theoretically and experimentally studied [34, 183–187] considering the transient regime as a mechanical motion of a solid where the characteristic time τ is associated to inertia. Analogously, this approach associates an effective mass to a DW [34]:

$$m = \frac{1 + \alpha^2}{\frac{\gamma_0}{2\mu 0 M_S} \partial_\varphi^2 \sigma |_{t=0}} \propto \tau \quad (2.33)$$
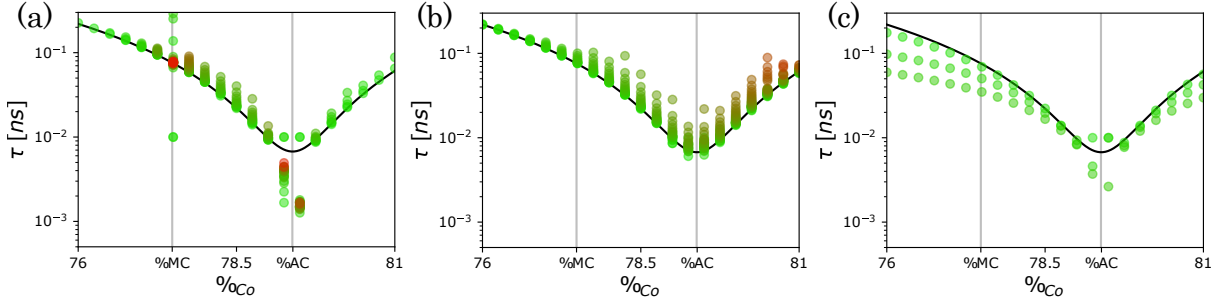
Figure 2.20 – Characteristic time τ of the DW transient regime for different driving forces, from simulations (points) and analytical model (black lines; using Eq. 2.32 and effective parameters). All simulations take a DMI amplitude of $D = 1.10^{-4}$ J/m^2 (like in previous cases). (a) τ of the field-driven transient regime. Green to red points correspond to simulations with low to high field. (b) τ of the STT-driven transient regime (with $\beta = 0.2$). Green to red points correspond to simulations with increasing current, all below the Walker threshold. (c) τ of the SOT-driven transient regime, with $\Theta_{SH} J = 40$, 100 and 160GA/m^2.

In a ferrimagnet, considering variable effective parameters, it is expected that this transient regime duration τ changes with %Co. Fig. 2.20 shows the characteristic time τ extracted from the numerical simulations for a DW driven by (a) a field, (b) the STT and (c) the SHE. For all simulations, a DMI of $D = 1.10^{-4}$J/m^2 is considered. As expected, the characteristic time τ of the transient regime changes with %Co. The black line corresponds to its analytical expression (Eq. 2.32). It is possible to verify that τ is the same for all type of forces (H, STT and SHE, for low field or current). For a DW driven by

field or STT, τ does not depend on the magnitude of the force (below the Walker threshold). For larger H or STT, the observed rising time τ is longer than the theoretical expectation. Indeed, for larger H or STT, the angle φ is larger and the over estimation of the DMI gives a theoretical value of τ shorter than the reality. This effect of the non-validity of the low angle approximation is more visible for SHE-driven DW where the velocity law is non-linear and both the SHE and the DMI effects are overestimated. Out of this case, the theoretical expression of τ (Eq. 2.32) is in very good agreement with the micromagnetic simulations except around the ACP. It is possible to see that the transient duration is minimum but non-zero at the ACP. Here, the minimum of τ is around $6.0 \ 10^{-3}$ns. In this situation, the transient regime is as short as possible and the DW is quasi-directly in its steady-state regime. The fact that τ does not fully vanish is expected for a DW driven by STT. Indeed, as previously shown, the in-plane angle of the DW $\varphi(t)$ changes at the ACP. At this point, a step of current always induces transient dynamics to reach $\varphi_0 \neq 0$. For a DW driven by field or SHE at the ACP, the extracted τ are not reproduced by the theoretical values. At the ACP, the DW does not precess and the equilibrium $\varphi(t = 0)$ before turning on the force is the same as the one during the motion φ_0, which suppresses the transient regime.

Fig. 2.21 shows the time evolution of $\varphi(t)$ and $v(t)$ *versus* $\%Co$ for DW driven by (a) a field, (b) the STT and (c) the SHE. The colors correspond to the configurations in different moments of the transient regime. The black line shows the values of φ_0 and v_0 in the steady-state regime. Thin color lines correspond to the analytical model using Eq. 2.31 with effective parameters. It is possible to see that the analytical model describes with a good agreement the values of $\varphi(t)$ and $v(t)$ from the simulations for the first configuration (which corresponds to the validity range of the small φ approximation). In this plot, values of $\%Co$ without transient regime directly appear as a crossing point between all curves.

For the DW driven by a field (Fig. 2.21 (a)), two $\%Co$ with no transient regime are observed: for the MCP and the ACP. At the MCP the field does not have any effect on the net magnetization and the DW is un-susceptible to its action. Both the in-plane angle φ and the DW position remain in their static equilibrium values and the velocity v remains zero. Here, the static φ_0 is zero as imposed by the DMI. At the ACP, under a field, magnetization has a precession-free reversal dynamics, so the propagation of the DW is uncorrelated to the in-plane angle. Under a field step, the DW moves directly in its steady-state regime without any modification of $\varphi(t)$. Due to the DMI, here $\varphi(t)$ remains zero. Note that even if the analytical model describes well this transition-free dynamics, the micromagnetic simulations differ in the first picoseconds. Indeed, for micromagnetic simulations, the exchange coupling is finite, which allows a tilt between the sub-lattices magnetization and deviates from the effective parameter model (as discussed in the following section).

For the STT-driven DW (Fig. 2.21 (b1) and (b2)), there is always a transient regime for $\beta = 0.2$ (b1). Even at the ACP, it is possible to see the non-instantaneous variation of $\varphi(t)$ with a characteristic time τ as discussed before. Due to the competition between adiabatic and non-adiabatic torques, no precession-free dynamics is obtained in the investigated range of $\%Co$ which induces a rising time required to reach the steady-state regime of DW propagation. However, at the ACP, even if the evolution of $\varphi(t)$ is non-instantaneous, the DW velocity $v(t)$ reaches instantaneously its steady-state value. This is due to the term $\frac{\beta - \alpha}{(1 + \alpha^2)\beta}$ (in Eq. 2.31) which diverges at the ACP dominating the time evolution of $v(t)$ (but not the one of $\varphi(t)$). Interestingly, in this configuration, the DW moves at the same velocity but with different in-plane angle and the DW velocity and angle are not correlated anymore. For larger values of β, it is possible to reach a precession-free dynamics as shown Fig. 2.21(b2) for $\beta = 0.6$. As expected, the vanishing of the precession deletes the transient regime. Both $\varphi(t)$ and $v(t)$ have fixed values for the same reasons given above for a DW driven by field at the ACP.

For the SOT-driven DW (Fig. 2.21 (c)), the precession vanishes at the ACP, which deletes the transient regime as for DW driven by field at the ACP. Note also that simulations and this model differ for the first picoseconds due to the finite exchange coupling taken into account in the simulation.
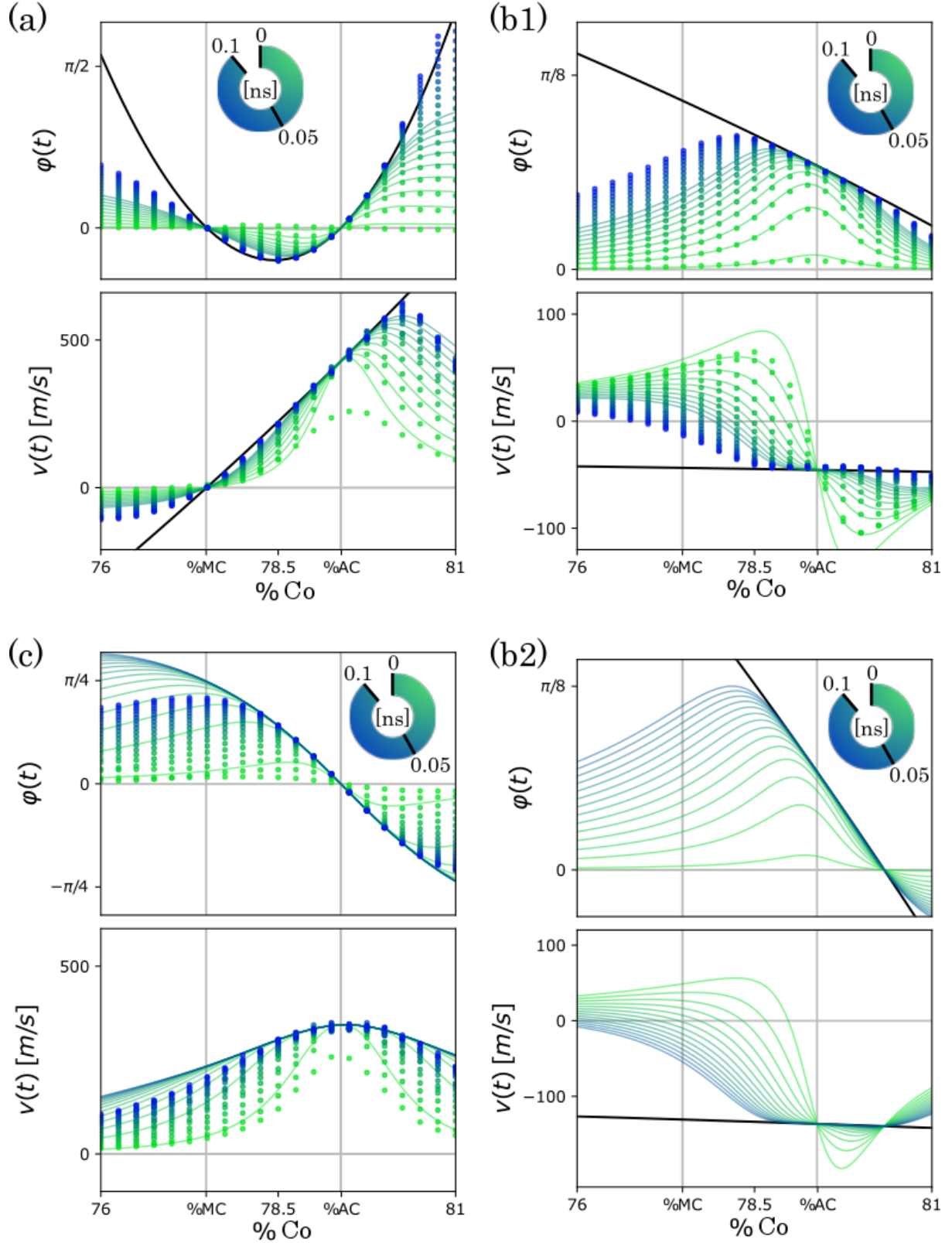
Figure 2.21 – Transient regime of the domain wall motion. Time evolution of $v(t)$ and $\varphi(t)$ versus %Co for a DW driven by a step of (a) field ($\mu_0 H$=10mT), (b) STT ($PJ = 100\text{GA/m}^2$ with $\beta = 0.2$ for (b1) and $\beta = 0.6$ for (b2)) and (c) SHE ($\Theta_{SH}J = 100\text{GA/m}^2$). Color points are from micromagnetic simulation considering a DMI of $D = 1.10^{-4}\text{J/m}^2$. The color indicates the time of the successive configurations. The color lines show the analytical model from Eq. 2.31 with effective parameters. Black lines correspond to the associated quantity in the steady-state regime φ_0 and v_0 (from Table 2.1).

Summary: In this part, we demonstrated the existence of instantaneous dynamics of a DW driven by a field, STT and SHE for specific ferrimagnetic configurations. The main factor leading lead to the vanishing of the transient regime is the precession-free reversal of the magnetization. Indeed, in this condition, there is no correlation between the DW position (*i.e.* v) and the in-plane angle φ and no inertia-like dynamics. This precession free dynamics is obtained under field or SHE at the ACP or under STT at $\alpha = \beta$. Interestingly, for a DW driven by STT (with a non-zero β), at the ACP the velocity of the DW reaches instantaneously its steady-state value whereas its in-plane angle requires a finite characteristic time τ to reach its non-zero steady-state value. Experimentally, it is very challenging to measure this transient regime because after the end of the step of force, the opposite transient regime occurs. Furthermore, for measurements under current, the rising time of the steady-state regime is dominated by the heating of the magnet ($t_T \gg \tau$ as discussed in the part 3.5).

2.4.5 Dynamics with low coupling

As validated in all previous parts, the ferrimagnet DW dynamics can be described considering a ferromagnetic-like material with effective parameters of the alloy. However, this approximation remains valid only if the inter-exchange between the two sub-lattices is stronger than the applied forces on the magnetic moment (Eq. 2.14). Otherwise, the difference between torques on the two sub-lattices induces a significant tilt between them and the ferromagnetic-like approach is no longer valid. To take into account this phenomenon, new models have to be developed. Few alternative theories have already been developed for antiferromagets dynamics [26, 147] or multi-layer systems [12, 15, 16]. However, in ferrimagnetic materials, due to the different nature of the two sub-lattices the considered simplifications are not valid. In the following part, we will develop a model that includes this canting in the resulting DW dynamics.
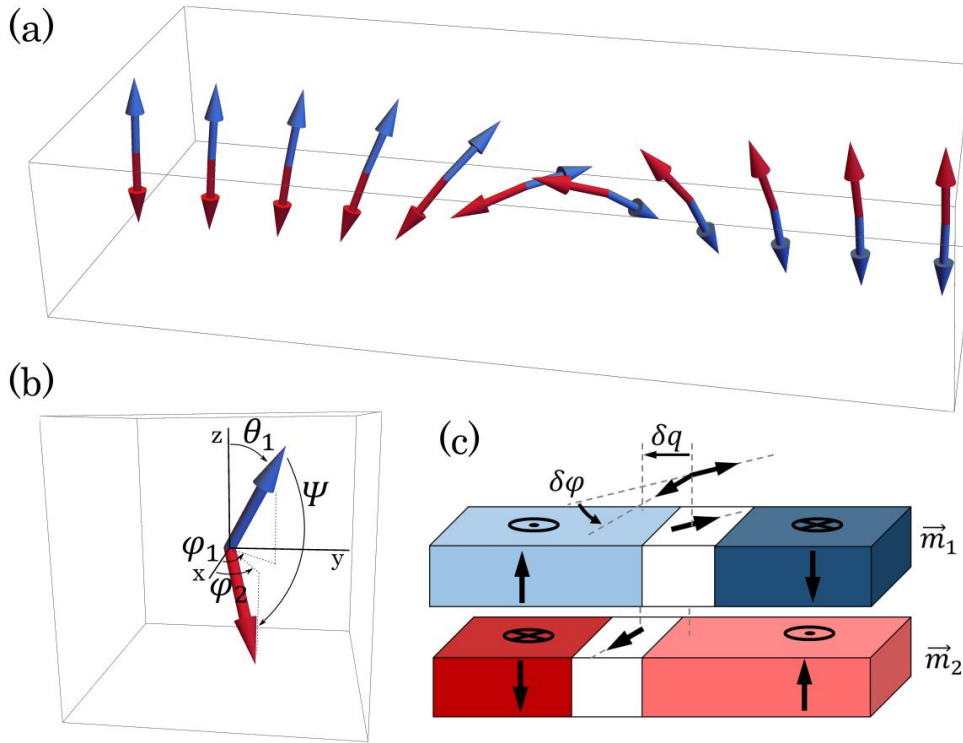
Figure 2.22 – Double DW description of ferrimagnetic DW. (a) Sketch of a ferrimagnetic DW. (b) Spherical description of $\vec{m}_1$ and $\vec{m}_2$ (c) $\delta q - \delta \varphi$ description of a ferrimagnetic DW

To describe the DW behavior in a ferrimagnet including the canting between sub-lattices magnetization, we propose to consider a ferrimagnetic DW as two ferromagnetic DW textures, one for each magnetic sub-lattices (Fig. 2.23) interacting by exchange torque [12, 15]. The resulting ferrimagnetic DW can be described by 4 collective coordinates (2 for each ferromagnetic DW): q_1 and q_2 the center

of the DWs in each sub-lattice and φ_1 and φ_2 their in-plane angles (as shown Fig. 2.23). Assuming an ↑↓ DW for the sub-lattice labeled 1, ↓↑ DW for the sub-lattice labeled 2, the two DW profiles are $\theta_1(x) = \theta_{q_1,\Delta}(x)$ and $\theta_2(x) = \theta_{q_2,-\Delta}(x)$ where $\theta_{q,\Delta}(x)$ corresponds to the ferromagnetic DW profile defined in Eq 1.14. For simplicity, we consider the sub-lattice 1 as the main, and the sub-lattice 2 as a slave. It is also more convenient to describe the 2 DWs system by four new coordinates:

$$q1 \leftarrow q \quad , \quad \varphi1 \leftarrow \varphi$$
$$q2 \leftarrow q + \delta q \quad , \quad \varphi2 \leftarrow \varphi + \pi + \delta\varphi$$

as shown in Fig. 2.23 (c).

Fig. 2.23 (a) shows a sketch of the two DW profiles for $(\delta q, \delta\varphi) = (\frac{\Delta}{2}, 0)$. The canting between the sub-lattices, Ψ, depends on both, δq and $\delta\varphi$: $\Psi(x, \delta q, \delta\varphi) = \arccos(\vec{m}_1(x, q, \varphi) \cdot \vec{m}_2(x, q + \delta q, \varphi + \delta\varphi))$ with a maximum at the mean of the DW positions as shown Fig. 2.23 (b).

The two DWs interact *via* the antiferromagnetic inter-exchange coupling energy ϵ_{ex12} associated to the surface energy $\sigma_{ex} = \int_{-\infty}^{+\infty} \epsilon_{ex12}(x)dx$ with $\epsilon_{ex12}(x) = J_{ex12}\cos(\Psi(x, \delta q, \delta\varphi))$:

$$\sigma_{ex} - \sigma_{ex\,0} = 2J_{ex12}\Delta\left(\frac{\delta q}{\Delta}\right)\operatorname{csch}\left(\frac{\delta q}{\Delta}\right)\left(\cosh\left(\frac{\delta q}{\Delta}\right) - \cos(\delta\varphi)\right) \tag{2.34}$$

where J_{ex12} is the inter-exchange coupling per unit of volume and $\sigma_{ex\,0}$ is the surface exchange energy for $(\delta q, \delta\varphi) = (0,0)$. Fig 2.23 (b) shows the inter-exchange coupling surface energy *versus* δq and $\delta\varphi$. For large δq (larger than 2Δ), the level lines of σ_{ex} are vertical which means σ_{ex} does not depend of $\delta\varphi$. In this range of δq, the two DWs are no longer coupled. For smaller δq and moderate $\delta\varphi$, σ_{ex} can be linearized and:

$$\sigma_{ex} - \sigma_{ex\,0} \approx J_{ex12}\Delta\left(\delta\varphi^2 + \left(\frac{\delta q}{\Delta}\right)^2\right) \tag{2.35}$$
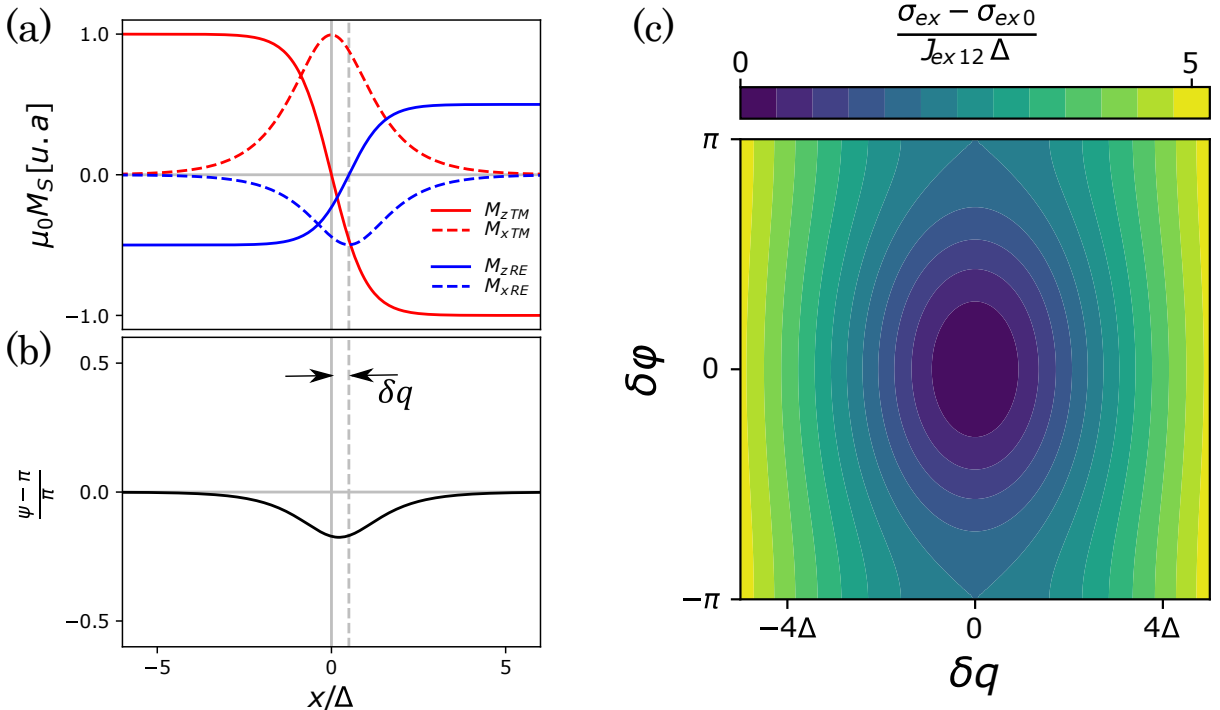
Figure 2.23 – Double DW analytical model. (a) Model of the two DW structures associated with the two sub-lattices (in red and blue). (b) Resulting angle Ψ between the magnetization of the two sub-lattices. (c) Surface energy plot of σ_{ex} versus δq and $\delta\varphi$

In this range, the energy cost of $\delta\varphi$ and δq are comparable. Note that this general calculation over-estimates σ_{ex}. Indeed, it considers just two DWs with rigid profiles. In a more realistic case, the profiles of the two DWs should change to minimize the total energy, which becomes lower compared to the rigid case. Likewise, the resulting Ψ angle is also overestimated.

The evolution of these coordinates can be determined by two $q - \varphi$ systems with different parameters for each sub-lattice. We directly consider the RE-TM alloy case where DMI and spin torques can be neglected in the RE sub-lattice (here indexed 2). In this case:

$$
\begin{cases}
\begin{cases}
\frac{\alpha_1}{\Delta}\dot{q} + \dot{\varphi} = \gamma_{01}\left(H + \frac{\pi}{2}H_{SHE\,1}\cos(\varphi) + \frac{J_{ex12}}{\mu_0 M_1 \Delta}\delta q\right) + \frac{\beta_1 u_1}{\Delta} \\[2mm]
\frac{\dot{q}}{\Delta} - \alpha_1\dot{\varphi} = \gamma_{01}\left(\frac{\pi}{2}H_{DMI\,1}\sin(\varphi) - \frac{J_{ex12}}{\mu_0 M_1}\delta\varphi\right) + \frac{u_1}{\Delta}
\end{cases} \\[4mm]
\begin{cases}
-\frac{\alpha_2}{\Delta}\left(\dot{q} + \dot{\delta q}\right) + (\dot{\varphi} + \dot{\delta\varphi}) = \gamma_{02}\left(H + \frac{J_{ex12}}{\mu_0 M_2 \Delta}\delta q\right) \\[2mm]
-\frac{\left(\dot{q} + \dot{\delta q}\right)}{\Delta} - \alpha_2(\dot{\varphi} + \dot{\delta\varphi}) = \gamma_{02}\frac{J_{ex12}}{\mu_0 M_2}\delta\varphi
\end{cases}
\end{cases}
\tag{2.36}
$$

We solved these equations completely. Doing so, it is possible to calculate the internal deformation of the DW δq and $\delta\varphi$ during its motion and the resulting DW velocity $v = \dot{q}$ and its in-plane angle φ or its precession rate $\dot{\varphi}$. This approach of two coupled DWs leads to a very large number of cases and requires specific approximations to handle each of them analytically. Here, we consider a steady-state motion of the DW in translational or asymptotic precessional regimes and we do not consider time variation of δq, $\delta\varphi$, v and φ (and $\dot{\varphi}$ for the precessional regime). This is equivalent to considering the time-averaged quantities for the moving DWs. Table. 2.3 contains solutions of Eqs. 2.36 for both propagation regimes and for all driving forces.

Very interestingly, it is possible to see that no calculated value of velocities and precession rates diverges across the MCP. Also, the calculated expressions of v, φ or $\dot{\varphi}$ are the same as in the effective parameter approach. As for the calculated internal distortions, both δq and $\delta\varphi$ are proportional to the driving force (H or J) and inversely proportional to the the inter-exchange coupling J_{ex12}.

Force	Regime	
H	Steady	$v = v_{eff}$ $\varphi = \varphi_{eff}$ $\delta q = -\dfrac{\mu_0 H \Delta}{J_{ex12}} \dfrac{M_1 M_2}{L_\alpha} \left(\dfrac{\alpha_1}{\gamma_{01}} + \dfrac{\alpha_2}{\gamma_{02}} \right)$ $\delta\varphi = -\dfrac{\mu_0 M_S H}{J_{ex12}} \dfrac{1}{\alpha_2 + \alpha_1 \frac{M_1 \gamma_{01}}{M_2 \gamma_{02}}}$
	Precessional	$v = v_{eff}$ $\dot\varphi = \dot\varphi_{eff}$ $\delta q = -\dfrac{\mu_0 H \Delta}{J_{ex12}} \dfrac{M_1 M_2}{L_S^2(1+\alpha_{eff}^2)} \left(M_1\left(\dfrac{1+\alpha_1^2}{\gamma_{01}^2}\right) + M_2\left(\dfrac{1+\alpha_2^2}{\gamma_{02}^2}\right) + (M_1+M_2)\left(\dfrac{\alpha_1\alpha_2-1}{\gamma_{01}\gamma_{02}}\right) \right)$ $\delta\varphi = -\dfrac{\mu_0 M_S H}{J_{ex12}} \dfrac{M_1 M_2}{L_S^2(1+\alpha_{eff}^2)} \left(\dfrac{\alpha_1+\alpha_2}{\gamma_{01}\gamma_{02}} \right)$
STT	Steady	$v = v_{eff}$ $\varphi = \varphi_{eff}$ $\delta q = -\dfrac{\beta}{J_{ex12}} \dfrac{\mu_0 u_{eff} M_S}{\gamma_{0eff}} \dfrac{1}{1+\frac{M_1}{M_2}\frac{\alpha_1}{\alpha_2}\frac{\gamma_{02}}{\gamma_{01}}}$ $\delta\varphi = -\dfrac{\beta}{J_{ex12}\Delta} \dfrac{\mu_0 u_{eff} M_S}{\gamma_{0eff}} \dfrac{1}{\alpha_2+\alpha_1\frac{M_1}{M_2}\frac{\gamma_{02}}{\gamma_{01}}}$
	Precessional	$v = v_{eff}$ $\dot\varphi = \dot\varphi_{eff}$ $\delta q = -\dfrac{\beta}{J_{ex12}} \dfrac{\mu_0 u_{eff} M_S}{\gamma_{0eff}L_S^2(1+\alpha_{eff}^2)} \left(M_2^2\left(\dfrac{1+\alpha_2^2}{\gamma_{02}^2}\right) + \dfrac{M_1 M_2}{\gamma_{01}\gamma_{02}}\left(\dfrac{\alpha_1+\alpha_2}{\beta} + \alpha_1\alpha_2 - 1\right) \right)$ $\delta\varphi = -\dfrac{\beta}{J_{ex12}\Delta} \dfrac{\mu_0 u_{eff} M_S}{\gamma_{0eff}L_S^2(1+\alpha_{eff}^2)} \left(\dfrac{M_2^2}{\beta}\left(\dfrac{1+\alpha_2^2}{\gamma_{02}^2}\right) + \dfrac{M_1 M_2}{\gamma_{01}\gamma_{02}}\left(-(\alpha_1+\alpha_2) + \dfrac{\alpha_1\alpha_2}{\beta} - \dfrac{1}{\beta}\right) \right)$
SOT	Steady	$v = v_{eff}$ $\varphi = \varphi_{eff}$ $\delta q = \dfrac{\Delta}{J_{ex12}}\mu_0 M_S \dfrac{\pi}{2} H_{SHE\,eff} \dfrac{\alpha_2 \frac{\gamma_{01}}{M_1}}{\sqrt{\left(\frac{H_{SHE\,eff}}{H_{DMI\,eff}}\right)^2\left(\frac{\gamma_{01}}{M_1}-\frac{\gamma_{02}}{M_2}\right)^2 + \left(\alpha_2\frac{\gamma_{01}}{M_1}+\alpha_1\frac{\gamma_{02}}{M_2}\right)^2}}$ $\delta\varphi = -\dfrac{1}{J_{ex12}}\mu_0 M_S \dfrac{\pi}{2} H_{SHE\,eff} \dfrac{\frac{\gamma_{01}}{M_1}}{\sqrt{\left(\frac{H_{SHE\,eff}}{H_{DMI\,eff}}\right)^2\left(\frac{\gamma_{01}}{M_1}-\frac{\gamma_{02}}{M_2}\right)^2 + \left(\alpha_2\frac{\gamma_{01}}{M_1}+\alpha_1\frac{\gamma_{02}}{M_2}\right)^2}}$

Table 2.3 – Solutions of the $q-\varphi$ model with low coupling for v, φ, $\dot\varphi$, δq and $\delta\varphi$ for a DW driven by field, STT or SOT in translational and asymptotic precessional regimes. The δq and $\delta\varphi$ are considered constant. Values indexed X_{eff} correspond to the quantities in the effective parameter approach (from Eq 2.16 and Table. 2.1). Note that for the STT values: $\frac{u_{eff}\mu_0 M_S}{\gamma_{0eff}} = \frac{\hbar}{2e}PJ$ and that for the SOT values: $\mu_0 M_S H_{SHE} = \frac{\hbar}{2e}\frac{\Theta_{SH}}{t}J$

.

Inter-sublattice angle   Considering these expressions of $\delta q/\Delta$, $\delta\varphi$, it is possible to calculate the maximum canting between the two sub-lattices:

$$\Psi(x) < \Psi_{max} = \arccos\left(-\cos\left(\delta\varphi\right)\operatorname{sech}\left(\frac{\delta q}{2\Delta}\right)^2 + \tanh\left(\frac{\delta q}{2\Delta}\right)^2\right) \qquad (2.37)$$

Fig 2.24 shows the evolution of δq and $\delta\varphi$ and the resulting Ψ *versus* the alloy composition. For the considered antiferromagnetic coupling J_{ex12}, Ψ remains negligible, $|\Psi - \pi| \ll 1\%\pi$, which validates the assumption of a perfect anti-alignment of the two sub-lattices.

In Fig. 2.24, it is also possible to see that, even if δq and $\delta\varphi$ depend on %Co, they do not vanish at the ACP. At this point, due to the finite velocity of both DWs, the time required to establish the steady-state values of δq and $\delta\varphi$ is non-zero and the transient regime of DW still exists. By linearizing the Eq. 2.36 (considering the small angle approximation: $\sin(\varphi) \approx \varphi$ and $\cos(\varphi) \approx 1$) it is possible to calculate the new rise time τ required to reach the transient regime. This transient regime is visible on the numerical points Fig. 2.21, as the exchange coupling is finite in the numerical simulations, which induces a transient regime.
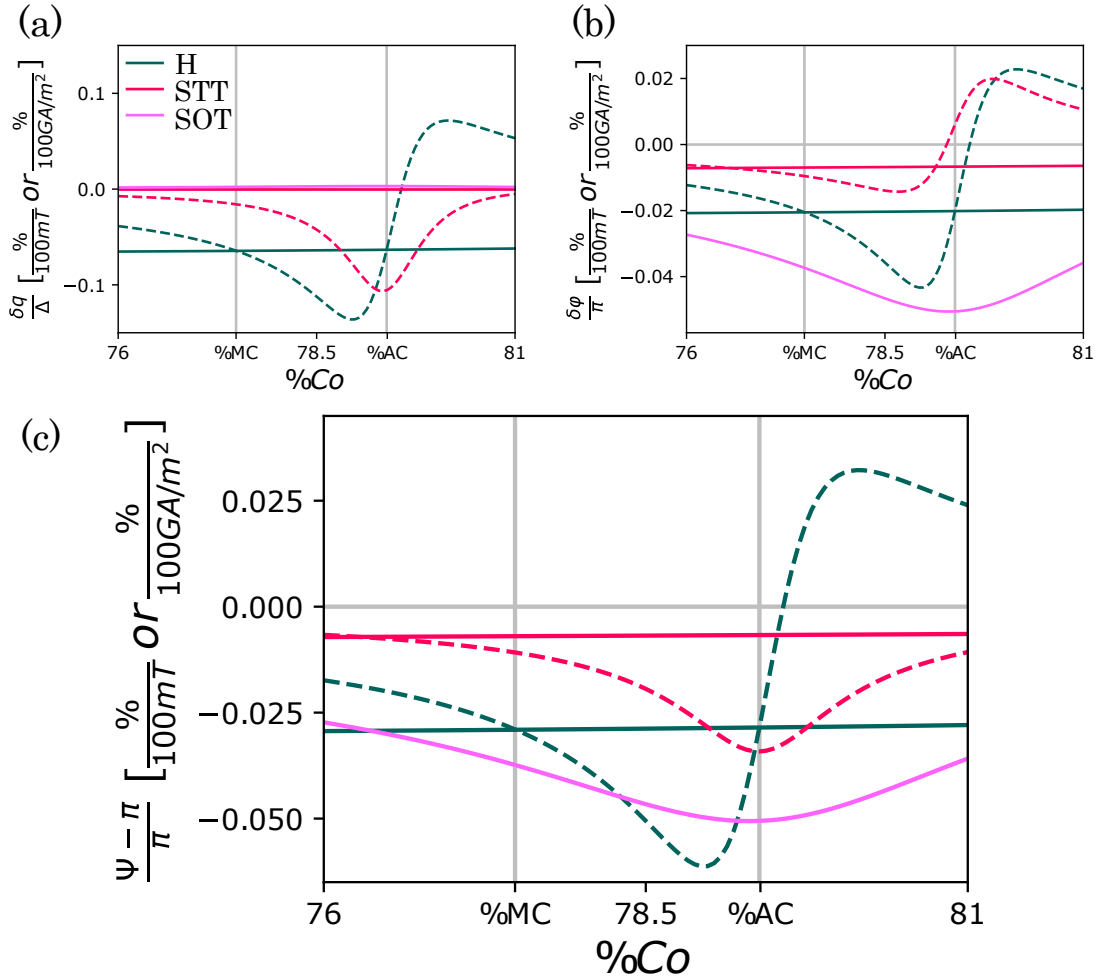
Figure 2.24 – Internal distortion and canting of a moving DW. (a), (b) and (c) show the evolution of δq, $\delta\varphi$ and the resulting Ψ angle *versus* the alloy composition. For each driving force (H, PJ for STT and $\Theta_{SH}J$ for SOT) the full lines corresponds to a DW moving in the translational regime and dashed lines in the precessional regime. We consider applied forces of $\mu_0 H = 100$mT, $PJ = 100$GA/m^2 and $\Theta_{SH}J = 100$GA/^{2}.

Summary: In this section, in contrast to the effective parameter approach, we consider the ferrimagnetic material as two magnetic sub-lattices coupled by a finite antiferromagnetic exchange interaction. The DW motion is the resulting motion of two DWs (one in each sub-lattice) described by four collective coordinates: q and φ for the resulting dynamics of the DW, and δq and $\delta \varphi$ for its internal dynamics. Considering a large (but finite) coupling, it is possible to obtain the analytical expression for all the four collective coordinates by solving two coupled $q - \varphi$ models (Tab. 2.3). The analytical expressions from the effective parameter model are recovered for the DW velocity v, the in-plane angle φ and the precession rate $\dot{\varphi}$. It is also possible to verify that the internal collective coordinates δq and $\delta \varphi$ are proportional to the applied force and inversely proportional to the coupling constant J_{ex12} and so, vanish for infinite J_{ex12}. However, at the ACP, their magnitudes are not necessarily zero, which induces a transient regime. To conclude, this approach validates the effective parameter model developed in previous parts and reveals the internal dynamics, specially relevant for the transient regime investigation where internal canting between sub-lattices induces additional rise times.

2.5 Conclusion

In this chapter, the dynamic behavior of RE-TM ferrimagnetic alloys was investigated. We developed a new effective-parameter model to describe the dynamics of two magnetic sub-lattices antiferromagnetically coupled applied to the ferrimagnetic case. In this frame, the ferrimagnet is considered as a ferromagnetic material with effective parameters. Two interesting points occur: the magnetic and angular compensation. Roughly speaking: at the magnetic compensation point, all static parameters diverge or vanish and, at the angular compensation point, all dynamic parameters diverge. In these two situations, the ferrimagnet exhibits new interesting dynamics of the magnetization (explained by the effective parameter approach), such as the high spin torque efficiency or the precession-free reversal. This effective parameter approach is also applied to describe the dynamics of a DW driven by field, spin transfer torques or spin Hall effect. New properties are highlighted such as: the reversal of DW propagation or precession, the vanishing of the precession, the decorrelation between internal structure and DW velocity, or the vanishing of the transient propagation regime. The same effective parameter model explains all experimental results existing in the literature for DW dynamics in ferrimagnets. Finally, another model considering a finite coupling between sub-lattices validates the obtain results of the effective parameter approach and allows the calculation of the inter-sublattice angle.

2.6 Perspectives

The developed effective model of both the statics and dynamics of ferrimagnetic DWs can also be applied to describe the dynamics of other spin textures. To extend this study, it could be interesting to investigate what are the effects of the ferrimagnetic behavior (detailed above) in more complex systems including non-trivial topology. In this part, we present first steps of a study of skyrmions in ferrimagnets in the light of this new approach.

2.6.1 Skyrmion dynamics

Skyrmions are non-trivial topological magnetic textures very well studied in the last years [4,81,83, 188]. They can be manipulated by electrical current [4,17,83,189] and, due to their small size, possibility of confinement, and other interesting properties, they could be a very convenient information carrier, promising for future devices for non-volatile storage or processing of information [5–7,190]. Due to their non-trivial topology, the manipulation of these spin textures induces a deflection which reduces the velocity along the desired direction [4,17,189]. On top of the optimization of current manipulation (a goal shared with the DW studies), two additional issues remain for skyrmions: minimizing their size, and increasing their velocity by reducing the topological deflection. Skyrmions have already been observed in RE-TM ferrimagnetic alloy thin films [14,22] and seem to present desirable properties to surpass these two limitations.

First, the skyrmion size results from the competition between exchange, anisotropy, DMI and demagnetization effects (see part. 1.3.1). In ferrimagnets, due to their low magnetization, the stray field is very low (compared to ferromagnetic materials) which should reduce the size of these magnetic structures [32, 106, 107]. Fig. 2.25 (a) shows the calculated skyrmion radius r_{sk} using the model presented in [107] with previous GdCo parameters. It is possible to see that the skyrmion is the smallest at T_{MC} where the demagnetization effects vanish. At this point, the minimum skyrmion radius depends just on the DMI, exchange and anisotropy. Record sizes of ~ 10 nm have been observed in GdCo thin films close to the MCP [14] (consistent with this calculation).
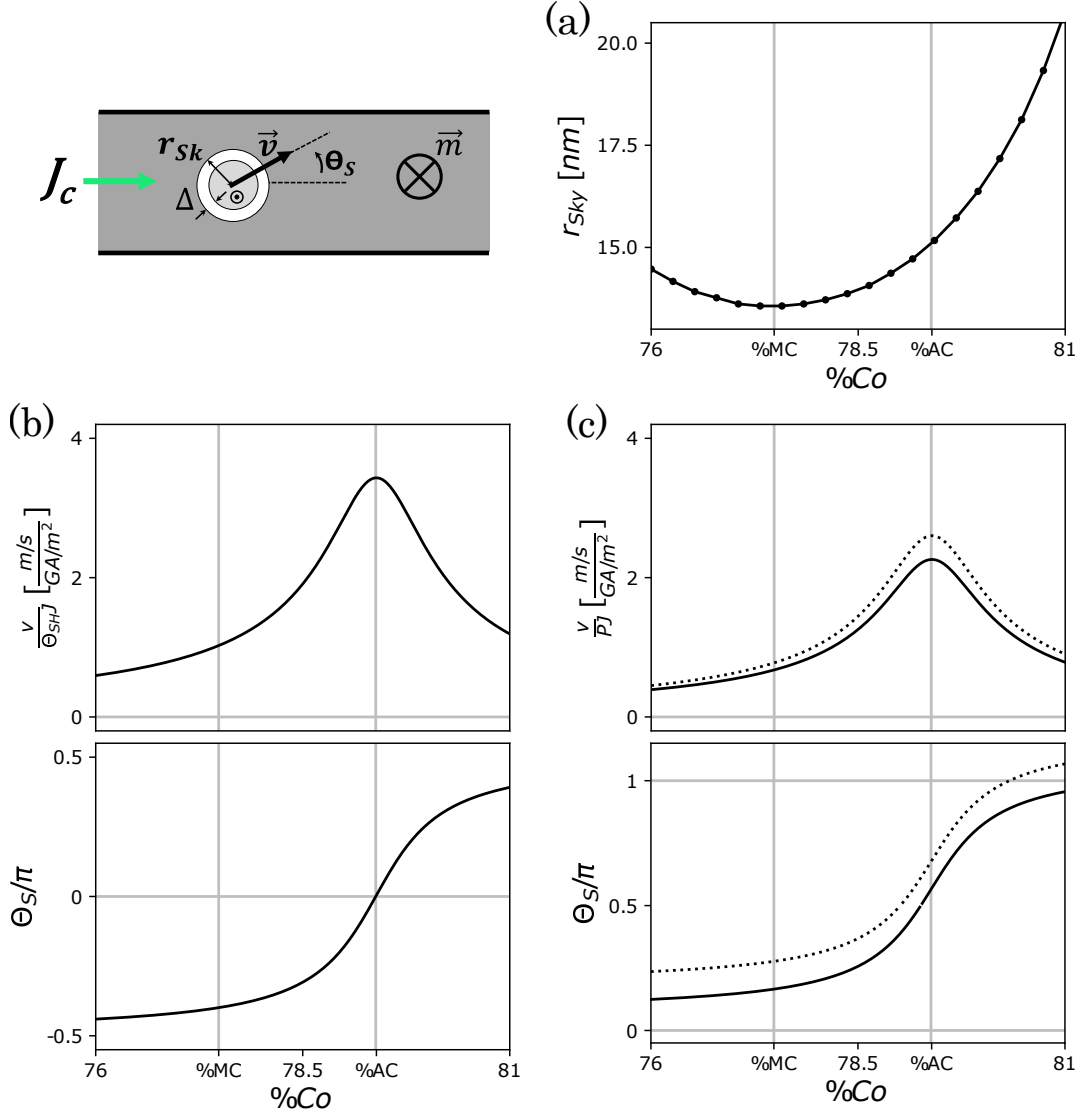
Figure 2.25 – Skyrmion statics and dynamics in RETM ferrimagnets calculated using the GdCo parameters of Tab. 2.2. A lower anisotropy of $K/3$ was used to obtain stable skyrmions (i.e. $r_{Sky} \neq 0$ or ∞). For this calculation, a DMI magnitude of $D = 1.10^{-3}$ J/m^2 is considered. (a) Calculated skyrmion radius r_{sk} versus the alloy composition considering the model of ref. [107]. (b) and (c) Calculated Skyrmion mobility v/J and deflection angle Θ_S *versus* alloy composition. (b) Skyrmion dynamics driven by SHE and (c) Skyrmion dynamics driven by STT. For the STT calculations, $\beta = 0.2$ (full line) and $\beta = 0.6$ (dashed line) are considered. For these two simulations, the skyrmion radius is taken as a constant parameter $r_{sk} = 20$ nm. A DW width parameter Δ is the one of the DW to have a quantitative comparison between both skyrmion and DW mobility.

Secondly, RE-TM ferrimagnetic skyrmions should also present a vanishing deflection angle at the angular compensation point [21, 22]. To calculate the skyrmion dynamics, it is required to use another collective coordinate approach which describes the motion of a spin texture in the 2D plane (x, y) known as the Thiele equation [191]. It considers the skyrmion as a rigid texture defined by its radius r_{sk} and its width parameter of the turning region Δ. Here the applied torques are associated to forces:

$$\vec{G} \times (\vec{v} - \vec{u}) - [D] (\alpha \vec{v} - \beta \vec{u}) + \vec{F}_{SHE} = 0 \tag{2.38}$$

with $\vec{G}$, the gyro-vector of the texture which takes into account its topology, $[D]$ the dissipation matrix which describes the dissipative forces, and $\vec{F}_{SHE}$ the resulting forces exercised on the skyrmion by the SHE. For the case of a skyrmion moving in a 2D plane: $\vec{G}$ is along the z direction with $G_z = \frac{\mu_0 M_S t}{\gamma_0} 4\pi$, $[D]$ is diagonal with $D_{xx} = D_{yy} = \frac{\mu_0 M_S t}{\gamma_0} \frac{2\pi r_{sk}}{\Delta}$ and $D_{zz} = 0$. $\vec{F}_{SHE}$ is in the x direction with $F_{SHE} = \mu_0 M_S H_{SHE} t r_{sk} \pi^2$. In this model, γ_0, H_{SHE}, Δ and α are defined exactly like for a DW. Note that we consider the case of a large skyrmion ($r_{sk} \gg \Delta$), although the results should be similar for small skyrmions. Solving the Thiele equation, it is possible to calculate the skyrmion velocity v (along its motion direction) and its deflection associated to the rate $v_y/v_x = \frac{2\Delta}{\alpha r_{sk}}$.

$$\begin{cases} v = \frac{\pi r_{sk}}{4} \frac{\gamma_0 H_{SHE}}{\sqrt{1+\eta^2}} \\ \\ \frac{v_y}{v_x} = \frac{1}{\eta} \end{cases} \qquad \text{SOT-driven skyrmion} \tag{2.39}$$

$$\begin{cases} v = u \sqrt{\frac{1 + \left(\frac{\beta}{\alpha}\right)^2 \eta^2}{1+\eta^2}} \\ \\ \frac{v_y}{v_x} = \frac{\eta\left(\frac{\beta}{\alpha} - 1\right)}{\eta^2 \frac{\beta}{\alpha} + 1} \end{cases} \qquad \text{STT-driven skyrmion} \tag{2.40}$$

where $\eta = \frac{\alpha r_{sk}}{2\Delta}$. Here, the skyrmion deflection can be associated to the angle $\Theta_S = \mathrm{atan}(v_y/v_x)$.

Applying the effective parameters on this formula, it is possible to predict the skyrmion dynamics in a RE-TM ferrimagnet. Fig. 2.25 (b) and (c) show the skyrmion mobility $\mu = v/J$ and its topological deflection angle for respectively SOT and STT driving forces. The skyrmion mobility is of the same order of magnitude as the DW for the SOT and STT driving forces. It is also possible to see that in both cases the mobility exhibits a peak at the ACP. More interestingly, for a SOT driving force, the skyrmion deflection vanishes at ACP. In this situation the benefit for the skyrmion manipulation is double: the mobility is maximum and the skyrmion moves only along the desired direction. For STT driving force, it is possible to see that Θ_S does not vanish at all and is even maximum just before ACP. At this point, the skyrmion just moves transversely to the current flow. After this point it moves opposite to the current direction. As for a DW, this behavior depends of the β term: the maximum of deflection occurs where $\alpha = -\frac{1}{\beta} \left(\frac{2\Delta}{R}\right)^2$. Considering the variation of the effective α, it occurs before the ACP (where it is negative). The full lines corresponds to calculations considering $\beta = 0.2$ and the dashed lines $\beta = 0.6$. It is possible to verify that for larger β, the maximum of deflection occurs at higher $\%Co$ than ACP. It is also possible to see that the deflection also vanishes, but above the ACP, where $\beta = \alpha$. Note that, at in this configuration, $\Theta_S = \pi$, $i.e.$ the skyrmion moves against the the electron flow. For $\beta = 0$: the topological deflection diverges ($i.e.$ $\Theta_S = \frac{\pi}{2}$) at the ACP and never vanishes for the STT-driven skyrmion.

The vanishing of the topological deflection of ferrimagnetic skyrmions driven by SOT has already been observed in GdFeCo multi-layer stack [22] or more clearly measuring the deflection of chiral bubble in GdFeCo thin film [21]. However, the manipulation of these skyrmions is still challenging [22].

2.7 Contribution and publications

2.7.1 Collaborations

All the presented work in this section was done in our laboratory. The micromagnetic numerical simulations were performed using the collaborative *Mumax3* software [177].

2.7.2 Publication

This work will be presented in an upcoming article grouping both analytical and numerical results: the effective approach of ferrimagnets, the DW dynamics map, the transient regime and the finite coupling approach. Note that few of these results were predictive and just recent experimental measurements validate this model.

Combined effects of field and spin transfer torque in the creep regime

In this chapter, the efficiency of the spin transfer torque in ferrimagnets is investigated. STT occurs when a polarized current traverses a non-uniform magnetization, which means the only way to measure it is to observe the dynamics of a magnetic texture, which complexifies its measurement. Furthermore, STT is typically small in amplitude and its determination requires a large current density which induces a strong heating of magnetic patterned devices. In this study, the non-linearity of the creep regime is used to exacerbate both effects of current: heating and STT. A new analysis of velocity is then used to separate the amplitudes of these two effects. In section 3.3, the DW motion in creep driven just by field is investigated in order to characterize creep dynamics properties of the DW propagation. In section 3.4 the DW motion driven by combined field and current is observed. Using an equivalent field approach (see section 3.4.2), it is possible to separate the two main current effects: Joule heating (see section 3.5) and spin torque effect (see section 3.6).

3.1 Spin transfer torque in ferrimagnets

In the absence of a heavy metal adjacent layer, the main mechanism for current-induced DW motion is the relaxation of a spin current in the magnetic structure. If the current is polarized inside the magnetic material, we speak about STT. As detailed in chapter 3.1, the efficiency of the polarized current action on a magnetic texture is proportional to u, a drift speed [131]:

$$u = \gamma_0 \frac{\hbar}{2e} \frac{1}{\mu_0 M_S} P J \tag{3.1}$$

with P is the spin polarization of the current and J its density. M_S is the net magnetization of this medium and γ_0 is the gyromagnetic ratio. In ferromagnetic transition metals that are often studied, P and M_S share the same physical origin and so the same dependence in temperature, and therefore the ratio P/M_S which governs the STT efficiency is fixed [192]. In contrast, in RE-TM ferrimagnets, as said in section 1.1.3, the current polarization is mostly due to valence electrons (TM) whereas the net magnetization M_S is the sum of all moments (RE and TM) which gives a vanishingly small magnetization and yet a sizable spin polarization.

As said in part. 2.2.2, it is challenging to measure the STT efficiency without dynamic effects which are dominant. A few results exist showing clearly current-driven DW motion in ferrimagnetic thin films via STT, however, only in the quasi-static situation where the DW can be considered as fixed [155, 193]. Li *et al.* measured the depinning field (or 'pinning field') and the depinning current required to induce DW motion in a TbFeCo 8 μm-wire (Fig. 3.1 (a)). In order to change the pinning strength, they change the thickness of the film (from 30 nm to 60 nm) and, by interpolating depinning field and current, they

extract an STT efficiency of $1.08 \times 10^{-3} \frac{mT}{GA/m^2}$ (Fig. 3.1 (b)). Ngo *et al.* directly measure the current-driven DW motion in a TbFeCo wires ($20nm$ thick and width from 0.8 to $1.5\mu m$) (Fig. 3.1 (c)). They measured a non-linear velocity law with mobility around $\mu = 0.16 \frac{m/s}{GA/m^2}$ (Fig. 3.1 (d)). Finally, both efficiency and mobility of DWs driven by STT are relatively promising if we compare to ferromagnetic materials at room temperature: $\lesssim 10^{-3} \frac{mT}{GA/m^2}$ [165]. However, in both experiments, high current densities were applied in thick magnetic wires, which induces a strong heating, not taken into account in the analysis.
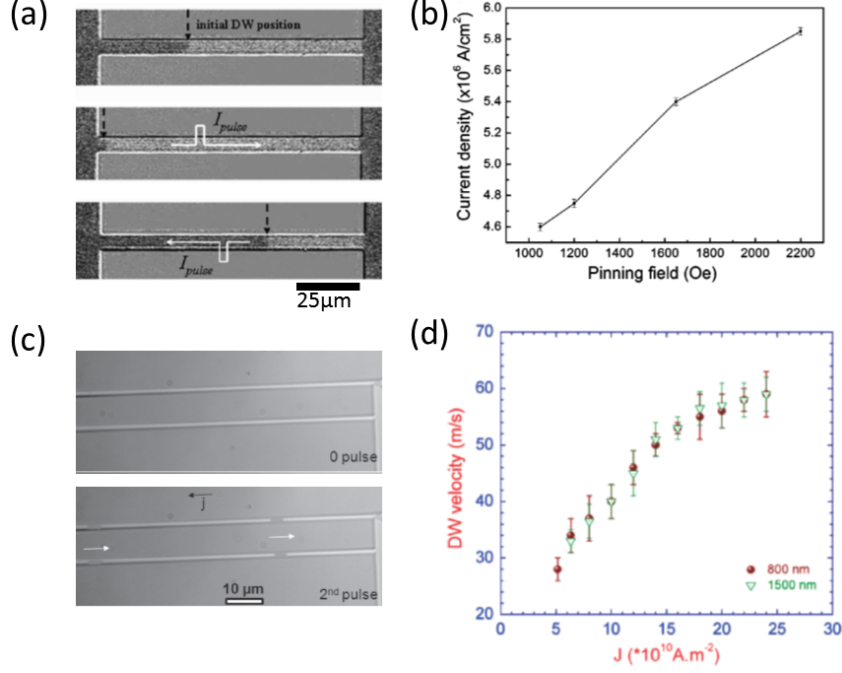
Figure 3.1 – Main results of the DWM driven by current via STT mechanism from Li et al. [155] in (a) and (b): in (a) it is possible to see subtracted Kerr images of DWM after depinning under current along a 8 μm magnetic wire and in (b) the evolution of the current density required to induce DWM vs perpendicular field required to induce DWM. Results from Ngo et al. [193] in (c) and (d): in (c) it is possible to see substracted Kerr images of DWM under current along magnetic wire of 8 μm and in (d) the velocity of the DW versus the current density.

Here, we use the non-linearity of the DW velocity in the creep regime to measure both expected effects of current (heating and STT). Even if previous studies of the creep regime in current-driven DWs lead to non-consensual interpretations [194–196], here we propose a robust analysis based on creep theory [197] to distinguish both current effects. The challenge is double: measure very low effects of STT in magnetic wires and account fully for the Joule heating in a dynamical regime that relies on thermal activation.

3.2   Sample parameters

The studied film is a 7 nm-thick amorphous $Tb_{21}Fe_{79}$ alloy with 5 nm Al caping layer deposited by co-evaporation on a Si/SiO_x (500nm) substrate (see part 1.2). The film was characterized by Magneto-optic Kerr Effect (Kerr) and Anomalous Hall Effect (AHE) resistivity measurements (see part. 1.3). Both effects are mainly proportional to spin-polarization of electrons at the Fermi level (equivalent to P) for the considered photon energy [30, 63]. The net magnetization M_S was measured by Vibrating Sample Magnetometry (VSM). The polarization and magnetization results are shown in Fig. 3.2 (a) as a function of temperature. From the orientation of Hall and Kerr loops, it is possible to say that the alloy is Fe dominated and that the magnetic compensation temperature is well below the smallest

experimental temperature range and was not observed (so that, if it exists, $T_{MC} < 50$ K). The Curie temperature is 375 K. Despite being quite noisy ($\mu_0 M_S \approx 0.3$T at room temperature), M_S exhibits a thermal evolution obviously different from that of P. We performed mean field calculations of coupled RE and TM sub-lattice magnetizations (as detailed in part. 1.1.3). The temperature evolution of the AHE and Kerr data was adjusted to match to the TM magnetization (considering a corrective factor). The net magnetization curve superimposed naturally on the experimental VSM data. The main feature extracted from Fig. 3.2(a) is that P/M_S is larger than in usual ferromagnets. Note that in this sample, the investigated temperature range is far from T_{MC} (if it exists) so that the ferrimagnetic alloy can just be considered as a classical ferromagnetic material with non-diverging parameters in the investigated temperature range (above the room temperature).
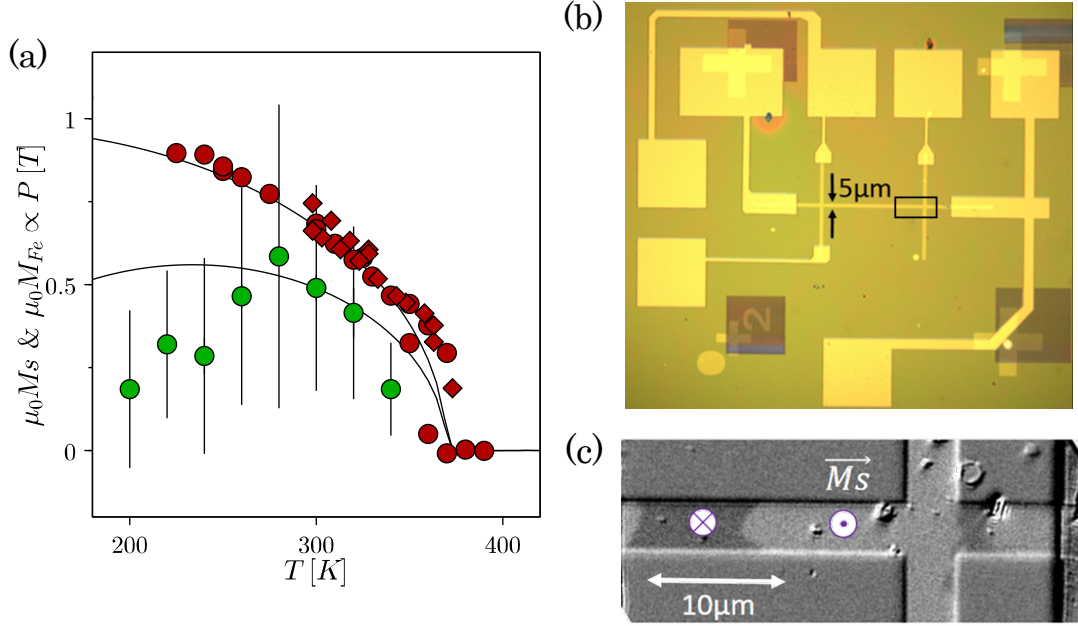
Figure 3.2 – Magnetic properties of the TbFe film in temperature and micropatterned tracks for STT experiments. (a) Magnetic properties of TbFe film versus temperature. Green circles correspond to the net magnetization M_S obtained from VSM, red diamonds correspond to MOKE amplitude, and red circles to Hall resistivity. The continuous lines correspond to the theoretical net magnetization and magnetization of the Fe sub-lattice calculated *via* the mean field approach. MOKE and Hall amplitude values are renormalized by an arbitrary prefactor to overlap experimental data on the associated theoretical curve. (b) Optical image of the patterned magnetic $5\mu m$ wire. (c) Kerr image of magnetic domains in the wire. Orientations of the net magnetization associated to each gray domains are not by the purple arrows.

In order to inject large current densities, the sample is structured in tracks of 5 μm width by electron beam lithography and Ar$^+$ ion beam etching (Fig. 3.2(b)). Contacts made of Ti(5 nm)/Au(50 nm) are deposited and connected to a voltage pulser. However, the high resistance of the wire limits the current density: $V_{max} = 100V \rightarrow J_{max} \approx 100$ GA/m^2. The sample is fixed on a heater with an integrated temperature control which keeps the sample temperature at a set-point noted T_{SP}. To observe directly the DW motion (Fig. 3.2(c)), we use a commercial Kerr microscope [100].

3.3   Domain wall motion driven by field

To determine the dynamic regime of the DWs, we first measure the velocity under continuous perpendicular field (without current, $J = 0$) at different set-point temperatures T_{SP}. The velocity of the field-driven DW is shown in Fig. 3.3. We observe a nonlinear behavior of velocity *versus* the applied field

and a strong dependence on T_{SP}. This DW dynamics is characteristic of the creep regime.

The creep regime is one of the possible DW propagation regimes which can occur when the DW moves in a non-negligible pinning potential [197, 198]. In this regime, the DW is pushed by the field and its motion occurs by thermally activated discrete hopping between pinned configurations below a critical depinning field H_d [199]. Considering the DW motion in this pinning landscape, its velocity can be described by an Arrhenius law (Eq. 3.2), with v_0 a prefactor homogeneous to a speed, k_B the Boltzmann constant, $k_B T_d$ the pinning barrier amplitude and ΔE the energy barrier. Jeudy *et al.* show that this energy barrier follows a universal behavior which depends just on few creep parameters H_d, T_d, v_0, and on the dimensionality of the system [197, 200]. In our case, the DW motion through a pinning potential can be associated to a motion of a 1D elastic interface in a 2D media which yields [197, 200]:

$$v_{creep}(T,H) = v_0 \exp\left(-\frac{\Delta E}{k_B T}\right) \text{ with } \Delta E = k_B T_{dep}\left(\left(\frac{H}{H_{dep}}\right)^{-1/4} - 1\right) \tag{3.2}$$

Plotting velocity in logarithmic scale and the field in $H^{-1/4}$ scale (Fig. 3.3 (c)), the expected behavior is obtained: $\ln(v) \propto H^{-1/4}$.
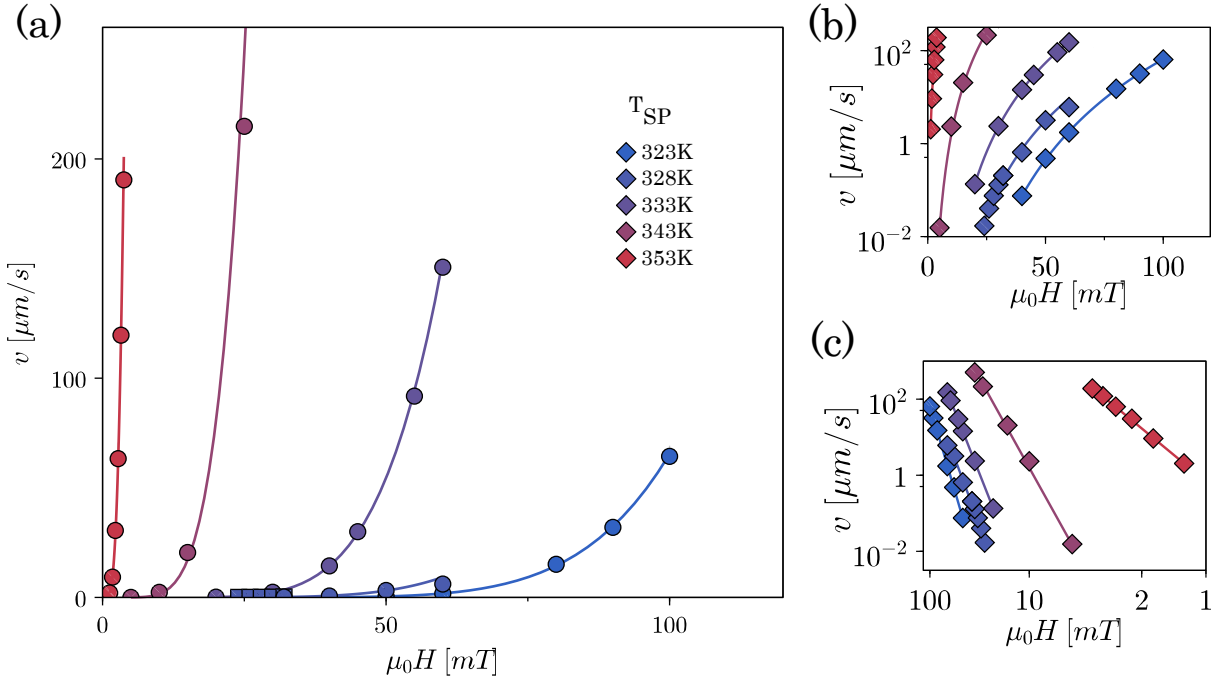
Figure 3.3 – (a) DW velocities v versus applied field $\mu_0 H$ for different T_{SP}. (b &c) The same data are plotted in different scales: (b) $Log_{10}(v)$ vs $\mu_0 H$ and (c) $Log_{10}(v)$ vs $(\mu_0 H)^{-1/4}$. Lines correspond to fits using Eq. 3.3.

All the three parameters v_0, T_d and H_d are *a priori* temperature-dependent whatever the material [197]. Moreover, in our sample, the impact of temperature is exacerbated by the strong dependence of its magnetic properties. Furthermore, our measured velocity data does not cover a sufficiently large range needed to determine unambiguously all these three parameters and various combinations of very different v_0, T_d and H_d produce valid fits. To overcome this issue, we consider two effective parameters C_V and C_H which combine v_0, T_d and H_d. They are homogeneous to a velocity and to the inverse of a field such as:

$$v_{creep}(T,H) = C_V e^{-(C_H H)^{-1/4}} \tag{3.3}$$

These two parameters can be associated with the reduced creep parameters:

$$C_V = v_0 e^{\left(\frac{T_d}{T}\right)} \text{ and } C_H = \frac{1}{H_d}\left(\frac{T}{T_d}\right)^4 \tag{3.4}$$

Considering this compact creep law (Eq. 3.3), it is possible to directly extract C_V and C_H from measured velocities *via* an unambiguous linear regression for each temperature. The temperature dependence of $C_V(T)$ and $C_H(T)$ obtained from the velocities fitting (Fig. 3.3) is shown in Fig. 3.4. They exhibit a large variation with temperature as expected in thermally-activated dynamics in ferrimagnets (as measured in [178]). This means that the DW motion is very sensitive to temperature. Furthermore, the large values of C_V mean that even a small variation in field induces a large change of the DW velocity. In the following part, we use this double sensitivity in temperature and in field to exacerbate effects of an electrical current on the DW dynamics.
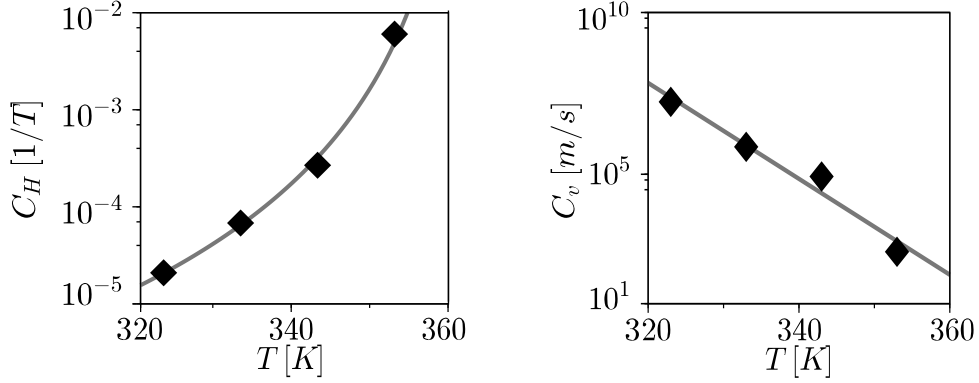
Figure 3.4 – Creep parameters $C_H(T)$ and $C_V(T)$ versus set-point temperature for $(J = 0)$. The solid lines are polynomial fits used in the following fitting process.

3.4 Domain Wall Motion driven by combined effects of field and current

3.4.1 STT-like and heating effects of current
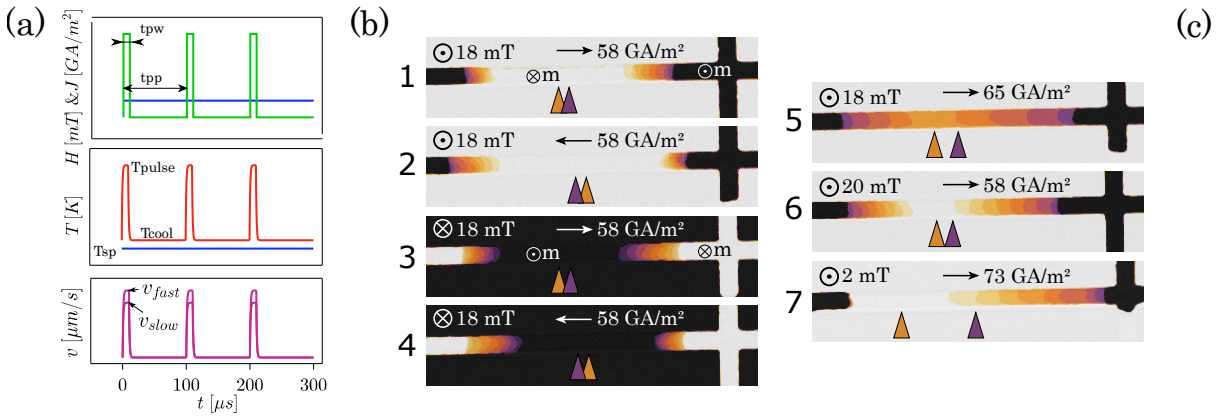
Figure 3.5 – Domain wall motion driven by current and field. (a) Time-line of the experiments and of the corresponding parameters. (b) Illustrative superposition of Kerr images (taken every 0.1 s) at $T_{sp}=328$ K for field and current indicated in each numbered picture. Dark regions (respectively bright) correspond to up (down) magnetization. A sequence of magnetic fields was used to nucleate and drive two DWs to the initial configuration. The purple triangle represents the central position of the initial domain. Following images appear with an orange contrast and the center of the remaining central domain is illustrated by an orange triangle. The difference $v_{fast} - v_{slow}$ is directly illustrated by the distance between both markers

.

Next, we measured DW motion induced by the combined effects of current pulses superimposed with continuous perpendicular magnetic field. The current pulses were $t_{pw} = 10\ \mu$s long with a $t_{pp} = 100\ \mu$s period at a temperature set-point of T_{sp}=328 K, as detailed in the timeline Fig. 3.5(a). Before each measurement, a field sequence is used to prepare the wire with two DWs at each extremity and a central domain. Fig. 3.5(b) shows a false-color juxtaposition of a series of typical Kerr images of DW motion taken with an image period between 0.1 s and 1 s depending on the DW velocity. All measurements were repeated for the two current directions, up or down central domain magnetization, and +/- field. For each configuration of H and J, we distinguish a fast and a slow DW with velocity v_{fast} and v_{slow}. The initial position of the middle of the central domain is indicated by a purple triangle and the final position is marked by an orange triangle. The difference $v_{fast} - v_{slow}$ is directly linked to the relative positions of both triangles. If the current is reversed, the fast DW becomes the slow, and *vice-versa* (as can be seen comparing images 1 and 4 in Fig. 3.5(b)). If the current density is increased (image 1 *versus* 5), the difference $v_{fast} - v_{slow}$ increases, but also v_{fast} and v_{slow}. If the applied field is increased (1 *versus* 6), both v_{fast} and v_{slow} increase, but also the difference $v_{fast} - v_{slow}$. Actually, with these measurements, it is possible to directly observe the two main effects of current on the DW motion. First, Joule heating modifies the creep dynamics and makes DW motion faster in both directions. This is why in 1 *versus* 5, both DWs were faster. Second, an STT-like action pushes DWs along the electron flow and adds or subtracts to the field action. This is why in 1 *versus* 5 the difference $v_{fast} - v_{slow}$ is larger. From 1 *versus* 6, both velocities increase but the fact that $v_{fast} - v_{slow}$ increases as well demonstrates the non-linearity of velocity versus current and field: a small modification of the applied forces on the DW has a larger effect if the initial force is high than if it is low. If the applied magnetic field is decreased and the current increased (1 *versus* 7), both effects are larger.

We reproduce these measurements changing applied field and current keeping a temperature set-point of T_{sp}=328 K. Fig. 3.6(b) shows velocities as a function of H for a few values of J. For all the configurations with the same $|H|$ and $|J|$, all v_{fast} are the same (as well as all v_{slow}) and the average value is shown for clarity. For a given (H, J), two points are depicted but each pair is the results of 8 independent experiments ($\pm H$; $\pm J$; up-down/ down-up walls). Both effects of the current are directly observable: the STT-like action separate velocities of fast and slow DW and heating increase the mean velocity. Furthermore, due to non-linearity of the creep law, for a given current density, effects are more visible for high field.
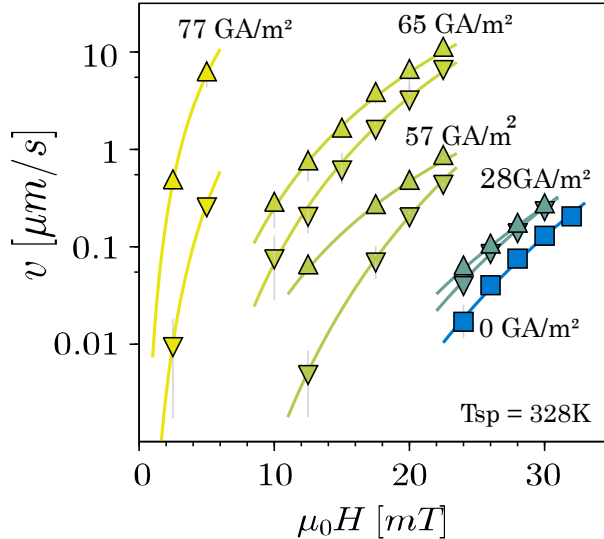
Figure 3.6 – Velocity (v_{fast} up-triangles/ v_{slow} down-triangles) versus H at different J and at T_{sp}=328 K (in agreement within the conditions given FIG.3.5: continuous field and pulsed current at t_{pw}=10μs and t_{pp}=10t_{pw}). Continuous lines are fitted using the creep law given by Eq. 3.3 as discussed below.

.

3.4.2 Equivalent field approach of the spin transfer torques

To quantify the action of the current, we consider an effective field H_{eq}, equivalent to the STT-like action on the DW. This H_{eq} is the field required to induce the same macroscopic DW motion as a given current density. As explained, a small variation of the resulting field applied to the DW $H \pm H_{eq}$ is exacerbated by the creep dynamics. To extract the values of H_{eq} from fitting of measured velocities, a more complex velocity law has to be considered. This one considers the two alternating parts of the DW motion: during the current pulse and between pulses, and we consider that the measured velocity is the average of both parts. During the t_{pw}-long current pulse, both the current and the field act on the DW with a force $H \pm H_{eq}$ depending of J, and the wire heats up to a temperature T_{pulse} depending of $|J|$. Between pulses, during the period of $t_{pp} - t_{pw}$, the field acts on the DW and the wire cools down to a temperature T_{cool} (possibly depending of the previous heating T_{pulse}) (see Figs. 3.5(a)). We take the approximation that the temperature during the pulses and between the pulses is constant (a hypothesis that we will examine later). Therefore, for each value of $|J|$ and each one of four configurations ($\pm H$; $\pm J$; up-down/ down-up walls), we fit the measured velocities with the compact creep law (Eq. 3.6):

$$\langle v \rangle (H, J) = \frac{t_{pw}}{t_{pp}} v_{creep}(T_{pulse}, H \pm H_{eq}(J)) + \frac{t_{pp} - t_{pw}}{t_{pp}} v_{creep}(T_{cool}, H) \tag{3.5}$$

Note that here, T_{pulse} and *a priori* T_{cool} also depend on the current. As C_V and C_H are temperature-dependent, this becomes

$$\langle v \rangle (H, J) = \frac{t_{pw}}{t_{pp}} C_{V(T_{pulse})} e^{-(C_{H(T_{pulse})}(H \pm H_{eq}))^{-1/4}} + \frac{t_{pp} - t_{pw}}{t_{pp}} C_{V(T_{cool})} e^{-(C_{H(T_{cool})}H)^{-1/4}} \tag{3.6}$$

In this model, the sign $\pm$ before H_{eq} corresponds to electron flow opposed or along the field induced propagation. As the evolution with temperature of C_V and C_H is known (Fig. 3.4), the fitting procedure only has three fitting parameters (per value of $|J|$): T_{pulse}, T_{cool}, and H_{eq}. We have assumed two reasonable fit bounding conditions: that $T_{pulse} > T_{cool} > T_{sp}$, (within a 1 K tolerance) and that the heating amplitude, $\Delta T = T_{pulse} - T_{cool}$, follows within a 50% margin a Joule heating law $\Delta T = \kappa J^2$. The determination of κ is independent of the DW motion and is described in the following section. This last bounding condition is very loose, and does not bind the fitted parameters nor their evolution with J except at very low currents, where it leads to a reduced dispersion of the fitted parameters and imposes $T_{pulse} - T_{cool} \to 0$ when $J \to 0$. The simultaneous fits of v_{fast} and v_{slow} are solid lines in Fig. 3.6.

In the following parts, the two effects of the current on the DW dynamics (STT-like and heating) are detailed.

3.5 Joule heating

We first comment on the temperatures T_{pulse}, T_{cool} deduced from the fits and shown in Fig. 3.7(a). The temperature during the pulse T_{pulse} increases quadratically with the current density, as expected for a Joule heating phenomenon (with a heating parameter of $\kappa = 5.3 \times 10^{-3}$ K/(GA/m^2)^2). The variation of several tens of degrees reveals the significance of the Joule heating. On the contrary, the values obtained for T_{cool} are very close to T_{sp}. It possible to see a small dependence on the current density due to the non-zero cooling time. However, for large current values, there are some points that deviate from T_{SP}. At large J, $T_{pulse} \gg T_{cool}$ and the velocity during the current pulse dominates the time averaged measured velocity. Therefore, the temperature T_{cool} at high J does not affect the measured velocity, and the fitted T_{cool} is neither accurate nor relevant. On the contrary, the values obtained for T_{cool} for small J are accurate and relevant.

Fig. 3.7 (b) shows the creep parameters C_V and C_H versus current deduced from the fitted T_{cool} and T_{pulse} (red and blue points and bottom axis), juxtaposed to the $C_V(T)$ and $C_H(T)$ at zero current (grey lines and top axis, from Fig. 3.4). The temperature axis was scaled relatively to the current axis according to the heating law obtained before. C_v and C_H change by several orders of magnitude due to the Joule heating, showing its very large effect on the dynamics of a creeping DW. As expected and observed, current pulses induce strong Joule heating in our magnetic wire. As explained, this increase

in temperature has a major impact in the thermally-activated creep regime. Therefore, a precise knowledge of the temperature profile is required to avoid misinterpreting the data when dealing with DWs in the creep regime. To characterize Joule heating independently, we have determined two features: its amplitude and its time profile.
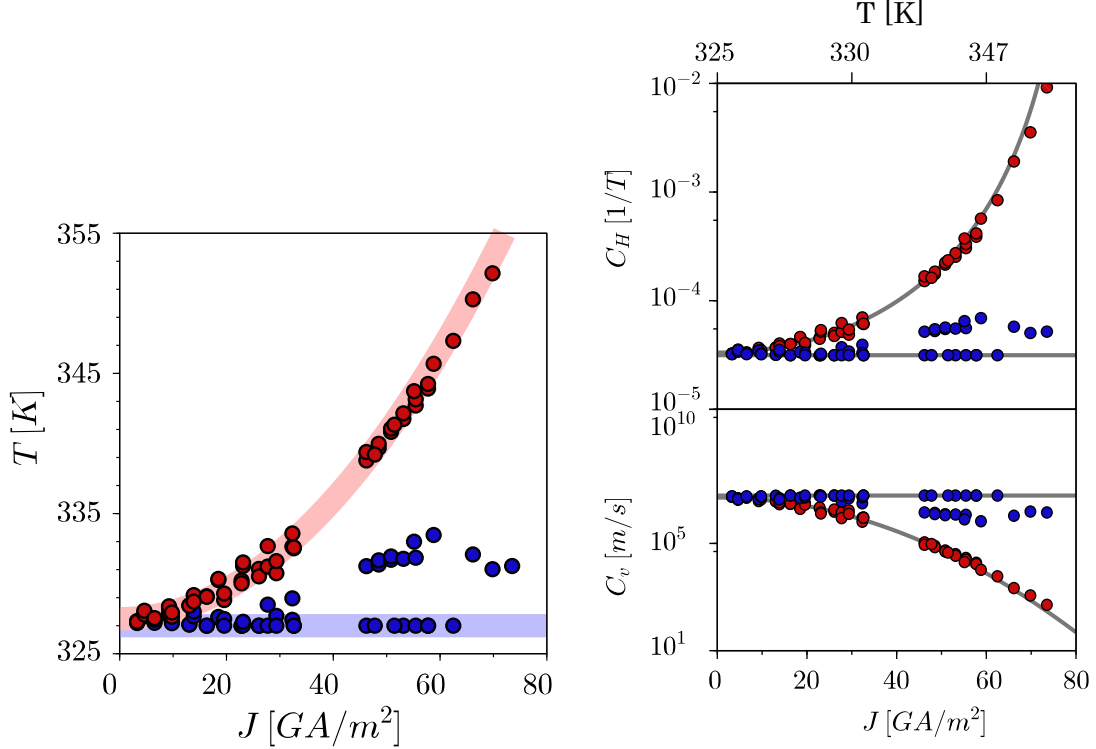
Figure 3.7 – (a) T_{pulse} and T_{cool} extracted from Fig. 3.6 as a function of the current density J. The light red line corresponds to the Joule heating amplitude determined experimentally and the blue one to the set-point temperature. (b) Reduced creep parameters C_H and C_V as a function of current density (bottom axis) and temperature (top axis), using the temperatures extracted from (a). The lines represent $C_H(T_{sp}, J = 0)$ and $C_V(T_{sp}, J = 0)$ determined without current for different T_{sp} shown in Fig. 3.4.

Amplitude of Joule heating We investigate the amplitude of Joule heating in the wire *versus* current density. We measure hysteresis loops under field by the Kerr effect on the same magnetic wire than previous measurements (shown Fig. 3.5 (b)). We compare loops at different sample holder temperatures (323 K < T_{SP} < 353 K) and zero current ($J = 0$) (shown Fig. 3.8(a)) with loops at fixed sample holder temperature ($T_{SP} = 323$ K) for different current densities ($0 < J < 70$GA/m^2) (shown Fig. 3.8(b)). With this method, the magnetic wire is saturated and there is no magnetic textures so the current does not exert any STT and we just measure the heating amplitude. Our microscope is not calibrated in Kerr amplitude, so we choose an arbitrary scale. Furthermore, its lenses are sensitive to the Faraday effect, which induces a loop deformation. However, the coercive field of the loops H_C are not affected by these two effects. We superimposed the coercive fields of these two sets of loops considering the law $T_J = T_{sp} + \kappa J^2$ to overlap both coercive field values as shown Fig. 3.8(c). The best match is obtained for $\kappa = 5.3 \times 10^{-3}$ K/(GA/m^2)^2. This value is used to plot the red envelope in Fig. 3.7(a) which shows the good agreement between heating amplitude extracted by this method and heating extracted by velocity analysis.
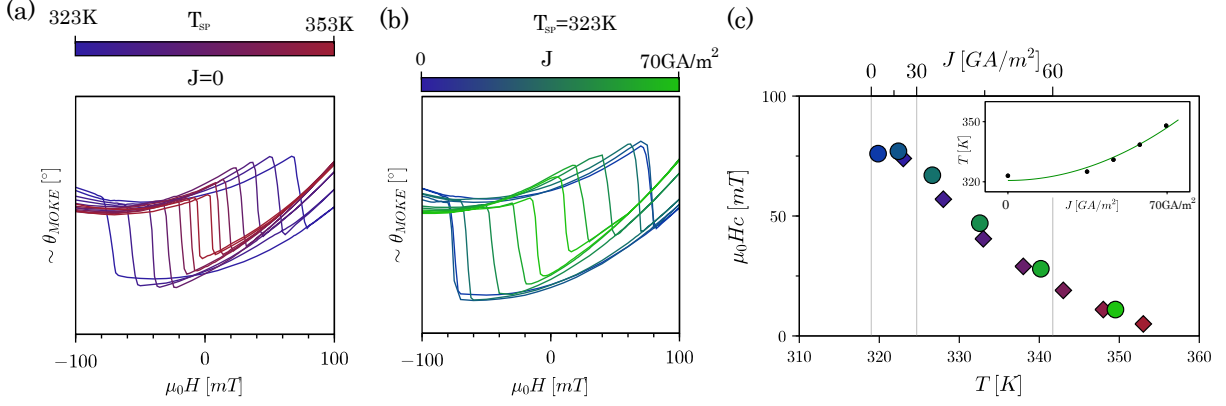
Figure 3.8 – Evolution of Kerr hysteresis loops without current for increasing temperatures (a) and at fixed set-point temperature with increasing current density (b). (c) Coercive fields as a function of temperature (bottom axis) and current density (top axis; quadratic scale) allowing to determine the relation between T, T_{sp} and J. The insert shows the extracted heating law: black dots are from coercive interpolations ($H_c(T, J = 0) \leftrightarrow H_c(T = 323K, J)$) and the line is the heating law with a heating parameter $\kappa = 5.3 \times 10^{-3} \mathrm{K}/(\mathrm{GA/m}^2)^2$.

Time profile of heating effects To characterize the heating rising time, we measured the DW velocity under combined effects of field and current at fixed temperature set-point T_{sp}=328 K and fixed current density but, now, with current pulses of variable width t_{pw} and period t_{pp}. As before, we just measure the mean speed $\langle v \rangle$ after many current pulses. The idea is to reconstruct the time profile of the temperature $T_J(t)$ using the mean velocity $\langle v \rangle$ for different pulse width t_{pw}. Figure 3.9 (a) shows the DW velocity of fast and slow DWs for a field of 16mT and a current amplitude of 53GA/m^2 measured for different pulse width t_{pw} from 100 ns up to 5 s. For all measurements we adjust the pulse period such as $t_{pp} = 10 \times t_{pw}$.

It is possible to decompose the mean velocity (Eq. 3.7) in two parts: the velocity v_{pulse} during the current pulse t_{pw} (with an additional field H_{eq} and with modified creep parameters) and the velocity v_{cool} during the cooling time $t_{pp} - t_{pw}$ (with just modified creep parameters due to cooling):

$$\langle v \rangle (H, \pm J) = \frac{1}{t_{pp}} \int_0^{t_{pp}} v(H, \pm J(t), T(t)) \, dt \tag{3.7}$$

$$= \frac{1}{t_{pp}} \overbrace{\int_0^{t_{pw}} v(H, \pm J, T(t)) \, dt}^{v_{pulse}} + \frac{1}{t_{pp}} \overbrace{\int_{t_{pw}}^{t_{pp}} v(H, 0, T(t)) \, dt}^{v_{cool}}$$

Taking the difference $\Delta v(t)$ between $\langle v \rangle_{fast}$ and $\langle v \rangle_{slow}$ enables to remove the v_{cool} contribution:

$$\Delta \langle v \rangle = \langle v \rangle (H, +J) - \langle v \rangle (H, -J) = \frac{1}{t_{pp}} \int_0^{t_{pw}} v(H, +J, T(t)) - v(H, +J, T(t)) \, dt = \frac{1}{t_{pp}} \int_0^{t_{pw}} \Delta v(t) dt \tag{3.8}$$

For a fixed H and J, $\Delta v(t)$ only depends on T and is monotonous with T. Therefore, the rise time of $\Delta v(t)$ is approximately the same as that of $T(t)$ (as illustrated in the insert Fig. 3.9(b)):

$$\Delta v(t) = v(H, +J, T(t_{pw})) - v(H, -J, T(t_{pw})) \approx \frac{\partial \Delta \langle v \rangle}{\partial t_{pw}} t_{pw}$$

Fig. 3.9 (b) shows the experimental $\Delta v(t_{pw})$ calculated from $\langle v \rangle_{fast}(t_{pw})$ and $\langle v \rangle_{slow}(t_{pw})$ in Fig. 3.9(a). When $\Delta v(t)$ no longer changes with t_{pw}, it implies that the temperature does not change either. It is important to note that we used a constant duty cycle (here t_{pw}/t_{pp}=10%), so that the temperature at the beginning of every pulse is the same and does not vary with the pulse width t_{pw} [201]. Then, we can see that the heating time is about 2.5μs (Fig. 3.9(b)). This results is in agreement with theoretical studies [201–204].
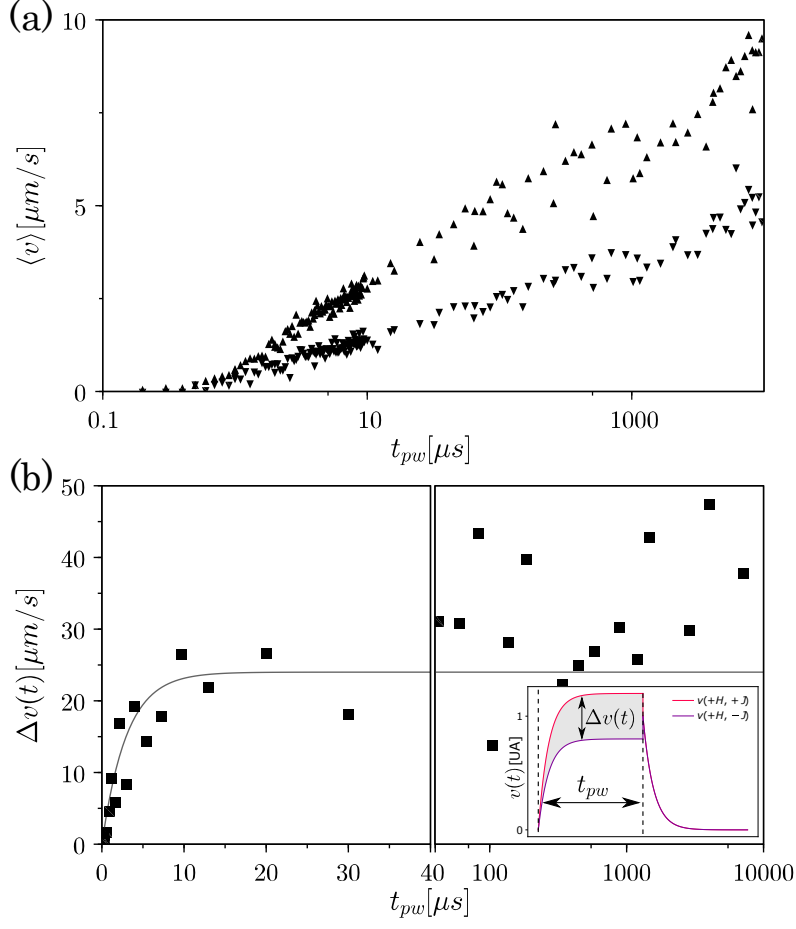
Figure 3.9 – (a) Evolution of the mean velocity of fast and slow DWs ($\langle v \rangle_{fast}$ up-triangles and $\langle v \rangle_{slow}$ down-triangles) as a function of t_{pw}. (b) Instantaneous velocity difference. Note the change in the time scale around 40 μs (linear/log). The gray line corresponds to a rising exponential law with a rise time of 2.5 μs. The insert shows a sketch of fast and slow DW velocities that enables to extract the heating time from Δv.

With this method, we extracted the heating time from DW velocities and considered that the characteristic time to reach the uniform regime is dominated by the heating. However, other phenomena (as pinning, non-perfect square current pulses etc.) can increase this rise time and lead to an overestimation of the heating time. The extracted characteristic time is still well shorter than the used t_{pw}, that is why it is possible to consider a square evolution of temperature and approximate the temperature time profile by two constant temperatures, T_{pulse} during the current pulse and T_{cool} in-between, as we have done.

In this section, we propose a robust method to measure both STT and heating effect of current considering them as independent parameters of the modify creep law. We do not constrain drastically any of them and we validate the extracted heating amplitude with an independent method.

3.6 Spin transfer torque

3.6.1 Strength of H_{eq} from the velocity fit

Firstly, a strong efficiency of SST-like effect is demonstrated by the adjusted H_{eq} values shown Fig. 3.10. We measure a ratio $H_{eq}/J \approx 2\cdot10^{-2}$ mT/(GA/m^2) , which is large if we compare to other more conventional materials (same units): $5\cdot10^{-4}$ for NiFe [205] and $3\cdot10^{-7}$ for FePt [206]. It is about the same value as reported at low temperature for Pt/Co/Pt [207] (a few 10^{-2}). Above 300 K, H_{eq} reaches the large value obtained for the archetypical (SOT-driven) Pt/Co/AlOx [167]. As expected, we observe that the H_{eq} increases with current. Despite the values of H_{eq} being extracted from fits of DW velocity for many values of field, and derived from the same range of DW velocities, the accuracy of our H_{eq} data is worse at low current. In this case, $T_{pulse} \approx T_{cool}$ and the measurement is dominated by the 9 times longer period between pulses that carries no information on H_{eq}. The current dependence of H_{eq} is discussed in following.
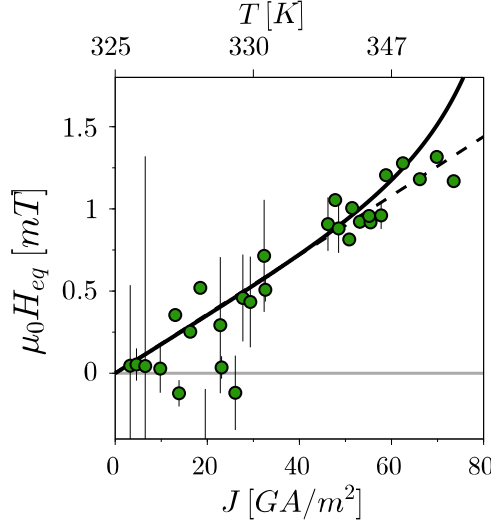
Figure 3.10 – H_{eq} versus J averaged for each value of $|J|$. The solid line corresponds to a single behavior over the entire current range considering $u(T)/J \propto P/M_s$ as determined in Fig. 3.2. The dotted line corresponds to the situation where P/M_s is constant. The current (bottom axis) and temperature (top axis) are related using the Joule heating amplitude.

3.6.2 Model 1D $q - \varphi$ with (and without) pinning

To understand the evolution of H_{eq} in our system where a creep behavior is observed, we extend the common 1D $q-\varphi$ model [131] (see part. 2.3.1.1) to describe a pinned DW [206,208–210]. To take pinning into account, we consider an additional energy expressed by a space-dependent surface pinning potential $\sigma_{pin}(q,\varphi)$. Minima of σ_{pin} correspond to preferential positions for the DW in the (q,φ) space and play the role of pinning centers. In the creep regime, far from the depinning transition (for $H \ll H_d$), the DW is blocked in pinned configurations most of the time and the macroscopic DW velocity is mostly determined by the thermal depinning rate as an Arrhenius law with a characteristic hopping time of: $\frac{1}{\tau} \propto e^{-\frac{\Delta E}{k_b T}}$. This depinning rate is a function of the energy barrier ΔE to get out of the trap and to reach the next stable pinned configuration in a surface energy landscape σ_{pin} (with $\Delta E \propto \Delta\sigma_{pin}$). Implementing this pinning surface energy, the $q - \varphi$ model becomes:

$$
\begin{cases}
\alpha\frac{\dot{q}}{\Delta} + \dot{\varphi} & = \gamma_0 \left(H - \frac{1}{2\mu_0 M_s}\partial_q\sigma_{pin} \right) + \beta\frac{u}{\Delta} \\[2mm]
\frac{\dot{q}}{\Delta} - \alpha\dot{\varphi} & = \gamma_0 \left(H_{BN}\frac{Sin(2\varphi)}{2} + \frac{1}{2\Delta\mu_0 M_s}\partial_\varphi\sigma_{pin} \right) + \frac{u}{\Delta}
\end{cases}
\tag{3.9}
$$

Note that here, no DMI effect is considered since the absence of adjacent heavy-metal layer and the temperature range (far from the T_{MC}). At the equilibrium position of the DW in the trap energy potential,

the DW is pinned and its velocity is zero: $\dot{q} = 0$. Considering these equations, it is possible to see that the field just pushes the DW inside the pinning well (increasing q) up to the equilibrium configuration. In contrast, the current has two actions: it pushes the DW (as the field) but it also rotates the DW (changing φ) via respectively non-adiabatic and adiabatic STT torques (see Fig. 3.11(b)). As the DW is in a minimum of energy, both actions decrease the energy barrier $\Delta\sigma_{pin}$. Furthermore, changing φ, it modifies the trajectory of the DW in the pinning potential as discussed in the next paragraph.
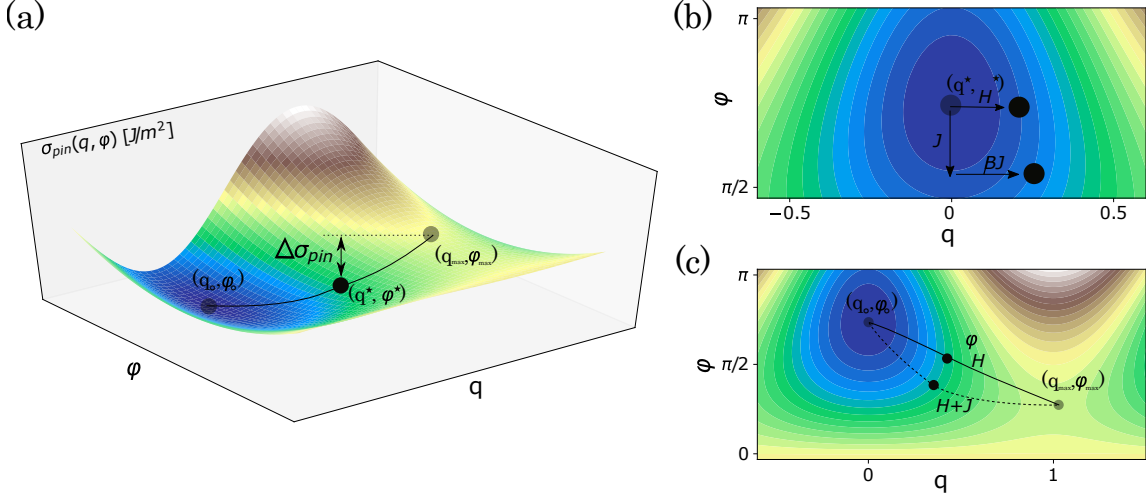
Figure 3.11 – Sketch of a DW configuration in the surface pinning energy landscape $\sigma_{pin}(q, \varphi)$. The black dot corresponds to the DW configuration at the equilibrium between pinning and applied field and current $(q^\star, \varphi^\star)$. Gray dots correspond to the minimum (q^0, φ^0) and to the maximum (q^{max}, φ^{max}) of pinning energy. The thin lines corresponds to one of possible depinning trajectories under H and J. (a) Example of a DW trajectory in the pinning potential under H and J. (b) Torques felt by the DW under applied field, adiabatic and non-adiabatic STT (written respectively H, J and βJ). (c) Trajectories induced by these torques.

Fig. 3.11 shows the DW configuration in the pinning potential $\sigma_{pin}(q, \varphi)$. The field and the current action deviate the DW configuration from the minimum of energy written (q^0, φ^0) up to the stable position $(q^\star, \varphi^\star)$. At this point, the depinning rate depends of the energy barrier $\Delta\sigma_{pin} = \sigma_{pin}(q^{max}, \varphi^{max}) - \sigma_{pin}(q^\star, \varphi^\star)$ where (q^{max}, φ^{max}) is the saddle point associated to the depinning.

3.6.3 Pinning potential dependant only on q: Precession of pinned DW

In a first approach, it is possible to consider a low angular dependence of the pinning energy compared to demagnetization effects ($\partial_\varphi \sigma_{pin}/\Delta << \mu_0 M_s H_{BN}$). The first equation of Eq. 3.9 directly shows the linearity between the applied field H and the drift speed u associated with the non-adiabatic action of the current. That further supports the fact that it is possible to consider the STT as a field equivalent to the current action H_{eq}. This equivalent field is proportional to J. Furthermore, the second equation of Eq. 3.9 gives a Walker condition depending on u. Surprisingly, two different behaviors of pinned DWs can still be predicted: a steady one where $\dot{\varphi} = 0$ (at low current) and a precessional one where $\dot{\varphi} \neq 0$ and $\langle\varphi\rangle = 0$, for high u above a Walker-like threshold u_W^{pin} independent of the applied field:

$$u_W^{pin} \approx \frac{1}{2} H_{BN} \gamma_0 \Delta \tag{3.10}$$

In the translational regime, for $u < u_W^{pin}$ (i.e $\dot{\varphi} = 0$):

$$\begin{cases} \frac{1}{2\mu_0 M_s} \partial_q \sigma_{pin} &= H + \beta \frac{u}{\gamma_0 \Delta} \\ \varphi^\star &= -\frac{1}{2} ArcSin\left(\frac{2}{H_{BN}} \frac{u}{\gamma_0 \Delta}\right) \end{cases} \tag{3.11}$$

As expected, the non-adiabatic torque of the current $\beta u/\gamma_0\Delta$ is directly added to the field contribution and the adiabatic torque $u/\gamma_0\Delta$ induces an angle of the DW magnetization φ. Here, we do not consider angular variations of σ_{pin} so this effect does not have any consequences on the energy barrier resulting from the equilibrium configuration. In the precessional regime, for $u > u_W^{pin}$ (i.e $\langle\varphi\rangle \approx 0$):

$$\begin{cases} \frac{1}{2\mu_0 M_s}\partial_q\sigma_{pin} & = H + \left(\beta + \frac{1}{\alpha}\right)\frac{u}{\gamma_0\Delta} \\ \dot{\varphi}^\star = -\frac{u}{\alpha\Delta} \end{cases} \tag{3.12}$$

H_{eq} is directly given by Eq. 3.11 for the steady tilted regime ($u < u_W^{pin}$) and Eq. 3.12 for the precessional regime ($u > u_W^{pin}$):

$$H_{eq} = \begin{cases} \frac{1}{\gamma_0\Delta}\beta u & \text{writen } H_{eq}^{<W} \text{ for } u < u_W^{pin} \\ \frac{1}{\gamma_0\Delta}(\beta + \frac{1}{\alpha})u & \text{writen } H_{eq}^{>W} \text{ for } u > u_W^{pin} \end{cases} \tag{3.13}$$

Furthermore, these two dynamic regimes do not exist for a pinned DW under field and only current can induce precession of a pinned or creeping DW *via* adiabatic STT torque since only current acts on φ as shown in Eq. 3.12. Indeed, a DW that precesses continuously dissipates energy, even if it does not move. As such, this precession cannot be induced by a conservative torque like the one of a static magnetic field whereas it can be the case for STT. Finally, it is possible to see that all values of u_W^{pin}, and $H_{eq}^{<W}$ $H_{eq}^{>W}$ are independent of the pinning potential expression (independent of $\partial_q\sigma_{pin}$), meaning that the equivalent field is the same for all pinning centers if $\partial_\varphi\sigma_{pin}/\Delta << \mu_0 M_s H_{BN}$. These calculations are summarized in table. 3.1, in comparison with the results of the free DW situation ($\sigma_{pin} = 0$). To simplify, we consider a simple quadratic energy potential: $\sigma_{pin}(q,\varphi) \approx P_{pin}q^2$ with P_{pin} as a strength parameter. It is possible to see that the increase of H_{eq} in the precessional regime relies on the efficiency of STT-like current action.

	Steady	Walker threshold	Precessional
Free DW	$\dot{\varphi} = 0$ and $\dot{q} \neq 0$		$\langle\varphi\rangle = 0$ and $\dot{q} \neq 0$
$\sigma_{pin} = 0$	$\dot{q} = \frac{\gamma\Delta}{\alpha}(H + \frac{\beta}{\gamma\Delta}u)$	$\left\|H + \frac{\beta-\alpha}{\gamma\Delta}u\right\| \leq \alpha\frac{H_{BN}}{2}$	$\dot{q} = \gamma\Delta\frac{\alpha}{1+\alpha^2}(H + \frac{\beta+\frac{1}{\alpha}}{\gamma\Delta}u)$
	$\sin(2\varphi) = \frac{2}{\alpha H_K}(H + \frac{\beta-\alpha}{\gamma\Delta}u)$		$\dot{\varphi} = \frac{\gamma}{1+\alpha^2}(H + \frac{\beta-\alpha}{\Delta\gamma}u)$
Pinned DW	$\dot{\varphi} = 0$ and $\dot{q} = 0$		$\langle\varphi\rangle = 0$ and $\dot{q} = 0$
$\sigma_{pin} \neq 0$	$q_{final} = \frac{1}{P_{pin}}(H + \frac{\beta}{\gamma\Delta}u)$	$u \leq \frac{1}{2}H_{BN}\gamma\Delta$	$q_{final} = \frac{1}{P_{pin}}(H + \frac{\beta+\frac{1}{\alpha}}{\gamma\Delta}u)$
$\partial_\varphi\sigma_{pin}=0$	$\sin(2\varphi) = \frac{2}{\gamma\Delta H_K}u$		$\dot{\varphi} = -\frac{1}{\gamma\Delta}u$

Table 3.1 – Summary of the $q-\varphi$ results in both free and pinned approach for the two motion regimes driven by combined H and J. Here the pinning is considered as a quadratic energy potential with P_{pin} as a strength parameter.

Coming back to the experimental dependence of the equivalent field with J (shown Fig. 3.2), it is possible to observe its quasi-linearity with J as shown in Fig. 3.10. Considering the thermal dependence of M_S and P and using the correspondence between J and T, we fit approximately the experimental values of H_{eq} (black line in Fig. 3.10) with a $H_{eq}/J \approx 0.018$ [mT/(GA/m^2)]. The overall increasing trend of $H_{eq}(J)$ is reproduced over the whole range of current density. The dotted line corresponds to a constant P/M_S ratio and could reproduce the data as well. It is not possible to observe the predicted two different slopes of $H_{eq}(J)$ (corresponding to the two propagation modes) (see Eq 3.13). Plotting the occurrence of the ratio H_{eq}/J (shown Fig. 3.12), it is nevertheless possible to see two peaks at positions H_{eq}/J =0.006 and 0.018 $mT/(GA/m^2)$. The first one corresponds to the ratio for low current density and the second one to the higher densities. Both peaks could correspond to different mobilities associated to two different regimes of propagation: a translational one and a processional one. In regards to the predictions of our theoretical model, the in-plane anisotropy field is small: $H_{BN} \approx 0.25M_S$. Assuming $\Delta = 5$ nm from independent measurements and $P = 0.5$, we can estimate u_W to occur for $J_W \approx 35 \pm 5$ GA/m^2. Although these estimations are compatible with our observations, it is difficult to detect different slopes of $H_{eq}(J)$ separated by a critical current, perhaps due to the large dispersion of H_{eq} data at low current.
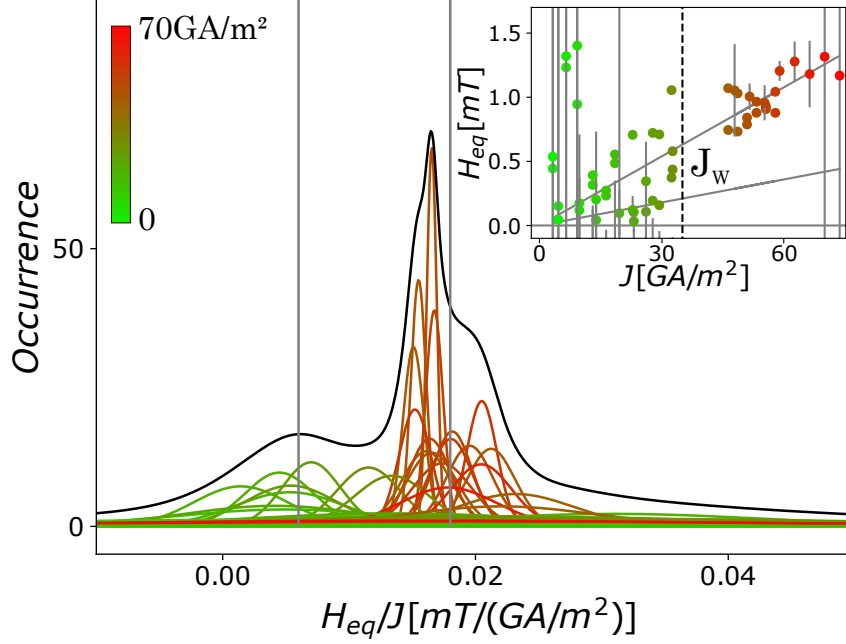
Figure 3.12 – Occurrence plot of all H_{eq}/J ratios measured. Each measured H_{eq} is associated with a normalized Gaussian centered in H_{eq}/J with a variance of δH_{eq} the standard error of H_{eq}. The colors lines correspond to the current amplitude (for more clarity, normalized Gaussians are plotted divided by a factor 5). The black line corresponds to the sum of all normalized Gaussians. Gray lines correspond to positions of 'maximum' values of the black line means the most frequent H_{eq}/J ratios. In the inset: all measured H_{eq} values (there are more points than in Fig. 3.10 as here the points were not averaged). The two gray lines corresponds to slope extracted from the occurrence plot (a) and the dotted line corresponds to the estimated Walker current J_W associated to u_W : $J_W \approx 30 \pm 5 GA/m^2$.

The ratio between theoretical slopes of H_{eq} in the previously discussed propagation regimes provides a quantitative evaluation of the product $\alpha\beta$ without any approximation on material parameters. It is given by Eq. 3.14.

$$\alpha\beta = \left(\frac{H_{eq}^{>W}/J}{H_{eq}^{<W}/J} - 1 \right)^{-1} \tag{3.14}$$

Here, it gives $\alpha\beta = 0.5$. However, for $J > J_W$, magnetization precesses inside the pinned DW. Due to magnetic inhomogeneities, precession should not be the same along the entire DW length which promotes the creation of Néel lines. These textures have a non-zero gyrovector which can modify the DW dynamics. Indeed, if we consider Néel lines in a rigid DW, due to their gyrovector, they are pushed along the (pinned) DW by current [211] which may induce an additional damping. The damping value determined from DW velocities may constitute a great overestimation of α depending on the occupation of lines along the DW.

This creep precessional regime should exist also in ferromagnets; however, it is harder to reach the critical current J_W^{pin} ($\propto M_s^2$) in materials with higher M_s.

3.6.4   Angular dependence of the pinning

In this part, we consider also the angular dependence of the pinning effect. A previously shown in Fig. 3.11, we notice the natural pinning situation configuration (q^0, φ^0) and (q^{max}, φ^{max}) the configuration of the next σ_{pin} maximum. Applying forces on the DW *via* field H or current J, the DW moves in the energy well up to an equilibrium configuration noted $(q^\star, \varphi^\star)$, directly depending on forces reducing the energy barrier $\Delta\sigma$ which increases the macroscopic DW motion. As proposed in [110,212] it is possible to calculate the equivalent field associated to current expanding the pinning surface energy $\sigma_{pin}(q, \varphi)$ around

the pinning configuration (q^0, φ^0) where σ_{pin} is minimum and saddle point (q^{max}, φ^{max}) corresponding to the next maximum of σ_{pin} :

$$\sigma_{pin}(q, \varphi) \approx \begin{cases} \sigma_{pin}^0(q, \varphi) = \frac{\partial_q^2 \sigma_{pin}^0}{2} + \left(q - q^0\right)^2 + \frac{\partial_\varphi^2 \sigma_{pin}^0}{2}\left(\varphi - \varphi^0\right)^2 & \text{for } (q, \varphi) \approx (q^0, \varphi^0) \\ \sigma_{pin}^{max}(q, \varphi) = \sigma_{max} + \frac{\partial_q^2 \sigma_{pin}^{max}}{2}\left(q - q^{max}\right)^2 + \frac{\partial_\varphi^2 \sigma_{pin}^{max}}{2}\left(\varphi - \varphi^{max}\right)^2 & \text{for } (q, \varphi) \approx (q^{max}, \varphi^{max}) \end{cases}$$

$$(3.15)$$

where $\partial_{q/\varphi}^2 \sigma_{pin}^{max}$ and $\partial_{q/\varphi}^2 \sigma_{pin}^0$ correspond to the energy stiffness of σ_{pin} around minimum and maximum energy configurations and σ_{max} the energy difference of between the minimum and the saddle point of σ_{pin}. Considering the nature of the minimum (q^0, φ^0) and of the maximum (q^{max}, φ^{max}) points, it is expected that $\partial_q^2 \sigma_{pin}^0$, $\partial_\varphi^2 \sigma_{pin}^0$ and $\partial_\varphi^2 \sigma_{pin}^{max}$ are positive whereas $\partial_q^2 \sigma_{pin}^{max}$ is negative. Applying forces on the DW, the dependence of the equilibrium position in the energy well $(q^\star, \varphi^\star)$ can be calculated and then the surface energy barrier is:

$$\Delta\sigma(H, u) = \Delta\sigma_0 + 2(\mu_0 M_s)^2 \Bigg(\left(\frac{1}{\partial_q^2 \sigma_{pin}^{max}} - \frac{1}{\partial_q^2 \sigma_{pin}^0} \right) \left(H + \frac{\beta u}{\gamma_0 \Delta} \right)^2$$
$$+ \left(\frac{\partial_\varphi^2 \sigma_{pin}^{max}}{\left(\partial_\varphi^2 \sigma_{pin}^{max} + 2\mu_0 M_s H_{BN} \cos(2\varphi^{max}) \right)^2} - \frac{\partial_\varphi^2 \sigma_{pin}^0}{\left(\partial_\varphi^2 \sigma_{pin}^0 + 2\mu_0 M_s H_{BN} \cos(2\varphi^0) \right)^2} \right) \left(\frac{u}{\gamma_0 \Delta} \right)^2 \Bigg) \quad (3.16)$$

where $\Delta\sigma_0$ corresponds to the surface energy barrier without forces. Just considering the first term, we can see that the linear relation between applied field H and the drift speed u remains and it could be possible to associate an equivalent fields $H_{eq} = \frac{\beta u}{\gamma_0 \Delta}$ to the STT effect (as in the previous simplest case Eq. 3.10). It is also possible to see that the prefactor $\left(1/\partial_q^2 \sigma_{pin}^{max} - 1/\partial_q^2 \sigma_{pin}^0\right)$ is negative, meaning that forces (H and u) decrease the initial energy barrier $\Delta\sigma_0$ anyway. As expected, the angular dependence of pinning modifies the DW configuration inside the energy potential adding the second term which depends on $\partial_\varphi^2 \sigma_{pin}$ and the adiabatic torque of STT u/Δ. This new contribution is directly related to the angular dependence of the pinning potential $\partial_\varphi^2 \sigma_{pin}$ and vanishes when it is neglected. Considering this new term, there is no longer a simple linear relation between H and J, and so the equivalent field approach is not valid anymore: it is no longer possible to consider a simple equivalent field H_{eq} associated to STT-like effects of the current. However, this new contribution depends of the geometry of the pinning potential. Both $\partial_\varphi^2 \sigma_{pin}^0$ and $\partial_\varphi^2 \sigma_{pin}^{max}$ are positive, that means that the adiabatic torque of STT can increase or decrease the energy barrier. For different pinning centers with different geometry, this contribution is different for each of them. If we consider a DW overcoming many pinning centers, which is the case during creep macroscopic motion, its averaged value vanishes. Similar theoretical approaches [110, 212] show that the angular dependence of the pinning potential gives an extra non-linear current contribution to the equivalent field due to adiabatic STT torque. This was also experimentally observed [213, 214]. However, those studies were focused on a single isolated pinning center with the same pinning potential geometry that gives a nonzero extra contribution of adiabatic torque. They also show that it vanishes for a DW motion through many pinning centers. These modifications just affect the translational regime and not the precessional one where $\langle \partial_\varphi \sigma_{pin} \rangle \approx 0$.

In our measurements, such a quadratic adiabatic contribution, being symmetric for $\pm J$, does not affect H_{eq} (Eq. 3.3), but instead would induce an overestimation of T_{pulse} (not visible considering the good overlap in Fig. 3.7).

3.7 Conclusion

In this chapter, we observed and quantified the effects of current on the DW motion in the creep regime. Being in the creep regime is in fact an advantage to analyze this phenomenon. Indeed, this non-linear speed law is very sensitive to both thermal and field variations and highlights the expected current effects. We first analyzed the dynamics of the DW driven by field in the creep regime considering compact creep parameters and their large temperature variation (part. 3.3). Secondly, measuring the DW motion driven by field and current, we identified two effects of the current on the DW dynamics: a STT-like action and Joule heating (part. 3.4). We proposed a robust analysis of velocity versus field and current that allows to separate the two effects. The STT-like action is quantified as an equivalent field H_{eq}. Its large strength is a consequence of the P/M_S properties of the ferrimagnetic alloy (part. 3.6). A parallel determination of both the heating amplitude and the heating time validated the extracted values of H_{eq} (part. 3.5). Finally, we predict a discontinuous current dependence of the equivalent field. This would be a signature of the existence of two propagation modes separated by a field-independent threshold current, associated with dynamic changes of the internal structure of the pinned DW. Due to the lack of accuracy of the low current data, we could not evidence these two regimes.

3.8 Perspectives

This method highlights the current effect (STT and heating) by the sensitivity of the creep dynamics of DWs. In this regime, the DW motion can be considered as quasi-static and it is possible to identify the STT efficiency independently from the dynamic properties of the alloy (as detailed in part. 2.4.2). To improve this method, it could be interesting to investigate temperature or field ranges where the creep dynamic changes more. Two possibilities exist: the magnetic compensation point of the alloy and the depinning even transition. Some preliminary studies have been done in order to reach these two configurations.

3.8.1 Domain wall motion at the magnetic compensation point

At the magnetic compensation point, the net magnetization M_S (with $\vec{m}$ taken along the TM sub-lattices) vanishes changing its sign. This induces a reversal of the DW propagation across this point as shown in Fig. 1.14 (a) and (b). Fig. 3.13 shows the DW velocity of a DW driven by a perpendicular field in a $Si/SiOx_{100nm}/Tb_{35\%}FeCo_{7nm}/Al_{5nm}$. First, it is possible to see that the DW is in the creep regime and that it is possible to extract reduced creep parameters C_v and C_H (shown in Fig. 3.13 (b)). Full lines in Fig. 3.13 (a) correspond to the theoretical velocity law of the creep (Eq. 3.3). Secondly, it is possible to see that the propagation direction of the DW is reversed at around $T_{MC} = 407$ K which corresponds to the magnetic compensation point in the sample. Crossing T_{MC}, the reduced creep parameters change drastically which indicates a stronger sensibility of the DW velocity in temperature compare to the previous case. Measuring the combined effect of the field and current in this region should reveal much more the heating effects of the current.

Being at the magnetic compensation point has other advantages. According to the effective drift speed u_{eff} (see part. 2.2.2), it is expected that the equivalent field associated to STT, $H_{eq} \propto 1/M_s$, diverges and a stronger STT amplitude should be observable. Furthermore, the Walker current J_W between both regimes (translational and processional) is directly proportional to M_s^2 and should change greatly around T_{MC}, where the demagnetization effect vanishes. Finally, it should be possible to measure the current dependence of the equivalent field in both translational and precessional creep regimes tuning the position of the Walker current.
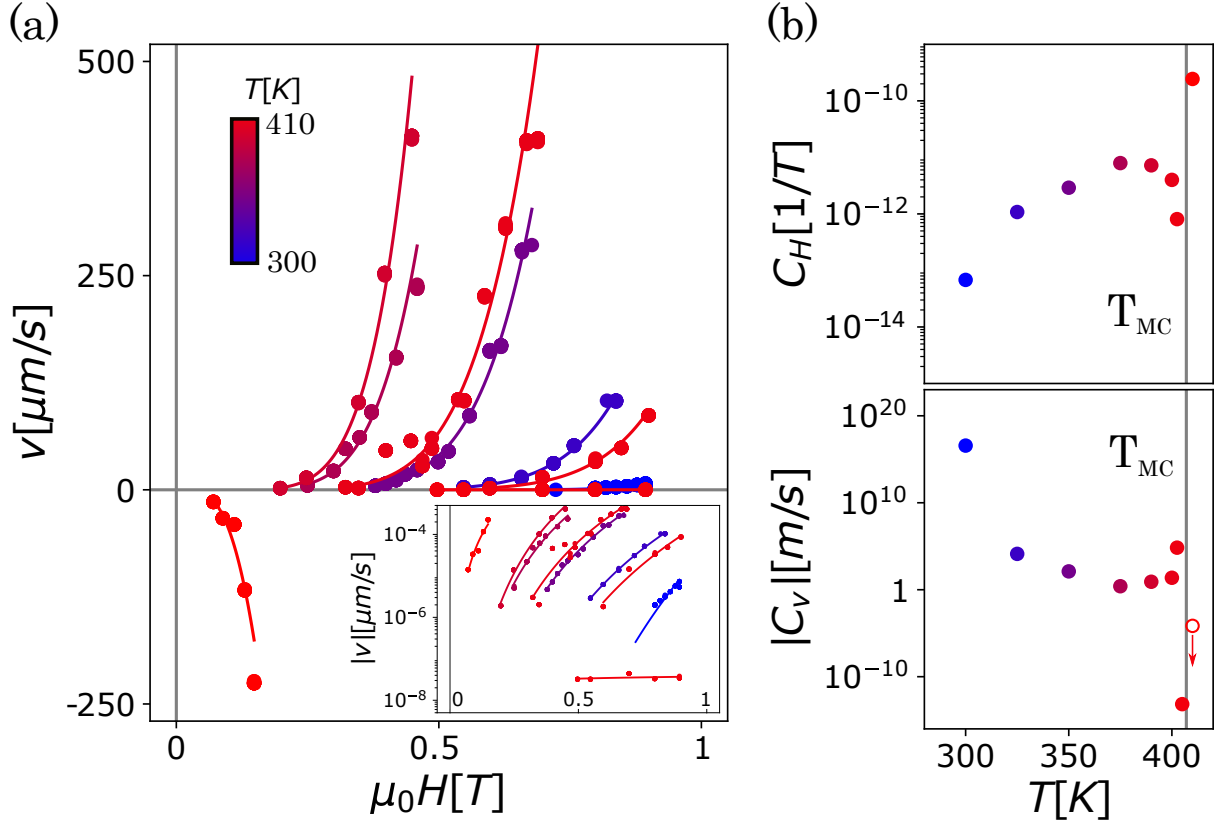
Figure 3.13 – Creep regime across magnetic compensation. (a) DW velocity of DW driven by perpendicular field in a unpatterned similar $Si/SiOx_{100nm}/Tb_{35\%}FeCo_{7nm}/Al_{5nm}$ thin film. The insert shows the same data in logarithm scale. Full lines correspond to the fitting with Eq. 3.3. (b) Reduced creep parameters C_H and C_v (in absolute value) extracted from velocity curves for each temperatures. The vertical line corresponds to the magnetic compensation temperature T_{MC}. Note that the values of C_v are positive below T_MC and negative above T_MC which corresponds to the reversal of the DW propagation direction under field.

3.8.2 Domain wall motion at the depinning transition

In order to improve this approach, it could also be interesting to study the DW motion in a more convex region of the creep law, closer to the depinning transition [197, 199]. In Tb-based alloy, this range of field is not reachable with our experimental setup ($\mu_0 H_{dep} > 1$T) but it is for Gd-based films. However, in this range of fields the DW velocity is too large to use standard electromagnets due to their too long rise times. To overcome this limitation, we patterned a 'U'-coil directly around a magnetic wire as shown Fig. 3.14. Injecting current ns-pulses in this 'U'-coil induces a field on the wire which drives the DW motion.

Fig. 3.14 (b) and (c) show DW velocity *versus* the applied field for different set-point temperatures. In contrast to previous measurements, it is clearly possible to identify the depinning transition associated to the inflection of the velocity curve. Using the theoretical law for the creep and the depinning transition [197, 199], it is possible to reproduce the experimental point behavior. It is possible to see that, at this depinning transition, the convexity of the curve is maximal which should increase much more the STT effect of an applied bias current.
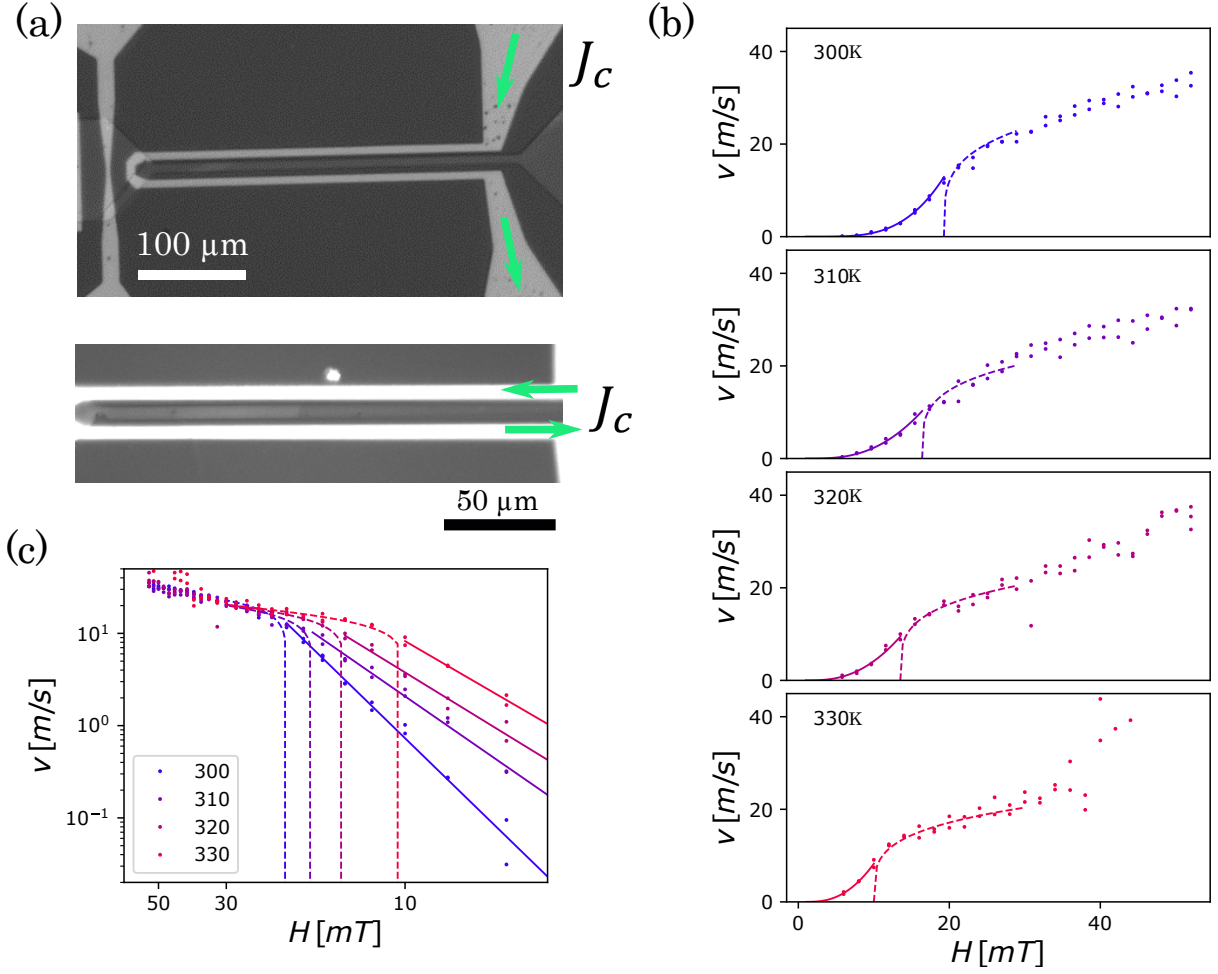
Figure 3.14 – Creep regime across close to the depinning transition. (a) Kerr image of a DW in the $Gd_{40\%}FeCo_{60\% \, 5nm}/SiOx_{5nm}$ $10\mu m$-wire driven by the field induced by the patterned 'U'coil. (b) and (c) DW velocity *versus* applied perpendicular field induced by the patterned 'U'-coil for different temperatures in linear scale (for (b)) and $\log_{10}(v)$ *vs* $H^{-1/4}$ scale (for (c)). Dots correspond to experimental velocity measurements. Continuous lines correspond to the adjusted theoretical creep law [197] and dashed lines to the theoretical law for the depinning transition [199]

3.9 Contribution and publications

3.9.1 Collaborations

The magnetization shown Fig. 3.2 (a) was measured in collaboration with Yves Dumont at Versailles Saint-Quentin University. All the presented work in this section was done in our laboratory.

3.9.2 Publication

The main part of these results is presented in an article published in PRB [41].

Precession-free dynamics in compensated ferrimagnets

In this chapter, the precession-free dynamics of the magnetization is investigated through the prism of DW dynamics driven by SOT. First, in the section 4.3, I present the measured DW motion driven by SOT. In order to characterize the internal DW dynamics, I show the effect of in-plane fields along and transverse to the DW propagation direction (in respectively sections 4.4 and 4.5. Finally, using the effective parameter model, I show that the precession fully vanishes at the angular compensation point.

4.1 Precession-free dynamics and domain wall motion

One of the remarkable properties of the ferrimagnetic dynamics is the possible vanishing of precession. Indeed, at the angular compensation point, a magnetic moment reversal driven by a field-like torque does not present any precession motion (see part 2.2.2). The experimental proof of this precession-free dynamics by a direct measurement of the reversal process remains challenging and indirect evaluation of associated features like damping give unclear results [151, 152] (as shown Fig. 2.5 (a) and (b)). Another approach consists in measuring the effects of this precession-free dynamics on the dynamics of a magnetic texture. Considering a moving 180° DW (see part 1.4.1), the precession of the individual magnetic moments induces a resulting canting of the central magnetization of the DW. Without precession, this in-plane direction remains in its equilibrium configuration (as predicted in the former sections 2.4.3, 2.4.1 and 2.4.4). This vanishing of the precession induces a peak of mobility for a DW driven by field (see part 2.4.1), a saturation-less velocity for a DW driven by SOT (see part 2.4.3) and a transition-less dynamic of a DW in both cases (see part 2.4.4). To experimentally probe precession, we investigate the motion of a DW driven by SOT. As seen before, in this situation, the DW velocity is directly correlated to its internal structure [85, 134]:

$$v \propto J \cos(\varphi) \tag{4.1}$$

where J is the current density and φ the in-plane angle of the DW magnetization (as detailed in part 2.4.3). Here, measuring the DW velocity directly gives information on the DW in-plane angle φ and, consequently, on the reversal processes of magnetic moments. At the ACP, it is expected that the precession-free dynamics does not drive any modification of the φ angle which is directly associated with a peak of the DW velocity versus T associated with the unsaturated velocity regime. This phenomena has already been experimentally observed in similar ferrimagnetic tracks [14, 20] (as shown in Fig. 2.18). However, as detailed below, this velocity approach is just an indirect measurement of φ and can be affected by parasitic effects such as DW pinning [215] or Joule heating. In this study, we investigate the DW dynamics driven by SOT under in-plane fields to have a better understanding of the internal DW dynamics.

4.2 Sample and experimental setup

We studied a $Si/SiOx_{(100nm)}//Gd_{40\%}Fe_{51\%}Co_{9\%~(5nm)}/Pt_{(7nm)}$ 10 μm wire deposited by co-evaporation (as detailed in part 1.2.1) and patterned by electron-beam lithography and ion-beam etching. The sample was characterized by Hall electrical and Kerr optical measurements (see parts 1.3.4 and 1.3.5). The magnetization was measured by SQUID. Fig 4.1 (a) shows the net magnetization $|M_S|$ of the virgin film and the coercive field of the patterned wire. The background line corresponds to the mean field calculation (see part 1.3.3). It is possible to see that the magnetization vanishes and the coercive field diverges at 310 K, which is the signature of the magnetic compensation temperature T_{MC} (see part 1.3.3).
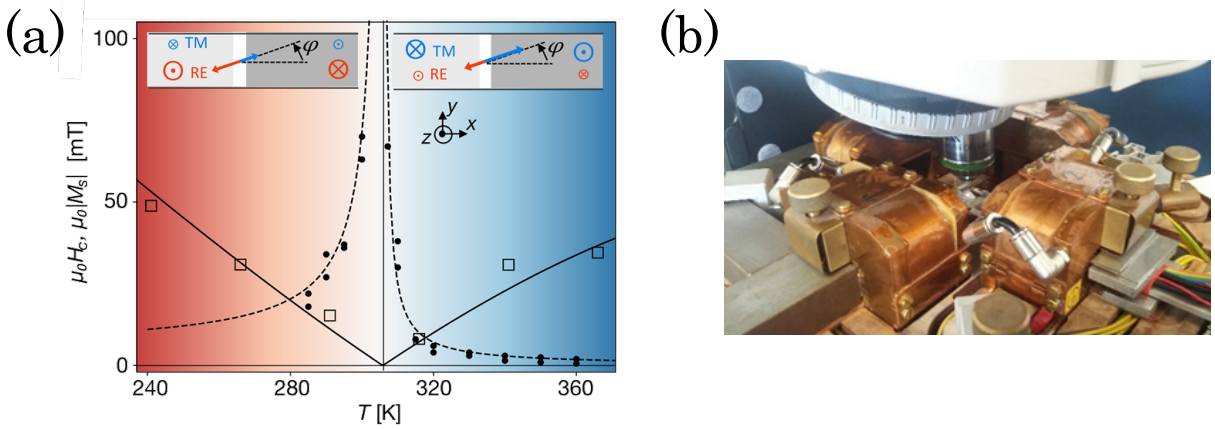
Figure 4.1 – (a) Properties of the studied $Si/SiOx_{(100nm)}//Gd_{40\%}Fe_{51\%}Co_{9\%~(5nm)}/Pt_{(7nm)}$ magnetic wire: net magnetization $|M_S|$ of the virgin film (squares) and coercive field H_c of the patterned track (circles; measured by Kerr effect) versus T. The M_S points were shifted by -25 K to account for Gd depletion during patterning (see part 1.2.4). The continuous line is the result of the mean-field model (see part 1.3.3). The background highlights the dominant sub-lattice (see part. 1.4.2). The inset represents a sketch of the magnetization of the TM and RE sub-lattices (in respectively red and blue) below and above T_{MC}. The size of the arrows represents their relative magnitude. The gray-scale corresponds to the domain Kerr contrast while the DW is depicted in white. The angle of the DW magnetization is given by φ defined considering the TM sub-lattice. (b) Kerr microscope setup.

Fig 4.1 (b) shows a sketch of the used setup to image the magnetic domains. It is a versatile commercial Kerr microscope [100] with special modifications for this study. The sample is fixed and connected to a heating holder inside a quadrupole in-plane electromagnet. A cryogenic gas (nitrogen) is injected close to the sample to cool the temperature around the sample down to 285 K. A heater is connected to a temperature PID-controller to stabilize the sample temperature at a set-point called T_{SP} in a range from 280 K to more than 400 K. The sample is connected to a voltage pulse generator able to generate single 25 ns-pulses up to ±900 GA/m^2 (corresponding to a voltage of 100 V). The in-plane electromagnet creates a continuous in-plane field up to 175 mT. An additional perpendicular coil (up to 50 mT) is used to compensate stray fields from the optical setup and from the parasitic perpendicular contribution of the in-plane electromagnet. In this experiment, due to space limitations, the sample is turned by 90° to apply H_x or H_y fields. The DW motion is recorded with a camera which takes a Kerr image after each pulse. The Kerr images are analyzed with developed routines to obtain the DW velocity and the macroscopic tilt angle of the DW during its motion with low error. The studied magnetic wire has a length of $\sim 200\mu$m which allows us to measure precisely DW velocities up to 1 km/s.

4.3 Domain wall driven by SOT

We investigate the DW motion driven by an electrical current without any in-plane field. Current pulses are injected in a track containing an up-down DW. Fig 4.2 (a) shows Kerr images after 300 GA/m^2 25 ns-pulses for a $T_{SP} = 300$ K. It is possible to see that the DW moves along the electrical current direction, which is compatible with SOT-driving of chiral Néel DWs with the two same relative sign of DMI and SHE as found in ferromagnetic Pt/Co wires [12,79,164,170]. Fig 4.2 (b) shows the dependence of the DW velocity with the pulse duration for pulses between 25 and 250 ns for two different current densities: 180 and 360 GA/m^2. For each configuration, the two markers represent the velocity for a positive and a negative current. The similarity between the velocities with positive and negative currents shows that the perpendicular field has been well-compensated. The linearity of the DW displacement with the pulse number and duration allows the robust and non-stochastic determination of the propagation velocity v.
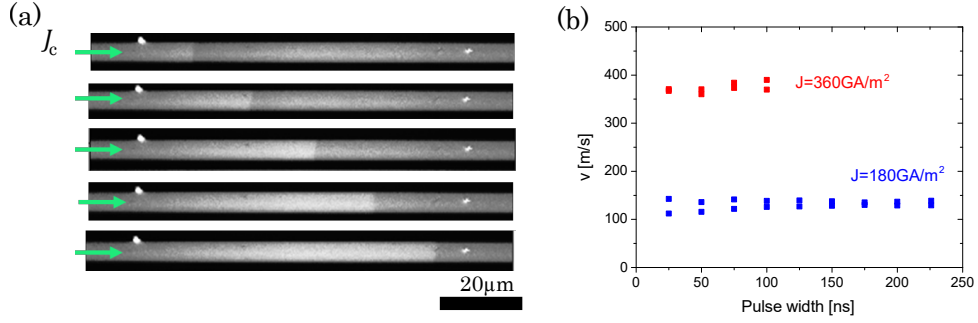
Figure 4.2 – Kerr images of the SOT-driven DW propagation in GdFeCo/Pt. (a) Kerr images of a DW driven by 300GA/m^2 current 25 ns-pulses in the GdFeCo$_{5nm}$/Pt$_{7nm}$ 10μm-track at temperature set-point of T_{SP}=300 K. (b) DW velocity for different current pulses width with amplitudes of 180 and 360 GA/m^2 at T_{SP}=300 K.
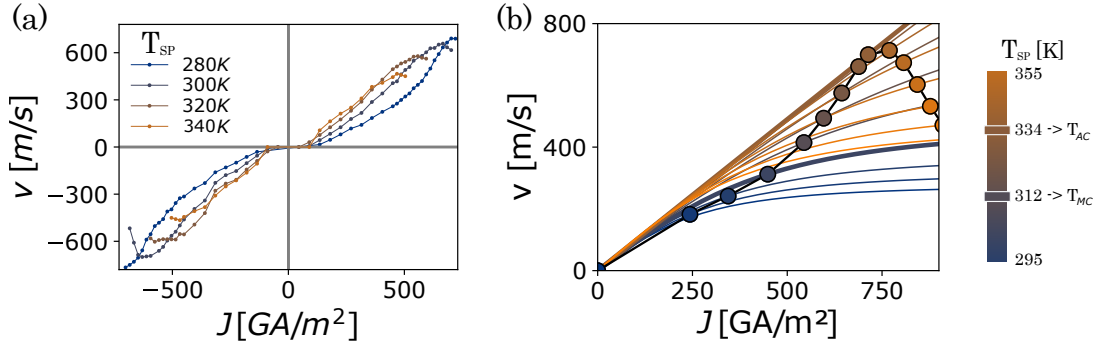
Figure 4.3 – (a) DW velocity *versus* the current density measured for different T_{SP}. (b) Calculated velocity of the DW *versus* the current density. The full curves on the background correspond to the theoretic velocity law considering a fixed T (similar to Fig. 2.17 (a)) and dots correspond to the obtained velocity curve considering a fixed T_{SP} and Joule heating. Here, T_{SP}=295 K and a heating parameter of $\kappa = 8.4\,10^{-5} K/\frac{GA}{m^2}$ are considered. The values of other parameters are detailed in part 4.6.

Fig 4.3 (a) shows the DW velocity v versus the current density J for different T_{SP}. High DW velocities (>700 m/s) are observed, as previously reported in similar alloys [14, 20] but for much lower current density J (less than 600 GA/m^2). Two significant differences are observed between the measured $v(J)$ and the theoretical predictions shown in Fig. 4.3 (b) (and in part 2.4.3). Firstly, the motion of the DW occurs only above a threshold current of few tens of GA/m^2. It can be attributed to the DW pinning at defects. This is supported by the fact that the threshold decreases when T_{SP} increases. Similar behavior is often found in current-driven DWs, both in ferromagnets [170] and in ferrimagnets [14, 20]. In our wire, the threshold current is about 50 GA/m^2, a few times lower than in previous studies [14, 20].

Secondly, for a given T_{SP}, the velocity exhibits a non-monotonous behavior, while it is expected that the velocity is always increasing with J or remains constant in the saturated regime [164, 170] (Fig 4.3 (a)). This variation of $v(J)$ measured at fixed T_{SP} can be understood by considering the theoretical $v(J)$ curves for different T as shown Fig 4.3 (b) (similarly to the Fig. 2.17 (a)). Due to the Joule heating, each current density induces heating of the track which changes the effective temperature T of the wire. We note $T \leftarrow T_{SP} + \kappa J^2$ where κ is the heating coefficient. The velocity law is strongly temperature-dependent. Each measured $v(J)$ at fixed T_{SP} corresponds to a point in a theoretical $v(J)$ curve of progressively higher T as J increases, which produces a peak. Fig 4.3 (b) shows a calculated curve $v(J)$ considering a heating parameter of $\kappa = 8.4\,10^{-5} K/\frac{\text{GA}}{m^2}$ (extracted from the following measurements). For this calculation, the pinning of the DW is not taken into account.

Mobility approach To avoid this, we consider the mobility $\mu = v/J$ dependence on temperature. The mobility μ is expected to be maximum at T_{AC} (as calculated in part 2.4.3 and shown in Fig. 2.17). Fig. 4.4 (a) shows the DW mobility *versus* T_{SP} for different current densities. The mobility of the DW is very high and exhibits a peak of about $\mu \sim 1.3\frac{m/s}{GA/m^2}$ (indicated by star markers). Models predict that the SOT-driven DW velocity follows $v \propto J\cos(\varphi)$ where φ is the angle of the internal DW magnetisation [85]. In ferromagnets, φ is determined by the balance between DMI, which favours the Néel configuration ($\varphi = 0$), and the SOT, which increases $|\varphi|$ *via* the precession mechanism. In ferrimagnets, this precession depends on the temperature and is expected to vanish at T_{AC} creating a mobility peak (as shown part 2.4.3). Therefore, the observed mobility peak corresponds to minimal $|\varphi|$, and it can be deduced that the temperature of the maxima is T_{AC} as previously done in [14, 20] (see Fig. 2.18).
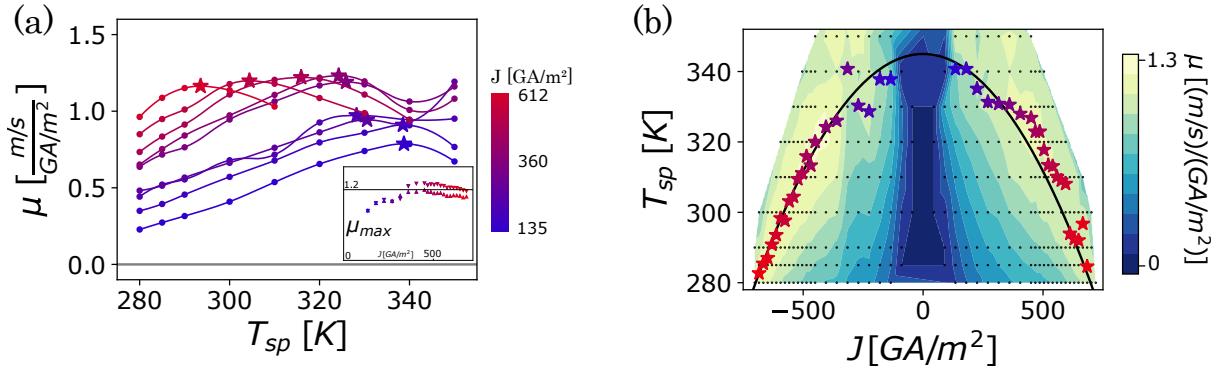
Figure 4.4 – DW mobility in GdFeCo/Pt under SOT. (a) Mobility curves *versus* T_{SP} for different current densities. Stars indicate the maximum for all curves. The inset show the maximum of mobility μ_{max} *versus* the current density. (b) Mobility color-plot in the (J, T_{SP}) plane. Gray dotes correspond to the experimental measurements and stars show the maximum of the $\mu(T_{SP})$ curves. The black line shows the parabolic curve obtained from fitting the position of the maximum of mobility.

Fig. 4.4 (a) the position of the maximum decreases when J increases. This is consistent with Joule heating: $T_{AC} \leftrightarrow T_{SP} + \kappa J^2$ and if J increases, the T_{SP} required to reach T_{AC} decreases. In this representation, Joule heating just induces a horizontal shift between curves. It is also possible to see that the mobility has a constant maximum value for large currents as expected (shown Fig. 4.4 (a)). For low current the DWM is more sensitive to the pinning which reduces its mobility. The color-plot Fig. 4.4 (b) shows all the measured mobilities in the (J, T_{SP}) plane. Stars correspond to the position of the maximum of mobility for each current density. All maxima occur at the same temperature since it is possible to adjust their position with a parabolic curve, which is the signature of Joule heating. It is also possible to see the bad agreement for low currents (below 250GA/m^2) due to pinning. Measuring the parabolic parameter, it is possible to estimate the heating parameter κ, here: $1.1\,10^{-4} K/\frac{GA}{m^2}$. Considering the mobility *versus* T is much more convenient than considering the velocity *versus* J. Indeed, in the mobility approach, even if curves are distorted by Joule heating, they still exhibit a maximum at T_{AC} as shown Fig. 4.5.

Pinning and shape of the mobility curve However, due to pinning, the mobility curve can be distorted. The Fig. 4.5 shows the calculated velocity (in (a)) and their associated mobility (in (b)) *versus* the wire temperature for different current densities. Three cases are considered: (from left to right) no heating nor pinning, heating ($\Delta T = \kappa J^2$ with $\kappa = 8.4\,10^{-5} K \frac{GA}{m^2}$) but no pinning, and both pinning and heating. In the cases with heating, the mobility curves are subsequently shifted according to a heating law obtained by a parabolic fit of the maximum position versus J (as was done in the experiments). It is possible to see that, in the absence of pinning (middle plot), the maxima occur at a same (corrected) temperature. Here, the velocity curves are just shifted and the required parameter κ to superpose all mobility peaks matches the one used for the heating simulation. If the pinning is taken into account (right case), the mobility curves are much more modified. As experimentally observed, the pinning effect is larger for low current density and reduces the maximum value. Furthermore, the heating parameter required to rescale the position of the peak is larger that the one used for the heating simulation. Finally, the rescaled mobility curves indicate a peak at a temperature higher than T_{AC}. Here, the pinning is taken into account as a simplistic constant mean surface energy of $\partial_q \sigma_{pin} \approx 10^3$ J/m^3 (see Eq. 2.20) chosen to have a threshold of current at around 100 GA/m^2. This model mainly induces a vertical shift of the velocity (a) but modifies much more the mobility curves (b). Even if it does not induce important modifications of the DW velocity, it is enough to highlight the effect of the pinning. More complex effects have been reported in similar experiments measuring field-driven DW motion in the creep regime [215] revealing the vanishing of the expected DW dynamics under the depinning threshold.
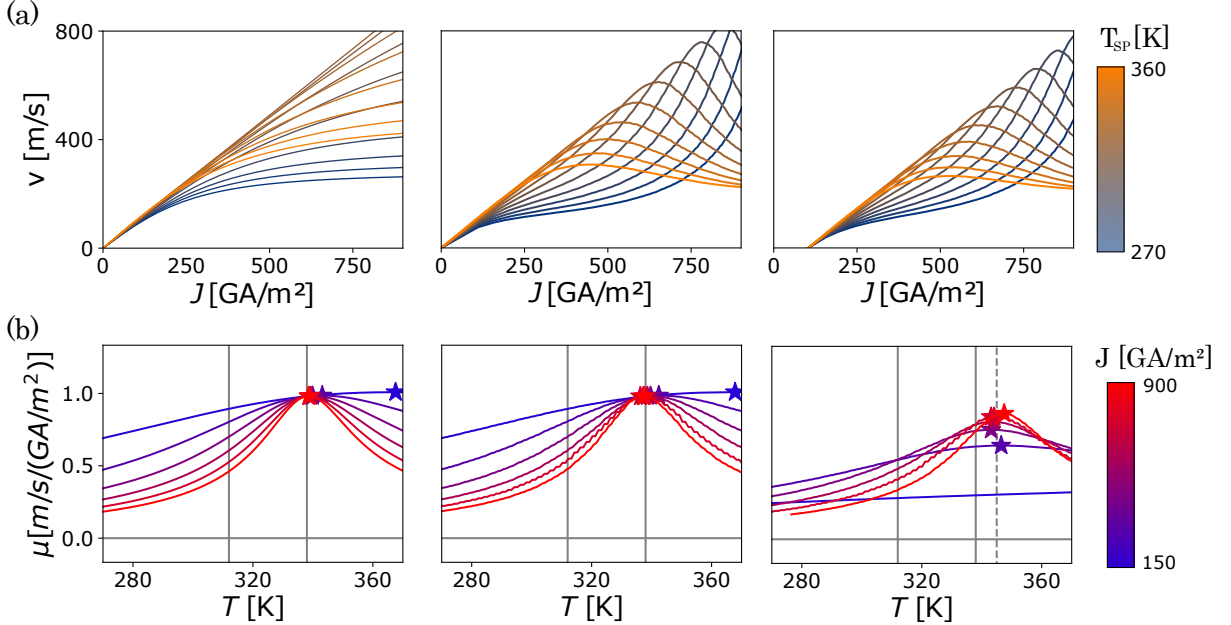
Figure 4.5 – Calculated DW velocity (a) and their associated mobility (b) under SOT considering (from left to right) no heating nor pinning, heating and no pinning, and both heating and pinning. Here, a heating parameter of $\kappa = 8.4\,10^{-5} \frac{GA}{m^2}$ is considered to simulate heating. For both the second and the third cases the mobility curves are horizontally shifted using a heating law to obtain a good match between the position of the maxima. The used heating parameters consider for the re-scaling are $\kappa = 8.4\,10^{-5}$ and $1\,10^{-4} K \frac{GA}{m^2}$. For the third case including both pinning and heating, pinning is taken into account as a simple constant mean surface energy of $\partial_q \sigma_{pin} \approx 10^3$ J/m^3 (see Eq. 2.20) chosen to have a threshold of current at around 100 GA/m^2. The small steps visible in the second and the third curves are due to numerical rounding required for the calculation.

4.4 Domain wall driven by SOT under H_x

In order to better characterize the internal DW dynamics, we apply a continuous in-plane field to interact with the in-plane DW component, *i.e.* φ. First we apply an in-plane field along the current direction, H_x, *i.e.* parallel or opposite to the DMI field. The idea was to reduce the DMI and increase saturation effects.
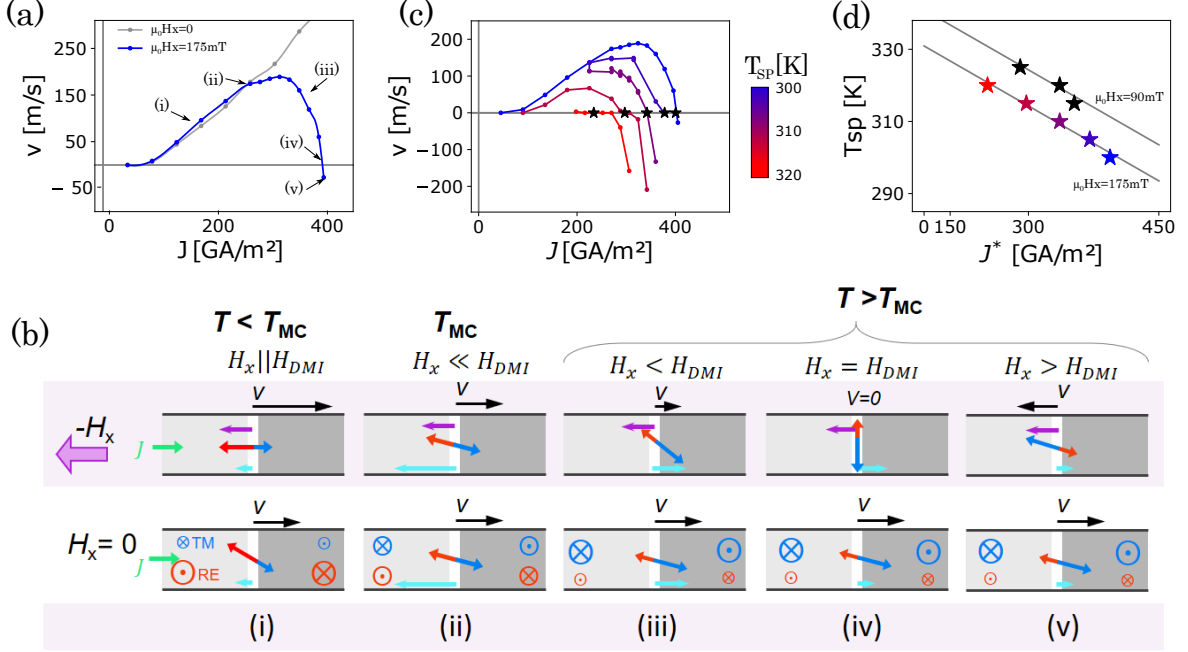
Figure 4.6 – DW propagation under SOT and an in-plane field H_x. (a) In blue: DW velocity driven by SOT under in-plane field $-\mu_0 H_x = 175$ mT opposite to the DMI field at T_{SP}=300K. In gray, the DW velocity driven by SOT without any field (at T_{SP}=300K). (b) Table showing a sketch of the DW dynamics for each configuration **(i-v)** indicated in (a). The red and blue arrows correspond to the magnetization of both sub-lattices. The purple and cyan arrows show respectively the H_x and the DMI field. The above black arrow corresponds to the DW velocity. In all these sketches the sign of the φ angle is arbitrarily chosen but the opposite sign gives the same resulting DW velocity behavior. (c) DW velocity *versus* J for different T_{SP}. The crossing points (for which $v = 0$) are marked by a star. (d) T_{SP} associated to each reversal current $J^\star$ for two different in-plane field H_x=175 and 90mT.

Fig. 4.6 (a) shows the velocity of the DW *versus* the current density for a constant in-plane field of 175 mT (in blue). The negative velocities correspond to a reversal of the propagation direction. The gray line corresponds to the velocity without any in-plane field. Five zones are identifiable (indicated in the figure). **(i)** The DW moves along the current direction faster than in the zero-field case. **(ii)** The DW velocity are the same with and without field. **(iii)** The DW velocity decreases down to zero and **(iv)** reverses its propagation direction. The DW behavior in all these regions can be explained considering the Joule heating and the DMI field dependence in temperature (see Fig. 2.9 and 2.10). Fig. 4.6 (b) shows in more detail the magnetization state of each sub-lattice under current, in-plane field and for different temperatures. All indexed situations are reported in the bottom line of the table. For low current density (i) the wire is below its magnetic compensation $T_{MC} \approx 310K > T_{SP} = 300K$ and the effective DMI field is negative. In this temperature range, applying a negative in-plane $-H_x$ field directly increases the DMI effect favoring the $\varphi = 0$ Néel configuration. In this situation, φ is lower with the $-H_x$ field and the DW velocity is higher. At the T_{MC} (ii), the applied field $-H_x$ is negligible compared to the diverging effective DMI field. Here the φ angle is the same with or without field and the DW velocity are equal. Another argument is to say that the magnetizations of the two sub-lattices are equal and the field has no net effect. The sign of the DMI field reverses at the magnetic compensation, as does the magnetization (see Fig. 2.9 (c)). Then, just above T_{MC} (iii) the effects of the field and the DMI

are opposed and the resulting φ angle is larger with field than without, and the DW velocity is slower. Increasing again the current density, T increases and the DMI field decreases. For a given current density (iv), the in-plane field is exactly opposed to the DMI field. Here, the DW is Bloch and the SOT does not drive any motion. Above this point (v), the in-plane field is larger than H_{DMI} and the DW has the opposite chirality: $\varphi \approx \pi$ and moves in the opposite direction. All these regions can also be explained considering the φ dependence of the H_x in-plane field:

$$\varphi = \arctan\left(\frac{H_{SHE}}{\alpha\left(H_{DMI} + H_x\right)}\right) \tag{4.2}$$

Obviously from Eq. 4.2, if H_x is larger than the DMI field H_{DMI} in the opposite direction, the φ angle is reversed which induces a reversal of the DW propagation direction. Also, if the in-plane field is exactly opposed the DMI effect, $H_x = -H_{DMI}$ then $\varphi \rightarrow \pm\pi/2$ *i.e.* the DW goes to its Bloch state.

Fig. 4.6 (c) shows the same type of DW velocity for different set-point temperatures T_{SP}. The other investigated temperatures are higher than T_{MC} that is why the configurations (iii-v) remain visible but not (i-ii). The current for which the propagation direction is reversed, denoted $J^\star$, is indicated by a star. It is possible to see that this reversal current decreases when T_{SP} increases which is consistent with a thermal effect: the temperature at which $H_x = H_{DMI}$ can be reached increasing T_{SP} or increasing J. Fig. 4.6 (d) shows for each T_{SP} the associated reversal current $J^\star$ (in a quadratic scale) for two different applied fields H_x: 90 and 175 mT. The quadratic relation between T_{SP} and the reversal current $J^\star$ validates the Joule heating process. The $J^\star$ are higher for lower H_x. Indeed, due to the decreasing of H_{DMI} after T_{MC}, the crossing between the fixed in-plane field H_x and the DMI field occurs for higher temperature (*i.e.* higher $J^\star$) if H_x is lower. The intersection of the two plotted lines corresponds to the temperature for which the DMI field is equal to the used H_x. Here $\mu_0 H_{DMI}=$ 90mT at $\sim 332K$ and 175 mT at $\sim 342K$.

To conclude, in this part we probe the DW motion driven by SOT under an in-plane field that can oppose the DMI field. This study allows us to get information about the internal DW in-plane angles φ that changes from $\varphi = 0 \rightarrow \pm\pi$. This reversal of φ gives information on the effective DMI field and confirms that it decreases just above the T_{MC}. At the opposite of classical procedure for measuring the DMI field with a variable in-plane field [14,20,86], here the in-plane field is fixed and the DMI is modified with the current (due to the Joule heating).

4.5 Domain wall driven by SOT under Hy

To get information about the sign of the DW in-plane angle φ, we measure the DW velocity driven by SOT under a transverse field $\pm H_y$ perpendicular to the current flow.

Fig. 4.7 (a) shows the DW velocity *versus* T_{SP} for a current density of $J=360\text{GA/m}^2$ and transverse fields of $\mu_0 H_y=0$ and ± 90 mT. With H_y, as without ($H_y=0$), the DW moves along the current direction but, for some ranges of T_{SP}, the DW is faster with positive H_y while in other ranges it is faster with negative H_y. Two crossing points are observed where $v(T_{SP}, +H_y) = v(T_{SP}, -H_y)$. They are more readily distinguished by plotting $\Delta v(T_{SP}) \equiv v(T_{SP}, +H_y) - v(T_{SP}, -H_y)$, shown in the bottom panel of Fig. 4.7 (a). Here the two crossing points are at $T_{SP}=$ 300 and 328 K. These observations hold for both current directions $\pm J$. Note that in this plot the Joule heating just induces a horizontal shift of the curves without any distortion.

Fig. 4.7 (b) shows all measured Δv in a color-plot as a function of T_{SP} and J. Three regions can be observed with, successively, $\Delta v < 0$, $\Delta v > 0$ and $\Delta v < 0$, separated by the two sets of crossing points plotted in white. The two sets of crossing points follow a parabolic relation, ($T_{crossing-point}(J) = T_{sp} + \kappa J^2$) consistent with the Joule heating. This shows that both crossing points occur at the same track temperatures independently of J. The fits of the two sets of crossing points (parallel parabolic lines in Fig. 4.7 (b)) are independent and give the same heating parameter. Here it is possible to say that all

crossing points occur along two isotherm lines which correspond to two temperatures of 312 K and 334 K.
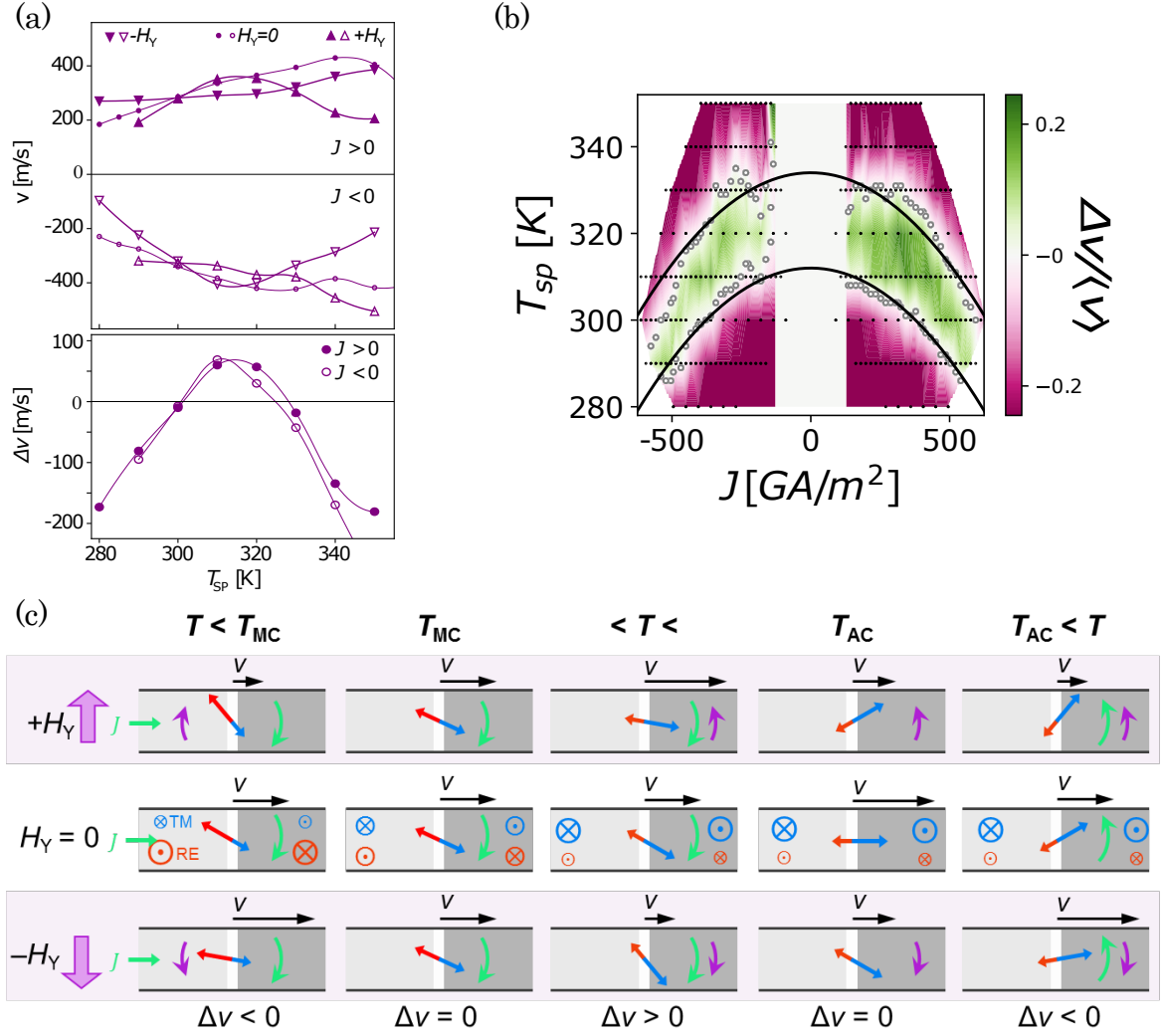
Figure 4.7 – SOT-driven DW with H_y. (a) Measured DW velocity v versus sample holder temperature T_{SP} with $H_y = \pm 90$ mT marked by up and down triangles or 0 mT indicated by dots, for $J = \pm 360 GA/m^2$. The down panel shows the velocity difference $\Delta v(T_{SP}) \equiv v(T_{SP}, +H_y) - v(T_{SP}, -H_y)$ for the same H_y and J of top panel. (b) Colour-plot in the plane (J, T_{SP}) of the normalized $\Delta v(T_{SP})/\langle v \rangle$ (with $\langle v \rangle = v(T_{SP}, +H_y) + v(T_{SP}, -H_y)$). Black points correspond to the experimental measurements. White points correspond to crossing points where $\Delta v = 0$. The black lines are two independent parabolic fits of the two sets of crossing points considering a Joule heating law. (c) Diagram of the sub-lattice orientations in a SOT-driven DW under H_y across compensation points. The red and blue arrows correspond to RE and TM, respectively. The purple curved arrows represent the torque due to H_y, and the green ones due to SOT.

To understand the effect of H_y on SOT-driven DWs in ferrimagnets, we first consider the well-understood ferromagnetic case. The transverse field H_y changes the velocity by affecting the angle of the DW magnetization φ [170]. The balance between the DMI (that stabilizes the Néel configuration, $\varphi = 0$), the torques induced by current (SOT) and the external field (through Zeeman interaction) gives:

$$\varphi = \arctan\left(\frac{\Delta}{D}\left(\frac{\hbar\Theta_{SH}}{2et}\frac{J}{\alpha} + \mu_0 M_S H_y\right)\right) \tag{4.3}$$

where Δ is the DW width parameter, D is the DMI parameter, α is the Gilbert damping parameter, $\hbar$ is the reduced Planck constant, e is the fundamental charge, Θ_{SH} is the spin Hall angle of the Pt layer,

and t is the magnetic film thickness. As $v \propto \cos(\varphi)$, the sign of Δv clearly shows whether H_y rotates φ closer to or farther from the Néel configuration of the DW. A positive Δv means that J and $+H_y$ have opposite contributions to φ, and that $+H_y$ brings the DW closer to the Néel configuration $\varphi \to 0$ increasing the DW velocity. Conversely, a negative Δv means that J and $+H_y$ contributions are in the same direction and push the DW farther than its Néel configuration reducing the DW velocity.

As discussed before (in section 1.3.4), in the RE-TM ferrimagnetic case, the field acts on both RE and TM sub-lattices, whereas the spin current interacts mostly with the TM sub-lattice (see [37] and references therein). The DW velocity can still be described with the same model using the φ angle of the TM sub-lattice and effective parameters of the alloy: $M_S \leftarrow (M_{TM} - M_{RE})$ and $\alpha \leftarrow \alpha_{eff}$ (as detailed in the part 2.2). The sign of these parameters changes with temperature, M_S at T_{MC} and α_{eff} at T_{AC}. The sketch in Fig. 4.7 (c) shows the effects of the SOT (green arrows) and H_y (purple arrows) on φ for different temperatures. Knowing beforehand the sign of M_S and measuring Δv, the sign of the effect of J on φ can be determined, which is a unique feature from DW propagation experiments. At $T < T_{MC}$, the RE sub-lattice is dominant ($M_{RE} > M_{TM}$) and M_S is negative. $+H_y$ rotates φ clockwise (CW). A negative Δv means that the current contribution to φ is also CW (1st column of Fig. 4.7 (c)). Above T_{MC}, M_S becomes positive and the effect of external fields is reversed. Now, a positive Δv means that the current contribution to φ is counterclockwise (CCW), whereas a negative Δv means that the current contribution is CW. At $T = T_{MC}$, M_S is 0 and H_y affects neither φ nor v (2nd column of Fig. 4.7 (c)) and $\Delta v = 0$. Furthermore, at this point, all the velocities with and without in-plane field are the same. The remarkable dynamic properties of ferrimagnets drastically change at $T = T_{AC}$; in particular, α_{eff} is expected to diverge and change sign (as detailed in the part 2.2) [146, 151, 152]. Consequently, from Eq. 4.3, the current contribution to φ should change sign across T_{AC} inducing a reversion of the Δv. Furthermore, at $T = T_{AC}$, the current effect on φ should vanish, $i.e.$ the DW should remain Néel (without field). Here, positive and negative H_y will induce a φ of opposite sign but of equal amplitude, decreasing equally the velocity, and thus $\Delta v = 0$ (4th column of Fig. 4.7 (c)). In a ferrimagnet, therefore, Δv changes sign at T_{MC} and T_{AC}. In the measurements, the two crossing points correspond to T_{MC} and T_{AC}, separating the three types of dynamics described in Fig. 4.7 (a) and (b). In particular, at T_{MC} the three velocities with all H_y configurations are equal: $v(\pm H_y) = v(H_y = 0)$ which corresponds to the first crossing point (Fig. 4.7 (a)). At the T_{AC}, the two velocities with $\pm H_y$ are equal and lower than without field: $v(+H_y) = v(-H_y) < v(H_y = 0)$ which corresponds to the second crossing point. It is possible to determine both the magnetic and angular compensation temperature: T_{MC}=312K and T_{AC}=334K. Note that these obtained T_{MC} and T_{AC} are consistent with the previous measurements of $Hc(T)$ and $|M_S|(T)$ (Fig. 4.1 (a)) and $\mu(J)$ in Fig. 4.4 (b)): $T_{MC} \approx$308 K and $T_{AC} \approx$342 K.

This study can be used as a routine method for determining both T_{MC} and T_{AC}. Indeed, this approach determines precisely the sense of the DW precession using a very large difference of DW velocity ($\Delta v \approx 100$m/s in the down panel Fig. 4.7 (a)) that gives T_{MC} and T_{AC} without requiring any material parameters. An other advantage is that we directly obtain the temperature difference between the two compensation points. As T_{MC} can be easily determined (See part 1.3), this method is an easy way to measure the T_{AC} which is usually much more challenging (as discussed in part 2.2.2). Furthermore, unlike the method of the peak of the DW mobility, this determination of T_{AC} is based on the intrinsic DW dynamics and so it is unaffected by pinning (as discussed above). Here, if a DW motion is observed, the binary character of Δv with $\pm H_y$ gives the value of the T_{MC} and the T_{AC}. Finally, changing the current density, this method also provides the heating law as fitted in the Fig. 4.7 (b). Fig. 4.8 shows the rescaled $\Delta v(T)$ curves using the measured heating law.

Finally, more than a new method to measure both magnetic and angular compensation temperatures, this study directly probes the magnetization reversal and shows that, at the angular compensation point, the in-plane angle of the DW φ remains zero during the DW propagation, $i.e.$ the magnetic moments do not precess during the reversal process. This measurement directly highlights the precession-free dynamics of the magnetic moments at the angular compensation point.
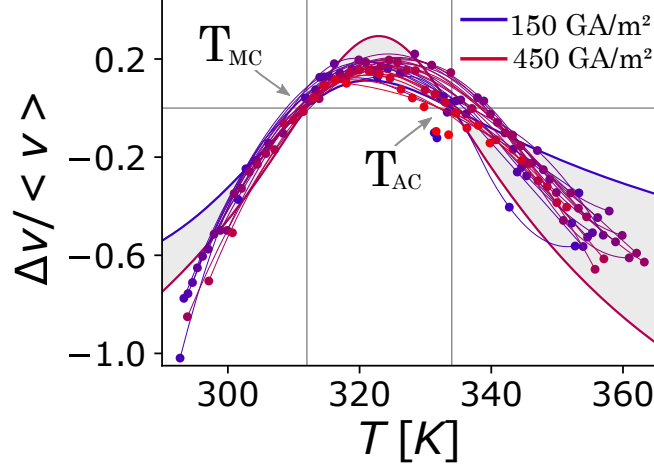
Figure 4.8 – Normalized $\Delta v / \langle v \rangle$ rescaled using the obtained heating parameter $\kappa = 8.4 \, 10^{-5} \frac{K}{GA/m^2}$ for all positive current densities. The envelope corresponds to the calculated values of $\Delta v / \langle v \rangle$ between $J = 150$ and $450 GA/m^2$ using the effective parameters as detailed in part 4.6.

4.6 Analytical calculation of SOT-driven domain wall dynamics with in-plane field

To validate our measurements, we calculate the expected behavior of the different measured quantities using the effective parameters approach presented in part. 2.2. Fig. 4.9 shows the ad-hoc effective parameters. Full lines correspond to the considered effective parameters and points correspond to experimental measurements: (a) the magnetization measured by SQUID, (b) the SOT efficiency measured by second harmonic Hall voltage (see Fig. 2.3) and the DMI field from the DW motion under H_x measurements (see Fig. 4.6). Here, only two parameters are not experimentally determined: Δ the domain wall width parameter and $\alpha(T)$ the effective damping parameter. We consider $\Delta = 20$ nm which is coherent with the XPEEM measurements (see Fig. **??**). We know that the effective damping parameter $\alpha(T)$ diverges at T_{AC} and we approximate it by an inverse linear law $\alpha(T) = \frac{12 \, K}{(T - T_{AC})}$, chosen to best reproduce the shape of the experimental curves. This value of $\alpha(T)$ can also be obtained considering $\alpha_{TM} = 3 \, 10^{-3}$ and $\alpha_{RE} = 9 \, 10^{-3}$ for each sub-lattice (see eq.2.16).
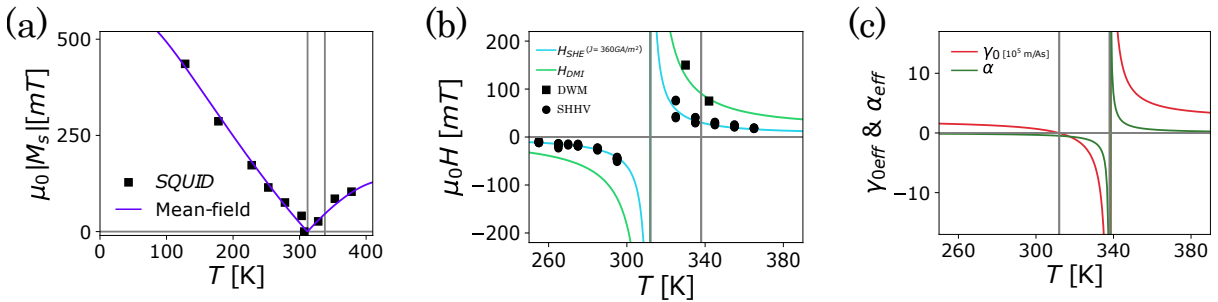
Figure 4.9 – Effective parameters used for the calculations of SOT-driven DW with in-plane field. (a) M_S measured by SQUID (squares) and calculated by the mean field model (line). (b) Effective SHE and DMI field H_{SHE} (blue) and H_{DMI} (green). Black dots show experimental values of H_{SHE} measured by second harmonic Hall voltage measurement (see Fig. 2.3) and black squares correspond to the measured H_{DMI} *via* DWM under SOT and H_x (see Fig. 4.6). (c) Effective gyromagnetic ratio γ_{0eff} (red curve), taking $\gamma_{0RE} = 2.21 \, 10^5 m/As$ and $\gamma_{0TM} = 2.27 \, 10^5 m/As$ to have the correct spacing between T_{MC} and T_{AC}. Effective damping parameter α_{eff} (green curve) considering $\alpha_{TM} = 3 \, 10^{-3}$ and $\alpha_{RE} = 9 \, 10^{-3}$.

Using these parameters, it is possible to calculate the theoretical DW dynamics driven by SOT under continuous external fields. Using the $q - \varphi$ model (see part 2.2), it is possible to determine both the DW velocity and the associated in-plane angle φ:

$$\begin{cases} v = \frac{\gamma_0 \Delta}{\alpha} \frac{\pi}{2} H_{SHE} \cos(\varphi) \\ \\ \varphi = \arctan\left(\frac{\frac{H_{SHE}}{\alpha} + H_y}{H_{DMI} + H_x}\right) \end{cases} \tag{4.4}$$

for $H_z = 0$. For H_z inferior to the Walker threshold ($H_z \ll \frac{\pi}{2} |\alpha H_{DMI}|$):

$$\begin{cases} v = \frac{\gamma_0 \Delta}{\alpha} \frac{\alpha^2 H_z\left((H_{DMI}+H_x)^2+H_y^2\right)+\alpha H_{SHE}\left(H_y H_z+(H_{DMI}+H_x)\sqrt{A\left(\frac{\pi}{2}\right)^2-H_z^2}\right)}{A} \\ \\ \varphi = \arccos\left(\frac{\frac{\alpha v}{\gamma_0 \Delta}-H_z}{\frac{\pi}{2}H_{SHE}}\right) \end{cases} \tag{4.5}$$

with $A = H_{SHE}^2 + 2\alpha H_{SHE} H_y + \alpha^2\left((H_{DMI}+H_x)^2 + H_y^2\right)$.
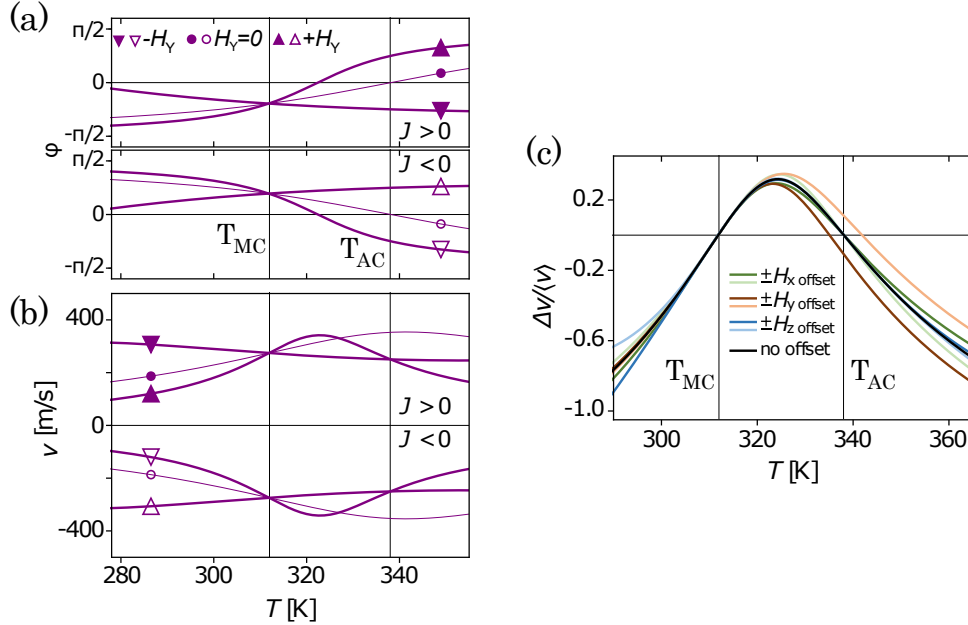
Figure 4.10 – Calculated internal angles φ and DW velocity using the effective parameter approach. (a) and (b) Internal DW angles φ and associated DW velocity from Eq.4.4 for $J = \pm 360 GA/m^2$ and $H_x = \pm 90$mT using the effective parameter approach shown Fig. 4.9 (similar to Fig. 4.7). (c) Normalized velocity difference: $\Delta v / \langle v \rangle = \frac{v(j,+H_x)-v(j,-H_x)}{v(j,+H_x)+v(j,-H_x)}$ for $J = \pm 360 GA/m^2$ and $H_x = \pm 90$mT (similar to Fig. 4.8) considering an external offset field of $\mu_0 H_{offset} = \pm 10$mT in the three directions (x, y, z) from Eq.4.5

Using this formula with the above effective parameters and considering the $\kappa = 8.4\,10^{-5} \frac{K}{GA/m^2}$ heating parameter, it is possible to reproduce with a relatively good agreement the measured velocity law as plotted Fig. 4.7 (a). Fig. 4.10 (a) shows the calculated φ angles of the DW driven by a 360GA/m^2 current density under or without a transverse in-plane field of $\mu_0 H_y = 90$ mT. As detailed in Fig. 4.7, at T_{MC} the field does not have any effect and the obtained in-plane angles are the same with and without transverse field. At the T_{AC}, without field, the φ angle is zero but with field the φ angle has the same amplitude but opposite direction for $\pm H_y$. It is possible to verify that this phenomenon does not depend on the current direction. Fig. 4.10 (b) shows the associated velocity of the angles shown in (a). There is a very good agreement with experimental data shown Fig. 4.7 (a). This good agreement allows us to roughly evaluate the DW internal angle $\varphi(T)$ using this calculation. We can check that at the first

crossing point, all three velocities (with and without field) are the same and, at the second crossing, that the velocities under $\pm H_y$ are equal and lower than without field. Calculating the normalized $\Delta v / \langle v \rangle$ it is also possible to reproduce the experimental values as shown with the envelope in Fig. 4.8.

We also use these theoretical calculations to measure the robustness of our measurement to an external parasitic offset field H_{offset}. Fig. 4.10 (c) shows the normalized $\Delta v / \langle v \rangle$ quantity for $\mu_0 H_y = \pm 90$ mT and $J = 360$ GA/m^2 considering an external offset field of $\mu_0 H_{offset} = \pm 10mT$ in the three directions (x, y, z). It is possible to verify the obtained $\Delta v / \langle v \rangle$ is the same at T_{MC} where the magnetic field does not have any effect, and that it deviates a little at the T_{AC} only for an offset field along the y direction. In addition to validating the robustness of the measurement, this calculation also shows that eventual effects such as, field-like torque or Oersted fields do not affect significantly the obtained results. The tiny different between $\Delta v(+J)$ and $\Delta v(-J)$ visible Fig. 4.7 (a) can come from these effects.

4.7   Conclusion

In this chapter, we investigated the precession-free dynamics of the magnetic reversal under the prism of the DW dynamics driven by SOT. First, we measured the DW motion without any field and we observed a mobility peak which is an indirect proof of the precession-free dynamics. In order to better characterize the internal DW dynamics, we probe its motion under an in-plane field opposed to the DMI. The reversal of its propagation direction gives directly its chirality and the magnitude of the DMI field. Secondly, we measured the DW dynamics under an in-plane field transverse to its propagation direction. This measurement allowed us to deduce the effect of the current on the internal magnetization of the DW, *i.e.* on the precession during the reversal process. This measurement directly reveals that the precession fully vanishes and changes its sign at the angular compensation point.

4.8   Perspectives

In order to probe the internal dynamics of a DW driven by SOT, another approach considering the macroscopic tilt of the DW can be used.

4.8.1   Macroscopic tilt of the domain wall

In the absence of an applied field, measuring the DWM driven by SOT along the magnetic track, a macroscopic tilt angle χ of the DW is observed [216]. Fig. 4.11 (a) shows a Kerr image of the macroscopic tilt of the DW in the absence of in-plane field. Fig. 4.11 (b) shows the measured DW tilt angle χ for different current densities and for different temperatures (rescaled considering the heating law measured in Fig. 4.7 (b)). It is possible to see that, by changing the current direction, the χ angle changes. Also, for a given current direction, the χ angle seems change its sign at the T_{AC}.

Two scenarios are proposed to explained this macroscopic tilt angle as shown in the Fig. 4.11 (c). On the one hand, due to SOT mechanism, during the DWM, the in-plane magnetization at the center of the DW deviates from its Néel configuration increasing the $|\varphi|$ angle and increasing the DMI energy. To reduce the DMI energy term, the DW tilts to reduce the angle between the internal magnetization and the normal of the DW $(q - \varphi - \chi$ model) [173]. One the other hand, it is proposed that during its propagation, the DW is bent. Combining this bending with the in-plane direction of the DW at its center, it is possible to see that the SOT is more efficient in one region of the DW (on the bottom part in the sketch) where φ is more perpendicular to the spin direction $\vec{\sigma}$. This part of the DW is faster, which induces a macroscopic tilt of the DW [217]. The validity of both scenarios depends on the width of the track, on the pinning at the track edges, and the stiffness of the DW, but in both theories the macroscopic tilt angle χ reveals the direction of the precession driven by SOT. Here χ seems to change its sign at the value of T_{AC} determined before, which could be another proof of the precession-free dynamics at this compensation point.
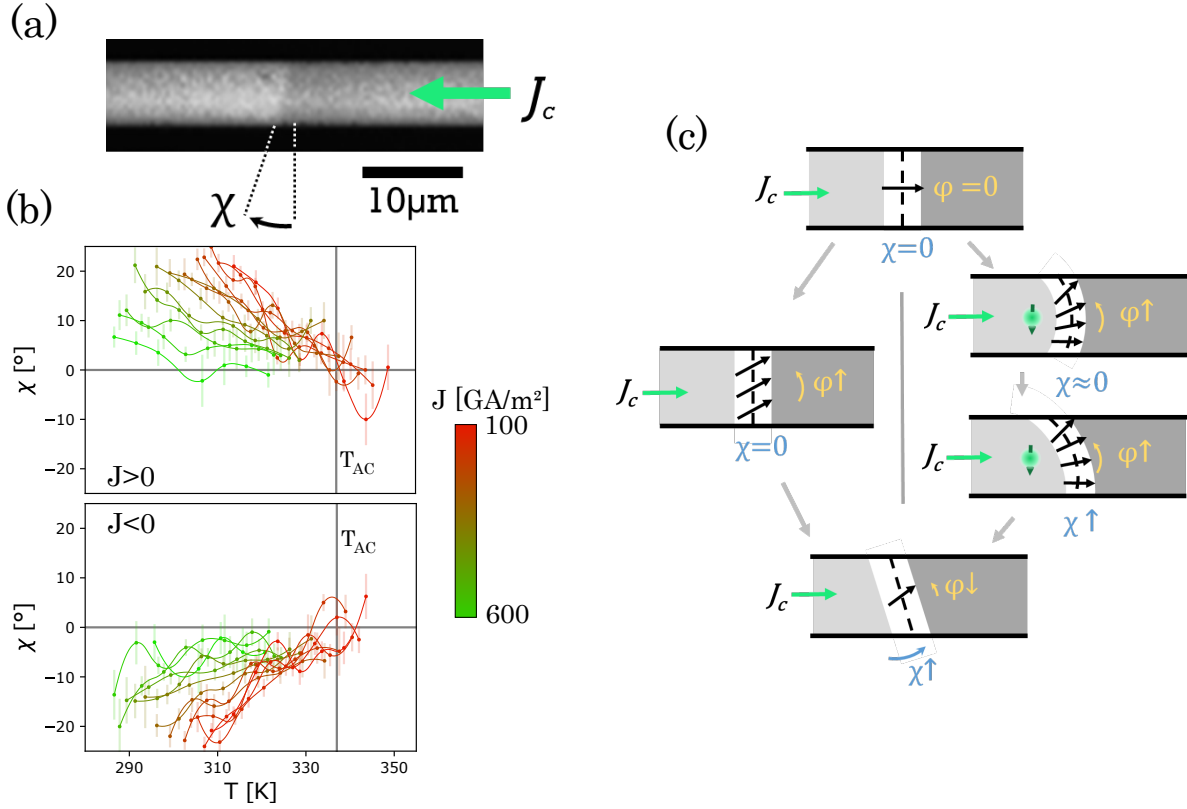
Figure 4.11 – Tilt of a SOT-driven DW. (a) Kerr image of the DW tilt angle χ. (b) Measured χ angle for different values of J and T_{SP} versus track temperature deduced using an heating parameter $\kappa = 8.4 \, 10^{-5} \frac{K}{GA/m^2}$ determined above. (c) Sketch of the two scenarios [173, 217] explaining the macroscopic DW tilting.

4.9 Contribution and publications

4.9.1 Collaborations

The magnetization shown Fig. 4.1 (a) was measured by Richard Mattana at the Unité Mixte de Physique CNRS/Thales in Palaiseau. All the presented work in this section was done in our laboratory. Torques measurements shown Fig. 4.9 (a) were down by Sachin Krishnia, a post-doc in our team.

4.9.2 Publication

The main part of these results is presented in an article on arXiv [42] and submitted to PRL.

Conclusions

In this manuscript, I presented the main results obtained on domain wall structure and dynamics in RE-TM ferrimagnetic alloys obtained during my thesis work.

- **Chapter 1** I investigated experimentally the static magnetic properties of RE-TM ferrimagnetic thin films deposited by co-evaporation. A large set of experimental methods was used to characterize the deposited thin films. This points out the coexistence of two different sub-lattices in these material. This study also demonstrates the complementarity of the sensitivity of the techniques. The spatial magnetization distribution was also probed using imaging techniques that revealed a perpendicularly magnetized domain pattern with suitable Domain Wall propagation properties. Finally, the correlation between a depth chemical gradient in films and interface-like effects which leads, for instance, to stabilized Néel DWs in stacks without any heavy-metal interface was highlighted.

- **Chapter 2** I developed a new effective model able to deal with both the static and dynamic properties of ferrimagnets and to support all experimental observations obtained in the thesis or in the literature. Using this model, the domain wall dynamics driven by field or spin-current was analyzed in details comparing analytical and numerical approaches. This study reveals new propagation regimes at the compensation points such as a precession-free dynamics or the vanishing of transient DW motions. Three methods corroborate the results obtained during this study: two methods based on collective coordinates by considering a finite or infinite coupling between sub-lattices and a numerical approach allowing much more degrees of freedom for the DW dynamics.

- **Chapter 3** I investigated experimentally the effect of the current on DWs in ferrimagnetic materials. Measuring the DW motion driven by combined effects of field and current in the creep regime, it was possible to quantify both the spin transfer-torque stiffness and the Joule heating amplitude. This study highlighted the high efficiency of the electrical manipulation of magnetic textures in these materials.

- **Chapter 4** I experimentally investigated the propagation of a magnetic DW driven by spin-orbit torque in a stack including a heavy-metal layer. Using in-plane fields, it was possible to fully resolve the internal DW structure during its motion. This study directly revealed DW record mobilities at the vanishing of the precession during the magnetization reversal at the angular compensation point.

All these results point out that RE-TM ferrimagnets have the required properties to be the future core element for the next spintronic developments. In particular, at compensation points, they have very interesting properties such a minimum size of magnetic textures or fast dynamic without any precession which address the two key challenges for future spintronic applications.

Perspectives

In order to continue this study, few perspectives should be addressed in priority.

From a material point of view, one of the main obstacles for the study of these artificial alloys is the high reactivity of their rare-earth components and the strong macroscopic consequences induced by their migration in the sample stacks. To limit the RE atoms migration or its effects, it could be interesting to spatially separate chemical components of the alloy like: GdCo→Co/Gd/Co or Gd/Co. In the first proposed configuration, the migration of Gd atoms is limited by the two Co layers and, in the second one, it should have less impact on the resulting magnetic properties. However, two drastic changes should impact the resulting magnetic properties. First, the antiferromagnetic inter-exchange coupling should be much lower due to the reduced number of Gd-Co atomic pairs. Secondly, the demagnetization effects can not be neglected anymore and should affect the resulting magnetization dynamics in such materials. Note that including these two proposed ferrimagnet-like stacks with peripheral Co layers in stacks containing heavy metal layer like Pt should increase the spin injection by SHE, the perpendicular anisotropy and the DMI, known to be very efficient for Pt/Co interfaces.

Both magnetic and angular compensation points present very interesting properties and, in the long term, it will be interesting to reduce the gap between these two points of interest as much as possible to take full benefits of all the advantages offered by ferrimagnetic alloys. In order to reduce this distance, it could be interesting to study more complex alloys mixing different rare-earth or transition-metal (like GdTbCo or GdFeCo) in order to have equal gyromagnetic ratios: $\gamma_{TM} = \gamma_{RE}$ and no longer a difference between both compensation points. However, it can be very complex to experimentally predict the variation of the gyromagnetic ratios of RE and TM components in the alloy structure. A DFT approach could give some interesting predictions.

To the best of our knowledge, the effective approach seems to corroborate all the experimental results measured in ferrimagnetic systems based on large-scale observations like spin texture dynamics. The existing results do not reveal independently variations of all the effective parameters. Even if the static parameters (like magnetization or field associated to spin torques or DMI) can be individually addressed by investigating saturated samples [45, 46] it is not the case for the dynamic parameters (γ_0 and α) where the existing results [151, 152] are not sufficient to validate the effective parameter model. In order to obtain clearer results, it could be interesting to probe these dynamic effective parameters, by measuring the magnetic resonance of saturated layers by Brilouin Light Scattering (BLS) [118]. Indeed, due to the chemical selectivity, this optical method addresses only one of the sub-lattices and, due to the strong magneto-optical activity of RE-based films, it should give a strong signal using the appropriated wave length. Preliminary results obtained in the group are indeed very promising. Furthermore, this method addresses directly the dynamic properties of the material (here the magnetic resonance) and, if it works, it can become a very efficient and easy way to measure the angular compensation point where these dynamic properties drastically change.

Finally, it seems very interesting to study the impact of the new ferrimagnetic dynamics in other magnetic textures including non trivial topologies such as vortex DW or skyrmions. Indeed, in these types of texture, the precession induces complex dynamics (like the well-known topological deflection of skyrmions) and it could be interesting to study these dynamics when the precession vanishes or is reversed.

[1] Jacob Torrejon, Mathieu Riou, Flavio Abreu Araujo, Sumito Tsunegi, Guru Khalsa, Damien Querlioz, Paolo Bortolotti, Vincent Cros, Kay Yakushiji, Akio Fukushima, Hitoshi Kubota, Shinji Yuasa, Mark D. Stiles, and Julie Grollier. Neuromorphic computing with nanoscale spintronic oscillators. *Nature*, 547(7664):428–431, jul 2017.

[2] Stuart Parkin and See-Hun Yang. Memory on the racetrack. *Nature Nanotechnology*, 10(3):195–198, mar 2015.

[3] A. J. Annunziata, M. C. Gaidis, L. Thomas, C. W. Chien, C. C. Hung, P. Chevalier, E. J. O'Sullivan, J. P. Hummel, E. A. Joseph, Y. Zhu, T. Topuria, E. Delenia, P. M. Rice, S. S. P. Parkin, and W. J. Gallagher. Racetrack memory cell array with integrated magnetic tunnel junction readout. In *2011 International Electron Devices Meeting*, number c, pages 24.3.1–24.3.4. IEEE, dec 2011.

[4] Albert Fert, Vincent Cros, and João Sampaio. Skyrmions on the track. *Nature Nanotechnology*, 8(3):152–156, 2013.

[5] R Tomasello, E Martinez, R Zivieri, L Torres, M Carpentieri, and G Finocchio. A strategy for the design of skyrmion racetrack memories. *Scientific Reports*, 4(1):6784, may 2015.

[6] George Bourianoff, Daniele Pinna, Matthias Sitte, and Karin Everschor-Sitte. Potential implementation of reservoir computing models based on magnetic skyrmions. *AIP Advances*, 8(5), 2018.

[7] D. Pinna, F. Abreu Araujo, J. V. Kim, V. Cros, D. Querlioz, P. Bessiere, J. Droulez, and J. Grollier. Skyrmion Gas Manipulation for Probabilistic Computing. *Physical Review Applied*, 9(6):64018, 2018.

[8] Zhaochu Luo, Trong Phuong Dao, Aleš Hrabec, Jaianth Vijayakumar, Armin Kleibert, Manuel Baumgartner, Eugenie Kirk, Jizhai Cui, Tatiana Savchenko, Gunasheel Krishnaswamy, Laura J. Heyderman, and Pietro Gambardella. Chirally coupled nanomagnets. *Science*, 363(6434):1435–1439, 2019.

[9] Steven Lequeux, Joao Sampaio, Vincent Cros, Kay Yakushiji, Akio Fukushima, Rie Matsumoto, Hitoshi Kubota, Shinji Yuasa, and Julie Grollier. A magnetic synapse: multilevel spin-torque memristor with perpendicular anisotropy. *Scientific Reports*, 6(1):31510, nov 2016.

[10] Jong Min Lee, Kaiming Cai, Guang Yang, Yang Liu, Rajagopalan Ramaswamy, Pan He, and Hyunsoo Yang. Field-Free Spin-Orbit Torque Switching from Geometrical Domain-Wall Pinning. *Nano Letters*, 18(8):4669–4674, 2018.

[11] Kamil Olejník, Tom Seifert, Zdeněk Kašpar, Vít Novák, Peter Wadley, Richard P. Campion, Manuel Baumgartner, Pietro Gambardella, Petr Němec, Joerg Wunderlich, Jairo Sinova, Petr

Kužel, Melanie Müller, Tobias Kampfrath, and Tomas Jungwirth. Terahertz electrical writing speed in an antiferromagnetic memory. *Science Advances*, 4(3):eaar3566, mar 2018.

[12] See-Hun Yang, Kwang-Su Ryu, and Stuart Parkin. Domain-wall velocities of up to 750 m s-1 driven by exchange-coupling torque in synthetic antiferromagnets. *Nature Nanotechnology*, 10(3):221–226, mar 2015.

[13] Kab-Jin Kim, Se Kwon Kim, Yuushou Hirata, Se-Hyeok Oh, Takayuki Tono, Duck-Ho Kim, Takaya Okuno, Woo Seung Ham, Sanghoon Kim, Gyoungchoon Go, Yaroslav Tserkovnyak, Arata Tsukamoto, Takahiro Moriyama, Kyung-Jin Lee, and Teruo Ono. Fast domain wall motion in the vicinity of the angular momentum compensation temperature of ferrimagnets. *Nature Materials*, 16(12):1187–1192, dec 2017.

[14] Lucas Caretta, Maxwell Mann, Felix Büttner, Kohei Ueda, Bastian Pfau, Christian M. Günther, Piet Hessing, Alexandra Churikova, Christopher Klose, Michael Schneider, Dieter Engel, Colin Marcus, David Bono, Kai Bagschik, Stefan Eisebitt, and Geoffrey S.D. Beach. Fast current-driven domain walls and small skyrmions in a compensated ferrimagnet. *Nature Nanotechnology*, 13(12):1154–1160, 2018.

[15] Robin Bläsing, Tianping Ma, See-Hun Yang, Chirag Garg, Fasil Kidane Dejene, Alpha T. N'Diaye, Gong Chen, Kai Liu, and Stuart S. P. Parkin. Exchange coupling torque in ferrimagnetic Co/Gd bilayer maximized near angular momentum compensation temperature. *Nature Communications*, 9(1):4984, dec 2018.

[16] Ales Hrabec, Viola Krizakova, Stefania Pizzini, João Sampaio, André Thiaville, Stanislas Rohart, and Jan Vogel. Velocity Enhancement by Synchronization of Magnetic Domain Walls. *Physical Review Letters*, 120(22):227204, may 2018.

[17] A. Hrabec, J. Sampaio, M. Belmeguenai, I. Gross, R. Weil, S. M. Chérif, A. Stashkevich, V. Jacques, A. Thiaville, and S. Rohart. Current-induced skyrmion generation and dynamics in symmetric bilayers. *Nature Communications*, 8:1–6, 2017.

[18] Can Onur Avci, Ethan Rosenberg, Lucas Caretta, Felix Büttner, Maxwell Mann, Colin Marcus, David Bono, Caroline A. Ross, and Geoffrey S. D. Beach. Interface-driven chiral magnetism and current-driven domain walls in insulating magnetic garnets. *Nature Nanotechnology*, 14(6):561–566, jun 2019.

[19] T. Jungwirth, X. Marti, P. Wadley, and J. Wunderlich. Antiferromagnetic spintronics. *Nature Nanotechnology*, 11(3):231–241, 2016.

[20] Saima A. Siddiqui, Jiahao Han, Joseph T. Finley, Caroline A. Ross, and Luqiao Liu. Current-Induced Domain Wall Motion in a Compensated Ferrimagnet. *Physical Review Letters*, 121(5):57701, 2018.

[21] Yuushou Hirata, Duck Ho Kim, Se Kwon Kim, Dong Kyu Lee, Se Hyeok Oh, Dae Yun Kim, Tomoe Nishimura, Takaya Okuno, Yasuhiro Futakawa, Hiroki Yoshikawa, Arata Tsukamoto, Yaroslav Tserkovnyak, Yoichi Shiota, Takahiro Moriyama, Sug Bong Choe, Kyung Jin Lee, and Teruo Ono. Vanishing skyrmion Hall effect at the angular momentum compensation temperature of a ferrimagnet. *Nature Nanotechnology*, 14(3):232–236, 2019.

[22] Seonghoon Woo, Kyung Mee Song, Xichao Zhang, Yan Zhou, Motohiko Ezawa, Xiaoxi Liu, S. Finizio, J. Raabe, Nyun Jong Lee, Sang Il Kim, Seung Young Park, Younghak Kim, Jae Young Kim, Dongjoon Lee, Oukjae Lee, Jun Woo Choi, Byoung Chul Min, Hyun Cheol Koo, and Joonyeon Chang. Current-driven dynamics and inhibition of the skyrmion Hall effect of ferrimagnetic skyrmions in GdFeCo films. *Nature Communications*, 9(1):9–16, 2018.

[23] F. Keffer and C. Kittel. Theory of antiferromagnetic resonance. *Physical Review*, 85(2):329–337, 1952.

[24] P. Stremoukhov, A. Safin, M. Logunov, S. Nikitov, and A. Kirilyuk. Spintronic terahertz-frequency nonlinear emitter based on the canted antiferromagnet-platinum bilayers. *Journal of Applied Physics*, 125(22), 2019.

[25] Se-Hyeok Oh, Se Kwon Kim, Dong-Kyu Lee, Gyungchoon Go, Kab-Jin Kim, Teruo Ono, Yaroslav Tserkovnyak, and Kyung-Jin Lee. Coherent terahertz spin-wave emission associated with ferrimagnetic domain wall dynamics. *Physical Review B*, 96(10):1–5, 2017.

[26] E. V. Gomonay and V. M. Loktev. Spintronics of antiferromagnetic systems (Review Article). *Low Temperature Physics*, 40(1):17–35, 2014.

[27] Panagiotis Ch Filippou, Jaewoo Jeong, Yari Ferrante, See-Hun Yang, Teya Topuria, Mahesh G. Samant, and Stuart S. P. Parkin. Chiral domain wall motion in unit-cell thick perpendicularly magnetized Heusler films prepared by chemical templating. *Nature Communications*, 9(1):4653, dec 2018.

[28] S. K. Malik, F. J. Arlinghaus, and W. E. Wallace. Spin-polarized energy-band structure of YCo5, SmCo5 and GdCo5. *Physical Review B*, 16(3):1242–1248, aug 1977.

[29] Hiroshi Tanaka and Shinji Takayama. Electronic structure calculations for GdCo amorphous alloys. *Journal of Applied Physics*, 70(10):6577–6579, nov 1991.

[30] P. Hansen, C. Clausen, G. Much, M. Rosenkranz, and K. Witter. Magnetic and magneto optical properties of rare earth transition metal alloys containing Gd, Tb, Fe, Co. *Journal of Applied Physics*, 66(2):756–767, jul 1989.

[31] Yuushou Hirata, Duck Ho Kim, Takaya Okuno, Tomoe Nishimura, Dae Yun Kim, Yasuhiro Futakawa, Hiroki Yoshikawa, Arata Tsukamoto, Kab Jin Kim, Sug Bong Choe, and Teruo Ono. Correlation between compensation temperatures of magnetization and angular momentum in GdFeCo ferrimagnets. *Physical Review B*, 97(22):1–6, 2018.

[32] Felix Büttner, Ivan Lemesh, and Geoffrey S.D. Beach. Theory of isolated magnetic skyrmions: From fundamentals to room temperature applications. *Scientific Reports*, 8(1):1–12, 2018.

[33] K. Xu, J. S. Feng, Z. P. Liu, and H. J. Xiang. Origin of Ferrimagnetism and Ferroelectricity in Room-Temperature Multiferroic μ-Fe2O3. *Physical Review Applied*, 9(4):1–7, 2018.

[34] A.P. Malozemoff and J.C. Slonczewski. Magnetic Domain Walls in Bubble Materials. In *Magnetic Domain Walls in Bubble Materials*, pages 269–292. Elsevier, 1979.

[35] J. J.M. Franse and R. J. Radwański. Chapter 5 Magnetic properties of binary rare-earth 3d-transition-metal intermetallic compounds. *Handbook of Magnetic Materials*, 7:307–501, 1993.

[36] D. Weller, W. Reim, and P. Schrijner. Electronic and magneto-optical properties of ion beam sputtered rare earth-FeCo thin films. *IEEE Transactions on Magnetics*, 24(6):2554–2556, 1988.

[37] E. Haltz, R. Weil, J. Sampaio, A. Pointillon, O. Rousseau, K. March, N. Brun, Z. Li, E. Briand, C. Bachelet, Y. Dumont, and A. Mougin. Deviations from bulk behavior in TbFe(Co) thin films: Interfaces contribution in the biased composition. *Physical Review Materials*, 2(10):104410, oct 2018.

[38] J. Daval and B. Bechevet. Rare earth transition metal alloys for magneto-optical recording. *Journal of Magnetism and Magnetic Materials*, 129(1):98–107, jan 1994.

[39] S. Mangin, M. Gottwald, C-H. Lambert, D. Steil, V. Uhlíř, L. Pang, M. Hehn, S. Alebrand, M. Cinchetti, G. Malinowski, Y. Fainman, M. Aeschlimann, and E. E. Fullerton. Engineered materials for all-optical helicity-dependent magnetic switching. *Nature Materials*, 13(3):286–292, mar 2014.

[40] Birgit Hebler, Alexander Hassdenteufel, Patrick Reinhardt, Helmut Karl, and Manfred Albrecht. Ferrimagnetic Tb-Fe Alloy Thin Films: Composition and Thickness Dependence of Magnetic Properties and All-Optical Switching. *Frontiers in Materials*, 3(February):1–8, feb 2016.

[41] E. Haltz, J. Sampaio, R. Weil, Y. Dumont, and A. Mougin. Strong current actions on ferrimagnetic domain walls in the creep regime. *Physical Review B*, 99(10):104413, mar 2019.

[42] E. Haltz, J. Sampaio, S. Krishnia, L. Berges, R. Weil, and A. Mougin. Precession-free domain wall dynamics in compensated ferrimagnets. (Dmi), aug 2019.

[43] Niklas Roschewsky, Tomoya Matsumura, Suraj Cheema, Frances Hellman, Takeshi Kato, Satoshi Iwata, and Sayeef Salahuddin. Spin-orbit torques in ferrimagnetic GdFeCo alloys. *Applied Physics Letters*, 109(11):9–12, 2016.

[44] Kohei Ueda, Maxwell Mann, Paul W.P. De Brouwer, David Bono, and Geoffrey S.D. Beach. Temperature dependence of spin-orbit torques across the magnetic compensation point in a ferrimagnetic TbCo alloy film. *Physical Review B*, 96(6):1–6, 2017.

[45] Woo Seung Ham, Sanghoon Kim, Duck Ho Kim, Kab Jin Kim, Takaya Okuno, Hiroki Yoshikawa, Arata Tsukamoto, Takahiro Moriyama, and Teruo Ono. Temperature dependence of spin-orbit effective fields in Pt/GdFeCo bilayers. *Applied Physics Letters*, 110(24), 2017.

[46] Niklas Roschewsky, Charles Henri Lambert, and Sayeef Salahuddin. Spin-orbit torque switching of ultralarge-thickness ferrimagnetic GdFeCo. *Physical Review B*, 96(6):1–5, 2017.

[47] I. A. Campbell. Indirect exchange for rare earths in metals. *Journal of Physics F: Metal Physics*, 2(3), 1972.

[48] J J Cuomo, P. Chaudhari, and R. J. Gambino. Amorphous Metallic Films for Bubble Domain. *IBM Journal of Research and Development*, 17(1), 1973.

[49] Ales Hrabec. *Domain wall dynamics in magnetic nanostructures : Effect of magnetic field and electric current.* PhD thesis, Univ Grenoble, 2012.

[50] M. D. Kuz'min, Y. Skourski, D. Eckert, M. Richter, K.-H. Müller, K. P. Skokov, and I. S. Tereshina. Spin reorientation in high magnetic fields and the Co-Gd exchange field in GdCo. *Physical Review B*, 70(17):172412, nov 2004.

[51] Nguyen Thanh Nam. *Fabrication and Study of magnetic and transport properties of GdCo thin films, GdCo-based multilayers and Fe/Cr multilayers.* PhD thesis, Univ Grenoble, 2007.

[52] A. Gangulee and R. C. Taylor. Mean field analysis of the magnetic properties of vapor deposited amorphous Fe-Gd thin films. *Journal of Applied Physics*, 49(3):1762–1764, 1978.

[53] J. M.D. Coey. Amorphous magnetic order. *Journal of Applied Physics*, 49(3):1646–1652, 1978.

[54] Christoph J. Raub. *Handbook of magnetic materials, volume 6*, volume 191. 1993.

[55] Michel Cyrot, Michel Decorps, Bernard Dieny, Olivier Geofroy, Damien Gignoux, Claudine Lacroix, Jean Laforest, Philippe Leuthuillier, Pierre Molho, Jean-Claude Peuzin, Jacques Pierre, Jean-Louis Porteseil, Pierre Rochette, Michel-Francois Rossignol, Michel Schlenker, Christoph Segebarth, Yves Souche, Etienne du Tremolet de Lacheisserie, and Jea-Paul Yonnet. *Magnetisme I Fondements.* Edp scienc edition, 2000.

[56] E C Stoner. Collective electron specific heat and spin paramagnetism in metals. *Proceedings of the Royal Society of London. Series A - Mathematical and Physical Sciences*, 154(883):656–678, may 1936.

[57] The Heisenberg. Collective electron ferronnagnetism. *Proceedings of the Royal Society of London. Series A. Mathematical and Physical Sciences*, 165(922):372–414, apr 1938.

[58] J. P. Liu, X. P. Zhong, F. R. de Boer, and K. H. J. Buschow. Magnetic coupling in CaCu5-type rare-earth cobalt compounds. *Journal of Applied Physics*, 69(8):5536–5538, apr 1991.

[59] Pierre Weiss. L'hypothèse du champ moléculaire et la propriété ferromagnétique. *J. Phys. Theor. Appl.*, (6):661–690, 1907.

[60] T. M. Danh, N. H. Duc, and N. P. Thuy. Exchange interactions in amorphous Gd-Fe alloys. *Journal of Magnetism and Magnetic Materials*, 185(1):105–108, 1998.

[61] G. S. Cargill. Ferromagnetism in amorphous solids. In *AIP Conference Proceedings*, volume 24, pages 138–144. AIP, 1975.

[62] M. Mansuripur and M. Ruane. Mean-field analysis of amorphous rare earth-transition metal alloys for thermomagnetic recording. *IEEE Transactions on Magnetics*, 22(1):33–43, 2004.

[63] T Shirakawa, Y Nakajima, K Okamoto, S Matsushita, and Y Sakurai. The Kerr and the Hall Effects in Amorphous Magnetic Films. *AIP Conference Proceedings*, 34(1):52–55, 1976.

[64] L. G. Parratt. Surface Studies of Solids by Total Reflection of X-Rays. *Physical Review*, 95(2):359–369, jul 1954.

[65] Yoshio Murakami, Takayuki Shingyoji, and Kenichi Hijikata. Uniformity and composition of Tb x Fe 1-x films prepared by magnetron sputtering using different types of targets. *Journal of Applied Physics*, 68(4):1866–1868, aug 1990.

[66] C.-O. Bacri, C. Bachelet, C. Baumier, J. Bourçois, L. Delbecq, D. Ledu, N. Pauwels, S. Picard, S. Renouf, and C. Tanguy. SCALP, a platform dedicated to material modifications and characterization under ion beam. *Nuclear Instruments and Methods in Physics Research Section B: Beam Interactions with Materials and Atoms*, 406:48–52, sep 2017.

[67] Wei-Tan Chu, James W Mayer, and Marca Nicolet. Backscattering Spectrometry. *Academic press New York San Francisco London 1978*, 1978.

[68] Maria Varela, Jaume Gazquez, Timothy J Pennycook, Cesar Magen, Mark P Oxley, and Stephen J Pennycook. *Scanning Transmission Electron Microscopy*. Springer New York, New York, NY, 2011.

[69] N. Bergeard, A. Mougin, M. Izquierdo, E. Fonda, and F. Sirotti. Correlation between structure, electronic properties, and magnetism in GdxCo1-x thin amorphous films. *Physical Review B*, 96(6):064418, aug 2017.

[70] Duck Ho Kim, Mitsutaka Haruta, Hye Won Ko, Gyungchoon Go, Hyeon Jong Park, Tomoe Nishimura, Dae Yun Kim, Takaya Okuno, Yuushou Hirata, Yasuhiro Futakawa, Hiroki Yoshikawa, Wooseung Ham, Sanghoon Kim, Hiroki Kurata, Arata Tsukamoto, Yoichi Shiota, Takahiro Moriyama, Sug Bong Choe, Kyung Jin Lee, and Teruo Ono. Bulk Dzyaloshinskii-Moriya interaction in amorphous ferrimagnetic alloys. *Nature Materials*, 18(7):685–690, 2019.

[71] D. Mergel, H. Heitmann, and P. Hansen. Pseudocrystalline model of the magnetic anisotropy in amorphous rare-earth-transition-metal thin films. *Physical Review B*, 47(2):882–891, jan 1993.

[72] S. Miyanishi, K. Kojima, J. Sato, K. Takayama, H. Fuji, A. Takahashi, K. Ohta, and H. Katayama. High-density laser-assisted magnetic recording on TbFeCo media with an Al underlayer. *Journal of Applied Physics*, 93(10 3):7801–7803, 2003.

[73] David Jiles. *Introduction to Magnetism and Magnetic Materials*. Springer US, Boston, MA, 1991.

[74] F.J.A den Broeder, W. Hoving, and P.J.H Bloemen. Magnetic anisotropy of multilayers. *J. Magn. Magn. Mater.*, 93(C):562–570, 1991.

[75] Hyung Keun Gweon, Seok Jin Yun, and Sang Ho Lim. A very large perpendicular magnetic anisotropy in Pt/Co/MgO trilayers fabricated by controlling the MgO sputtering power and its thickness. *Scientific Reports*, 8(1):1266, dec 2018.

[76] V.G. Harris, K.D. Aylesworth, B.N. Das, W.T. Elam, and N.C. Koon. Structural origins of magnetic anisotropy in amorphous Fe-Tb films and multilayers. In *1992. Digests of Intermag. International Magnetics Conference*, volume 69, pages 355–355. IEEE, 1992.

[77] Tôru Moriya. Anisotropic Superexchange Interaction and Weak Ferromagnetism. *Physical Review*, 120(1):91–98, oct 1960.

[78] I. E. Dzialoshinskii. Thermodynamic theory of weak ferromagnetism in antiferromagnetic substances. *Soviet Physics Jetp-Ussr*, 5:1259, 1957.

[79] Hongxin Yang, André Thiaville, Stanislas Rohart, Albert Fert, and Mairbek Chshiev. Anatomy of Dzyaloshinskii-Moriya Interaction at Co/Pt Interfaces. *Physical Review Letters*, 115(26), 2015.

[80] X. Z. Yu, Y. Onose, N. Kanazawa, J. H. Park, J. H. Han, Y. Matsui, N. Nagaosa, and Y. Tokura. Real-space observation of a two-dimensional skyrmion crystal. *Nature*, 465(7300):901–904, 2010.

[81] Olivier Boulle, Jan Vogel, Hongxin Yang, Stefania Pizzini, Dayane De Souza Chaves, Andrea Locatelli, Alessandro Menteş, Tevfik Onur Sala, Liliana D. Buda-Prejbeanu, Olivier Klein, Mohamed Belmeguenai, Yves Roussigné, Andrey Stashkevich, Salim Mourad Chérif, Lucia Aballe, Michael Foerster, Mairbek Chshiev, Stéphane Auffret, Ioan Mihai Miron, and Gilles Gaudin. Room-temperature chiral magnetic skyrmions in ultrathin magnetic nanostructures. *Nature Nanotechnology*, 11(5):449–454, 2016.

[82] W. Jiang, P. Upadhyaya, W. Zhang, G. Yu, M. B. Jungfleisch, F. Y. Fradin, J. E. Pearson, Y. Tserkovnyak, K. L. Wang, O. Heinonen, S. G. E. te Velthuis, and A. Hoffmann. Blowing magnetic skyrmion bubbles. *Science*, 349(6245):283–286, jul 2015.

[83] Seonghoon Woo, Kai Litzius, Benjamin Krüger, Mi Young Im, Lucas Caretta, Kornel Richter, Maxwell Mann, Andrea Krone, Robert M. Reeve, Markus Weigand, Parnika Agrawal, Ivan Lemesh, Mohamad Assaad Mawass, Peter Fischer, Mathias Kläui, and Geoffrey S.D. Beach. Observation of room-temperature magnetic skyrmions and their current-driven dynamics in ultrathin metallic ferromagnets. *Nature Materials*, 15(5):501–506, 2016.

[84] I. Gross, W. Akhtar, V. Garcia, L. J. Martínez, S. Chouaieb, K. Garcia, C. Carrétéro, A. Barthélémy, P. Appel, P. Maletinsky, J. V. Kim, J. Y. Chauleau, N. Jaouen, M. Viret, M. Bibes, S. Fusil, and V. Jacques. Real-space imaging of non-collinear antiferromagnetic order with a single-spin magnetometer. *Nature*, 549(7671):252–256, 2017.

[85] André Thiaville, Stanislas Rohart, Émilie Jué, Vincent Cros, and Albert Fert. Dynamics of Dzyaloshinskii domain walls in ultrathin magnetic films. *EPL (Europhysics Letters)*, 100(5):57002, dec 2012.

[86] A. Hrabec, N. A. Porter, A. Wells, M. J. Benitez, G. Burnell, S. McVitie, D. McGrouther, T. A. Moore, and C. H. Marrows. Measuring and tailoring the Dzyaloshinskii-Moriya interaction in perpendicularly magnetized thin films. *Physical Review B - Condensed Matter and Materials Physics*, 90(2):1–5, 2014.

[87] Emilie Jué, C. K. Safeer, Marc Drouard, Alexandre Lopez, Paul Balint, Liliana Buda-Prejbeanu, Olivier Boulle, Stephane Auffret, Alain Schuhl, Aurelien Manchon, Ioan Mihai Miron, and Gilles Gaudin. Chiral damping of magnetic domain walls. *Nature Materials*, 15(3):272–277, mar 2016.

[88] L. Rondin, J. P. Tetienne, T. Hingant, J. F. Roch, P. Maletinsky, and V. Jacques. Magnetometry with nitrogen-vacancy defects in diamond. *Reports on Progress in Physics*, 77(5), 2014.

[89] J. P. Tetienne, L. Rondin, P. Spinicelli, M. Chipaux, T. Debuisschert, J. F. Roch, and V. Jacques. Magnetic-field-dependent photodynamics of single NV defects in diamond: An application to qualitative all-optical magnetic imaging. *New Journal of Physics*, 14, 2012.

[90] J. P. Tetienne, T. Hingant, L. J. Martínez, S. Rohart, A. Thiaville, L. Herrera Diez, K. Garcia, J. P. Adam, J. V. Kim, J. F. Roch, I. M. Miron, G. Gaudin, L. Vila, B. Ocker, D. Ravelosona, and V. Jacques. The nature of domain walls in ultrathin ferromagnets revealed by scanning nanomagnetometry. *Nature Communications*, 6:1–6, 2015.

[91] E. H. Hall. On the new action of magnetism on a permanent electric current. *American Journal of Science*, s3-20(117):161–186, 1880.

[92] E.H. Hall. On the Rotational Coefficient in nickel and cobalt. *The London, Edinburgh, and Dublin Philosophical Magazine and Journal of Science*, 12(74):157–172, sep 1881.

[93] L. Berger and G. Bergmann. The Hall Effect of Ferromagnets. In *The Hall Effect and Its Applications*, pages 55–76. Springer US, Boston, MA, 1980.

[94] R. C. Barklie. The Hall effect in Permaloy. *Philosophical Magazine*, 23(181):175–189, jan 1971.

[95] Emerson M. Pugh and Norman Rostoker. Hall effect in ferromagnetic materials. *Reviews of Modern Physics*, 25(1):151–157, 1953.

[96] J. M. Luttinger. Theory of the Hall Effect in Ferromagnetic Substances. *Physical Review*, 112(3):739–751, nov 1958.

[97] A. Gerber, A. Milner, A. Finkler, M. Karpovski, L. Goldsmith, J. Tuaillon-Combes, O. Boisron, P. Mélinon, and A. Perez. Correlation between the extraordinary Hall effect and resistivity. *Physical Review B - Condensed Matter and Materials Physics*, 69(22):1–8, 2004.

[98] L. Berger. Side-jump mechanism for the Hall effect of ferromagnets. *Physical Review B*, 2(11):4559–4566, 1970.

[99] John Kerr. On rotation of the plane of polarization by reflection from the pole of a magnet. *The London, Edinburgh, and Dublin Philosophical Magazine and Journal of Science*, 3(19):321–343, may 1877.

[100] R.Schaefer. *Handbook of Magnetism and Advanced Magnetic Materials, 5 Volume Set*. 2007.

[101] Z Q Qiu and S D Bader. Surface magneto-optic Kerr effect Surface magneto-optic Kerr effect. *Review of Scientific Instruments*, 71(3):1243, 2000.

[102] Jaroslav Hamrle. *Magneto-optical determination of the in-depth magnetization profile in magnetic multilayers.* PhD thesis, Charles Univ. Prague, 2003.

[103] Amalio Fernández-Pacheco, Robert Streubel, Olivier Fruchart, Riccardo Hertel, Peter Fischer, and Russell P. Cowburn. Three-dimensional nanomagnetism. *Nature communications*, 8:15756, 2017.

[104] A. Masseboeuf, O. Fruchart, J. C. Toussaint, E. Kritsikis, L. Buda-Prejbeanu, F. Cheynis, P. Bayle-Guillemaud, and A. Marty. Dimensionality crossover in magnetism: From domain walls (2D) to vortices (1D). *Physical Review Letters*, 104(12):2–5, 2010.

[105] Stavros Komineas and Nikos Papanicolaou. Dynamics of vortex-antivortex pairs in ferromagnets. *arXiv*, pages 1–18, dec 2007.

[106] S. Rohart and A. Thiaville. Skyrmion confinement in ultrathin film nanostructures in the presence of Dzyaloshinskii-Moriya interaction. *Physical Review B - Condensed Matter and Materials Physics*, 88(18):1–8, 2013.

[107] Anne Bernand-Mantel, Lorenzo Camosi, Alexis Wartelle, Nicolas Rougemaille, Michaël Darques, and Laurent Ranno. The skyrmion-bubble transition in a ferromagnetic thin film. *SciPost Physics*, 4(5):027, may 2018.

[108] Lorenzo Camosi, Nicolas Rougemaille, Olivier Fruchart, Jan Vogel, and Stanislas Rohart. Micromagnetics of antiskyrmions in ultrathin films. *Physical Review B*, 97(13), 2018.

[109] A. Mougin, M. Cormier, J. P. Adam, P. J. Metaxas, and J Ferré. Domain wall mobility, stability and Walker breakdown in magnetic nanowires. *Europhysics Letters (EPL)*, 78(5):57007, jun 2007.

[110] Jisu Ryu, Sug Bong Choe, and Hyun Woo Lee. Magnetic domain-wall motion in a nanowire: Depinning and creep. *Physical Review B - Condensed Matter and Materials Physics*, 84(7):1–12, 2011.

[111] Paul Bouquin, Siddharth Rao, Gouri Sankar Kar, and Thibaut Devolder. Size dependence of spin-torque switching in perpendicular magnetic tunnel junctions. *Applied Physics Letters*, 113(22), 2018.

[112] I. M. Miron, P. J. Zermatten, G. Gaudin, S. Auffret, B. Rodmacq, and A. Schuhl. Domain wall spin torquemeter. *Physical Review Letters*, 102(13):1–4, 2009.

[113] A. V. Khvalkovskiy, D. Apalkov, S. Watts, R. Chepulskii, R. S. Beach, A. Ong, X. Tang, A. Driskill-Smith, W. H. Butler, P. B. Visscher, D. Lottis, E. Chen, V. Nikitin, and M. Krounbi. Erratum: Basic principles of STT-MRAM cell operation in memory arrays. *Journal of Physics D: Applied Physics*, 46(13):139601, apr 2013.

[114] J. P. Adam, S. Rohart, J. P. Jamet, J. Ferré, A. Mougin, R. Weil, H. Bernas, and G. Faini. Magnetization reversal by confined droplet growth in soft/hard hybrid nanodisks with perpendicular anisotropy. *Physical Review B - Condensed Matter and Materials Physics*, 85(21):1–7, 2012.

[115] David P. Bernstein, Björn Bräuer, Roopali Kukreja, Joachim Stöhr, Thomas Hauet, Julien Cucchiara, Stéphane Mangin, Jordan A. Katine, Tolek Tyliszczak, Kang W. Chou, and Yves Acremann. Nonuniform switching of the perpendicular magnetization in a spin-torque-driven magnetic nanopillar. *Physical Review B - Condensed Matter and Materials Physics*, 83(18):1–4, 2011.

[116] L. Herrera Diez, V. Jeudy, G. Durin, A. Casiraghi, Y. T. Liu, M. Voto, G. Agnus, D. Bouville, L. Vila, J. Langer, B. Ocker, L. Lopez-Diaz, and D. Ravelosona. Wire edge dependent magnetic domain wall creep. *Physical Review B*, 98(5):1–7, 2018.

[117] Peter Fischer and Hendrik Ohldag. X-rays and magnetism. *Reports on Progress in Physics*, 78(9):94501, 2015.

[118] Mohamed Belmeguenai, Jean Paul Adam, Yves Roussigné, Sylvain Eimer, Thibaut Devolder, Joo Von Kim, Salim Mourad Cherif, Andrey Stashkevich, and André Thiaville. Interfacial Dzyaloshinskii-Moriya interaction in perpendicularly magnetized Pt/Co/AlOx ultrathin films measured by Brillouin light spectroscopy. *Physical Review B - Condensed Matter and Materials Physics*, 91(18):1–4, 2015.

[119] R. J. Radwański. Anisotropic ferrimagnets in high magnetic fields. *Physica B+C*, 142(1):57–64, 1986.

[120] I. Gross, W. Akhtar, A. Hrabec, J. Sampaio, L. J. Martínez, S. Chouaieb, B. J. Shields, P. Maletinsky, A. Thiaville, S. Rohart, and V. Jacques. Skyrmion morphology in ultrathin magnetic films. *Physical Review Materials*, 2(2):1–6, 2018.

[121] L. Landau and E. Lifshitz. On the theory of the dispersion of magnetic permeability in ferromagnetic bodies. In *Perspectives in Theoretical Physics*, pages 51–65. Elsevier, 1992.

[122] T.L. Gilbert. Classics in Magnetics A Phenomenological Theory of Damping in Ferromagnetic Materials. *IEEE Transactions on Magnetics*, 40(6):3443–3449, nov 2004.

[123] Ryoichi Kikuchi. On the Minimum of Magnetization Reversal Time. *Journal of Applied Physics*, 27(11):1352–1357, nov 1956.

[124] Arne Brataas, Andrew D. Kent, and Hideo Ohno. Current-induced torques in magnetic materials. *Nature Materials*, 11(5):372–381, 2012.

[125] J.C. Slonczewski. Current-driven excitation of magnetic multilayers. *Journal of Magnetism and Magnetic Materials*, 159(1-2):L1–L7, jun 1996.

[126] A. V. Khvalkovskiy, V. Cros, D. Apalkov, V. Nikitin, M. Krounbi, K. A. Zvezdin, A. Anane, J. Grollier, and A. Fert. Matching domain-wall configuration and spin-orbit torques for efficient domain-wall motion. *Physical Review B*, 87(2):020402, jan 2013.

[127] A. Manchon and S. Zhang. Theory of spin torque due to spin-orbit coupling. *Physical Review B*, 79(9):094422, 2009.

[128] Jack Bass and William P. Pratt. Spin-diffusion lengths in metals and alloys, and spin-flipping at metal/metal interfaces: an experimentalist's critical review. *Journal of Physics: Condensed Matter*, 19(18):183201, may 2007.

[129] S. Zhang and Z. Li. Roles of Nonequilibrium Conduction Electrons on the Magnetization Dynamics of Ferromagnets. *Physical Review Letters*, 93(12):127204, sep 2004.

[130] A. Vanhaverbeke and M. Viret. Simple model of current-induced spin torque in domain walls. *Physical Review B - Condensed Matter and Materials Physics*, 75(2):1–5, 2007.

[131] A. Thiaville, Y. Nakatani, J. Miltat, and Y. Suzuki. Micromagnetic understanding of current-driven domain wall motion in patterned nanowires. *Europhysics Letters*, 69(6):990–996, 2005.

[132] M.I. Dyakonov and V.I. Perel. Current-induced spin orientation of electrons in semiconductors. *Physics Letters A*, 35(6):459–460, jul 1971.

[133] C. Stamm, C. Murer, M. Berritta, J. Feng, M. Gabureac, P. M. Oppeneer, and P. Gambardella. Magneto-Optical Detection of the Spin Hall Effect in Pt and W Thin Films. *Physical Review Letters*, 119(8):087203, aug 2017.

[134] Ioan Mihai Miron, Gilles Gaudin, Stéphane Auffret, Bernard Rodmacq, Alain Schuhl, Stefania Pizzini, Jan Vogel, and Pietro Gambardella. Current-driven spin torque induced by the Rashba effect in a ferromagnetic metal layer. *Nature Materials*, 9(3):230–234, 2010.

[135] L. Liu, C.-F. Pai, Y. Li, H. W. Tseng, D. C. Ralph, and R. A. Buhrman. Spin-Torque Switching with the Giant Spin Hall Effect of Tantalum. *Science*, 336(6081):555–558, may 2012.

[136] T. A. Moore, I. M. Miron, G. Gaudin, G. Serret, S. Auffret, B. Rodmacq, A. Schuhl, S. Pizzini, J. Vogel, and M. Bonfim. High domain wall velocities induced by current in ultrathin Pt/Co/AlOx wires with perpendicular magnetic anisotropy. *Applied Physics Letters*, 93(26):1–4, 2008.

[137] Satoru Emori, Uwe Bauer, Sung-Min Ahn, Eduardo Martinez, and Geoffrey S. D. Beach. Current-driven dynamics of chiral ferromagnetic domain walls. *Nature Materials*, 12(7):611–616, jul 2013.

[138] G. Dresselhaus. Spin-Orbit Coupling Effects in Zinc Blende Structures. *Physical Review*, 100(2):580–586, oct 1955.

[139] A. Manchon and S. Zhang. Theory of nonequilibrium intrinsic spin torque in a single nanomagnet. *Physical Review B - Condensed Matter and Materials Physics*, 78(21):1–4, 2008.

[140] O. Chubykalo-Fesenko, U. Nowak, R. W. Chantrell, and D. Garanin. Dynamic approach for micromagnetics close to the Curie temperature. *Physical Review B - Condensed Matter and Materials Physics*, 74(9):1–5, 2006.

[141] D A Garanin. Fokker-Planck and Landau-Lifshitz-Bloch equations for classical ferromagnets. *Physical Review B*, 55(5):3050–3057, feb 1997.

[142] R. F.L. Evans, D. Hinzke, U. Atxitia, U. Nowak, R. W. Chantrell, and O. Chubykalo-Fesenko. Stochastic form of the Landau-Lifshitz-Bloch equation. *Physical Review B - Condensed Matter and Materials Physics*, 85(1):1–9, 2012.

[143] William Fuller Brown. Thermal fluctuations of a single-domain particle. *Physical Review*, 130(5):1677–1686, 1963.

[144] See Hun Yang, Kwang Su Ryu, and Stuart Parkin. Supplementary information of Domain-wall velocities of up to 750 m s -1 driven by exchange-coupling torque in synthetic antiferromagnets. *Nature Nanotechnology*, 10(3):221–226, 2015.

[145] Roald K. Wangsness. Sublattice Effects in Magnetic Resonance. *Physical Review*, 91(5):1085–1091, sep 1953.

[146] F. B. Hagedorn, C. D. Graham, and J. J. Rhyne. Domain wall motion in bubble materials. volume 72, pages 72–90, 1972.

[147] Erlend G. Tveten, Alireza Qaiumzadeh, O. A. Tretiakov, and Arne Brataas. Staggered dynamics in antiferromagnets by collective coordinates. *Physical Review Letters*, 110(12):1–5, 2013.

[148] Masamitsu Hayashi, Junyeon Kim, Michihiko Yamanouchi, and Hideo Ohno. Quantitative characterization of the spin-orbit torque using harmonic Hall voltage measurements. *Physical Review B - Condensed Matter and Materials Physics*, 89(14):1–15, 2014.

[149] Kevin Garello, Ioan Mihai Miron, Can Onur Avci, Frank Freimuth, Yuriy Mokrousov, Stefan Blügel, Stéphane Auffret, Olivier Boulle, Gilles Gaudin, and Pietro Gambardella. Symmetry and magnitude of spin-orbit torques in ferromagnetic heterostructures. *Nature Nanotechnology*, 8(8):587–593, aug 2013.

[150] Tomek Schulz, Kyujoon Lee, Benjamin Krüger, Roberto Lo Conte, Gurucharan V. Karnad, Karin Garcia, Laurent Vila, Berthold Ocker, Dafiné Ravelosona, and Mathias Kläui. Effective field analysis using the full angular spin-orbit torque magnetometry dependence. *Physical Review B*, 95(22):1–6, 2017.

[151] C. D. Stanciu, A. V. Kimel, F. Hansteen, A. Tsukamoto, A. Itoh, A. Kirilyuk, and Th Rasing. Ultrafast spin dynamics across compensation points in ferrimagnetic GdFeCo: The role of angular momentum compensation. *Physical Review B - Condensed Matter and Materials Physics*, 73(22):1–4, 2006.

[152] M. Binder, A. Weber, O. Mosendz, G. Woltersdorf, M. Izquierdo, I. Neudecker, J. R. Dahn, T. D. Hatchard, J. U. Thiele, C. H. Back, and M. R. Scheinfein. Magnetization dynamics of the ferrimagnet CoGd near the compensation of magnetization and angular momentum. *Physical Review B - Condensed Matter and Materials Physics*, 74(13):1–5, 2006.

[153] Soong-Geun Je, Gilles Gaudin, Olivier Boulle, Juan-Carlos Rojas-Sánchez, Thai Ha Pham, Pierre Vallobra, Gregory Malinowski, Daniel Lacour, Thibaud Fache, Michel Hehn, Stéphane Mangin, Marie-Claire Cyrille, Dae-Yun Kim, Sug-Bong Choe, and Mohamed Belmeguenai. Spin-orbit torque-induced switching in ferrimagnetic alloys: Experiments and modeling. *Applied Physics Letters*, 112(6), 2018.

[154] Kyoung Woong Moon, Changsoo Kim, Jungbum Yoon, Jun Woo Choi, Dong Ok Kim, Kyung Mee Song, Dongseuk Kim, Byong Sun Chun, and Chanyong Hwang. A spin torque meter with magnetic facet domains. *Nature Communications*, 9(1), 2018.

[155] Hajime Nakamura, Songtain Li, Xiaoxi Liu, and Akimitsu Morisako. Current-Induced Domain Wall Motion in TbFeCo micro wire. *Journal of Physics: Conference Series*, 266(6):012082, 2011.

[156] Xin Jiang, Li Gao, Jonathan Z. Sun, and Stuart S P Parkin. Temperature dependence of current-induced magnetization switching in spin valves with a ferrimagnetic CoGd free layer. *Physical Review Letters*, 97(21):1–4, 2006.

[157] Duck Ho Kim, Takaya Okuno, Se Kwon Kim, Se Hyeok Oh, Tomoe Nishimura, Yuushou Hirata, Yasuhiro Futakawa, Hiroki Yoshikawa, Arata Tsukamoto, Yaroslav Tserkovnyak, Yoichi Shiota, Takahiro Moriyama, Kab Jin Kim, Kyung Jin Lee, and Teruo Ono. Low Magnetic Damping of Ferrimagnetic GdFeCo Alloys. *Physical Review Letters*, 122(12):127203, 2019.

[158] Simone Moretti. *Micromagnetic study of magnetic domain wall motion : thermal effects and spin torques.* PhD thesis, Univ. Grenoble, 2017.

[159] A. A. Thiele. Steady-State Motion of Magentic Domains. *Physical Review Letters*, 30(6):230, 1973.

[160] J. C. Martinez and M. B.A. Jalil. Topological dynamics and current-induced motion in a skyrmion lattice. *New Journal of Physics*, 18(3), 2016.

[161] Q. Mistral, M. Van Kampen, G. Hrkac, Joo Von Kim, T. Devolder, P. Crozat, C. Chappert, L. Lagae, and T. Schrefl. Current-driven vortex oscillations in metallic nanocontacts. *Physical Review Letters*, 100(25):1–4, 2008.

[162] N. L. Schryer and L. R. Walker. The motion of 180° domain walls in uniform dc magnetic fields. *Journal of Applied Physics*, 45(12):5406–5421, 1974.

[163] Geoffrey S.D. Beach, Corneliu Nistor, Carl Knutson, Maxim Tsoi, and James L. Erskine. Dynamics of field-driven domain-wall propagation in ferromagnetic nanowires. *Nature Materials*, 4(10):741–744, 2005.

[164] Kwang Su Ryu, See Hun Yang, Luc Thomas, and Stuart S.P. Parkin. Chiral spin torque arising from proximity-induced magnetization. *Nature Communications*, 5(May):1–8, 2014.

[165] O. Boulle, G. Malinowski, and M. Kläui. Current-induced domain wall motion in nanoscale ferromagnetic elements. *Materials Science and Engineering R: Reports*, 72(9):159–187, 2011.

[166] G. S D Beach, C. Knutson, C. Nistor, M. Tsoi, and J. L. Erskine. Nonlinear domain-wall velocity enhancement by spin-polarized electric current. *Physical Review Letters*, 97(5):8–11, 2006.

[167] Ioan Mihai Miron, Thomas Moore, Helga Szambolics, Liliana Daniela Buda-Prejbeanu, Stéphane Auffret, Bernard Rodmacq, Stefania Pizzini, Jan Vogel, Marlio Bonfim, Alain Schuhl, and Gilles Gaudin. Fast current-induced domain-wall motion controlled by the Rashba effect. *Nature Materials*, 10(6):419–423, 2011.

[168] Masamitsu Hayashi, Luc Thomas, Charles Rettner, Rai Moriya, and Stuart S.P. Parkin. Direct observation of the coherent precession of magnetic domain walls propagating along permalloy nanowires. *Nature Physics*, 3(1):21–25, 2007.

[169] Stuart S P Parkin, Masamitsu Hayashi, and Luc Thomas. Magnetic Domain-Wall Racetrack Memory. *Science*, 320(5873):190–194, apr 2008.

[170] Kwang-Su Ryu, Luc Thomas, See-Hun Yang, and Stuart Parkin. Chiral spin torque at magnetic domain walls. *Nature Nanotechnology*, 8(7):527–533, 2013.

[171] J. P. Adam, N. Vernier, J. Ferré, A. Thiaville, V. Jeudy, A. Lemaître, L. Thevenard, and G. Faini. Nonadiabatic spin-transfer torque in (Ga,Mn)As with perpendicular anisotropy. *Physical Review B - Condensed Matter and Materials Physics*, 80(19):2–5, 2009.

[172] O. Boulle, L. D. Buda-Prejbeanu, M. Miron, and G. Gaudin. Current induced domain wall dynamics in the presence of a transverse magnetic field in out-of-plane magnetized materials. *Journal of Applied Physics*, 112(5), 2012.

[173] O. Boulle, S. Rohart, L. D. Buda-Prejbeanu, E. Jué, I. M. Miron, S. Pizzini, J. Vogel, G. Gaudin, and A. Thiaville. Domain wall tilting in the presence of the Dzyaloshinskii-Moriya interaction in out-of-plane magnetized magnetic nanotracks. *Physical Review Letters*, 111(21):1–5, 2013.

[174] J. Vandermeulen, S.A. Nasseri, B. Van de Wiele, G. Durin, B. Van Waeyenberge, and L. Dupré. Comparison between collective coordinate models for domain wall motion in PMA nanostrips in the presence of the Dzyaloshinskii-Moriya interaction. *Journal of Magnetism and Magnetic Materials*, 449:337–352, mar 2018.

[175] Derek Lau, Vignesh Sundar, Jian Gang Zhu, and Vincent Sokalski. Energetic molding of chiral magnetic bubbles. *Physical Review B*, 94(6):1–5, 2016.

[176] J. P. Pellegren, D. Lau, and V. Sokalski. Dispersive Stiffness of Dzyaloshinskii Domain Walls. *Physical Review Letters*, 119(2):1–5, 2017.

[177] Arne Vansteenkiste, Jonathan Leliaert, Mykola Dvornik, Mathias Helsen, Felipe Garcia-Sanchez, and Bartel Van Waeyenberge. The design and verification of MuMax3. *AIP Advances*, 4(10), 2014.

[178] Tomoe Nishimura, Duck Ho Kim, Yuushou Hirata, Takaya Okuno, Yasuhiro Futakawa, Hiroki Yoshikawa, Arata Tsukamoto, Yoichi Shiota, Takahiro Moriyama, and Teruo Ono. Correlation between magnetic properties and depinning field in field-driven domain wall dynamics in GdFeCo ferrimagnets. *Applied Physics Letters*, 112(17), 2018.

[179] Takaya Okuno, Duck-Ho Kim, Se-hyeok Oh, Se Kwon Kim, Yuushou Hirata, Tomoe Nishimura, Woo Seung Ham, Yasuhiro Futakawa, Hiroki Yoshikawa, Arata Tsukamoto, Yaroslav Tserkovnyak, Yoichi Shiota, Takahiro Moriyama, Kab-jin Kim, Kyung-jin Lee, and Teruo Ono. Spin-transfer torques for domain wall motion in antiferromagnetically coupled ferrimagnets. *Nature Electronics*, 2(9):389–393, sep 2019.

[180] B. F. Miao, S. Y. Huang, D. Qu, and C. L. Chien. Inverse spin Hall effect in a ferromagnetic metal. *Physical Review Letters*, 111(6):1–5, 2013.

[181] Luqiao Liu, O. J. Lee, T. J. Gudmundsen, D. C. Ralph, and R. A. Buhrman. Current-Induced Switching of Perpendicularly Magnetized Magnetic Layers Using Spin Torque from the Spin Hall Effect. *Physical Review Letters*, 109(9):096602, aug 2012.

[182] K. Ando, S. Takahashi, K. Harii, K. Sasage, J. Ieda, S. Maekawa, and E. Saitoh. Electric Manipulation of Spin Relaxation Using the Spin Hall Effect. *Physical Review Letters*, 101(3):036601, jul 2008.

[183] Werner Döring. Über die Trägheit der Wände zwischen Weißschen Bezirken. *Zeitschrift für Naturforschung A*, 3(7):373–379, jul 1948.

[184] A. Stankiewicz, A. Maziewski, K. A. Safaryan, and B. A. Ivanov. On the Calculation of Magnetic Domain Wall Mass. *IEEE Transactions on Magnetics*, 30(2):878–880, 1994.

[185] Mahdi Jamali, Kyung-Jin Lee, and Hyunsoo Yang. Effect of nonadiabatic spin transfer torque on domain wall resonance frequency and mass. *Applied Physics Letters*, 98(9):092501, feb 2011.

[186] F. H. De Leeuw and J. M. Robertson. Observation and analysis of magnetic domain wall oscillations in Ga:YIG films. *Journal of Applied Physics*, 46(7):3182–3188, 1975.

[187] Eiji Saitoh, Hideki Miyajima, Takehiro Yamaoka, and Gen Tatara. Current-induced resonance and mass determination of a single magnetic domain wall. *Nature*, 432(7014):203–206, 2004.

[188] Wanjun Jiang, Gong Chen, Kai Liu, Jiadong Zang, Suzanne G.E. te Velthuis, and Axel Hoffmann. Skyrmions in magnetic multilayers. *Physics Reports*, 704:1–49, 2017.

[189] Kai Litzius, Ivan Lemesh, Benjamin Krüger, Pedram Bassirian, Lucas Caretta, Kornel Richter, Felix Büttner, Koji Sato, Oleg A. Tretiakov, Johannes Förster, Robert M. Reeve, Markus Weigand, Iuliia Bykova, Hermann Stoll, Gisela Schütz, Geoffrey S.D. Beach, and Mathias Klaüi. Skyrmion Hall effect revealed by direct time-resolved X-ray microscopy. *Nature Physics*, 13(2):170–175, 2017.

[190] Diana Prychynenko, Matthias Sitte, Kai Litzius, Benjamin Krüger, George Bourianoff, Mathias Kläui, Jairo Sinova, and Karin Everschor-Sitte. Magnetic Skyrmion as a Nonlinear Resistive Element: A Potential Building Block for Reservoir Computing. *Physical Review Applied*, 9(1):14034, 2018.

[191] A. A. Thiele. Applications of the gyrocoupling vector and dissipation dyadic in the dynamics of magnetic domains. *Journal of Applied Physics*, 45(1):377–393, jan 1974.

[192] V. Jeudy, J. Curiale, J. P. Adam, A. Thiaville, A. Lemaître, and G. Faini. Current induced domain wall motion in GaMnAs close to the Curie temperature. *Journal of Physics Condensed Matter*, 23(44), 2011.

[193] Duc-The Ngo, Kotato Ikeda, and Hiroyuki Awano. Direct Observation of Domain Wall Motion Induced by Low-Current Density in TbFeCo Wires. *Applied Physics Express*, 4(9):093002, aug 2011.

[194] Kyoung Woong Moon, Duck Ho Kim, Sang Cheol Yoo, Cheong Gu Cho, Sungmin Hwang, Byung-nam Kahng, Byoung Chul Min, Kyung Ho Shin, and Sung Bong Choe. Distinct universality classes of domain wall roughness in two-dimensional Pt/Co/Pt films. *Physical Review Letters*, 110(10):1–5, 2013.

[195] Takuya Taniguchi, Kab-Jin Kim, Yoko Yoshimura, Takahiro Moriyama, Hironobu Tanigawa, Tetsuhiro Suzuki, Eiji Kariyada, and Teruo Ono. Different stochastic behaviors for magnetic field and current in domain wall creep motion. *Applied Physics Express*, 7(5):053005, may 2014.

[196] S. DuttaGupta, S. Fukami, B. Kuerbanjiang, H. Sato, F. Matsukura, V. K. Lazarov, and H. Ohno. Magnetic domain-wall creep driven by field and current in Ta/CoFeB/MgO. *AIP Advances*, 7(5), 2017.

[197] V. Jeudy, A. Mougin, S. Bustingorry, W. Savero Torres, J. Gorchon, A. B. Kolton, A. Lemaître, and J. P. Jamet. Universal Pinning Energy Barrier for Driven Domain Walls in Thin Ferromagnetic Films. *Physical Review Letters*, 117(5):1–5, 2016.

[198] S. Lemerle, J. Ferré, C. Chappert, V. Mathet, T. Giamarchi, and P. Le Doussal. Domain Wall Creep in an Ising Ultrathin Magnetic Film. *Physical Review Letters*, 80(4):849–852, 1998.

[199] R. Diaz Pardo, W. Savero Torres, A. B. Kolton, S. Bustingorry, and V. Jeudy. Universal depinning transition of domain walls in ultrathin ferromagnets. *Physical Review B*, 95(18):1–7, 2017.

[200] W Savero Torres, R Díaz Pardo, S Bustingorry, A B Kolton, A Lemaître, and V Jeudy. Universal dimensional crossover of domain wall dynamics in ferromagnetic films. *Physical Review B*, 99(20):201201, may 2019.

[201] Chun Yeol You, In Mo Sung, and Byung Kyu Joe. Analytic expression for the temperature of the current-heated nanowire for the current-induced domain wall motion. *Applied Physics Letters*, 89(22):22–24, 2006.

[202] J. Curiale, A. Lemaître, T. Niazi, G. Faini, and V. Jeudy. Joule heating and current-induced domain wall motion. *Journal of Applied Physics*, 112(10), 2012.

[203] Chun Yeol You and Seung Seok Ha. Temperature increment in a current-heated nanowire for current-induced domain wall motion with finite thickness insulator layer. *Applied Physics Letters*, 91(2):10–13, 2007.

[204] Kab Jin Kim, Jae Chul Lee, Sug Bong Choe, and Kyung Ho Shin. Joule heating in ferromagnetic nanowires: Prediction and observation. *Applied Physics Letters*, 92(19):1–4, 2008.

[205] N. Vernier, D. A. Allwood, D. Atkinson, M. D. Cooke, and R. P. Cowburn. Domain wall propagation in magnetic nanowires by spin-polarized current injection. *Europhysics Letters*, 65(4):526–532, 2004.

[206] C. Burrowes, A. P. Mihai, D. Ravelosona, J. V. Kim, C. Chappert, L. Vila, A. Marty, Y. Samson, F. Garcia-Sanchez, L. D. Buda-Prejbeanu, I. Tudosa, E. E. Fullerton, and J. P. Attané. Non-adiabatic spin-torques in narrow magnetic domain walls. *Nature Physics*, 6(1):17–21, 2010.

[207] O. Boulle, J. Kimling, P. Warnicke, M. Kläui, U. Rüdiger, G. Malinowski, H. J.M. Swagten, B. Koopmans, C. Ulysse, and G. Faini. Nonadiabatic spin transfer torque in high anisotropy magnetic nanowires with narrow domain walls. *Physical Review Letters*, 101(21):1–4, 2008.

[208] V. Lecomte, S. E. Barnes, J. P. Eckmann, and T. Giamarchi. Depinning of domain walls with an internal degree of freedom. *Physical Review B - Condensed Matter and Materials Physics*, 80(5):1–5, 2009.

[209] J. Wunderlich, D. Ravelosona, C. Chappert, F. Cayssol, V. Mathet, J. Ferre, J.-P. Jamet, and A. Thiaville. Influence of geometry on domain wall propagation in a mesoscopic wire. *IEEE Transactions on Magnetics*, 37(4):2104–2107, jul 2001.

[210] T. Suzuki, S. Fukami, N. Ohshima, K. Nagahara, and N. Ishiwata. Analysis of current-driven domain wall motion from pinning sites in nanostrips with perpendicular magnetic anisotropy. *Journal of Applied Physics*, 103(11):113913, jun 2008.

[211] Yoko Yoshimura, Tomohiro Koyama, Daichi Chiba, Yoshinobu Nakatani, Shunsuke Fukami, Michihiko Yamanouchi, Hideo Ohno, Kab Jin Kim, Takahiro Moriyama, and Teruo Ono. Effect of spin Hall torque on current-induced precessional domain wall motion. *Applied Physics Express*, 7(3), 2014.

[212] Joo-Von Kim and C. Burrowes. Influence of magnetic viscosity on domain wall dynamics under spin-polarized currents. *Physical Review B*, 80(21):214424, dec 2009.

[213] Kab Jin Kim, Jisu Ryu, Gi Hong Gim, Jae Chul Lee, Kyung Ho Shin, Hyun Woo Lee, and Sug Bong Choe. Electric current effect on the energy barrier of magnetic domain wall depinning: Origin of the quadratic contribution. *Physical Review Letters*, 107(21):1–5, 2011.

[214] Jae Chul Lee, Kab Jin Kim, Jisu Ryu, Kyoung Woong Moon, Sang Jun Yun, Gi Hong Gim, Kang Soo Lee, Kyung Ho Shin, Hyun Woo Lee, and Sug Bong Choe. Universality classes of magnetic domain wall motion. *Physical Review Letters*, 107(6):1–5, 2011.

[215] Yuushou Hirata, Duck-Ho Kim, Takaya Okuno, Woo Seung Ham, Sanghoon Kim, Takahiro Moriyama, Arata Tsukamoto, Kab-Jin Kim, and Teruo Ono. Distinct domain-wall motion between creep and flow regimes near the angular momentum compensation temperature of ferrimagnet. *arXiv*, may 2017.

[216] Dong Li, Baoshan Cui, Jijun Yun, Minzhang Chen, Xiaobin Guo, Kai Wu, Xu Zhang, Yupei Wang, Jian Mao, Yalu Zuo, Jianbo Wang, and Li Xi. Current-Induced Domain Wall Motion and Tilting in Perpendicularly Magnetized Racetracks. *Nanoscale Research Letters*, 13, 2018.

[217] E. Jué, A. Thiaville, S. Pizzini, J. Miltat, J. Sampaio, L. D. Buda-Prejbeanu, S. Rohart, J. Vogel, M. Bonfim, O. Boulle, S. Auffret, I. M. Miron, and G. Gaudin. Domain wall dynamics in ultrathin Pt/Co/AlOx microstrips under large combined magnetic fields. *Physical Review B*, 93(1):1–11, 2016.

Titre : Dynamique de paroi de domaine sous courant de spin dans des alliages ferrimagnétiques

Mots clés : Parois Magnétiques, Dynamique d'aimantation, Couple de Spin, Materiaux Ferrimagnetics

Résumé : Malgré les grands succès de la spintronique ces dernières années, plusieurs questions demeurent quant à l'efficacité et la rapidité de la manipulation électrique de l'aimantation. Ces problèmes semblent pouvoir être résolus en considérant des nouveaux matériaux plus exotiques mélangeant différents sous-réseaux magnétiques. Les alliages ferrimagnétiques de type terrer rares-métaux de transitions sont composés de deux populations magnétiques couplées antiferromagnétiquement. Dans ces matériaux, deux configurations particulièrement intéressantes se distinguent : les points de compensation magnétique et angulaire auxquels l'aimantation ou le moment angulaire totale de l'alliage s'annulent. Dans ces configurations, les matériaux ferrimagnétiques présentent de nouvelles propriétés très intéressantes tant sur le plan fondamental que technologique. Dans cette thèse, la dynamique d'aimantation dans ces matériaux a été étudiée expérimentalement et théoriquement sous le prisme de la dynamique de la paroi de domaine magnétique sous courant de spin. Des alliages ferrimagnétiques (comme le TbFeCo ou le GdFeCo) ont été déposés en couches minces par co-évaporation et étudiés en combinant plusieurs méthodes : magnétiques, électriques et optiques ce qui révéla leur grand intérêts spintronic. Des techniques d'imagerie ont également montré une organisation en domaine magnétique, séparée par des parois facilement manipulables. Cette étude des propriétés statiques a également montré que l'existence d'un gradient chimique en épaisseur induit des effets habituellement surfaciques dans la zone centrale des films tel que le DMI. La dynamique de la paroi sous courant de spin (par couple de transfert de spin et spin-orbite) a été étudiée dans deux études qui ont mis en évidence l'efficacité et la rapidité du contrôle électrique de l'aimantation. L'une d'elle a également révélé une dynamique particulière qui est la signature directe d'un retournement magnétique sans précession à la compensation angulaire. Enfin, un modèle théorique effectif des propriétés statique et dynamique des alliages ferrimagnétiques a été développé et a révélé de nouveaux modes de propagation de paroi comme le retournement sans précession ou la disparition des régimes transitoires.

Title : Domain Wall Dynamics driven by spin-current in Ferrimagnetic alloys

Keywords : Magnetic Domian Wall, Magnetization Dynamics, Spin-Torques, Ferrimagnets

Abstract : Despite the large success in spintronics, several questions remain in the field among which improving the efficiency and the speed of the magnetization manipulation by electrical current. Those issues can be addressed through research on new exotic materials that mix different magnetic sub-lattices. Rare earth-transition metal ferrimagnetic alloys are composed by two different magnetic sub-lattices antiferromagneticaly coupled which makes them promising. Specifically, two interesting configurations can emerge called the magnetic and the angular compensation point at which the alloy's net magnetization or net angular momentum independently vanishes. In these configurations, ferrimagnets seem present new and very convenient properties interesting both fundamentally and technologically. In this thesis, these materials were experimentally and theoretically studied through the prism of the magnetic domain wall dynamics driven by spin-currents. Ferrimagnetic alloys (such as TbFeCo or GdFeCo) were grown in thin film by co-evaporation. Their structural and magnetic properties were studied combining magnetization, electrical and optical methods which has revealed their spintronic interests. Imaging techniques shown a perpendicularly magnetized domain organization separated by easily handled domain walls. These statics properties studies also shown a chemical depth gradient which induces surface-like effects in the bulk region of films such as DMI. The domain wall dynamics driven by spin current was investigated in two studies reveling very high efficiency and speed of their electrical manipulation. First, the efficiency of the current manipulation via spin-transfer torque was measured by studing the domain wall motion under combined effects of field and current in the creep regime. Secondly, the domain wall dynamics driven by spin-orbit torque was fully characterized using in-plane fields. This measurement have revealed a singular dynamic of the domain wall at the angular compensation which is the direct signature of the precession-free reversal of the magnetization. Finally, an effective theoretical model of both the static and the dynamics of ferrimagnets was developed. It allows to describe all the observed experimental results. Using this formalism, we study analytically and numerically the domain wall dynamics driven by field or spin-currents reviling new propagation regimes like the precession-free dynamics or the vanishing of the transient motions.